1-1-2013

Benthic Boundary Layer Processes: Bedform Evolution and Bottom Turbulence

Timothy Robert Nelson
University of South Carolina

BENTHIC BOUNDARY LAYER PROCESSES: BEDFORM EVOLUTION AND BOTTOM TURBULENCE

by

Timothy Robert Nelson

Bachelor of Science
University of Kentucky, 2004

Master of Science
University of South Carolina, 2011

Submitted in Partial Fulfillment of the Requirements

For the Degree of Doctor of Philosophy in

Geological Sciences

College of Arts and Sciences

University of South Carolina

2013

Accepted by:

George Voulgaris, Major Professor

Alexander E. Yankovsky, Committee Member

Scott M. White, Committee Member

John C. Warner, Committee Member

Lacy Ford, Vice Provost and Dean of Graduate Studies

ACKNOWLEDGEMENTS

Financial support for this work was partially provided by the National Science Foundation (NSF OCE-0451989, OCE-0535893, and OCE-1132130, awarded to George Voulgaris) and by the South Carolina Coastal Erosion Project, a cooperative study supported by the US Geological Survey and the South Carolina Sea Grant Consortium (Sea Grant Project no: R/CP-11). The Georgia data set was collected onboard the R/V Savannah of the Skidaway Institute of Oceanography while the Long Bay data set was collected onboard the R/V Dan More with assistance from the US Geological Survey field support personnel. Additional support was provided in the form of instructional assistantships through the University of South Carolina.

I would like to express my personal gratitude to my advisor, Dr. George Voulgaris, for the opportunity to work in his lab and his guidance throughout graduate school. I also express my thanks to my committee members Dr. Alexander Yankovsky, Dr. Scott White, and Dr. John Warner for their helpful feedback. Previous and current members of the CPSD lab have been invaluable with data collection, interpretation, and have been there to answer any questions.

I would also like to thank my family, without whom I would not have finished. My parents, Robert and Marijo Nelson, and grandfather, Donald Keil, have always been a constant source of encouragement and motivation throughout my life and always encouraged me to follow my dreams. I would also like to thank my in-laws, Dwayne and Marcella Styles, who opened their home to me while I was continuing to pursue my

degree. My deepest heart felt gratitude goes to my awesome wife Tania Nelson, who has always encouraged me to pursue my goals, provided tremendous support through rough days, and has been very understanding of the long work hours and months apart while working on research. Her constant support, encouragement, and love have kept me going throughout graduate school.

ABSTRACT

Bedform roughness, caused by ripples on the seabed, plays an important role in controlling sediment dynamics in the nearshore region. In this dissertation, the temporal and spatial evolution of ripples from two field sites located in the South Atlantic Bight, offshore Long Bay, SC and Georgia are used to relate wave-induced ripple geometry (wavelength and orientation) to near bed directional wave velocities. 2-D spectral analysis techniques were developed to automate detection of ripple wavelength, direction, and irregularity. This analysis showed that magnitude, direction, and duration of wave forcing controls ripple geometry and irregularity. During highly energetic events, ripple geometry changes rapidly and the ripples align with the main wave direction. During periods of low energy conditions, close to the critical conditions for initiation of sediment motion, ripple evolution occurs at a much slower rate often leading to irregularities such as terminations and bifurcations along the ripple crest. Under constantly changing wave direction, the rippled bed becomes highly disorganized.

Equilibrium ripples were found to occur only when either strong wave forcing was present or the forcing remained constant for a long duration. These equilibrium ripples, when combined to a database of existing published ripple measurements, were found to have a wavelength that scales with the wave orbital semi-excursion and sediment grain diameter. Ripple steepness was found to remain relatively constant and it only slightly increased for shorter ripple wavelengths. These findings allowed for the

development of a new equilibrium ripple predictor suitable for application in a wide range of wave and sediment conditions.

In order to describe the temporal variability between equilibrium states, a 2-D time-variable ripple prediction model developed. This new model allowed for the prediction of ripple wavelength, height, and orientation. Since ripple irregularity is associated with directionality, the new model also predicts the irregularity of the rippled seabed and second order ripples (i.e. cross-ripples). This model was tested against existing time-dependent models and found to improve predictions of wavelength, height, and orientation, especially for relict ripples.

Turbulence was measured via the eddy correlation and inertial dissipation methods from which drag coefficients were calculated. The data reveal a trend of decreasing drag for increasing ripple irregularity and increasing ripple height. In similar fashion, suspended sediment concentrations were calculated from ABS systems and it was found that convective sediment resuspension extended to greater elevation above the seabed when ripples were more regular.

TABLE OF CONTENTS

LIST OF TABLES

LIST OF FIGURES

CHAPTER 1

INTRODUCTION

1.1. Background

As surface gravity waves propagate from deep water into shallow water, their orbital motions begin to interact with the seabed sediment. As the wave orbital motions increase, the bed sediment begins to move back and forth forming parallel ridges on the seabed [*Bagnold*, 1946; *Sleath*, 1984]. These features play an important role in boundary layer processes. As the ripple steepness (height (η) to wavelength (λ) ratio) increases, a vortex forms on the lee side of the ripple. This erodes the ripple and traps sediment eroded from the crest. Upon flow reversal, the vortex is ejected up and over the ripple crest and the sediment is convected to greater heights than if the bed were flat [e.g. *Thorne et al.*, 2003]. A rippled bed increases the roughness of the seabed, which alters the mean current profile [*Grant and Madsen*, 1986] and increases nearbed turbulence. The enhanced turbulence increases the capability of the flow to keep sediment in suspension, thereby increasing the vertical distribution of sediment in suspension and resulting in greater sediment transport by mean flows.

The roughness due to ripples, termed form roughness, has been related to the ripple height and wavelength taking the form η^2/λ [*Grant and Madsen*, 1982; *Nielsen*, 1993]. Assuming constant steepness the form roughness can be written as a function of η alone [*Wikramanayake and Madsen*, 1994]. The form roughness was also found to be a function of the angle between the ripple crest and the mean current by *Powell et al.*

[2000] and *Madsen et al.* [2010]. This roughness can lead to significant wave energy attenuation (up to 93%) for large ripples present on wide continental shelves [*Ardhuin et al.*, 2003].

Ripples are also a source and/or sink of nutrients and contaminants [e.g., *Precht and Huettel*, 2004; *Rocha*, 2008 and references therein], which are released to the overlying water column when the ripple adjust geometries due to a change wave or current forcing. Furthermore, a pressure gradient forms between the high-pressure side and low-pressure side of the ripple, forcing fluid through the pore space and flushing out trapped nutrients. Ripples also improve the detection of buried objects by enhancing the penetration of acoustic energy into the seabed [*Chotiros et al*., 2002; *Jackson et al*., 2002; *Thorsos and Richardson,* 2002].

Ripples can form in various shapes and sizes depending on the strength and duration of the forcing. Once the forcing is large enough to mobilize sediment, ripples will continue to grow until a stable "equilibrium" geometry is obtained at which point the sediment removed from the ripple is the same as that added. As long as the flow remains the same strength, the ripple will not change in wavelength, height, or orientation. However, when the forcing changes, the ripple is no longer in equilibrium with the flow and begins to adjust towards a new equilibrium configuration. The amount of time required for the ripple to attain the new geometry depends on the strength of the flow and whether or not the flow is steady [*Davis et al.*, 2004; *Voropayev et al.*, 1999; *Soulsby and Whitehouse*, 2005; *Traykovski*, 2007; and references therein].

A number of studies on the equilibrium geometry (η and λ) of ripples have been conducted over the past century. Many of the early studies were conducted in laboratory

settings [e.g. *Yalin and Russell*, 1962; *Kennedy and Falcon*, 1965; *Lofquist*, 1978; and others] as field measurements were difficult to obtain. Subsequently divers [e.g., *Miller and Komar*, 1980] conducted surveys followed by the deployment of underwater cameras. Over the past two decades, acoustic imaging via stationary sector scanning sonar systems have been used [e.g., *Hay and Wilson*, 1994; *Traykovski et al.*, 1999; and others]. These new systems have allowed regular sampling over long deployments and have resulted in numerous databases of ripple geometries. As more data has been collected numerous methods have been developed to predict the equilibrium geometry for a specific forcing and sediment type [e.g., *Nielsen*, 1981; *Van Rijn*; 1993; *Wikramanayake and Madsen*; 1994; *Grant and Madsen*, 1982]; the various methods differ and often result in a wide range of predictions.

When ripples do not obtain equilibrium prior to the flow strength becoming too weak to mobilize sediment, the ripple becomes "frozen" and the geometry no longer changes due to waves or currents. These relict ripples can remain on the seabed for hours to months until the flow strength increases. While the flow does not alter the geometry, the ripple height does decay due to biological and diffusive processes [*Hay* 2008; *Voulgaris and Morin*, 2008]. Since these features can remain present on the seabed in a stable configuration for a long duration, their geometry can continue to influence turbulence and the mean flow structure. The prediction of this value is not as simple as assuming the previous equilibrium condition, since the ripple was likely not in equilibrium with the flow but in a transient stage.

During the transient stage, ripples actively adjust from one configuration to another, which may entail a change in wavelength and/or orientation. Most studies have

focused on the evolution of only ripple height and wavelength and these studies have found that the time required for adjustment depends on the strength of the flow and duration [*Davis et al.*, 2004, *Traykovski*, 2007; references therein]. These studies have led to the development of time dependent models that predict the evolution of ripple wavelength and height from one equilibrium geometry to another. However, these predictors ignore the influence of a change in ripple orientation due to a new forcing direction. The model of *Soulsby and Whitehouse* [2005] predicts a gradual change in orientation; however, this adjustment does not result in a change in ripple height or wavelength. Furthermore, the *Soulsby and Whitehouse* [2005] model cannot predict the presence of multiple ripple trains and does not provide information about the irregularity.

In order to predict the spatial geometry and irregularity of transient and relict ripples, the response of ripple height and wavelength to a change in orientation needs to be taken into account. Since seabed roughness has been shown to depend on both ripple height, wavelength, and orientation, all of these parameters need to be accurately calculated.

1.2. Scope of this Dissertation

The focus on this dissertation is the prediction of the temporal and spatial ripple evolution of ripple geometry and the influence of ripple irregularity on seabed roughness and sediment resupsension. In chapters 2 through 4, the temporal and spatial evolution of ripple geometry is examined. A new equilibrium ripple geometry model is developed in chapter 2. In chapter 3, the spatial configurations during various hydrodynamic forcing conditions are analyzed to determine which processes are important in the temporal evolution. In chapter 4, a new 2-D time dependent ripple model is developed which

addresses the ripple evolution observed in chapter 3. In chapters 5 and 6, the influence of ripple shape and geometry on turbulence and suspended sediment concentration is examined. A brief description of each chapter is given below.

1.2.1. Chapter 2

In this chapter, a new equilibrium ripple model is developed through the compilation of existing ripple geometries published in literature and two new field sites further discussed in chapter 3. The analysis focuses on the performance of existing predictors and the fit of the combined data set to various hydrodynamic parameters. From this analysis a new equilibrium predictor is developed which best describes the data set for the range of hydrodynamics present in the data set. The questions addressed in the chapter are:

(a) How well do existing equilibrium ripple models perform against the combined database?

(b) Is there a difference between ripple geometry due to regular vs. irregular waves?

(c) Which parameters scale best with equilibrium ripple geometry?

1.2.2. Chapter 3

In this chapter, the temporal and spatial evolution of ripples is described for a variety of storm conditions. The spectral characteristics are used to describe the ripple irregularity and provide a quantitative means of defining ripple shape. The main questions addressed in the chapter are:

(a) Can ripple shapes be defined quantitatively from the seabed spectra?

(b) What are the important forcings controlling transient ripple evolution?

(c) How do ripples respond to a change in wave direction?

1.2.3. Chapter 4

In this chapter, a 2-D time variable ripple model is developed to predict the transient, relict, and equilibrium ripple geometries as a function of time as well as predict multiple ripple trains and seabed irregularity. The main questions addressed in this chapter are:

(a) Can a 2-D spectral time dependent model accurately predict the spatial and temporal ripple evolution?

(b) What are the strength and weakness of the model and is there an improvement over existing methods of predicting ripple geometry?

1.2.4. Chapter 5

In this chapter, shear stresses are calculated using 3-D velocity time series. Drag coefficients are then calculated and compared to the ripple geometry and shape to determine which ripple characteristics are most important for calculating form drag. The main questions addressed in this chapter are:

(a) How do the estimates of shear stress using the eddy correlation and inertial dissipation method compare to each other?

(b) Which ripple characteristic (η, λ, orientation, or shape) or combination is most responsible for the shear stress experienced by currents?

1.2.5. Chapter 6

In this chapter, acoustic backscatter is converted to suspended sediment concentration. Their profiles are used to calculate reference concentrations and determine

the vertical extent of convective and diffusive sediment resuspension. The main questions addressed in this chapter are:

(a) Does the spatial configuration of ripple influence the near bed reference concentration?

(b) Does the spatial configuration of ripples influence the shape of the sediment suspension profile?

CHAPTER 2

PREDICTING WAVE-INDUCED RIPPLE EQUILIBRIUM GEOMETRY[1]

[1]Nelson, T. R., G. Voulgaris, and P. Traykovski. 2013. Journal of Geophysical Research - Oceans, 118, 3202–3220.
Reprinted here with permission of publisher.

2.1. Introduction

In the coastal ocean, ripples are formed by surface gravity waves travelling in water depths shallow enough for the oscillatory motion to be felt by the bed sediments. Once these oscillatory motions become large enough for the sediment grains to mobilize, the seabed begins to organize into a series of parallel ridges oriented perpendicular to the direction of wave propagation. These initial ripples have a small steepness (defined as the ratio of ripple height to wavelength) and are commonly known as rolling grain ripples [*Bagnold*, 1946]. Once the ripple steepness becomes greater than approximately 0.1, a vortex (eddy) forms on the lee side of the ripple that traps any sediment eroded from the ripple surface. Upon flow reversal, this sediment is ejected higher into the water column [*Bagnold*, 1946] contributing to increased sediment resuspension. In addition to their effect on resuspension, ripples play an important role in bottom friction as they affect turbulence levels and mean flow structure in the benthic boundary layer [e.g., *Grant and Madsen*, 1986] and also contribute to enhancing wave attenuation [e.g., *Ardhuin et al.*, 2003]. More recently, *Madsen et al.* [2010] showed that wave-induced ripples could also alter the direction of the mean current close to the seabed, possibly having implications on the overall direction of sediment transport.

Ripples can also act as a source (or sink) of seabed nutrients which are released to the overlying water column (or injected into the seabed) when they adjust their size, shape or are eroded during sheet flow conditions [e.g., *Precht and Huettel*, 2004]. Even under stable geometry, the pressure gradient forming between the high (stoss) and low

pressure (lee) sides of the ripple can contribute to fluid permeating the ripple body thereby flushing out nutrients or contaminants trapped in the space between the sedimentary particles that constitute the ripple [*Huettel et al.*, 1998; *Rocha*, 2008]. Furthermore, the presence of ripples affects the use of acoustics in the marine environment as they facilitate the penetration of acoustic waves in the seabed [*Chotiros et al.*, 2002; *Jackson et al.*, 2002; *Thorsos and Richardson*, 2002] a condition that improves the detection of buried objects. On the other hand, they provide a backscattering surface that complicates seabed classification using acoustic backscattering techniques [e.g., *Voulgaris et al.*, 1992; *Collins and Voulgaris*, 1993].

Because of their importance, a number of studies have been carried out aiming at predicting the ripple dimensions for a given wave forcing. Earlier studies focused on identifying the geometric characteristics of ripples (wavelength and height) for a given wave orbital velocity, wave period and sediment size [e.g., *Komar*, 1974; *Clifton*, 1976; *Nielsen*, 1981; *Grant and Madsen*, 1982; and references therein] and produced models that predict ripple wavelength and height assuming that a final form has been achieved (equilibrium ripple geometry). More recently, time-variable ripple prediction models [e.g., *Traykovski*, 2007; *Soulsby et al.*, 2012] have been developed that are able to predict ripple dimensions at any time independently if the ripples are in equilibrium or not. These models, based on sediment transport principles, assume that when the seabed is not in equilibrium with the hydrodynamic forcing, the ripple reorganizes itself in order to achieve the equilibrium conditions. As the wave forcing changes in time so does the ultimate geometry the seabed tries to achieve (the equilibrium conditions) and prediction of this intermediate geometry is the goal of the time dependent models which in turn

depends on the definition of the equilibrium ripple predictor. To date a large number of equilibrium models have been described in the literature. Table 1 shows the references of 13 most commonly used predictors spanning the years 1981 to 2009 as well as the type of data they used for deriving their corresponding model.

The basis for many of the equilibrium ripple predictors is a set of dimensionless parameters based on the flow properties and sediment characteristics. This approach was first used by *Yalin and Russell* [1962] and further developed by others [*Carstens et al.*, 1969; *Mogridge and Kamphuis*, 1972; *Dinger*, 1974; *Pedocchi and García*, 2009a]. The parameters commonly include wave bottom orbital velocity (u_b), wave period (T), median sediment grain diameter (D_{50}), sediment density (ρ_s), density of fluid (ρ_w), and gravity (g). This has led to the development of the following non-dimensional parameters:

$$\left[T \cdot \nu / D_{50}^2 \quad , \; u_b D_{50} / \nu \; , \; \sqrt{(s-1) g D_{50}^3} \Big/ \nu \quad , \; s-1 \quad , \; \phi \right] \tag{2.1}$$

where $s=\rho_s/\rho_w$, ν is the kinematic viscosity of the fluid and ϕ is the angle of repose which for sand is approximately equal to 32°. Various combinations of the above non-dimensional numbers constitute the basis for many of the parameters commonly used in sediment dynamics such as the mobility number, the wave Reynolds number, the non-dimensional sediment parameter, the wave period parameter, and the ratio of the wave orbital semi excursion to the sediment grain size (A_b/D_{50}). A detailed description of the derivation of these parameters can be found in *Pedocchi and García* [2009a] while the corresponding equations are further described in section 2.2.

The plethora of equilibrium ripple predictors, the different scaling used between them and the lack of agreement amongst them emphasizes the point that the problem has not been resolved yet. The discrepancies could be attributed to differences in the data sets

used in the development of these models, with some of them being obtained in the field and others in the laboratory; the quality of the data and the accuracy of the assumption that the data used represent real equilibrium conditions.

Many of the early studies were primarily conducted in laboratory settings where the hydrodynamics can be easily controlled and ripples consistently observed [e.g., *Yalin and Russell*, 1962; *Kennedy and Falcon*, 1965; *Carstens et al.*, 1969; *Lofquist 1978*). Later on, use of divers allowed for field observations under conditions conducive to the diver's safety and water visibility [e.g., *Inman*, 1957; *Miller and Komar*, 1980]. Subsequently, such observations were automated using underwater cameras which allowed for regular sampling intervals but were hindered by reduced visibility during energetic conditions [e.g., *Boyd et al.*, 1988; *Powell et al.*, 2000; *Xu*, 2005, and references therein]. During the past two decades, the use of a stationary sector scanning sonar system has allowed for continuous sampling during long deployments regardless of water visibility [e.g., *Hay and Wilson*, 1994; *Traykovski et al.*,1999; *Voulgaris and Morin*, 2008; *Warner et al.*, 2012] and wave activity levels. This proliferation of ripple measurements and the collection of additional data allow for testing the performance of existing models, their improvement, and possibly the development of a new model that better predicts wave-induced ripples in the marine environment.

The objectives of this study are to: (i) assemble all existing data (field and laboratory) of equilibrium ripples in a common database with commonly described hydrodynamic forcing; (ii) enrich this database with additional information that has become available; (iii) use this enriched database to evaluate already developed models; and (iv) if possible, present a new model that better fits all the data available to date. This

is attempted by collecting existing data of ripple measurements from the published literature as well as including data from two new field experiments. All data assembled are presented in an electronic tabular form (see auxiliary material) for use by other investigators and enrichment over time as new data become available.

The manuscript organization is so that section 2.2 presents a brief overview of the most widely used equilibrium ripple predictors. This is followed with a presentation of the ripple database and the source of the data (section 2.3). In section 2.4, an evaluation of the existing predictors against all the data assembled is carried out, while a discussion of their performance together with a new formulation is presented in section 2.5. Finally, in section 2.6 the conclusions of the study are presented.

2.2. Existing Equilibrium Models

In this section, selective existing equilibrium models (see Table 2.1) are briefly presented. The main criterion for their selection was their wide application in the literature and their diversity in terms of forcing parameters used. All of the models presented relate the ripple height and/or wavelength to hydrodynamic conditions usually normalized by parameters describing the sedimentary particles. At this junction it should be noted that different investigators have been defining the bottom orbital velocity parameter differently depending on the method they used to make their estimates (i.e., from direct velocity time-series or wave height measurements) and the statistical representation adopted. For example u_b in *Wikramanayake and Madsen* [1994] corresponds to standard deviation (σ) of oscillatory velocity, while in *Grant and Madsen* [1982] and *Styles and Glenn* [2002] the same parameter corresponds to amplitude of bottom orbital velocity which is defined as the $\sqrt{2}\sigma$. On the other hand, orbital velocities

derived from significant wave height measurements correspond to $2 \cdot \sigma$ [e.g., *Traykovski et al.*, 1999; *Wiberg and Sherwood*, 2008]. In order to avoid confusion, the parameters used

Table 2.1. Equilibrium ripple predictors examined in this study.

Model	Reference	Parameters	Data Type
NF	*Nielsen* [1981]	Mobility No.	Field
NL	*Nielsen* [1981]	Mobility No. Shields parameter	Lab
GM	*Grant and Madsen* [1982]	Shields parameter Dimensionless sediment parameter	Lab
Vr	*Van Rijn* [1993]	Mobility No.	Field
MO	*Mogridge et al.* [1994]	Period parameter	Lab & Field
WH	*Wiberg and Harris* [1994]	Orbital diameter Grain diameter	Lab & Field
WM	*Wikramanayake and Madsen* [1994]	Mobility No. Dimensionless sediment parameter	Field
SG	*Styles and Glenn* [2002]	Mobility No. Dimensionless sediment parameter	Field
FF	*Faraci and Foti* [2002]	Wave Reynolds No. Sediment Reynolds No. Mobility No.	Lab
GK	*Grasmeijer and Kleinhans* [2004]	Mobility No.	Field
SW	*Soulsby and Whitehouse* [2005]	Orbital amplitude Grain diameter	Lab & Field
Tr	*Traykovski* [2007]	Orbital diameter Settling velocity Radian wave frequency Orbital velocity	Field
PG	*Pedocchi and García* [2009a]	Dimensionless particle size Orbital velocity Settling velocity	Lab & Field

through the adoption of appropriate subscripts are used that reveal the method of estimation as well as the relationship between different parameters (see Table 2.2).

Table 2.2. Definitions and subscripts used for wave statistics.

Subscript	**Velocity**[a]	**Wave height**
rms	$u_{b,rms}=(\sigma_u^2+\sigma_v^2)^{1/2}$	$0.5 \cdot H_{sig}$
eq(br)	$u_{b,eq}=[2 \cdot (\sigma_u^2+\sigma_v^2)]^{1/2}$	$H_{rms}=\cdot H_{sig}/\sqrt{2}$
1/3	$u_{b,1/3}=2 \cdot (\sigma_u^2+\sigma_v^2)^{1/2}$	H_{sig}
1/10	$u_{b,1/10}=1.27 \cdot 2 \cdot (\sigma_u^2+\sigma_v^2)^{1/2}$	$H_{1/10}=1.27 \cdot H_{1/3}$

[a] σ_u^2 and σ_v^2 denote variance of wave induced velocity.

In the remainder of this section, the existing equilibrium models are described in sub-sections organized by the main parameter used in the model.

2.2.1. Mobility Number

One of the most common non-dimensional parameters used to determine ripple geometry is the mobility number (ψ), which represents the ratio of mobilizing forces acting on the sediment to the stabilizing forces:

$$\psi = u_b^2 \Big/ \left[(s-1) \cdot g \cdot D_{50} \right] \tag{2.2}$$

where s is the normalized sediment density, g is the acceleration due to gravity and D_{50} is the median particle size.

Nielsen [1981], proposed two sets of equations based on field/irregular and laboratory/regular wave conditions denoted as NF and NL, respectively. The equations developed for the regular monochromatic wave generated ripples were based on the studies of *Yalin and Russell* [1962], *Kennedy and Falcon* [1965], *Carstens et al.* [1969],

Mogridge and Kamphuis [1972], *Dingler* [1974], *Nielsen* [1979] and used laboratory data from the Danish Hydraulic Institute. *Nielsen* [1981] found these ripples to be best described by the equations:

$$\eta / A_{b,1/3} = 0.275 - 0.022 \cdot \sqrt{\psi_{1/3}} \tag{2.3}$$

$$\lambda / A_{b,1/3} = 2.2 - 0.345 \cdot \psi_{1/3}^{0.34} \tag{2.4}$$

where A_b is the wave orbital amplitude ($=2\pi \cdot u_b/T$) and T is the wave period.

For field conditions, *Nielsen* [1981] used data collected from *Inman* [1957], *Dingler* [1974], and *Miller and Komar* [1980] to propose the following set of equations:

$$\eta / A_{b,1/3} = 21 \cdot \psi_{1/3}^{-1.85} \quad , \ \psi_{1/3} > 10 \tag{2.5}$$

$$\lambda / A_{b,1/3} = exp\left[\left(693 - 0.37 \cdot ln^8 \psi_{1/3} \right) / \left(1000 + 0.75 \cdot ln^7 \psi_{1/3} \right) \right] \tag{2.6}$$

For $\psi_{1/3} < 10$, *Nielsen* [1981] recommends using the ripple height from equation (2.3). *Nielsen* [1981] also proposed a set of equations for ripple steepness based on the Shields parameter, which is further discussed in section 2.3.

Van Rijn [1993] (Vr), also noted the potential scaling of ripple geometry with the mobility number. He used ripple dimensions measured under irregular waves from *Inman* [1957], *Dingler* [1974], *Ribberink and Van Rijn* [1987], *Nieuwjaar and Van der Kaay* [1987] and *Van Rijn* [1987] and he suggested that equilibrium ripple geometry can be predicted by:

$$\eta / A_{b,1/3} = \begin{cases} 0.22 & , \quad \psi_{1/3} \le 10 \\ 2.8 \cdot 10^{-13} \left(250 - \psi_{1/3} \right)^5 & , \ 10 < \psi_{1/3} \le 250 \end{cases} \tag{2.7}$$

$$\eta / \lambda \quad = \begin{cases} 0.18 & , \quad \psi_{1/3} \le 10 \\ 2.0 \cdot 10^{-7} \left(250 - \psi_{1/3} \right)^{2.5} & , \ 10 < \psi_{1/3} \le 250 \end{cases} \tag{2.8}$$

Grasmeijer and Kleinhans [2004] (GK) analyzed the ripple measurements of *Inman* [1957], *Van Rijn et al.* [1993], *Van Rijn and Havinga* [1995], *Grasmeijer and Van Rijn* [1999] and *Hanes et al.* [2001] as well as their own data collected off the coast of Egmond aan Zee, Netherlands, and to suggest that:

$$\eta / A_{b,1/3} = \begin{cases} 0.275 - 0.022 \cdot \psi_{1/3}^{0.5} & , \psi_{1/3} \le 10 \\ 2 \cdot \psi_{1/3}^{-1} & , \psi_{1/3} > 10 \end{cases} \tag{2.9}$$

$$\eta / \lambda = \begin{cases} 0.14 & , \psi_{1/3} \le 10 \\ -0.078 + 0.355 \cdot \psi_{1/3}^{-0.221} & , \psi_{1/3} > 10 \end{cases} \tag{2.10}$$

One commonality between the latter two models (i.e., Vr and GK) is that wave steepness is assumed to be constant (0.14 and 0.18 for the GK and Vr models, respectively) for low energy flows while it decreases under more energetic wave activity.

2.2.2. Mobility Number & Dimensionless Sediment Parameter

Another non-dimensional parameter used to determine ripple geometry is the ratio of the mobility number (ψ) and the dimensionless sediment parameter (S_*) with the latter being defined as:

$$S_* = \sqrt{(s-1) \cdot g \cdot D_{50}^3} \Big/ 4 \cdot \nu \tag{2.11}$$

This parameter was first proposed by Wikramanayake and Madsen [1994] and later adopted by *Styles and Glenn* [2002]. In addition to taking into account the sediment properties and orbital wave forcing, this parameter also accounts for water viscosity (ν) and therefore requires knowledge of the water temperature, salinity and pressure (i.e., water depth).

Wikramanayake and Madsen [1994] (WM) utilized the data from the field measurements of *Inman* [1957], *Miller and Komar* [1980] and *Nielsen* [1984] and suggested the following equations to predict ripple height and wavelength:

$$\eta / A_{b,rms} = \begin{cases} 0.27\left(\psi_{rms} / S_*\right)^{-1/2}, & \psi_{rms} / S_* \le 3 \\ 0.52\left(\psi_{rms} / S_*\right)^{-1.1}, & \psi_{rms} / S_* > 3 \end{cases} \tag{2.12}$$

and

$$\lambda / A_{b,rms} = \begin{cases} 1.70\left(\psi_{rms} / S_*\right)^{-1/2}, & \psi_{rms} / S_* \le 3 \\ 2.10\left(\psi_{rms} / S_*\right)^{-0.7}, & \psi_{rms} / S_* > 3 \end{cases} \tag{2.13}$$

Equations (2.12) and (2.13) were later revised by *Styles and Glenn* [2002] (SG) who incorporated additional field data from *Wiberg and Harris* [1994] and *Traykovski et al.* [1999] to derive an improved fit between data and model so that:

$$\eta / A_{b,eq} = \begin{cases} 0.30\left(\psi_{eq} / S_*\right)^{-0.38}, & \psi_{eq} / S_* \le 2 \\ 0.48\left(\psi_{eq} / S_*\right)^{-1.1}, & \psi_{eq} / S_* > 2 \end{cases} \tag{2.14}$$

$$\lambda / A_{b,eq} = \begin{cases} 1.95\left(\psi_{eq} / S_*\right)^{-0.30}, & \psi_{eq} / S_* \le 2 \\ 2.80\left(\psi_{eq} / S_*\right)^{-0.82}, & \psi_{eq} / S_* > 2 \end{cases} \tag{2.15}$$

where ψ_{eq} is the mobility number attained from calculating u_b using the root mean square (*rms*) wave height (or $\sqrt{2}$ times the variance of flow velocity). At this juncture, it should be noted that equations (2.14) and (2.15) vary slightly from those in the original manuscript of *Styles and Glenn* [2002] due to a typographical error in the original manuscript [*Styles*, pers. comm.].

2.2.3. Shields Parameter Based Equilibrium Models

While *Nielsen* [1981] found that ripple wavelength and height were best described by the mobility number, he proposed a separate equation for steepness, which is based on

the wave Shields parameter (θ) [*Shields*, 1936]. For regular laboratory waves, *Nielsen* [1981] suggested:

$$\eta/\lambda = 0.182 - 0.24 \cdot \theta_{1/3}^{1.5} \tag{2.16}$$

while for irregular field waves, he proposed:

$$\eta/\lambda = 0.342 - 0.34 \cdot \sqrt[4]{\theta_{1/3}} \tag{2.17}$$

where θ is defined as:

$$\theta = 0.5 \cdot f_w \cdot u_b^2 / \left[(s-1) \cdot g \cdot D_{50} \right] \tag{2.18}$$

with the wave friction coefficient (f_w) defined as [*Jonsson*, 1966]:

$$f_w = \begin{cases} exp\left[5.213 \cdot \left(2.5 \cdot D_{50} / A_b \right)^{0.194} - 5.977 \right] & , A_b / \left(2.5 \cdot D_{50} \right) > 1.57 \\ 0.3 & , A_b / \left(2.5 \cdot D_{50} \right) \le 1.57 \end{cases} \tag{2.19}$$

Grant and Madsen [1982] (GM) utilized data from *Carstens et al.* [1969] and found a relationship between the Shields parameter and ripple dimensions that defines increasing ripple wavelengths with increasing Shields parameter value up to $1.8 \cdot S_*^2$ and decreasing wavelengths thereafter. This led to a new set of equations for the prediction of equilibrium ripples:

$$\eta / A_{b,eq} = \begin{cases} 0.22 \cdot \left(\theta_{eq} / \theta_{cr} \right)^{-0.16} & , \quad \theta_{eq} / \theta_{cr} \le 1.8 \cdot S_*^2 \\ 0.48 \cdot S_*^{0.6} \cdot \left(\theta_{eq} / \theta_{cr} \right)^{-1.5} & , \quad \theta_{eq} / \theta_{cr} > 1.8 \cdot S_*^2 \end{cases} \tag{2.20}$$

$$\eta / \lambda = \begin{cases} 0.16 \cdot \left(\theta_{eq} / \theta_{cr} \right)^{-0.04} & , \quad \theta_{eq} / \theta_{cr} \le 1.8 \cdot S_*^2 \\ 0.28 \cdot S_*^{0.6} \cdot \left(\theta_{eq} / \theta_{cr} \right)^{-1.0} & , \quad \theta_{eq} / \theta_{cr} > 1.8 \cdot S_*^2 \end{cases} \tag{2.21}$$

where θ_{cr} is the critical Shields parameter for sediment mobility.

2.2.4. Period Parameter

Mogridge et al. [1994] (MO) used the data of *Bagnold* [1946], *Inman* [1957], *Yalin and Russell* [1962], *Kennedy* [1965], *Horikawa* [1967], *Carstens et al.* [1969], *Mogridge* [1972], *Dingler* [1974], *Miller and Komar* [1980], and *Willis* [1993] to develop a set of equations that provide an upper limit on the ripple dimensions rather than an actual prediction. These upper limits were related to a newly defined parameter χ as follows:

$$\eta/D_{50} = 10^{8.542-10.822\chi^{0.03967}} \tag{2.22}$$

$$\lambda/D_{50} = \begin{cases} 1{,}394 & , \ \chi < 1.5\cdot 10^{-7} \\ 10^{13.373-13.772\chi^{0.02054}} & , \ \chi \geq 1.5\cdot 10^{-7} \end{cases} \tag{2.23}$$

where χ relates sediment size to wave period as follows:

$$\chi = \rho_w \cdot D_{50} \Big/ \left(\rho_s \cdot g \cdot T^2\right) \tag{2.24}$$

While *Nielsen* [1981] argued that this parameter does not have any physical meaning, *Mogridge et al.* [1994] suggested that the wave period directly reflects velocities, accelerations, and forces of the oscillatory motion. *Mogridge et al.* [1994] found η/D_{50} to be accurately described by a single equation; however, the ripple wavelength diverges at χ values smaller than 1.5×10^{-5}. They found that field data best conforms to a constant λ/D_{50} value of 1,394.

2.2.5. Orbital Excursion and Grain Size

Another parameter widely used to predict ripple dimensions is the wave orbital excursion ($d_o=2A_b$) normalized by the sediment grain diameter (d_o/D_{50}). *Clifton* [1976] and *Clifton and Dingler* [1984] first observed a dependence of ripple characteristics to different parameters depending on the value of the ratio of wave orbital excursion to

grain size (d_o/D_{50}). For smaller values of d_o/D_{50}, these orbital ripples have a wavelength that scales with the wave orbital diameter.

Wiberg and Harris [1994] proposed a set of equations based on orbital-suborbital-anorbital classification scheme using laboratory and field data from *Inman* [1957], *Kennedy and Falcon* [1965], *Carstens et al.* [1969], *Mogridge and Kamphuis* [1972], and *Dingler* [1974]. The original *Wiberg and Harris* [1994] model requires an iterative approach but *Malarkey and Davies* [2003] presented a modification that simplifies the estimation of ripple characteristics:

$$d_{o,1/3}/\eta = exp\left[C_1 - \sqrt{C_2 - C_3 \cdot ln\left(d_{o,1/3}/\lambda\right)}\right] \tag{2.25}$$

$$\lambda = \begin{cases} 0.62 \cdot d_{o,1/3} & , d_{o,1/3}/\eta_{ano} < 20 \\ 535 \cdot D_{50} \cdot exp\left[-ln\left(\dfrac{0.62 \cdot d_{o,1/3}}{535 D_{50}}\right) \cdot \dfrac{ln\left(0.01 \cdot d_{1/3}\right)}{ln(5)}\right] & , 20 \le d_{o,1/3}/\eta_{ano} \le 100 \\ 535 \cdot D_{50} & , d_{o,1/3}/\eta_{ano} < 100 \end{cases} \tag{2.26}$$

where $d_{o,1/3}/\eta_{ano}$ is calculated using equation (2.25) with $\lambda=\lambda_{ano}=535 \cdot D_{50}$, $C_1=7.59$, $C_2=33.60$, $C_3=10.53$, $d_{o,1/3}$ is the significant wave orbital diameter, (ano) indicates the anorbital ripple geometry and the equilibrium η is found using λ in equation (2.25).

Soulsby and Whitehouse [2005] (SW) used data from an extensive database of published ripple dimensions, including the ones mentioned above, to suggest that scaling of ripple geometry characteristics with the ratio of wave orbital semi-excursion of the highest 1/10 velocities ($A_{b,1/10}=1.27 \cdot A_{b,1/3}$) to the median particle diameter (D_{50}) provides the least scatter suggesting:

$$\lambda/A_{b,1/10} = \left(1 + 1.87 \cdot 10^{-3} \cdot A_{b,1/10}/D_{50} \cdot \left\{1 - exp\left[-\left(2 \cdot 10^{-4} \cdot A_{b,1/10}/D_{50}\right)^{1.5}\right]\right\}\right)^{-1} \tag{2.27}$$

$$\eta/\lambda = 0.15 \cdot \left\{1 - exp\left[-\left(5000 \cdot D_{50}/A_{b,1/10}\right)^{3.5}\right]\right\} \tag{2.28}$$

2.2.6. Orbital Excursion (d_o) and w_s/ω

Similar to the predictors described above, *Traykovski* [2007] also noted that ripples do tend to scale with orbital diameter. However, his predictor assumes that the cutoff for orbital ripples (i.e., where ripples scale with the orbital diameter) occurs at a value of $u_{b,1/3}/w_s \leq 4.2$. Above this value, the ripples scale as a function of sediment settling velocity (w_s) and wave radian frequency ($\omega=2\pi/T$). *Traykovski* [2007] found strong agreement between ripples observed off the coast of Martha's Vineyard [*Traykovski et al.*, 1999; *Traykovski*, 2007], using the following set of equations:

$$\lambda = \begin{cases} 0.75 \cdot d_{o,1/3} & , \quad u_{b,1/3}/w_s \leq 4.2 \\ 6.3 \cdot w_s/\omega & , \quad u_{b,1/3}/w_s > 4.2 \end{cases} \tag{2.29}$$

where w_s is the particle settling velocity calculated from *Gibbs et al.* [1971]. Assuming a constant value for ripple steepness of $\eta/\lambda = 0.16$, the ripple equilibrium height is obtained as:

$$\eta = \begin{cases} 0.12 \cdot d_{o,1/3} & , \quad u_{b,1/3}/w_s \leq 4.2 \\ 1.008 \cdot w_s/\omega & , \quad u_{b,1/3}/w_s > 4.2 \end{cases} \tag{2.30}$$

It is worth noting that according to equations (2.29) and (2.30), for $u_{b,1/3}/w_s > 4.2$, ripple geometry depends solely on wave period and sediment settling velocity. This follows the observations of *Mogridge et al.* [1994] and might explain some of the scatter and different trends observed in their predictor.

2.2.7. Reynolds Numbers

Faraci and Foti [2002] (FF) derived a relationship based on the wave (Re_w) and sediment (Re_d) Reynolds numbers, respectively defined as:

$$Re_w = u_{b,1/3} \cdot A_{b,1/3} / \nu \tag{2.31}$$

$$Re_d = u_{b,1/3} \cdot D_{50} / \nu \tag{2.32}$$

Using ripple geometry data from wave tank experiments with both monochromatic and irregular waves, they developed the following expressions for ripple wavelength and height:

$$\lambda / A_{b,1/3} = 12.0613 \cdot Re_d \cdot Re_w^{-0.68} \tag{2.33}$$

$$\eta / A_{b,1/3} = \left(1 - 0.022 \cdot \psi_{1/3}^{1/2} / 0.275\right) \cdot exp\left[-\left(0.0076 \cdot Re_w^{0.5} + 0.1681\right)\right] \tag{2.34}$$

Although they found the measured ripple steepness to agree with *Nielsen* [1979], they also noticed that the average steepness was 0.18, which corresponds to fully developed vortex ripples. They suggested that ripple steepness must depend on the angle of repose (ϕ) and recommended, as in *Nielsen* [1979, 1981], that:

$$\eta / \lambda = 0.32 \cdot \tan\phi \tag{2.35}$$

which leads to η/λ=0.185 if an angle of repose of 30° is assumed.

2.2.8. Orbital Velocity / Settling Velocity

Pedocchi and García [2009a] used published ripple dimension data as well as data from a wave tunnel experiment [*Pedocchi and García*, 2009b] to suggest that ripple dimensions should be related to the ratio of $u_{b,1/3}/w_s$ for three different grain size regimes based on the particle Reynolds number (Re_p). The latter relates to the dimensionless particle size parameter (S_*) as follows:

$$Re_p = \sqrt{(s-1) g D_{50}^3} / \nu = 4 \cdot S_* \tag{2.36}$$

Their study led to the following sets of equations:

$$\lambda/D_{50} = \begin{cases} 0.65\left[\left(0.050 \cdot u_{b,1/3}/w_s\right)^2 + 1\right]^{-1}, & Re_p \geq 13 \\ 0.65\left[\left(0.040 \cdot u_{b,1/3}/w_s\right)^2 + 1\right]^{-1}, & 9 \leq Re_p < 13 \\ 0.65\left[\left(0.054 \cdot u_{b,1/3}/w_s\right)^3 + 1\right]^{-1}, & Re_p < 9 \end{cases} \tag{2.37}$$

$$\eta/D_{50} = \begin{cases} 0.1\left[\left(0.055 \cdot u_{b,1/3}/w_s\right)^3 + 1\right]^{-1}, & Re_p \geq 13 \\ 0.1\left[\left(0.055 \cdot u_{b,1/3}/w_s\right)^4 + 1\right]^{-1}, & 9 \leq Re_p < 13 \\ 0.1\left[\left(0.055 \cdot u_{b,1/3}/w_s\right)^5 + 1\right]^{-1}, & Re_p < 9 \end{cases} \tag{2.38}$$

where w_s is the particle settling velocity calculated using the method of Dietrich (1982). These equations are divided into three grain size regions with Re_p=13 corresponding to 220 μm and Re_p=9 corresponding to 177 μm at 20$^{\circ}C$.

2.3. Data Availability

2.3.1. Existing Data Sources

Numerous experiments on oscillatory flow ripples have been carried out over the years resulting in a large number of ripple wavelength and height data for a variety of wave conditions and sediment sizes. Various subsets of these data were used in the development of the equilibrium prediction models described in section 2.2. As part of this study, all data available (see Table 2.3) are compiled into a single database to be used for the production of a more comprehensive formulation for ripple equilibrium dimensions that is not experiment or site specific. The ripple geometry data found in the literature include descriptions of hydrodynamic forcing, sediment type and ripple dimensions; however, not all sources provide the same parameters and for this reason, all hydrodynamic data have been converted to commonly defined parameters: significant

orbital velocity ($u_{b,1/3}$), wave period (T), median grain diameter (D_{50}), water temperature ($Temp$), water density (ρ_w), sediment density (ρ_s), water depth (h), salinity (S), ripple wavelength (λ) and ripple height (η). For the experiments where wave forcing was listed as wave height alone, the significant (1/3) bottom orbital velocity was calculated using linear wave theory:

$$u_{b,1/3} = H_{1/3} \cdot \omega \cdot \left[2 \cdot \sinh\left(kh\right) \right] \tag{2.39}$$

where ω is the wave radial frequency, $H_{1/3}$ is the significant wave height, k is the wavenumber, and h is the local water depth.

Another parameter, which is often omitted but required by several of the predictors presented in section 2.2, is the water viscosity (ν). When water temperature, salinity, and water depth data are provided, the viscosity is calculated from these values, otherwise a water temperature of 20°C and a salinity of 0 is assumed for laboratory experiments. For field experiments, temperature and salinity information obtained at a nearby buoy from the national data buoy center (http://www.ndbc.noaa.gov/) is used. When no historical data exist, an average (climatological) value of water temperature for the specified month(s) of the experiment is taken and if no salinity is recorded, a value of 35 psu is assumed.

2.3.2. New Data Sources

In addition to the existing data described above, new data sets from two experimental sites, representing different wave environments and sediment characteristics, are also included in this database and subsequent analysis. Both sites are located in the South Atlantic Bight offshore South Carolina and Georgia (USA),

Table 2.3. Data sources used in this study.

Source	**Setup**	**Wave Cond.[a]**	**$s = \rho_s/\rho_w$**	***T*** **(s)**	***$u_{b,1/3}$*** **(cm/s)**	***Depth*** **(m)**	***λ*** **(cm)**	***η*** **(cm)**
Inman [1957]	Field	IRG	2.65	0.5-16	10-310	0.03-33.5	4.3-125	0.5-22.9
Yalin and Russell [1962]	Flume	REG	1.48, 1.19, 2.7	1-4.3	9.5-50.5	0.7	2-15.2	N/A
Kennedy and Flacon [1965]	Flume	REG	1.03, 1.35, 2.67	1.1-7.3	0.6-42.1	0.4-5.8	1.7-8.6	0.1-1.7
Carstens et al. [1969]	Tunnel	REG	2.47 - 2.65	3.3-3.8	12.9-79.6	0.3	8.8-46.3	0.5-6.9
Mogridge and Kamphuis [1972]	Tunnel Flume	REG	2.65	1-14.1	1.4-68.5	1.2	3-101.7	0.4-18.4
Dingler [1974]	Field	IRG	2.65	6.9-13.9	19.8-127.3	0.5-8	7.2-79	0.1-13.5
	Tunnel	REG	2.65	1.7-5	14-68	1.2,1.7	6.9-39	0.8-6.3
Lofquist [1978]	Tunnel	REG	2.65	1.6-16	17.7-77.1	0.3	3.8-72.5	1.6-15.5
Nielsen [1979]	Flume	REG	2.65	1, 1.3, 1.7, 3	6.3-51.3	0.4	2.5-46	0.4-2.7
Miller and Komar [1980]	Field	IRG	2.65	6-18.2	4-158.5	3.1-32.9	7.6-27.1	N/A
Bosman [1981]	Tunnel	REG	2.65	0.5-20	13-78	0.4	1.7-30	0.4-4.5
Du Toit and Van Rijn [1981]	Flume	REG	2.65	3.2-5.8	8.8-27.7	0.48	6.5-25.3	1-4.4
Hayakawa et al. [1983]	Tunnel	REG	2.65	4,5,6	31.5-54.7	N/A	25.7-34.1	2.7-3.8

Nielsen [1984]	Field	IRG	2.65	5.3-14.4	39.1-113.6	0.8-1.8	5-150	0.5-20
Steetzel [1984]	Tunnel	REG IRG	2.65	3-7	20-50	N/A	13-31.5	2-4.5
Sakakiyama et al. [1985]	Flume	REG	2.65	3-12	17-197	N/A	14.3-148	1.9-11.7
Nieuwjaar and van der Kaay [1987]	Tunnel	IRG	2.65	2.4,2.5	21.2-47.6	N/A	8.5-9.3	1.1-1.8
Ribberink et al. [1987]	Tunnel	IRG	2.65	2-5	38.5-71.3	N/A	8-13.5	1-1.8
Boyd et al. [1988]	Field	IRG	2.65	3.1-11.4	6.4-121.6	9.6-12.5	7-24	N/A
Van Rijn [1987]	Tunnel	IRG	2.65	4.6-6.3	62.2-178.2	N/A	20	0.1-2
Southard et al. [1990]	Duct	REG	2.65	3.1-19.3	10-100	0.2	12-196	2.1-23.9
Van Rijn [1993]	Flume	IRG	2.65	2.2-2.7	13.7-36.1	0.5	6-20	0.6-2.9
Ribberink and Al-Salem [1994]	Tunnel	REG	2.65	2-12	20-150	0.8	8.4-270	0.3-35
Van Rijn & Havinga [1995]	Basin	REG IRG	2.65	2.1-2.3	14.4-29.9	0.4	5.9-11.1	0.6-1.4
Li & Amos [1998]	Field	IRG	2.65	8-12.8	1.9-28.8	38.7-40	7.7-15.4	0.8-2.2
Grasmeijer and Van Rijn [1999]	Flume	IRG	2.65	2.3	27-52.1	0.3-0.6	3.8-8.3	0.5-1.3
Hume et al. [1999]	Field	IRG	2.65	11	20-75	25	40-90	3-13
Traykovski et al. [1999]	Field	IRG	2.65	5.1-14.3	4.6-49.2	11.8-13.7	36.7-107	N/A
Doucette [2000]	Field	IRG	2.65	4.7-12.2	17-102.8	0.3-1.7	5-70	0.5-11

Khelifa and Ouellet [2000]	Basin	REG	2.65	0.9-1.4	8.2-25.5	0.3	2.8-12.1	0.4-1.7
Williams et al. [2000]	Flume	REG	2.65	3.5-5	19-69	6.5	8-35	1.5-6
Faraci and Foti [2001]	Flume	REG IRG	1.2, 2.65	1.3-4.2	5.4-86	0.2,0.3	3.7-12	0.4-2.1
Hanes et al. [2001]	Field	IRG	2.65	7.1-19.7	9.2-271.8	1.6-6.8	6-270	0.4-9.9
O'Donoghue and Clubb [2001]	Tunnel	REG IRG	2.65	2-15	18-106	0.6	6-121	0.9-19.4
Ardhuin et al. [2002]	Field	IRG	2.65	11.4-13.8	37-67	19.7-27.6	77-137	N/A
Doucette [2002]	Field	IRG	2.65	2.2-12.2	15.6-59.1	0.2-1.1	8-91	2-14
Faraci and Foti [2002]	Flume	REG IRG	2.65	1.3-4.2	12.7-35	0.3	4.4-10.7	0.7-2.1
Sleath and Walbridge [2002]	Tunnel	REG	2.65	2.8-6.8	8-164	0.3	10-50	1.7-9
Thorne et al. [2002]	Flume	IRG	2.65	4-6	25.7-65.8	4.5	26.2-51.3	4-6.5
Grasmeijer and Kleinhans [2004]	Field	IRG	2.65	4-10.5	23-98.5	2	19-200	0.7-10
Williams et al. [2004]	Flume	IRG	2.65	4-6	13.1-102.6	4,4.5	20-104	1-7
Dumas et al. [2005]	Tunnel	REG	2.65	7.9-11	20.1-165.3	0.7	6.5-723.8	0.4-53.2
Smith & Sleath [2005]	Tray	REG	2.65	0.9-3.8	15.6-49	0.4	3.5-30.7	0.3-4.1
Xu [2005]	Field	IRG	2.65	8.8-18.3	15.6-43.8	15	4.6-7.5	N/A
Brown [2006]	Flume	REG IRG	2.65	4,6,8	26.5-66.8	4.6	5.5-23	0.2-2.3

Doucette and O'Donoghue [2006]	Tunnel	REG IRG	2.65	2-12.5	29.8-146.6	0.5	8.7-82.3	1.3-12.8
O'Donoghue et al. [2006]	Tunnel	REG IRG	2.65	3.1-12.5	27-88	0.5,0.8	11.4-110.7	1.5-13.9
Traykovski [2007]								
Martha's Vineyard Coastal Observatory 2002	Field	IRG	2.65	1-12.9	5.5-133.1	12-13.9	10-127	N/A
2005	Field	IRG	2.65	6.2-11.6	12-80.9	12.3-13.7	39.4-127.8	2.9-16.6
Pedocchi and García [2009b]	Tunnel	REG	2.65	2-25	20-100	0.6	5-180	0.6-19
This Study								
Long Bay, SC	Field	IRG	2.65	4.8-12.7	6.6-43.9	8.2-10.6	7-22.4	N/A
Georgia Shelf	Field	IRG	2.65	6.5-12.3	3.1-45.6	26.1-29	9.5-75.8	N/A

[a]REG (IRG) denote regular (irregular) wave conditions.

respectively. The first field data set is from the shelf on the northern part of South Carolina (USA) off Long Bay (33° 43.35'N, 78° 46.75'W) (Figure 2.1). These data were collected as part of the U.S. Geological Survey's South Carolina Coastal Erosion Study, which took place from October 2003 to April 2004 [*Sullivan et al.*, 2006; *Schwab et al.*, 2009; *Warner et al.*, 2012]. The seabed sediment at this site consists of fine to medium quartz sand with a median grain diameter (D_{50}) of 177 μm. Data from the period 30 January 2004 to 15 March 2004 is used in this study as this provides the most complete record of hydrodynamic and bedform wavelength data. The second data set is from the continental shelf off the coast of Georgia, USA (31° 22.343'N, 80° 34.073'W) (Figure 2.2). The seabed at this site consists of medium to coarse sand with a mean diameter of 388 μm. Two periods of simultaneous hydrodynamic and bedform imagery data collection is used, corresponding to 16 September 2007 to 7 October 2007 and 13 December 2007 to 15 February 2008. These periods include several sediment mobilization events where bedforms change dimension and orientation (Figure 2.2). The detailed description of the experimental setup, hydrodynamic conditions, ripple evolution description as well as the methodologies used are presented in detail in chapter 3 and in *Voulgaris and Morin* [2008]. It should be noted that these data sets do not contain any ripple height observations and are limited to wavelength information only.

2.3.3. Equilibrium Ripple Criterion

Some of the data sources contain measurements of mega ripples with wavelengths of up to 8 m; since this study focuses on wave ripples only, any ripples with wavelengths greater than 1.5 m have been excluded from further analysis. A smaller cutoff of 1 m is applied to laboratory data as most of the larger ripples were the result of scaled

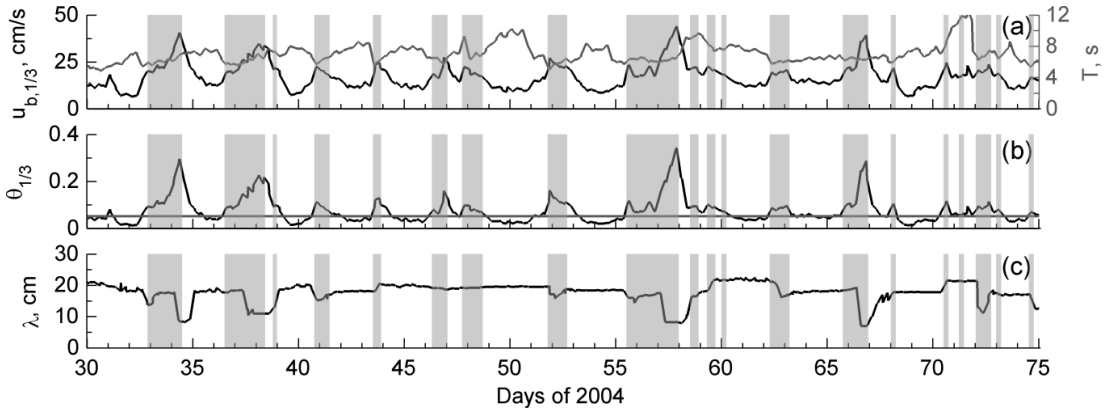

Figure 2.1. Time series of data collected in Long Bay, South Carolina (USA) during 2004: (a) significant wave orbital velocity (black) and wave period (gray); (b) wave Shields parameter (black) and critical Shields parameter (gray); (c) measured ripple wavelength. The shaded areas indicate periods when $0<d\theta/dt<0.1\cdot\theta_{1/3}(t)/T_k(t)$ and $\theta_{1/3}>1.5\theta_{cr}$ (see text).

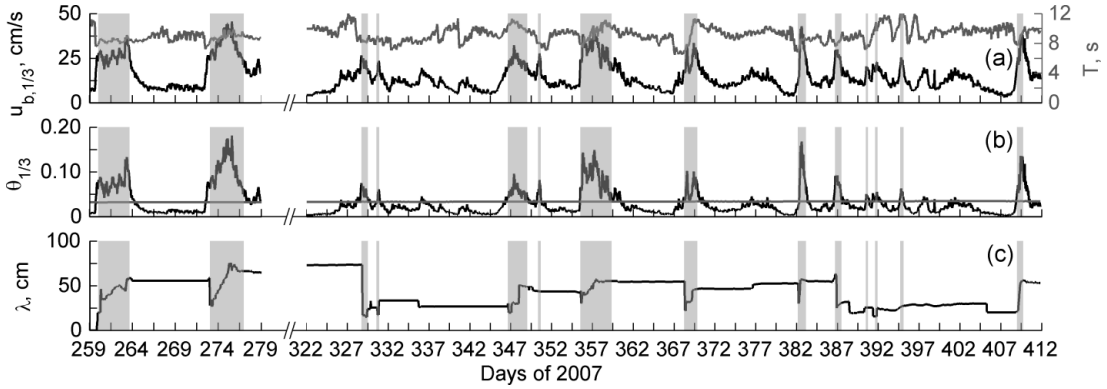

Figure 2.2. Time series of data collected in the South Atlantic Bight off Georgia (USA) during 2007-2008: (a) significant wave orbital velocity (black) and wave period (gray); (b) wave Shields parameter (black) and critical Shields parameter (gray); and (c) measured ripple wavelength. The shaded areas indicate periods when $0<d\theta/dt<0.1\cdot\theta_{1/3}(t)/T_k(t)$ and $\theta_{1/3}>1.5\theta_{cr}$ (see text).

experiments carried out at high water temperature (~60°C) [e.g., *Southard et al.*, 1990; *Dumas et al.*, 2005]. The following criteria were used to ensure that the data used represent equilibrium conditions with the flow. Since laboratory experiments are run until the ripples no longer show any significant change, any laboratory experiments with a

Shields parameter greater than the critical Shields parameter for sediment motion ($\theta_{1/3}>\theta_{cr}$), is assumed to represent ripples in equilibrium with the flow. For field conditions, where an objective definition of equilibrium is difficult without information of the time history of the ripple evolution, only ripple data corresponding to $\theta_{1/3}>2\cdot\theta_{cr}$ are considered to be in equilibrium. For the cases where time history of the ripple evolution is known (*Traykovski et al.* [1999], *Traykovski* [2007] and the data discussed in section 2.3.2), equilibrium ripples were identified as those recorded during periods where the hydrodynamic forcing (*i.e.*, excess Shields parameter) does not change significantly over the time required for a ripple to adjust itself to the given hydrodynamic forcing. This corresponds to the time scale (T_k) given in *Traykovski* [2007, equation (9)] and it is a function of the Shields parameter ($\theta_{1/3}$). Thus only ripple data corresponding to conditions where $0<d\theta_{1/3}/dt<0.1\cdot\theta_{1/3}(t)/T_k(t)$ are assumed to be in equilibrium with the flow. A further criterion of $\theta_{1/3}>1.5\cdot\theta_{cr}$ was applied to eliminated low energy conditions where the bed may only experience intermittent sediment mobilization during a wave group and hence would require more time than what the time scale T_k predicts.

The database developed from all sources of data described in the previous two sections includes ripple data from experiments conducted with both regular/monochromatic waves and irregular/random waves, with the former consisting of data from laboratory experiments only. After applying the wavelength and equilibrium criteria, the regular wave data set left consists of 1,145 measurements of wavelength and 1,049 measurements of ripple steepness. The irregular wave data set consists of all field data and a few laboratory experiments (see Table 2.3) resulting in 1,765 measurements of wavelength and 699 measurements of ripple steepness. The distribution of ripple

dimensions (height and wavelength), hydrodynamic conditions (wave period, orbital velocity and bottom excursion), and grain sizes incorporated in this data set are shown in Figure 2.3. The combination of regular and irregular wave data results in a total of 2,910 measurements of ripple wavelength and 1,748 measurements of ripple steepness.

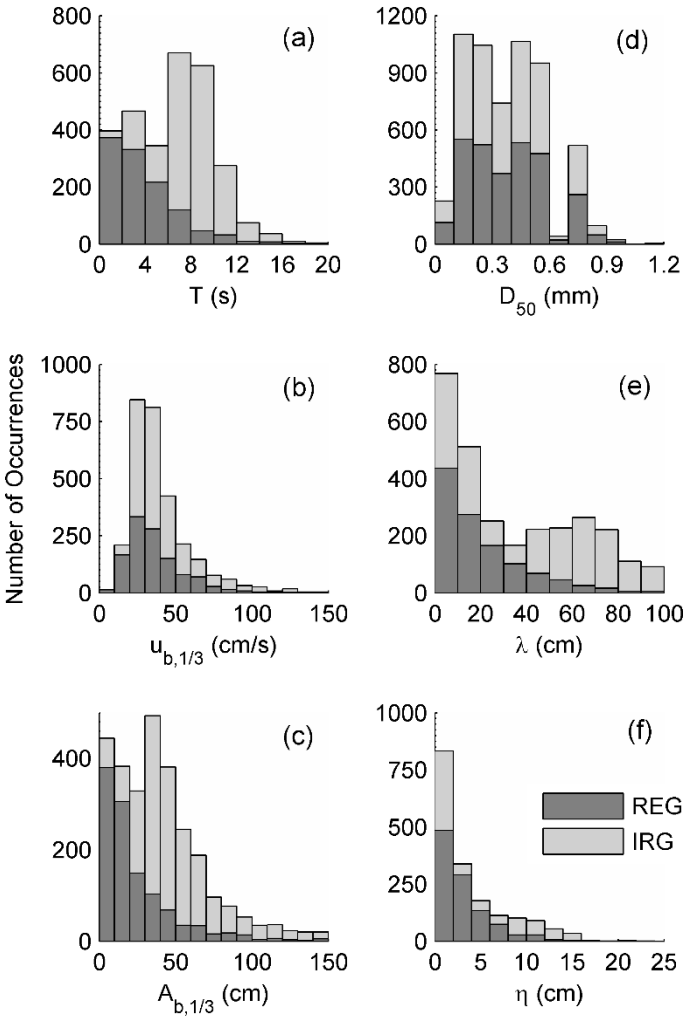

Figure 2.3. Frequency distribution of range of values for parameters representing hydrodynamic forcing and ripple dimensions for the ripple data sets compiled for this study (N=2,968). Data corresponding to regular (REG) and irregular (IRG) conditions are shown as stacked bars. For symbols, see text.

2.4. Results

In this section, all previously published and the newly collected data that have passed the equilibrium criteria are used to evaluate the predictors presented in section 2.2.

2.4.1. Mobility Number based Equilibrium Models

The predictions of equilibrium ripple length, height and steepness using the mobility number based models (i.e., NF, NL, Vr and GK) are plotted against the observations in Figure 2.4. All ripple dimensions have been normalized by the bottom orbital semi-excursion ($A_{b,1/3}$).

It is worth noting that all four models converge for $\psi_{1/3} < 10$ predicting a nearly constant value indicating a sole dependence of ripple dimensions on A_b. However, this trend is not supported by the data, which show a gradually increasing λ/A_b ratio for decreasing $\psi_{1/3}$. The ripple wavelength data (see Figure 2.4a) suggests either an inverse relationship between normalized wavelength and $\psi_{1/3}$ or a constant value that should be larger than that predicted by these models. For $\psi_{1/3} > 10$, the models start deviating from each other with the irregular wave data suggesting two trends. One trend follows the predictors of NL, Vr, and to an extent, that of GK while the remaining data follow that of NF and yield a smaller $\lambda/A_{b,1/3}$ ratio value for the same $\psi_{1/3}$. This deviation was also noted by *Nielsen* [1981], who attributed it to differences between laboratory/regular *vs.* field/irregular waves. However, this is not the case in here, as ripples under different wave forcing appear to follow either trend without a specific reference to regular/irregular forcing or sediment size.

The normalized ripple height (see Figure 2.4b) also follows the trend of decreasing $\eta/A_{b,1/3}$ with increasing $\psi_{1/3}$ although there are fewer measurements for height

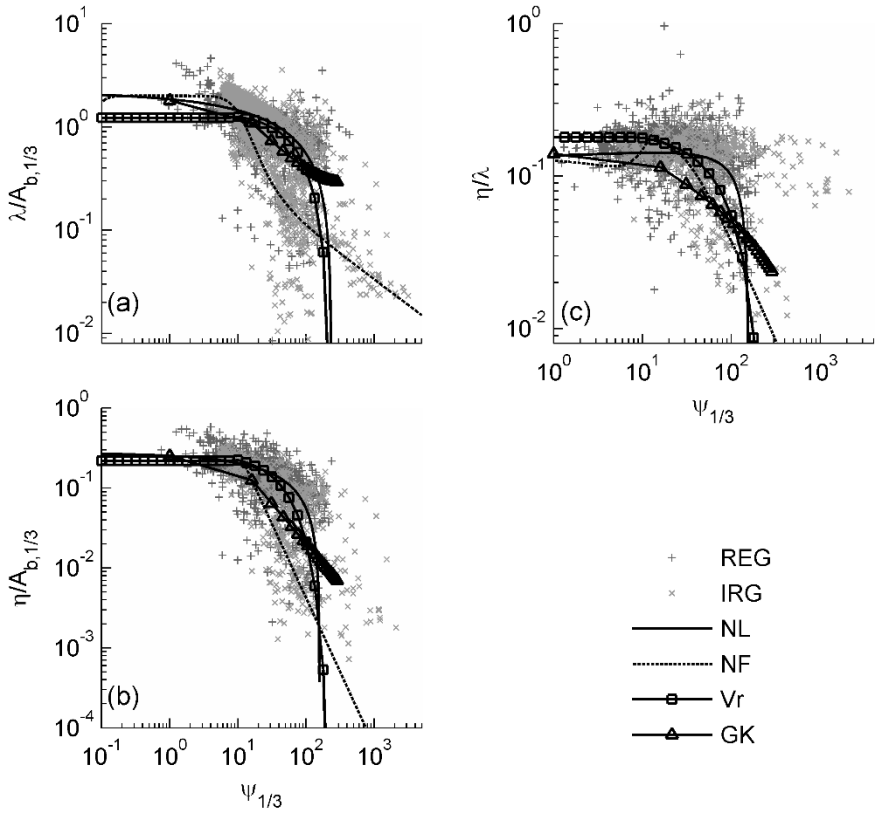

Figure 2.4. Scatter plot of (a) normalized ripple wavelength ($\lambda/A_{b,1/3}$), (b) normalized ripple height ($\eta/A_{b,1/3}$) and (c) ripple steepness (η/λ) against mobility number ($\psi_{1/3}$). Key: REG: regular wave ripples; IRG: irregular wave ripples; NL: *Nielsen* [1981] model for regular waves; NF: *Nielsen* [1981] model for irregular waves; Vr: *Van Rijn* [1993] model; GK: *Grasmeijer and Kleinhans* [2004] model.

than for wavelength. All of the predictors fail to yield an accurate ripple height for larger values of $\psi_{1/3}$. NF predicts a smaller height than observed while NL and Vr yield a flat bed at these larger values and the GK method yields increasing and exceptionally large ripple heights (for $\psi_{1/3}$>900). The steepness of these ripples estimated from the individual predictions of η and λ (see equations (2.3) to (2.6)) is shown in Figure 2.4c whereas with wavelength and height, two trends emerge. One trend suggests a nearly constant steepness of ~0.15, for $\psi_{1/3}$<10 which is successfully predicted by the models. However, there is significant scatter at larger values of $\psi_{1/3}$ with some ripples maintaining a

steepness of ~0.15 while others show a decrease in steepness with higher values of $\psi_{1/3}$. There is no clear distinction between regular and irregular wave induced ripples.

2.4.2. Mobility Number & Sediment Parameter

Both predictors of *Wikramanayake and Madsen* [1994, WM] and *Styles and Glenn* [2002, SG], based on the ratio of the mobility number to the non-dimensional sediment parameter, are shown in Figure 2.5. This ratio reduces some of the scatter and the dual trend in ripple wavelength observed with the predictors presented in the previous section. This is attributed mainly to the fact that this formulation accounts for differences in sediment size found in the data. The overall trend is a decreasing λ/A_b value for increasing ratio of ψ/S_*, with a greater rate of decrease for $\psi_{rms}/S_*>3$ for WM and $\psi_{eq}/S_*>2$ for SG. However, while the ripples tend to scale with ψ/S_*, the cutoff values of 2 and 3 used by these models are too small as the data suggest values between 8 and 9.

For non-dimensional height, both predictors capture the slope of the data for $\psi_{rms}/S_*>3$ and $\psi_{eq}/S_*>2$, while for smaller values of ψ/S_*, the predictors overestimate the rate of decrease. Ripple steepness (Figures 2.6c and f) suggest that some ripples maintain a nearly constant steepness between 0.15 and 0.20 while the remaining ripple data show evidence of a decreasing η/λ for increasing ψ/S_*. The ripple steepness converges around 0.15 for small ψ/S_* but begin to diverge and scatter over an order of magnitude for $\psi/S_*>2$. The WM predictor assumes a constant η/λ for $\psi_{rms}/S_*<2$ which agrees with the data, while SG predicts an increasing steepness for decreasing ψ_{eq}/S_* which is not observed. Both WM and SG were only validated over a range of ψ/S_* limited by the available data as shown by the short predicted lines.

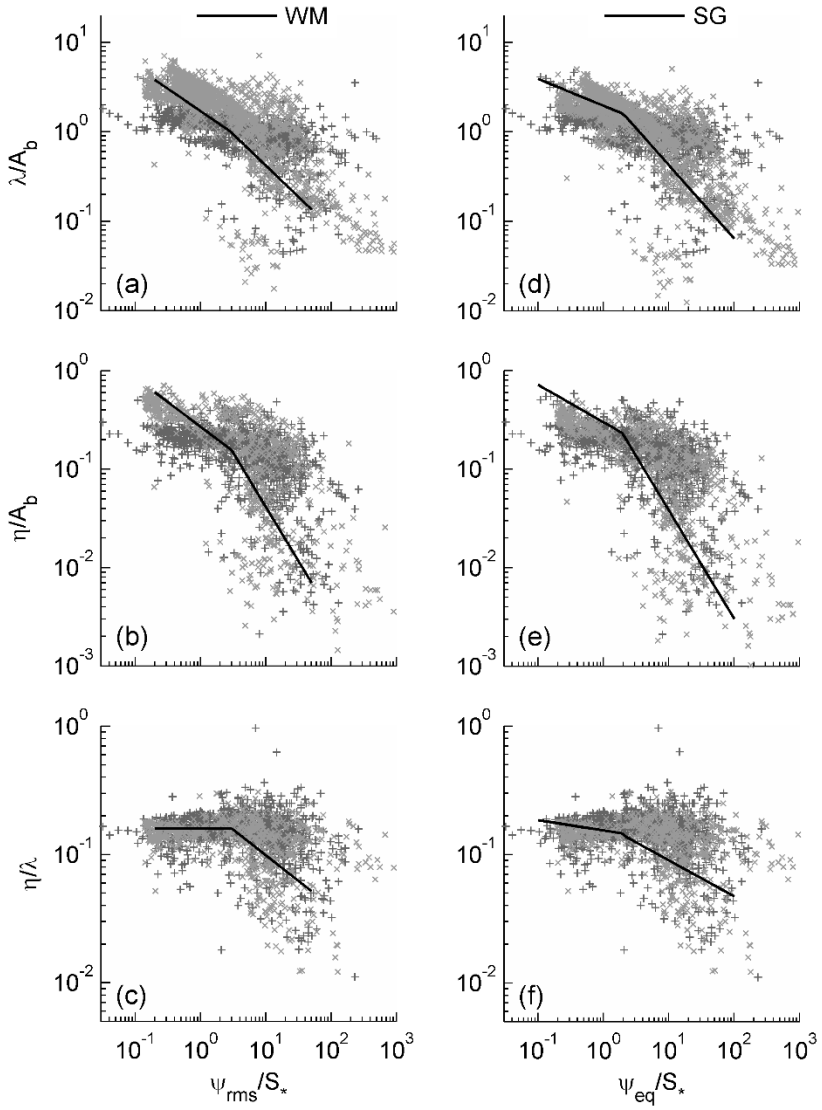

Figure 2.5. (a) to (c) evaluation of the *Wikramanayake and Madsen* [1994] ripple predictor (WM) where A_b and ψ are calculated using the *rms* wave orbital velocity. (d) to (f) evaluation of the *Styles and Glenn* [2002] ripple predictor (SG) where A_b and ψ are calculated using the equivalent wave orbital velocities (see text for details). Symbols + and × represent ripple data under regular and irregular wave conditions, respectively.

2.4.3. Shields Parameter

While *Nielsen* [1981] found ripple wavelength and height to vary as a function of the mobility number, he also noted that steepness is better described by the Shields

parameter (Figure 2.6). As with his equations for λ and η, he found a disparity between ripples under regular and irregular waves and he established two different equations to describe the observed measurements. However, as shown in Figure 2.6, these equations fail to accurately describe the observed trend. Similar to the dependence on the mobility number, the steepness follows two trends: constant and decreasing with increasing Shields parameter. Both predictors indicate a flatbed near a Shields parameter value of 1, which agrees with some of the data, but ripples clearly remain present at least up to Shields parameter values of 10.

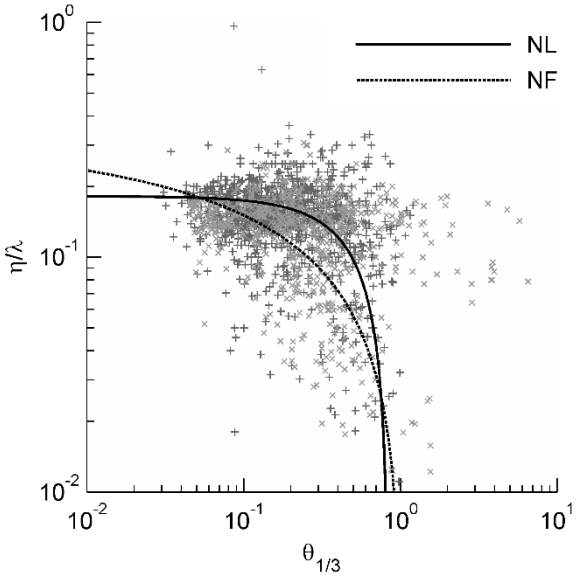

Figure 2.6. Scatter plot of ripple steepness (η/λ) as function of the Shields parameter ($\theta_{1/3}$) for data collected under regular (+) and irregular (×) wave conditions. The *Nielsen* [1981] ripple steepness predictions for regular (solid line) and irregular waves (dashed line) are also shown.

When using the *Grant and Madsen* [1982] model formulations the observations (Figure 2.7) show no clear trend when $S_* \leq 5$; for $S_* > 5$ the data plot together but they do not segregate as predicted by the GM equation. Better agreement is found for regular

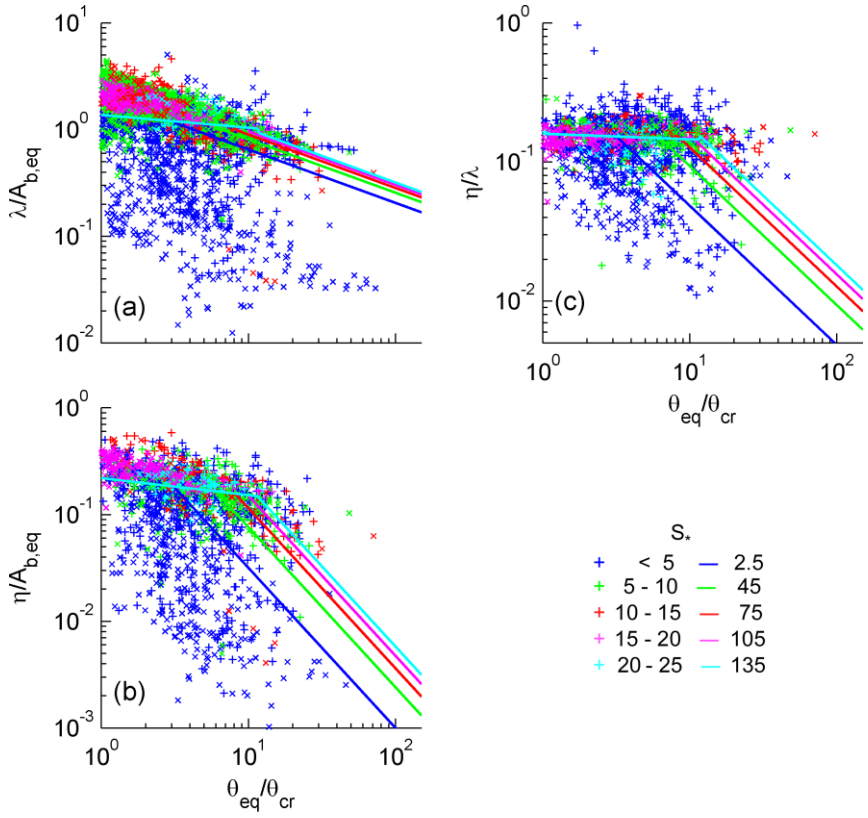

Figure 2.7. Scatter plot of (a) normalized ripple wavelength ($\lambda/A_{b,eq}$), (b) normalized ripple height ($\eta/A_{b,eq}$) and (c) ripple steepness (η/λ) against the ratio of θ_{eq}/θ_{cr} for regular (+) and irregular (×) wave conditions. The corresponding predictions based on the *Grant and Madsen* [1982] for the various ranges of sediment parameter (S_*) are also shown.

wave data although a significant amount of scatter is still notable. Ignoring data with $S_* \leq 5$, both the observed and predicted trends indicate a nearly constant to gradually decreasing $\lambda/A_{b,eq}$ for $\theta_{eq}/\theta_{cr} < 5$. For $\theta_{eq}/\theta_{cr} > 5$, the dimensionless ripple geometry decreases. The GM prediction for $\lambda/A_{b,eq}$ agrees with that observed with the exception of

the data not segregating by S_*. The ripple height as a function of θ_{eq}/θ_{cr} gradually decreases (on a log-log scale) and it does not follow the predicted ripple height of GM. As noted previously, the ripple steepness follows two trends, however, for $S_*>5$, the majority of the ripple data suggest a constant steepness for increasing θ_{eq}/θ_{cr}.

2.4.4. Period Parameter

Mogridge's et al. [1994] model (see Figure 2.8) appears to be successful in providing the upper limits for both wavelength and ripple height. However, the assumption of constant value of λ/D_{50} for $\chi<1.4\times10^{-7}$ in equation (2.24) (see dashed line in Figure 2.8a) does not seem to be supported by the data.

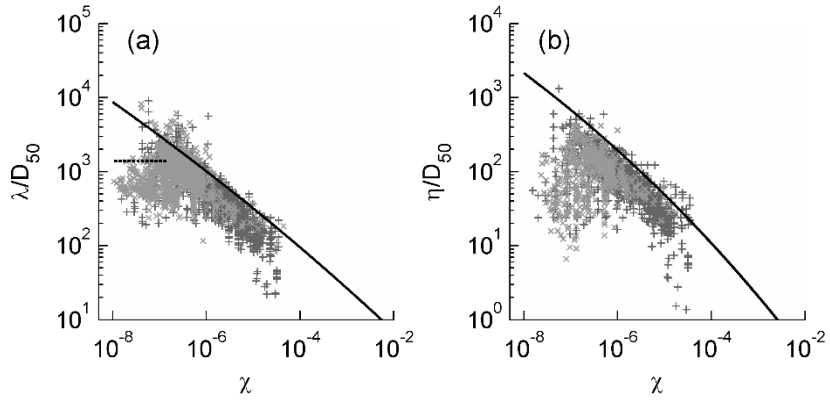

Figure 2.8. Scatter plot of (a) normalized ripple wavelength (λ/D_{50}) and (b) height (η/D_{50}) plotted against the parameter χ (see equations (22) and (23)) for regular (+) and irregular (×) wave conditions. The maximum equilibrium ripple conditions from the *Mogridge et al.* [1994] equations are also shown as solid lines. The dashed line indicates the equation for field wave conditions (equation (23)) when $\chi<1.5\times10^{-7}$.

2.4.5. Orbital Excursion

The predictors of *Wiberg and Harris* [1994] and *Soulsby and Whitehouse* [2005] are both based on variations of the wave orbital excursion and are shown against the data

in Figure 2.9. The WH predictor (based on $2 \cdot A_{b,1/3}/D_{50} = d_{o,1/3}/D_{50}$) captures the general trend of the data (although a high scatter is noted for larger values of $2 \cdot A_{b,1/3}/D_{50}$ (see Figure 2.9, left column)). The normalized wavelength (λ/D_{50}, Figure 2.9a) data for regular waves continue to follow the orbital trend well into the suborbital and anorbital regimes. If these data are excluded, the predicted characteristics for suborbital and anorbital ripples agree with the observed data. However, the regular wave data tend to have smaller λ/D_{50} ratios than the irregular ones, for the same $2 \cdot A_{b,1/3}/D_{50}$ values. Therefore, the predictor appears to slightly over-predict regular and under-predict irregular wave ripple dimensions. For normalized ripple height (η/D_{50}, Figure 2.9b), the regular and irregular wave ripple dimensions agree with the equations for orbital ripples, however, as with wavelength, some data continue along the trend for larger $2 \cdot A_{b,1/3}/D_{50}$ ratios. For suborbital ripples, the equations closely follow that of the data but tend to over-predict the regular wave data. For anorbital ripples, η/D_{50} scatters over an order of magnitude around the predicted dimensions. The ripple steepness (Figure 2.9c), still shows the dual trend observed in the previous predictors.

The SW predictor closely follows the trend of regular wave data for $A_{b,1/10}/D_{50} < 10^3$ (Figure 2.9, right column). For $A_{b,1/10}/D_{50} > 10^3$ the data follow two trends; that of fairly constant λ/D_{50} (≈ 1), and that, supported by the bulk of the data, of a gradually decrease in normalized wavelengths, as predicted by the equation. This decreasing trend also follows the measured irregular wave data; however, it does not follow a constant $\lambda/A_{b,1/10}$ for $A_{b,1/10}/D_{50} < 10^3$ but continues to increase. The predicted normalized ripple height shows a rapid decrease in $\eta/A_{b,1/10}$ with increasing $A_{b,1/10}/D_{50}$, while the data scatter exhibit a distribution very similar in shape with that of $\lambda\ A_{b,1/10}$ but reduced by a

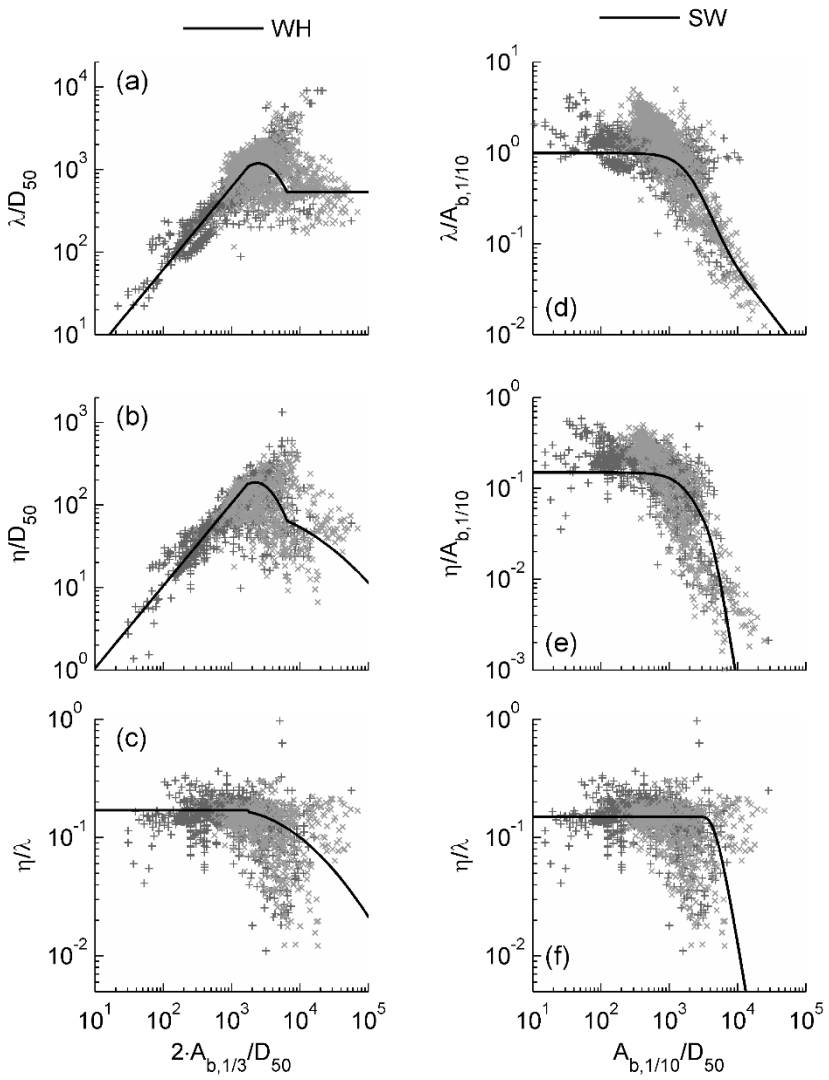

Figure 2.9. (a) to (c) scatter plots of normalized ripple wavelength (λ/D_{50}), height (η/D_{50}) and ripple steepness (η/λ) against normalized wave excursion ($2\cdot A_{b,1/3}/D_{50}$) as in the model of *Wiberg and Harris* [1994] (WH). (d) to (f) scatter plots of normalized ripple wavelength ($\lambda/A_{1/10}$), height ($\eta/A_{1/10}$) and ripple steepness (η/λ) against normalized wave excursion ($A_{b,1/10}/D_{50}$) as in the model of *Soulsby and Whitehouse* [2005] (SW). Solid lines show the predictions of the respective models, while data points with the symbols + and × represent ripple geometry data under regular and irregular wave conditions, respectively.

factor of ~10, something that suggests constant ripple steepness. As with other methods, the ripple steepness calculated from the predicted dimensions follows the same trend of

being constant initially and decreasing for increasing forcing. *Soulsby et al.* [2012] argue that their predictor worked best for a wide range of the published data; however, although it does appear to reduce the error for many conditions, it ultimately fails to predict ripple height and steepness.

2.4.6. Orbital Excursion and w_s/ω

Figure 2.10 shows that the *Traykovski* [2007] predictor is able to capture the overall ripple wavelength and height (and consequently steepness) trend although the data scatter around the model is higher for $u_{b,1/3}/w_s$ >4.2 (Figures 2.10d, e and f) than for $u_{b,1/3}/w_s$ <4.2 (see Figure 2.10a). A better agreement (less scatter) is found with the irregular wave data than with the regular ones.

2.4.7. Reynolds Numbers & Mobility Number

The *Faraci and Foti* [2002] equations predict that $\lambda/A_{b,1/3}$ decreases for increasing Re_w and increases for increasing Re_d (see Figure 2.11). The observed ripple dimensions follow the decreasing $\lambda/A_{b,1/3}$ for increasing Re_w pattern but the segregation by Re_d suggested by the model is not observable in the data (Figure 2.11). For ripple height, the observations do not reveal any correlation with Re_w and $\psi_{1/3}$ as suggested by equation (2.34). Taken as a single equation fit through the scatter the equation might perform well but the dependence on Re_d and Re_w is not evident. For steepness, FF predicted a value of ~0.18, which plots along the largest steepness observed (Figure 2.11c), thereby over predicting the majority of the observations.

2.4.8. Orbital Velocity, Settling Velocity & Re_p

The *Pedocchi and García* [2009a] equations (2.37) and (2.38) provide estimates of ripple dimensions normalized by grain size (see Figure 2.12). Under this classification,

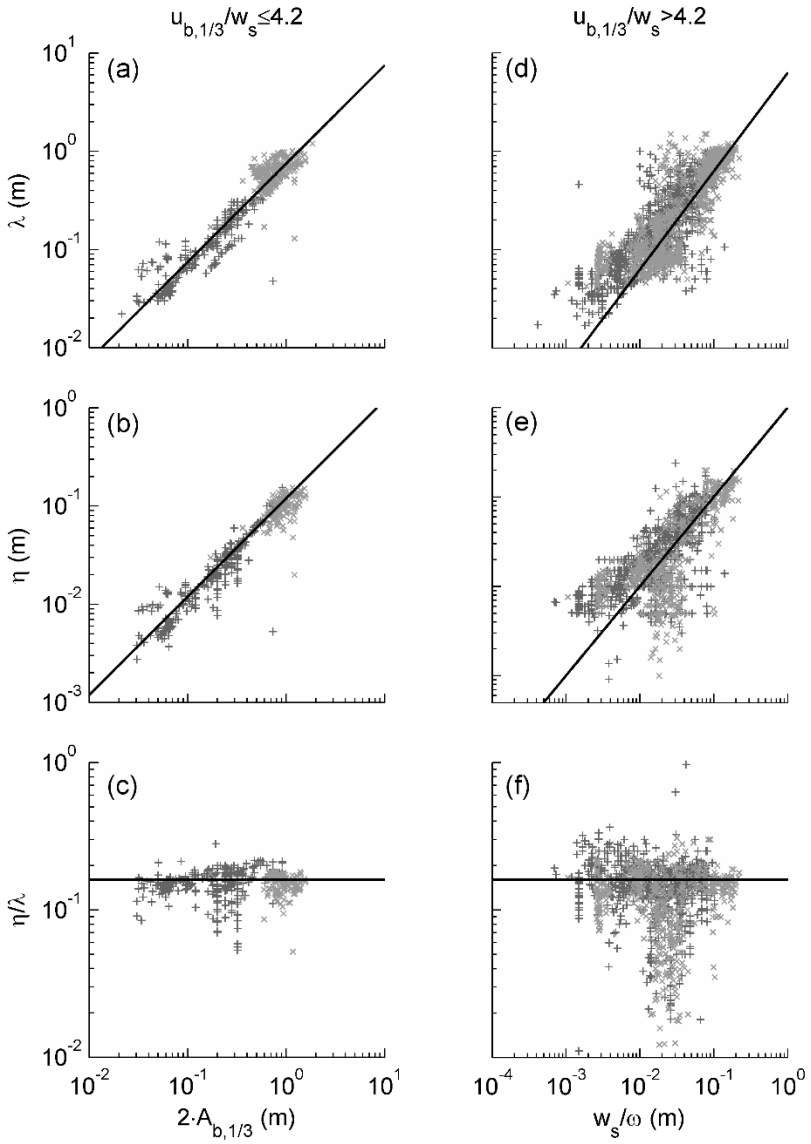

Figure 2.10. Scatter diagrams of ripple wavelength (λ), height (η) and steepness (η/λ) plotted against wave orbital excursion ($2 \cdot A_{b,1/3}$) ((a) to (c)) and against the ratio of settling velocity (w_s) over wave radial period (ω) ((d) to (f)) for data corresponding to conditions $u_{b,1/3} \leq 4.2 \cdot w_s$ and for $u_{b,1/3} > 4.2 \cdot w_s$ as suggested by *Traykovski* [2007]. Solid lines denote the predictions of the *Traykovski* [2007] (Tr) model. Data points with the symbols + and × represent ripple geometry data under regular and irregular wave conditions, respectively.

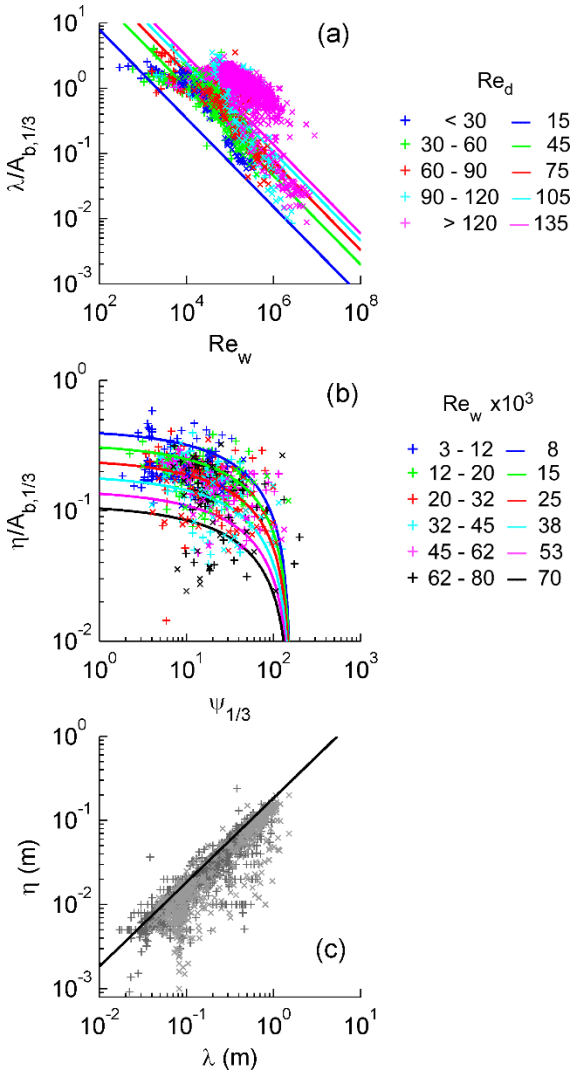

Figure 2.11. Scatter diagrams of: (a) normalized ripple wavelength ($\lambda/A_{b,1/3}$) against wave Reynolds number (Re_w); (b) normalized ripple height ($\eta/A_{b,1/3}$) against the mobility number ($\psi_{1/3}$); and (c) ripple height (η) against ripple wavelength (λ). Solid lines show the predictions of the *Faraci and Foti* [2002] model for the various ranges of sediment (Re_d) and wave (Re_w) Reynolds numbers where a 30° angle of repose is shown in (c) (for details see text). The symbols + and × denote ripple geometry data corresponding to regular and irregular wave conditions, respectively.

the dimensions for regular and irregular wave data cluster all together, however the PG predictor estimates do deviate from the observed data. This predictor captures the trend of the data with a decreasing $\lambda/d_{o,1/3}$ and $\eta/d_{o,1/3}$ for increasing $u_{b,1/3}/w_s$ but it either over- or under-predicts, depending on the Re_p value. When $Re_p \geq 13$, the data scatter show the $\lambda/d_{o,1/3}$ ratio to decrease at larger rate for smaller $u_{b,1/3}/w_s$ values than the equation predicts. This leads to under prediction for small and over prediction at larger $u_{b,1/3}/w_s$ values. Ripple steepness is poorly captured by this predictor as the observations suggest a constant value for $u_{b,1/3}/w_s < 0.18$ and a decrease for $u_{b,1/3}/w_s > 0.18$ following local increase at $u_{b,1/3}/w_s \sim 0.18$. When $9 \leq Re_p < 13$ (see Figures 2.12d, e and f), the predictor follows the general trend of the wavelength data only for small $u_{b,1/3}/w_s$ ratios; a better agreement is found with the normalized ripple height data ($\eta/d_{o,1/3}$) and ripple steepness. For $Re_p < 9$ (Figures 2.12g, h and i) the predictor under predicts both normalized ripple wavelength and height. The same applies for steepness as the observations follow only a weak decreasing trend and scatter almost as much along the $u_{b,1/3}/w_s$ axis as in η/λ.

2.5. Discussion

The qualitative comparison between the newly created ripple geometry database and the predictors presented in section 2.2 confirmed the widespread differences in performance. Some of the presented models failed to agree well with the data under large wave forcing conditions. In terms of wavelength, this was particularly the case for the *Van Rijn* [1993] and *Grasmeijer and Kleinhans* [2004] equations. *Van Rijn* [1993] used his data set to determine that a flatbed should occur at a mobility number of 250 and therefore derived an equation where the ripple geometry goes to zero at this value. However, the data set (see Figure 2.4) confirms the existence of ripples even when the

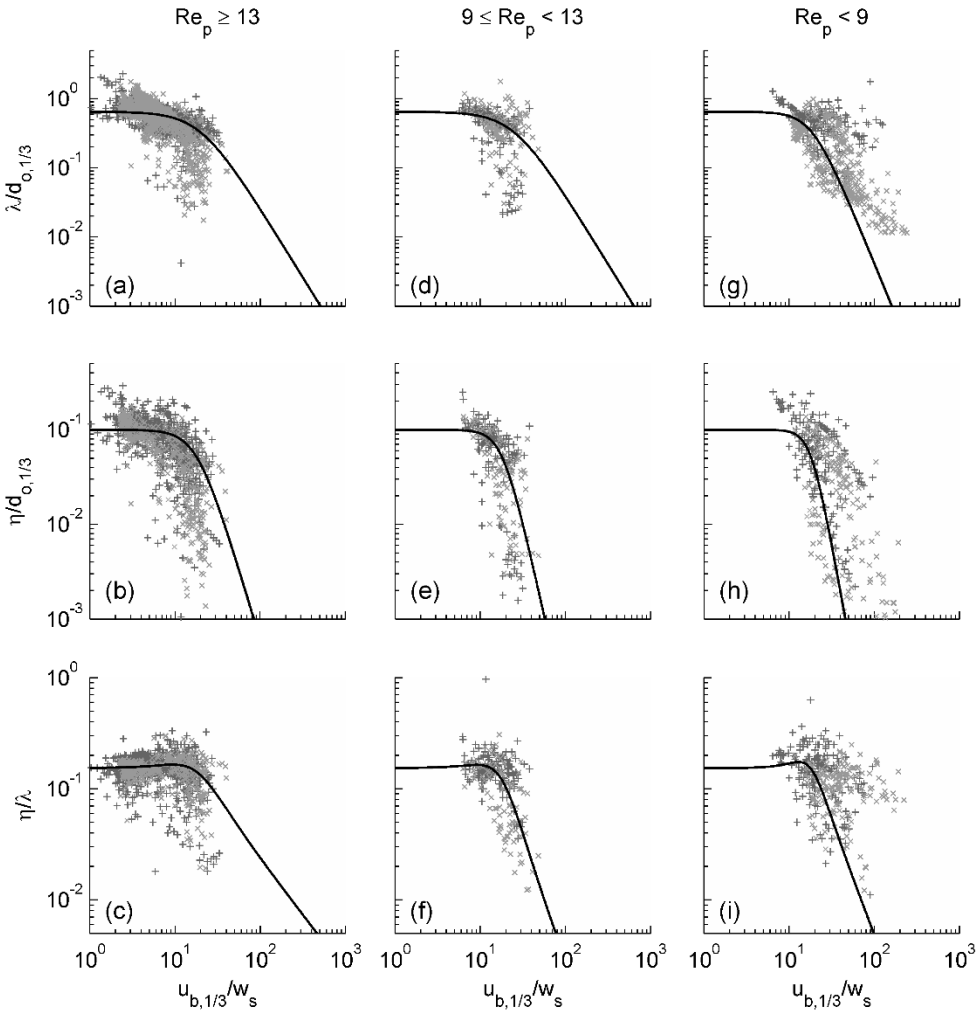

Figure 2.12. Scatter plots of ripple dimensions normalized by the wave orbital excursion ($d_{o,1/3}$) and ripple steepness against the ratio of wave orbital velocity over sediment settling velocity ($u_{b,1/3}/w_s$) for the various ranges of particle Reynolds number (Re_p) as suggested by the PG equilibrium model (equations (2.37) and (2.38)) of *Pedocchi and García* [2009a]. + and × denote data collected under regular and irregular waves, respectively.

mobility number value exceeds 250. Establishment of an accurate cutoff between a rippled and flat bed is not pursued here, as the goal is to have a predictor capable of predicting dimension over the whole range of conditions observed in this data set. The failure of the GK predictor is attributed mainly to the fact that the polynomial equation

describing the model yields increasing and exceptionally large values for mobility numbers greater than 900. Similarly, the predictors of *Nielsen* [1981] were introduced for $\theta_{1/3}<1$, as above this value *Nielsen* [1981] suggested the transition to a flat bed. However, in for this data set ripples are present for $\theta> 1$ so no limitation was imposed on the *Nielsen* [1981] models either. For ripple height, the predictors of NL, FF, GK, and the *Nielsen* [1981] for steepness have not shown a good agreement with the data especially under large wave forcing. These limitations, suggest that these predictors might not be suitable for use under all conditions but limited to cases with small mobility number and shear stress values only.

Throughout the comparison of models and data, a different response was present for monochromatic and irregular wave forcing. This explains some of the diverging trends observed in predictors such as SW and MO as well as in the original development of the two different predictors by *Nielsen* [1981]. Assuming that hydrodynamic processes are represented correctly by the corresponding hydrodynamic parameters, the geometry of the ripples should not be significantly different for monochromatic and random wave fields. This motivated *Soulsby and Whitehouse* [2005] and *Pedocchi and García* [2009a] to create a single predictor which incorporates both laboratory and field data. For the same wave parameters, different ripple characteristics might occur depending on the nature of the waves (i.e., directional spectral characteristics), their complexity (i.e., velocity asymmetry, acceleration skewness), and potential superposition of mean flows. However, these differences should not create significantly different ripple geometries as those identified in the data. This is investigated by initially examining the regular and irregular wave data sets separately.

2.5.1. Ripple Wavelength

Ripple wavelength is a quantity approximately 10 times larger than ripple height. Therefore, ripple wavelength measurements are expected to be more accurate than measurements of ripple height. Furthermore, qualitatively predictors such as that of WH and SW (see Figure 2.9) that relate ripple wavelength to the ratio of semi-orbital excursion (A_b) over median grain size (D_{50}) provided the best agreement with the enriched database. This is explored in Figure 2.13 where normalized ripple wavelength is plotted against the ratio of $A_{b,1/3}/D_{50}$ for regular (Figure 2.13a) and irregular (Figure 2.13b) wave conditions. The ripple wavelength normalization is done using mean particle size for irregular waves and wave excursion for regular waves. A clear linear trend (on a log-log scale) is identified between normalized ripple wavelengths and normalized wave excursion although the slopes of the two linear trends are opposite to each other while the correlation coefficients (r^2) are 0.73 and 0.78 for regular and irregular wave forcing, respectively. A least squares fitting on a log-log scale produces the following statistical models for normalized ripple wavelengths for regular waves (Fig. 2.13a):

$$\lambda/D_{50} = 6.76\left(A_{b,1/3}/D_{50}\right)^{0.68} \tag{2.40}$$

and for irregular waves:

$$\lambda/A_{b,1/3} = 2.22\cdot 10^{3}\left(A_{b,1/3}/D_{50}\right)^{-1.11} \tag{2.41}$$

Solving these equations for ripple wavelength results in:

$$\lambda = 6.76\cdot A_{b,1/3}^{0.68}\cdot D_{50}^{0.32} \tag{2.42}$$

$$\lambda = 2.22\cdot 10^{3}\cdot A_{b,1/3}^{-0.11}\cdot D_{50}^{1.11} \tag{2.43}$$

for ripples under regular and irregular wave forcing, respectively. Equation (2.42) clearly shows that for regular waves, orbital semi-excursion is the dominant parameter controlling ripple wavelength while for irregular waves (equation (2.43)) the median grain diameter is the dominant scaling factor. Based on the range of $A_{b,1/3}/D_{50}$ values found in these data sets (10 to 10^4 for regular waves, 10^2 to 5×10^5 for irregular waves) the monochromatic wave conditions extend to typically orbital scale ripples ($A_{b,1/3}/D_{50}<877$) with some suborbital ($877<A_{b,1/3}/D_{50}<2{,}794$) which partially explains the greater dependence on semi-excursion. On the other hand, ripples formed by irregular waves fall in the suborbital and anorbital ($A_{b,1/3}/D_{50}>2{,}794$) regimes where grain size becomes more important. However, at the overlapping suborbital region, the data from the monochromatic wave conditions (Figure 2.13a) trend in agreement with equation (2.42) well into the suborbital regime, while irregular wave formed ripples continue on an opposing trend into the orbital regime (see Figure 2.13b). One explanation for the scaling differences between these two types of waves is the consistency of the forcing present. Under monochromatic waves, the bed is subjected to the same orbital excursion with each passing wave, while under irregular waves the orbital excursion varies for each wave. Thus, the grain size acts as a filter and a limiting factor preventing or delaying the transition from suborbital to orbital scaling.

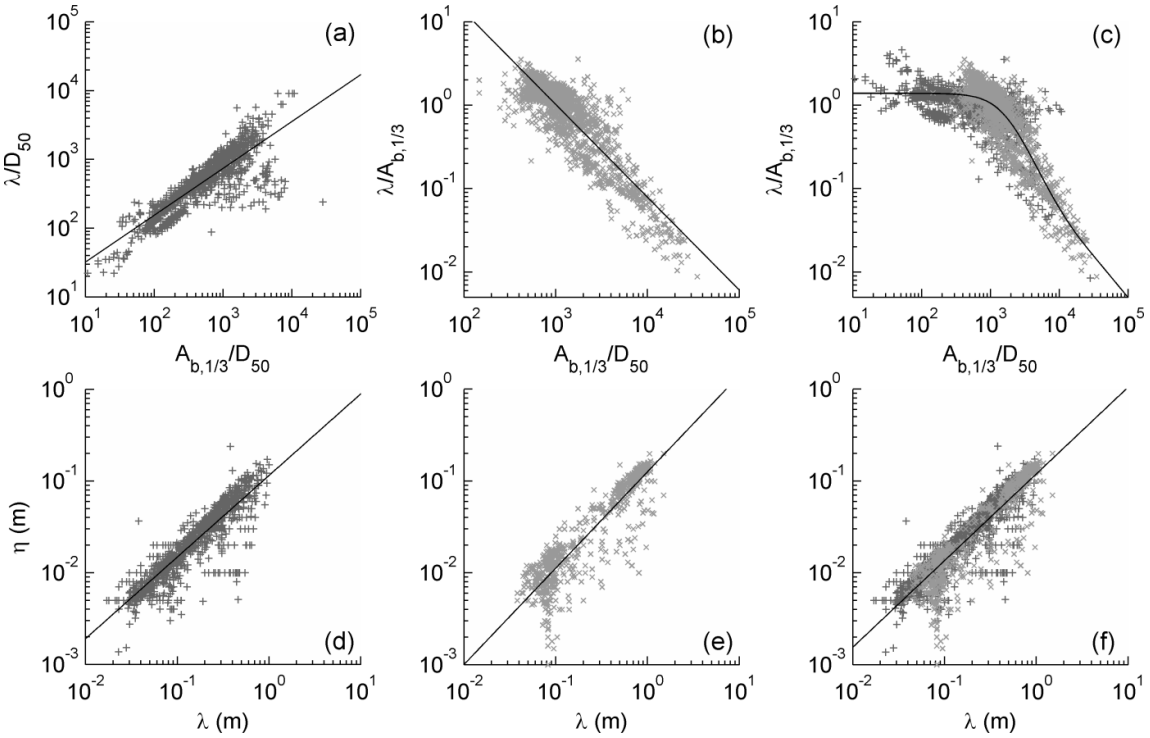

Figure 2.13. Top row: scatter plots of (a) ripple wavelength (λ) normalized by particle size (D_{50}) for regular wave conditions (equation (2.42)); (b) ripple wavelength (λ) normalized by wave semi-orbital excursion ($A_{b,1/3}$) for irregular wave conditions (equation (2.43)); and (c) the same as (b) but with all data combined (equation (2.44)). Bottom row: scatter plots of ripple height (η) *vs.* wavelength (λ) for (d) regular wave (equation (2.45)), (e) irregular wave (equation (2.46)), and (f) both regular and irregular wave conditions (equation (2.49)).

The best attempt to collapse both regular and irregular data using a common parameterization is achieved when $\lambda/A_{b,1/3}$ is plotted against $A_{b,1/3}/D_{50}$ (see Figure 2.13c) in a similar manner as in *Soulsby and Whitehouse* [2005]. Comparing the enriched data set to that used by *Soulsby and Whitehouse* [2005], the new data set includes significantly more field observations with smaller $A_{b,1/3}/D_{50}$ values that allow to define the trend of ripple characteristics over a larger range. Least squares fit, on a log-log scale, of an equation similar to that of SW (equation (2.27)) through the expanded data set leads to:

$$\lambda / A_{b,1/3} = \left(0.72 + 2.0 \cdot 10^{-3} \cdot A_{b,1/3} / D_{50} \cdot \left\{ 1 - \exp\left[-\left(1.57 \cdot 10^{-4} \cdot A_{b,1/3} / D_{50} \right)^{1.15} \right] \right\} \right)^{-1} \quad (2.44)$$

with a correlation coefficient (r^2) of 0.73. This equation captures the data trend for values of $A_{b,1/3}/D_{50} < 7{,}000$ but may over predict irregular wave ripples at larger $A_{b,1/3}/D_{50}$ values.

2.5.2. Ripple Height and Steepness

During the comparison of the data with existing predictors (see section 2.4), there were a number of occasions where ripple steepness appeared to be constant for a large range of values of the parameter used in the *x*-axis. Similar to wavelength, ripple steepness data (note that the new data set described in section 2.3.2 did not include ripple heights) are examined for monochromatic and irregular wave conditions, separately. A log-log scatter plot of ripple height *vs.* wavelength shows a linear trend. Least squares analysis on the data reveals the following best fit relationships for regular (Figure 2.13d) and irregular (Figure 2.13e) wave conditions:

$$\eta = 0.115 \cdot \lambda^{0.89} \quad (2.45)$$

$$\eta = 0.126 \cdot \lambda^{1.05} \quad (2.46)$$

with correlation coefficients (r^2), on a log-log scale, of 0.78 and 0.81, respectively. It should be noted that in the above equations both η and λ are in meters. Dividing both parts by wavelength, the following relationships for wave steepness are established

$$\eta / \lambda = 0.115 \cdot \lambda^{-0.11} = 0.093 \cdot A_{b,1/3}^{-0.075} \cdot D_{50}^{-0.035} \quad (2.47)$$

$$\eta / \lambda = 0.126 \cdot \lambda^{0.05} = 0.185 \cdot 10^{-2} \cdot A_{b,1/3}^{-0.006} \cdot D_{50}^{0.056} \quad (2.48)$$

for regular and irregular wave conditions, respectively. The data and equations (2.47) and (2.48) suggest that ripples formed under irregular wave conditions are slightly steeper (0.126) than those formed under regular wave conditions (0.115) with both having an almost constant steepness. The scatter of data points under the predicted line in Figure 2.13e are attributed to large errors associated with the measurements of very small ripple height (η < 1 mm) in the field and are considered to represent the experimental error.

Unlike for wavelength, when the two data sets are overlaid (see Figure 2.13f), they collapse on a single trend and least squares fitting produces the following steepness relationship:

$$\eta/\lambda = 0.120 \cdot \lambda^{-0.056} \tag{2.49}$$

with a correlation coefficient r^2 of 0.79. The small correction for very long wavelengths is attributed to the enhanced turbulence at the crests due to flow contraction over the ripples [*Du Toit and Sleath*, 1981; *Nielsen*, 1992]. Since ripple height increases with increasing wavelength, the enhancement will be greater for larger ripples.

2.5.3. Model Errors

The performance of the new models described in equations (2.40) to (2.49) is compared to that of all previously presented models (see section 2.2). For each model, the predicted ripple wavelength and height values are compared against the measured ones from the database; the scatter plots together with the 1:1 line are shown in Figures 2.14 and 2.15 for ripple wavelength and height, respectively. The least squares error of each predictor (in a log-log scale) was estimated using the root mean square error (RMS), normalized by the range of the observed values for each parameter predicted:

$$\varepsilon = \sqrt{1/N \cdot \sum \left(\log_{10}\left(X_p\right) - \log_{10}\left(X_m\right) \right)^2} \Big/ \left| \log_{10}\left(\max\left(X_m\right)\right) - log_{10}\left(min\left(X_m\right)\right) \right| \tag{2.50}$$

where X is the parameter evaluated (i.e., ripple wavelength, height, and steepness), while the subscripts m and p denote measured and predicted values, respectively. The errors associated with the existing ripple predictors and the newly developed ones (see equations (2.40) to (2.49)) are listed in Table 4. The error analysis was performed for all data collected under regular and irregular waves separately but also on the combined data set.

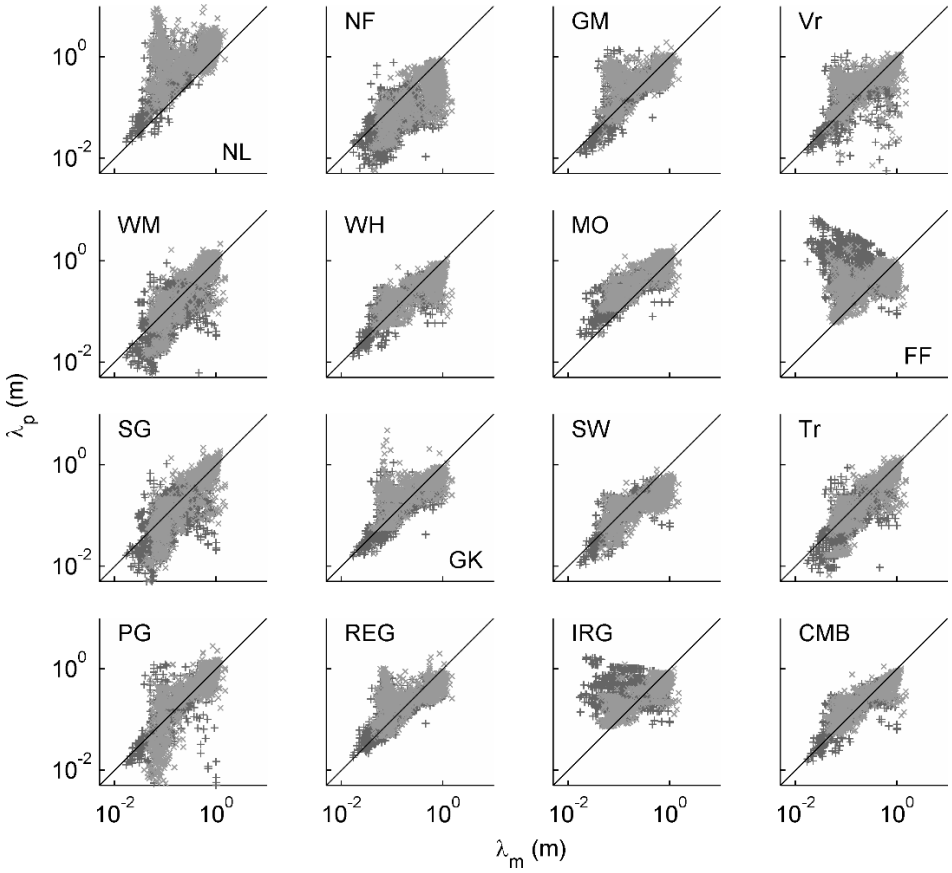

Figure 2.14. Comparison of predicted (λ_p) *vs.* measured (λ_m) ripple wavelengths for the various models examined in this study (see Table 2.2) and equations (2.42), (2.43) and (2.44) developed using data from regular (REG), irregular (IRG) and combined (CMB) wave conditions. Light and dark gray symbols represent data from irregular and regular wave conditions, respectively.

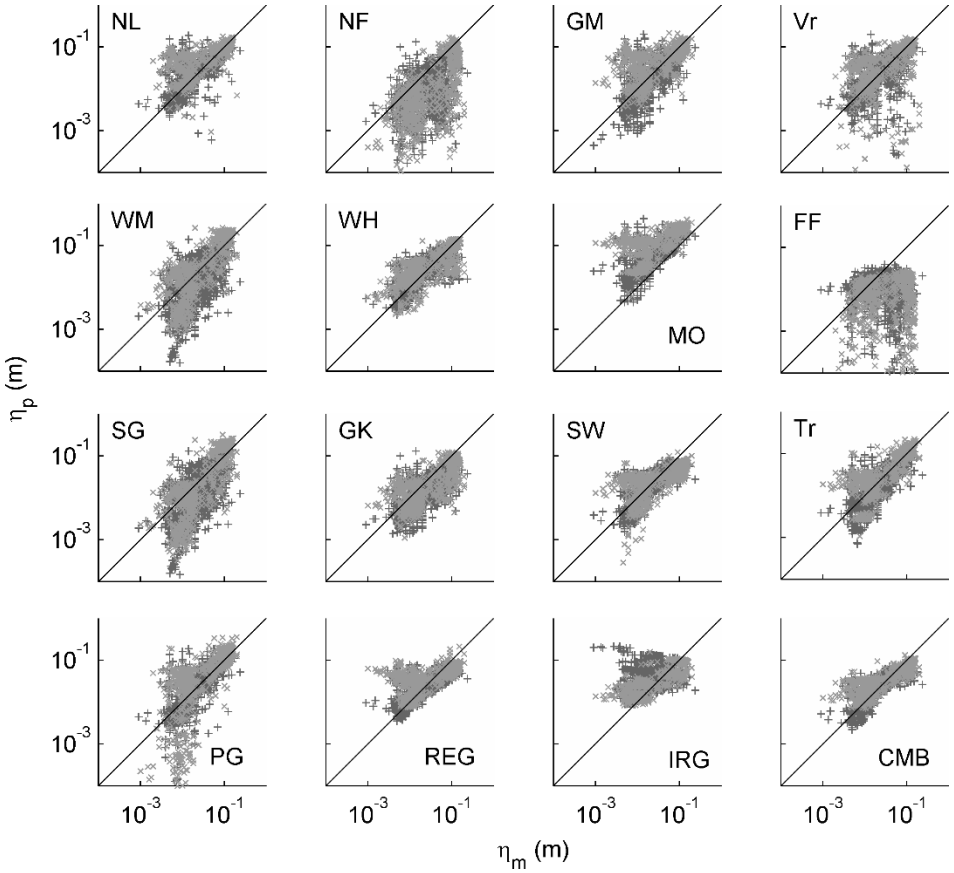

Figure 2.15. Comparison of predicted (η_p) *vs.* measured (η_m) ripple height for the various models examined in this study (see Table 2.2) and equations (2.45), (2.46) and (2.49) developed using data from regular (REG), irregular (IRG) and all (CMB) wave conditions. Light and dark gray symbols represent data from irregular and regular wave conditions, respectively.

Under regular waves, equations (2.44) and (2.49) yield the least error ($\varepsilon = 0.10$), despite the fact that they have been developed using the irregular wave data set. It is characteristic that the *Wiberg and Harris* [1994] and the *Soulsby and Whitehouse* [2005] predictors provide good agreements with the data as they are also based on the ratio A_b/D_{50}, with their errors being only 0.11. Equations (2.42) and (2.45) developed from the regular wave data provide an error similar to that of WH and SW ($\varepsilon = 0.11$).

For irregular wave ripples, the corresponding equations (2.43) and (2.46), equations (2.44) and (2.49) developed using all data, as well as the WH model provide the least error ($\varepsilon = 0.15$).

Comparing against the whole data set (combined data), neither the equations for regular nor irregular waves perform as well ($\varepsilon = 0.13$ and 0.17, respectively) as those developed using these data (equations (2.44) and (2.49)), which together with the WH equation, yield the smallest average error ($\varepsilon = 0.11$). The disparity between these models is mainly due to the different scaling of ripple wavelength between regular and irregular wave conditions. The former ripples scale with semi-orbital excursion length while the latter ones scale with the particle size.

Overall, the newly developed predictors provide the least normalized RMS errors for most of the cases, with that of *Wiberg and Harris* [1994] emerging as the second best. The strong performance of the newly developed models is not surprising as this is the only model that has been developed using the whole data set assembled in this database. It should be pointed out that equations (2.44) and (2.49) yield an identical mean error to the WH predictor, for both the irregular wave and the combined data sets ($\varepsilon = 0.15$ and $\varepsilon = 0.11$, respectively). These same equations perform better than WH for regular wave conditions. In terms of ripple wavelength, equations (2.44) and (2.49) yield the best predictions, for all three conditions, while for ripple height, these equations are as good as WH for the irregular wave, and better than any other model for the regular and combined data sets. Furthermore, equation (2.44) is in a simpler and easier to apply form whereas the WH predictor requires an iterative or a multi-step approach [*Malarkey and Davies*, 2003].

Table 2.4. Normalized RMS errors[a] between measurements and predictions (see text for details).

	Regular Waves				Irregular Waves				Combined			
	ε_λ	ε_η	$\varepsilon_{\eta/\lambda}$	Mean	ε_λ	ε_η	$\varepsilon_{\eta/\lambda}$	Mean	ε_λ	ε_η	$\varepsilon_{\eta/\lambda}$	Mean
NL	0.24	0.12	0.88	0.41	0.39	0.22	1.11	0.57	0.28	0.15	0.85	0.43
NF	0.27	0.27	0.14	0.22	0.24	0.32	0.25	0.27	0.22	0.28	0.16	0.22
GM	0.14	0.14	0.13	0.14	0.23	0.20	0.19	0.21	0.16	0.17	0.13	0.15
Vr	0.17	0.19	0.14	0.17	0.23	0.43	0.32	0.33	0.18	0.27	0.18	0.21
WM	0.21	0.21	0.12	0.18	0.15	0.18	***0.16***	0.16	0.16	0.20	0.12	0.16
WH	0.13	0.10	***0.09***	0.11	0.14	0.15	***0.16***	***0.15***	0.12	0.12	***0.10***	***0.11***
MO	0.18	0.20	0.15	0.18	0.18	0.31	0.35	0.28	0.16	0.24	0.20	0.20
FF	0.55	0.32	0.12	0.33	0.21	0.55	0.22	0.33	0.34	0.38	0.13	0.28
SG	0.23	0.22	0.12	0.19	0.16	0.20	***0.16***	0.17	0.17	0.21	0.12	0.16
GK	0.13	0.16	0.14	0.14	0.18	0.17	0.24	0.20	0.14	0.16	0.15	0.15
SW	***0.12***	0.10	0.10	0.11	0.24	0.18	0.19	0.20	0.17	0.14	0.11	0.14
Tr	0.18	0.13	0.10	0.13	0.14	0.16	0.19	0.16	0.14	0.14	0.11	0.13
PG	0.19	0.17	0.11	0.16	0.20	0.31	0.28	0.26	0.17	0.23	0.15	0.18
Eqns (2.42) & (2.45)	***0.12***	0.11	***0.09***	0.11	0.21	0.20	0.17	0.19	0.15	0.15	***0.10***	0.13
Eqns (2.43) & (2.46)	0.34	0.21	0.10	0.22	0.14	***0.14***	***0.16***	***0.15***	0.22	0.18	0.11	0.17
Eqns (2.44) & (2.49)	***0.12***	***0.09***	0.10	***0.10***	***0.13***	0.15	0.17	***0.15***	***0.11***	***0.11***	0.11	***0.11***

[a]Smallest error values are shown in bold italic fonts.

2.6. Conclusions

In this contribution, an extensive database of ripple dimensions was assembled that includes existing data from published literature and two additional field sites. The analysis showed that ripple steepness is a relatively constant number that slightly increases for decreasing ripple length. This applies for both regular and irregular wave conditions and it can be collapsed into a single model (equation (2.49)). According to this model, ripple steepness is 0.12 at large wavelengths (~1 m) increasing by approximately 29% (to 0.15) for ripples with a wavelength of only 1 cm.

For all practical applications, the equilibrium wavelength is better scaled by wave semi-orbital excursion rather than by particle size and it can be predicted by equation (2.44). This is similar to the equation presented by *Soulsby and Whitehouse* [2005] but with the fitting parameters defined from a larger range of experimental data. For field applications, with $A_{b,1/3}/D_{50}$ ratios smaller than 1,000, equation (2.43) is recommended.

Ripple height can be predicted from wave steepness (equation (2.49)), after the wavelength has been estimated from either equations (2.43) or (2.44).

The *Wiberg and Harris* [1994] predictor also provides good agreement with this extensive data set, however, the simplicity of this new model might make its application more attractive for inclusion in numerical models or in time-dependent ripple dimension prediction models.

Finally, it should be emphasized that these predictors provide equilibrium ripple conditions, which could resemble real ripple conditions only if enough time has lapsed for the ripples to adjust to the prevailing hydrodynamic forcing. Experience has shown that these dimensions might be close to reality during increasing hydrodynamic forcing;

they can deviate from reality during periods of descending wave energy as in such cases relic ripples dominate the environment.

CHAPTER 3

TEMPORAL AND SPATIAL EVOLUTION OF WAVE-INDUCED RIPPLE GEOMETRY: REGULAR *VS.* IRREGULAR RIPPLES

3.1. Introduction

Ripples are undulating geometric features commonly found on the seabed where waves and/or currents interact with the bed sediments. These features are commonly defined by their wavelength, height, and orientation; the latter relates to the direction of the flow, which tends to be perpendicular to the direction of the ripple crest. For a given hydrodynamic regime and sediment properties, ripple geometry (i.e., ripple height, length, and orientation) can vary leading to numerous plan view patterns. Ripples with linear crests and parallel to each other are usually called "regular" or "linear" [e.g., *Sleath*, 1984] while non-linear ripples are referred to as "irregular." Ripple irregularity can be due to defects [*Huntley et al*., 2008], bifurcations, sinuous crests, superposition of two or more ripple trains with different orientation (i.e., cross ripples), or a combination of all of the above.

Apart from their morphological description, ripple dimensions and directional characteristics are important for a variety of benthic boundary layer processes. The presence of ripples on the seabed leads to an increase in bottom bed roughness and wave dissipation [e.g., *Ardhuin et al.*, 2003]. The former enhances nearbed turbulence, affecting the vertical structure of the mean current in the benthic boundary layer [e.g., *Grant and Madsen*, 1986]. More recently, *Bhaganagar and Hsu* [2009] used direct

numerical simulations to show how turbulence statistics and the resultant flow structures depend on whether the ripples are regular or irregular. Increased turbulence levels due to the presence of ripples affect the ability of the flow to keep sediment in suspension and thus affects the vertical distribution of suspended sediment and depositional patterns [e.g., *Gutierrez et al.*, 2005]. *Murray and Thieler* [2004] and *Gutierrez et al.* [2005] have demonstrated how spatial differences in bottom roughness can lead to the development of larger scale bed features such as sorted rhythmic bedforms.

Differences between ripple orientation and mean current direction can also affect the degree of bed roughness experienced by the flow [*Barrantes and Madsen*, 2000; *Madsen et al.*, 2010]. *Powell et al.* [2000] used benthic boundary layer data from the North Sea to show that form drag can vary from zero for mean flows aligned with the ripple crest to a maximum drag when the mean current is perpendicular to the ripple crest. Later on, *Madsen et al.* [2010] showed that very close to the bed wave-induced ripples could even alter the direction of the mean current by causing it to align itself with the ripple crest orientation. This bedform-induced steering of the flow can have a significant impact on net sediment transport direction near the bed.

In addition to their effect on turbulence and sediment transport processes, ripples can also play an important role in biogeochemical processes [e.g., *Huettel et al.*, 1998; *Precht and Huettel*, 2003; *Rocha*, 2008] as well as penetration of acoustic energy in the seabed [e.g., *Chotiros et al.*, 2002; *Jackson et al.*, 2002; *Thorsos and Richardson*, 2002].

Given their importance, accurate prediction of ripple geometry is a prerequisite for a number of models concerned with the study and prediction of processes that depend on the presence of ripples. When the flow is energetic enough to move sediment, ripples

might start forming, but their dimensions might not be in equilibrium with the flow (i.e., "transient" or "non-equilibrium" ripples). In such a case, they will actively change height, wavelength, and/or orientation until they achieve equilibrium [*Davis et al.*, 2004; *Smith and Sleath*, 2005]. Under continuously changing wave conditions, the transient character of the ripples might continue for a long period. A number of laboratory and field studies have been carried out aiming at understanding ripple formation from a flat bed and the transition from one geometry to another [*Davis et al.*, 2004; *Jarno-Druaux et al.*, 2004; *Soulsby and Whitehouse*, 2005; *Testik et al.*, 2005; *Traykovski*, 2007]. These studies have led to the development of non-equilibrium, time-dependent models that can predict the evolution of ripples under varying wave conditions [i.e., *Traykovski*, 2007; *Soulsby and Whitehouse*, 2005]. These time-variable models are able to predict ripple height and wavelength, but they do not provide any information on the 2-dimensionality of the ripple field. They always assume the development of regular (linear), parallel ripple fields and as such they are not able to address the issue of ripple irregularity. Alternatively, non-time dependent parameterizations have been developed to determine whether a ripple will be regular or irregular. The parameters used include the ratio of orbital excursion to sediment diameter [*Carstens et al.*, 1969; *Sato*, 1984], mobility number [*Lofquist*, 1978], Reynolds numbers [*Pedocchi and García*, 2009a], amongst others. These methods do not take into account the temporal evolution of the seabed and may not always predict the correct ripple shape. Improved accuracy in simulating boundary layer flow and turbulence structures requires the development and use of ripple evolution models able to account for the occurrence and irregularity of ripples as well as the evolution of the

ripple's wavelength, height, and orientation under changing intensity and directions of wave forcing.

In this contribution, detailed field observations of seabed temporal evolution under a variety of wave conditions are presented. Specific emphasis is placed on describing the response of ripple geometry during changing wave forcing and most importantly, on how ripples behave in response to changes in wave directionality. The main objective of this study is to identify the conditions contributing to deviations in ripple linearity and quantify the degree of such irregularity. In section 3.2, the experimental setup used for the collection of field observations of ripple wavelength and orientation temporal evolution from 2 sites with different sediment size and wave forcing is presented. The analysis of the hydrodynamic and bed morphology data is presented in section 3.3, while section 3.4 presents the results regarding ripple evolution using a selected number of events from each experimental site. Section 3.5 discusses the major processes controlling bedform evolution with the conclusions of the study being presented in section 3.6.

3.2. Data Collection

Data from two experimental sites, representing environments with different wave and sediment characteristics, are used to determine the response of rippled beds to changes in hydrodynamics. Both sites are located in the South Atlantic Bight offshore the coastlines of South Carolina and Georgia, USA (Figure 3.1) and the experimental setup for each site is presented in some detail in the next two sub-sections.

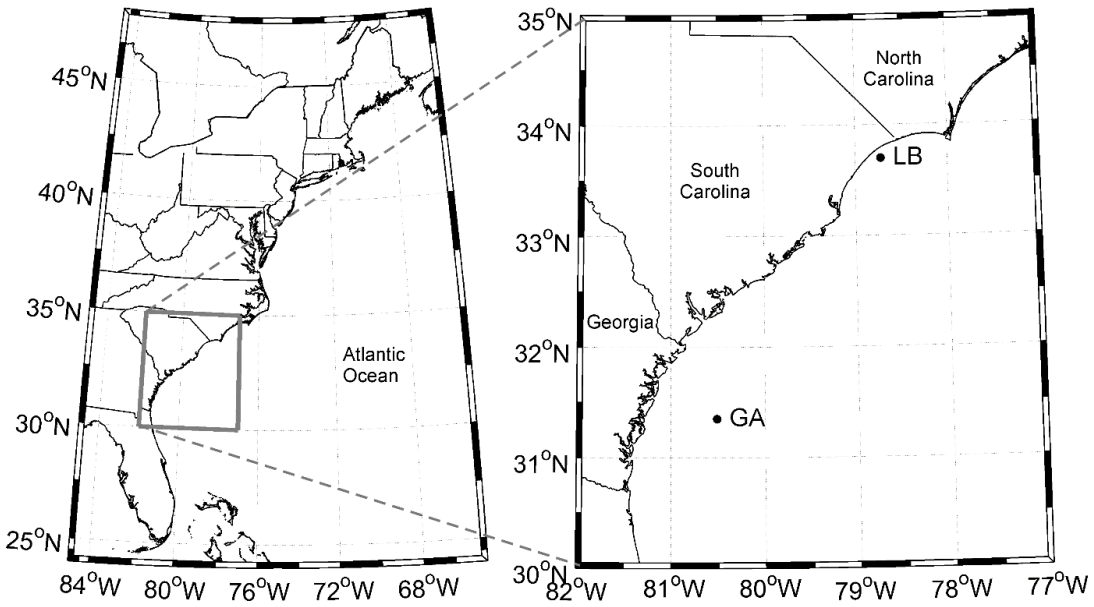

Figure 3.1. Location of experimental sites where simultaneous data on seabed state and hydrodynamics were collected and presented in this study. Key: LB: Long Bay, South Carolina; GA: Georgia Shelf.

3.2.1. The Long Bay, SC data set

The first data set used in this study is from the inner shelf of the northern part of South Carolina, off Long Bay (Fig. 3.1). These data were collected during the period October 2003 to April 2004 [i.e., *Baldwin et al.*, 2004; *Sullivan et al.*, 2006; *Barnhardt*, 2009; and *Warner et al.*, 2012]. The seabed sediment consists of fine to medium quartz sand with a median grain diameter (D_{50}) of 177 μm. Two instrumented tripods were deployed simultaneously at two sites (A and B) located 3.5 km off the coastline and at a mean water depth of 9.5 m; in order to avoid flow interference the two tripods were placed 240 m apart from each other. The tripod at site A was equipped with two acoustic Doppler velocimeters (ADV 5MHz, Sontek) measuring 3-D flows in 20 min bursts every 1 hour with a sampling frequency, within each burst, of 8 Hz. The sensor sample volumes were at 31 and 30 cm above the seabed. Pressure data were collected synchronously with

the flow data by 2 Paroscientific Digiquartz© pressure sensors. The tripod located on site B was equipped with a sector scanning sonar (Imagenex Model 881, 2.25 MHz) that was installed at 53 cm above the bed and provided seabed imagery at a rate of a 360^{o} sector scan every 30 min. This data collection regime (3 scans over a period of 1.5 hrs) was repeated every 5 hours. Data used from this study site (hereafter referred to as the LB data) cover the period 30 January 2004 to 15 March 2004 (days 30 to 75) as this provides the most complete data set of hydrodynamic and bedform information and corresponds to periods of active sediment transport.

3.2.2. The Georgia Shelf data set

The second data set of hydrodynamic and sonar images are from the continental shelf off Georgia. Seabed imagery data were collected using an Imagenex Model 881, digital rotating imaging system (2.25 MHz) with a tilted transducer head that was installed 60 cm above the seabed, at a water depth of 26 m. The seabed at this site consists of medium to coarse sand with a mean diameter of 388 μm. The sonar was cantilevered from a 3 m long stainless steel pipe jetted into the seabed. The unit was offset horizontally by 25 cm from the vertical pipe and the sensor head was tilted 9° from the vertical. Details of the bed observing system can be found in *Voulgaris and Morin* [2008]. Simultaneous hydrodynamic data were collected by a number of tripods that were deployed near the sonar site (< 200 m) and were turned over every 3 months. The hydrodynamic data were mainly ADV measurements of flow at 20 min bursts sampled at 8 Hz every hour. Two periods of simultaneously collected hydrodynamic and bedform imagery data are used in this analysis corresponding to the periods of 16 September 2007 to 7 October (days 259 to 279) and 22 November 2007 to 15 February 2008 (days 322 to

412), respectively. These periods consist of several sediment mobilization events in which the bedforms actively change dimension and orientation. This study site and data set hereafter are referred to as GA.

3.3. Methodology

3.3.1. Hydrodynamic data

Mean current velocities were estimated from the burst averages of the instantaneous horizontal velocity components recorded from each ADV and subsequently transformed into east (u) and north (v) components. The *rms* bottom wave orbital velocity was calculated from the eastward (S_u^2) and northward (S_v^2) velocity variances derived from spectral analysis of the instantaneous velocities and after integration over the frequency band 0.025 to 0.3 Hz as:

$$u_{b,rms} = \sqrt{S_u^2 + S_v^2} \qquad 3.1$$

The significant orbital velocity defined as $u_{b,1/3} = 2 \cdot u_{b,rms}$ [*Wiberg and Sherwood*, 2008] has been shown to be a better parameter for use with observed wave-induced ripple data [i.e., *Traykovski*, 2007; *Hay*, 2008] and as such this parameter is adopted in this study. Mean wave period (T) is calculated from the spectra of the eastward and northward velocities over the same frequency range as the wave orbital velocity using the moment method. Sediment mobility is assessed using the maximum wave-induced bottom stress, which is represented in a non-dimensional form by the wave Shields parameter (θ_w) [*Shields*, 1936] defined as:

$$\theta_w = \frac{0.5 f_w u_{b,1/3}^2}{(s-1) g D_{50}} \qquad 3.2$$

where s is the non-dimensional sediment density parameter, g is the acceleration due to gravity, D_{50} is the median sediment grain diameter and f_w is the wave friction coefficient defined by *Jonsson* [1966] as:

$$f_w = \begin{cases} \exp\left[5.213\left(2.5 \cdot D_{50} / A_{b,1/3}\right)^{0.194} - 5.977\right] & , A_{b,1/3} / \left(2.5 \cdot D_{50}\right) > 1.57 \\ 0.3 & , A_{b,1/3} / \left(2.5 \cdot D_{50}\right) \le 1.57 \end{cases} \qquad 3.3$$

where $A_{b,1/3} = u_{b,1/3} \cdot T / 2\pi$.

The skin friction current Shields parameter is used to represent the effect of the mean current on ripple processes, with the shear velocity defined through the quadratic relationship so that:

$$\theta_c = \frac{C_D \cdot U_z^{\,2}}{(s-1) g D_{50}} \qquad 3.4$$

where C_D is the drag coefficient that was estimated for the elevation (z) of the mean flow (U_z) measurement using the law of the wall with a roughness defined by the particle size (skin friction) only, as this is the sediment mobilizing force exerted on the seabed:

$$C_D = \left[\frac{0.40}{\ln\left[z / \left(D_{50} / 12\right)\right]}\right]^2 \qquad 3.5$$

For the LB and GA data sets, the estimated skin friction C_D values were 2.0×10^{-3}. The skin friction mean flow Shields parameter, after accounting for the presence of the wave boundary layer, is estimated using the parameterization of *Soulsby* [1995] as:

$$\theta_m = \theta_c \cdot \left[1 + 1.2 \cdot \left(\frac{\theta_w}{\theta_c + \theta_w}\right)^{3.2}\right] \qquad 3.6$$

while the combined maximum wave and current skin friction Shields parameter that is responsible of the mobilization of bed sediment is calculated by:

$$\theta_{wc} = \sqrt{\left[\theta_m + \theta_w \cdot \left|\cos\left(\alpha_{wc}\right)\right|\right]^2 + \left[\theta_w \cdot \left|\sin\left(\alpha_{wc}\right)\right|\right]^2} \qquad 3.7$$

where a_{wc} the angle between the mean current and wave directions. The latter was calculated using the angle of maximum variance [*Herbers et al.*, 1999] utilizing the instantaneous velocity data within each burst.

3.3.2. Sonar Imagery

Bedform dimensions were obtained from the returned echo intensity of the sector scanning sonar using the method described in *Voulgaris and Morin* [2008]. According to this method, the image of the recorded echo intensity is converted from the recorded polar into Cartesian coordinates and subsequently rotated so that that geographic North corresponds to the positive y-axis. Each rotated image of the seabed is sub-sampled into 8 square sub-regions (see Figure 3.2), which are then re-sampled into 128 ×128 grid points with a 2.5 cm resolution. The 8 sub-regions of the image are selected to be located close to the axis of rotation, an area with higher spatial resolution. Each of these sub-regions is subjected to a 2-D FFT analysis and an average wavelength spectrum ($S(k_x,k_y)$) of the 8 2-D spectra is obtained. From the resulting mean 2-D spectra (Figure 3.2), the ripple wavelength and orientation were determined using the spectral moments defined as:

$$m_{pq} = \iint k_y^q \cdot k_x^p \cdot S\left(k_x, k_y\right) \cdot dk_x \cdot dk_y \qquad 3.8$$

where p and q denote the spectral moment order in the x (eastward) and y (northward) directions, respectively. The average wavelength and orientation is then calculated by determining the coordinates of the spectrum's center of gravity which is given by:

$$(\overline{k_x},\ \overline{k_y}) = (m_{10} / m_{00},\ m_{01} / m_{00}) \qquad 3.9$$

such that the mean ripple wavenumber is $k = \sqrt{\overline{k_x}^2 + \overline{k_y}^2}$. Similarly, the mean orientation of the ripple (here defined as the orientation of a line perpendicular to ripple crest) is determined as:

$$\alpha_r = \tan^{-1}\left(\overline{k_y} / \overline{k_x}\right) \qquad 3.10$$

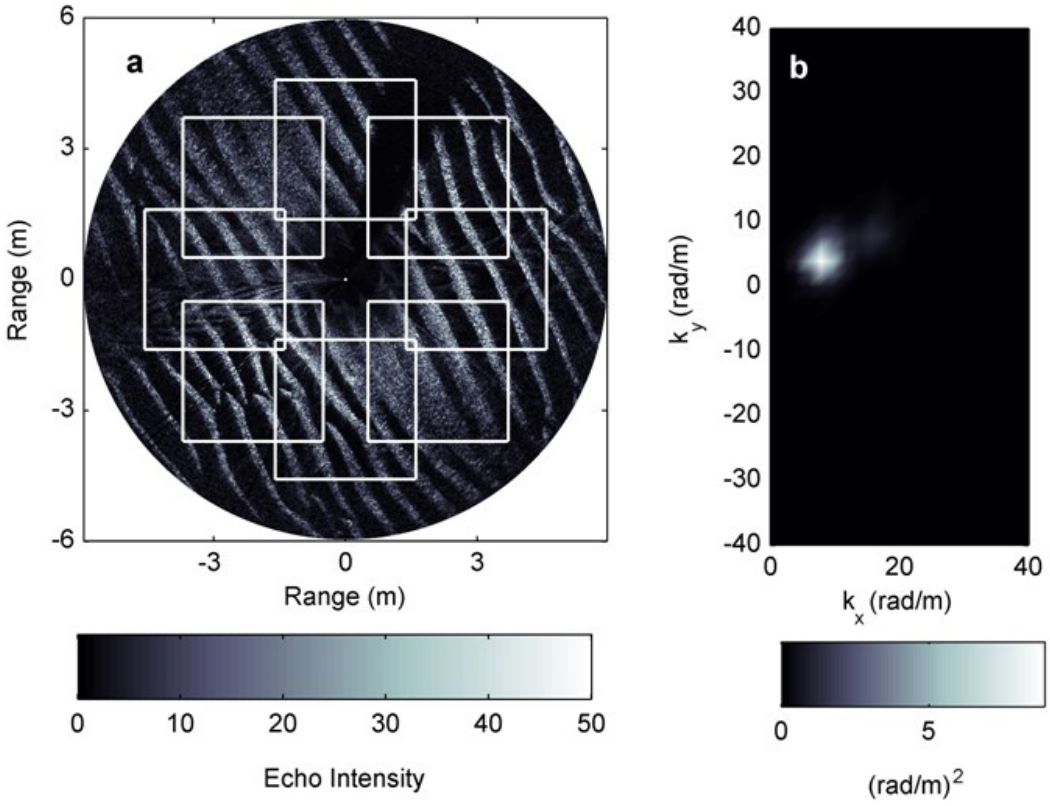

Figure 3.2. Example of sonar imagery analysis. (a) Acoustic image of the seabed from the returned echo intensity of the sonar system (echo intensity shown in arbitrary units). The 8 overlapping boxes indicate the sub-sampled regions used for estimating the individual 2-D spectra. (b) Averaged 2-D spectrum obtained from the 8 individual spectra estimated the sub-regions. The peak on the spectrum is used to estimate the wavelength and orientation of the ripples shown in (a). For more details see text.

3.3.2.1. Identifying multiple ripples systems

The spectral moments are calculated from the spectral energy over the entire range of wavenumbers ($S(k_x,k_y)$), and used to provide information on mean ripple parameters. When two or more spectral peaks are present, the area around each individual peak is first identified and then used to calculate its spectral moments so that multiple groups of ripple geometries (i.e., height, wavelength, and orientation) can be defined.

3.3.2.2. Ripple Irregularity

For the purposes of this study, any pattern that deviates from a linear 2-D ripple pattern is considered to represent ripple irregularity. Such irregularity can be due to variations in ripple wavelength between consecutive ripples, variations in orientation along a single or multiple ripple crests, or defects and bifurcations among adjacent ripples. The two parameters controlling these irregularities are wavelength and orientation, which can be represented by the spectral width of the 2-D spectrum. Therefore, the width of the spectrum is an indication of the uniformity of the ripple pattern as it represents the number of wavelengths and orientations present simultaneously on the image. This natural variability is calculated by converting the wavenumber components to a polar coordinate system $S(k,\alpha_r)$ where $k = \sqrt{k_x^2 + k_y^2}$ and $\alpha_r = \tan^{-1}\left(k_y / k_x\right)$ the spectral moments (see equation 3.8) can then be expressed in polar coordinates as:

$$m_{pq} = \iint k^q \cdot \alpha_r^p \cdot S\left(k,\alpha_r\right) \cdot k \cdot d\alpha_r \cdot dk \qquad 3.11$$

and when integrating over all orientations and solving for the omnidirectional wavenumber spectrum results in:

$$m_{k,p} = \int k^p \cdot S(k) \cdot k \cdot dk \qquad 3.12$$

Likewise, integrating over the wavenumber domain leads to the equations:

$$m_{\alpha,p} = \int \alpha_r^p \cdot S(\alpha_r) \cdot k \cdot d\alpha_r \qquad 3.13$$

the central spectral moments are then defined as:

$$m'_{k,p} = \int k^p \cdot S(k - \bar{k}) \cdot k \cdot dk \qquad 3.14$$

$$m'_{\alpha,p} = \int (\alpha_r - \bar{\alpha}_r)^p \cdot S(\alpha_r) \cdot k \cdot d\alpha_r \qquad 3.15$$

So that the directional and wavelength spectral widths can be estimated using:

$$(\sigma_k,\ \sigma_\alpha) = \left(\sqrt{m'_{k,2} / m_{k,0}}, \sqrt{m'_{\alpha,2} / m_{\alpha,0}}\right) \qquad 3.16$$

For the same variability in wavelength, the value of σ_k will vary depending on the absolute value of the ripple wavelength. Therefore, the σ_k value is normalized by the value of the mean wavenumber. The wavenumber (I_k) and orientation (I_a) irregularity parameters are then defined as:

$$[I_k,\ I_\alpha] = \left[\sigma_k / \bar{k}, \sigma_\alpha / (\pi / 2)\right] \qquad 3.17$$

3.4. Results

3.4.1. Long Bay (LB data set)

Time series of the hydrodynamic and corresponding ripple geometry data for LB are shown in Figure 3.3. The wave conditions in Long Bay are characterized by short periods (6 - 7 s) and relatively high orbital velocities (varying between 5 and 42 cm/s, see Fig. 3.3a, b) while the mean currents are relatively weak with flow speeds typically less than 10 cm/s (see Figure 3.3d). The mean current direction time series (Figure 3.3e) reveals that most of the mean current flow is due to tidal forcing and a stronger current

develops only during periods of increased wind activity [*Gutierrez et al.*, 2006; *Warner et al.*, 2012] as that recorded during days 55 to 63 (see Figure 3.3). Based on the hydrodynamic data alone, the periods where the maximum skin-friction bed shear stress exceeds the threshold condition for initiation of sediment motion are shown as shaded areas on Figure 3.3. Areas outside the shaded regions indicate periods of no sediment mobility so any changes in bedform characteristics can be attributed to biological or other diffusive processes. The duration of each event varied from a few hours up to 5 days.

The analysis of the acoustic images produced time series of ripple wavelengths (first and second order) with wavelengths varying from 7 to 22 cm (see Figure 3.3f). It is characteristic that changes in wavelength occur rather quickly and usually these are correlated with changes in wave orbital velocities and wave period. The occurrence of second-order ripple wavelengths identified are limited and usually associated with the early stages of a wave event when the seabed starts changing in response to the new hydrodynamic regime. Changes in the orientation of the ripples detected on the bed (Figure 3.3g) although correlate with energetic wave events they appear to lag behind changes in wave direction (Figure 3.3c).

The temporal variability of the estimated wavelength (I_k) and orientation (I_α) irregularity parameters (see equation (3.17)) during this period are shown in Figure 3.3h. Both parameters appear to co-vary although the absolute value of a particular type of variability is different. For demonstration purposes four images (denoted as h_1 to h_4), corresponding to different values of irregularity, are shown in Figure 3.3.The degree of irregularity exhibits a sharp increase shortly after the start of sediment motion within an event (shaded areas in Figure 3.3) as the rippled bed adjusts to a new equilibrium state.

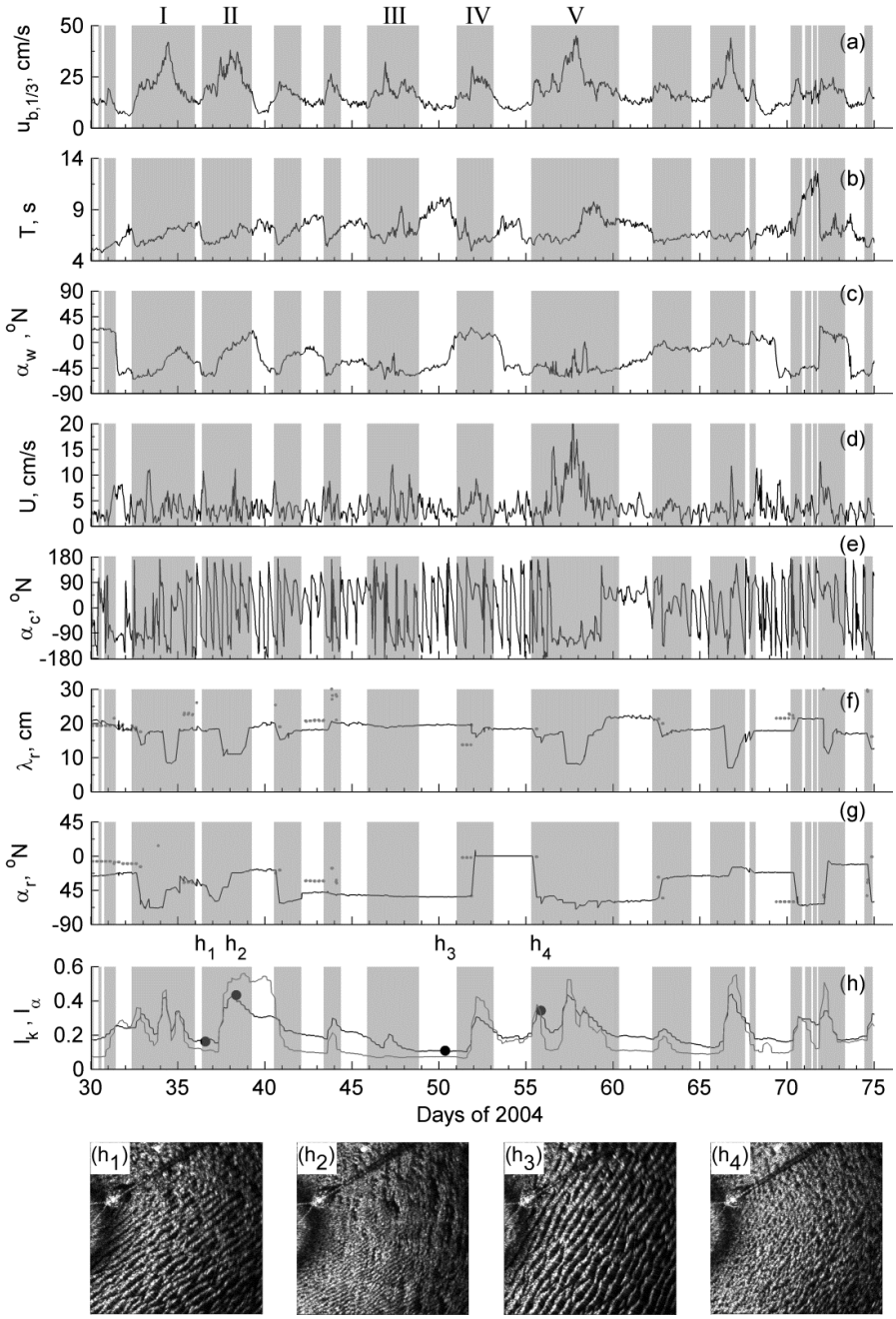

Figure 3.3. Time series of hydrodynamic and bed morphology parameters as extracted from the data collected in Long Bay, SC (LB). Hydrodynamic data: (a) significant wave orbital velocity; (b) wave period; (c) direction of wave propagation; (d) mean flow speed and (e) mean flow direction. Bedform morphology data: (f) first (solid line) and second (dots) order ripple wavelength; (g) first (solid line) and second (dots) order ripple orientation; (h) irregularity of wavenumber (I_k, black line) and orientation (I_α, gray line). Acoustic imagery (denoted as h_1 to h_4 in (h)) of the seabed for four times with different irregularity values are shown on the bottom of the figure. Shaded areas indicate periods where the combined wave and current shear stress (not shown here) exceeded the critical shear stress for sediment movement.

The larger I_k and I_α values correspond to seabed morphologies with high irregularity, as those shown in images h_2 and h_4 (Figure 3.3). Typically, within each event, irregularity decreases after the time of maximum hydrodynamic forcing and it remains unchanged during periods of no sediment motion (relict conditions) leading to more linearly arranged ripples (see images h_1 and h_3 in Figure 3.3).

From all events identified in Figure 3.3, 5 were selected as the most representative (events I to V, see Figure 3.3) for a more detailed description. A summary of the conditions and variability within each event can be found in Table 3.1. The time-series are presented in Figure 3.4, where the temporal variation of wave orbital semi-excursion ($A_{b,1/3}$), the maximum combined wave and current skin-friction Shields parameter, the ripple wavelength and the wave and ripple orientations are shown together with a selected number of acoustic images that provide a visual representation of the seabed.

The first event (event I, days 32.5 - 35.5) demonstrates how the seabed responds to changes in both forcing intensity and direction (see Figure 3.4). During this event the Shields parameter θ_{wc} and wave orbital semi-excursion ($A_{b,1/3}$) increase continuously until day 34, when maximum values of 0.3 and 45 cm are attained, respectively. Initially (day 32) wave and ripple orientations differ by 42°, causing the ripples to start aligning themselves with the wave forcing (see days 32.6 to 33). During this period, ripple wavelength is reduced (see Figure 3.3c) but it starts increasing again when the ripples have aligned with the prevailing wave field. On day 33.7, as the wave energy increases even more, the seabed is composed of bifurcating ripples with slight variations in orientation. As θ_{wc} continues to increase, the ripples start rotating towards north at a faster rate (see Fig. 3.4d, image 1). It is during this phase that the ripples start decreasing in

Table 3.1. Description of conditions related to each event in Long Bay (LB, see Figure 3.3) and Georgia (GA, see Figure 3.5).

Data Set	*Event*	*Duration (days)*	$A_{b,1/3}$ *(cm)*	*max* θ_{wc}	$\lvert\Delta\alpha_w\rvert$ *(deg)*[a]	*Initial Bed Conditions*	*Initial* $\lvert\alpha_w-\alpha_r\rvert$ *(deg)*
LB	I	3	12 - 45	0.30	69	Bifurcating	42
	II	3	14 - 40	0.23	79	Bifurcating	20
	III	1	17 - 26	0.16	32	Bifurcating	16
	IV	2	15 - 23	0.17	25	Bifurcating	66
	V	5	12 - 20	0.12	15	Irregular bed	16
GA	I	5	14 - 54	0.14	93	Flat bed	-
	II	8	14 - 68	0.21	60	Linear (eroded crests)	57[*]
	III	4	18 - 55	0.11	11	Highly disorganized bed	33
	IV	6	16 - 65	0.19	117	Linear	86
	V	1	12 - 58	0.18	29	Large linear (eroded crests)	27
	VI	4	18 - 38	0.12	55	Large linear (eroded crests)	48

[a]change in wave direction throughout the event
[*]following initial onset of motion

wavelength (Fig. 3.4, image 2) whilst at the same time both I_k and I_α irregularity values increase. This reorganization continues during the peak of the event until the diminishing stage of the storm commences (day 34.3); by then ripples have attained their smallest wavelength of approximately 9 cm (Figure 3.4, image 3). As wave energy decreases and longer ocean waves are more predominant, ripple wavelength increases (see Figure 3.3b, c). During this time, the seabed remains irregular with the smaller ripples being destructed as larger ripples form with wavelengths of approximately 25 cm and similar orientation as before (Figure 3.4, image 4). By the time θ_{wc} reduces to values smaller than

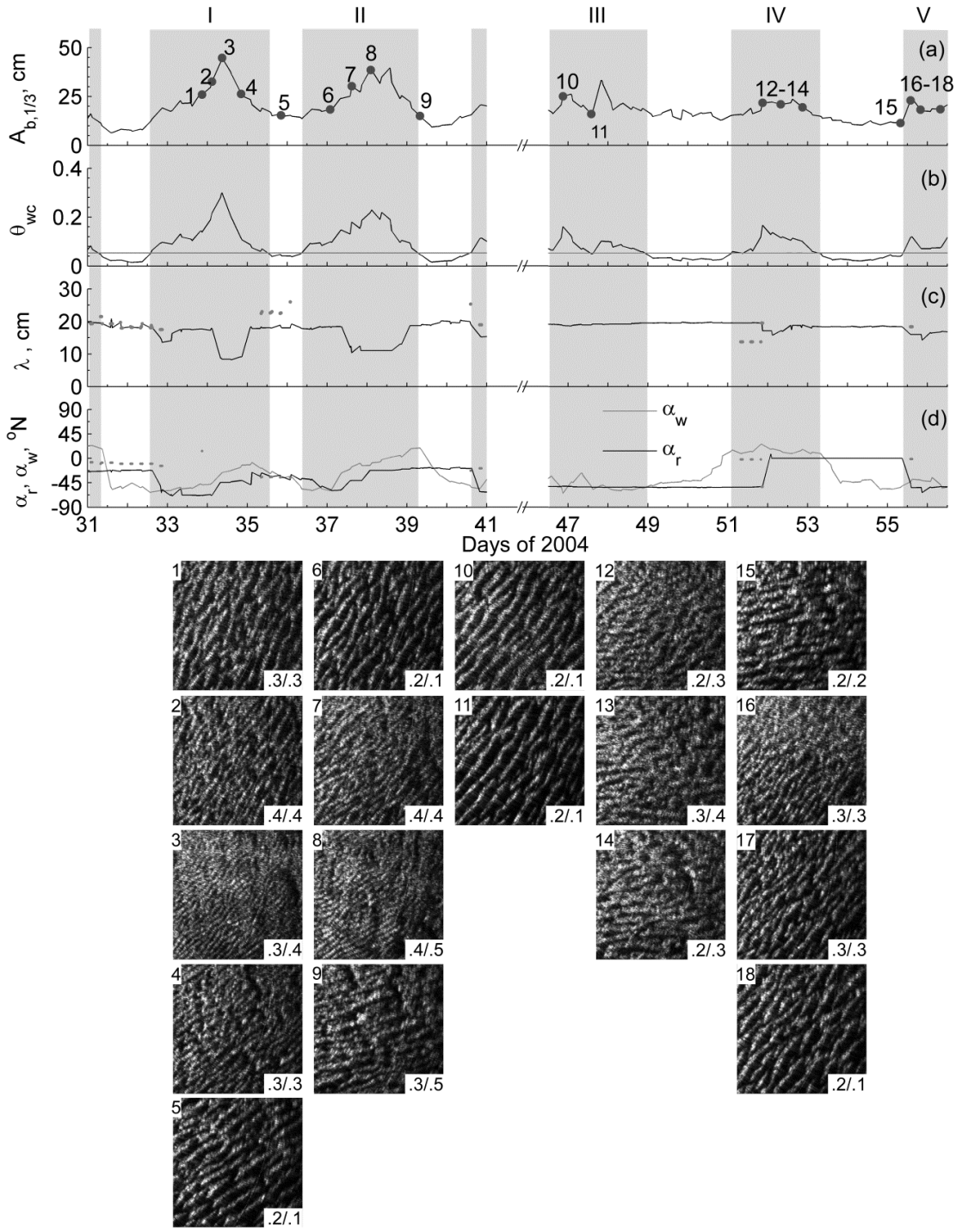

Figure 3.4. Details of the Long Bay events I to V identified in Fig. 3.3. (a) wave orbital excursion amplitude; (b) maximum combined wave-current Shields parameter; (c) first (solid line) and second (dots) order ripple wavelength; (d) orientation of first (grey solid line) and second (grey dots) order ripples and waves (black solid line). Selected imagery of the seabed from each event identified by a number (1-18) is shown with the I_k/I_α values for each image shown on the bottom right corner. The images shown correspond to individual fan beam images (2m x 2m).

the critical θ_{cr} (Figure 3.4, image 5), the smaller ripples have been completely reworked to create the larger wavelengths creating a more regular ripple pattern with decreased I_k and I_α values.

Event II occurs over a 3-day period beginning on day 36 and it is similar to event I but with weaker hydrodynamic forcing. As such, the seabed follows the same temporal and spatial variations as seen in event I (Figure 3.4, images 6 to 9) but the ripples remain more irregular. This is mainly due to the weaker hydrodynamics of this event that induce smaller sediment transport rates that do not allow the full development of linear ripples within the time available.

In event III (days 47 to 49, see Figure 3.4), a case of no change in ripple wavelength or orientation (see images 10 and 11 in Figure 3.4) is displayed. Wave direction remains the same during the two maxima in Shields parameter of this event and coincides with that of the ripples. Despite the fact that the two maxima are different, ripple wavelength does not really differ, probably due to the short duration of these maxima (< 24 hr.).

A case of different wave direction and relict ripple orientation is represented by the 2-day long event IV. Initially θ_{wc} just exceeds θ_{cr} on day 51 (see Figure 3.4b) and abruptly increases to a maximum value of 0.17 just before day 52. On day 51, α_w varies around a value of 15°, which is significantly different from the ripple direction (~-50°). It is during this time that secondary ripples appear with a direction similar to that of the predominant wave field and with smaller wavelength (see dots in Figures 3.4c and b). These secondary ripples evolve to become the main ripples once the wave forcing increases; their direction remains unchanged during the whole event while their

wavelength increases. This is shown on acoustic image 12 (in Figure 3.4) where cross ripples are present; at this time the ripple height is reduced in relation to the previous image (see image 11) but as the ripples realign themselves with the new wave direction, they become better defined (see images 13 and 14).

Finally, event V presents an example where waves with a direction different than that of the relict ripple field have been present for a period of 2 days (days 54 and 55) but due to their low energy levels they are not able to reorganize the bed. As soon as the wave energy increases, the bed responds by re-organizing itself into ripples with slightly smaller wavelengths and an orientation similar to the wave field. This transition is shown through the sequence of images 15 to 18 in Figure 3.4.

3.4.2. Georgia Shelf (GA data set)

The time series of the hydrodynamic conditions and ripple geometry for the GA experiment are shown in Figure 3.5. As in the case for the LB data set, several sediment mobilization events are identified (see shaded areas in Figure 3.5) that correspond to a number of storm events with elevated wave energy. Some of them (e.g., days 355 and 382) are characterized by a sudden increase of the wave energy, while others correspond to cases where a more gradual increase of wave energy takes place. The wave orbital velocities during the storm periods attain velocities up to 47 cm/s (Figure 3.5a) and the mean period of the waves reaching the seabed is approximately 9 s (Figure 3.5b). The mean flows, which are stronger than those found in the LB data set, are mainly tidal with some wind driven flows superimposed on them. Maximum mean current speeds observed were 40 cm/s. The mean current shear stress occasionally becomes just strong enough to mobilize the bed sediment (i.e., $\theta_c \approx \theta_{cr}$); these conditions occur mainly in periods

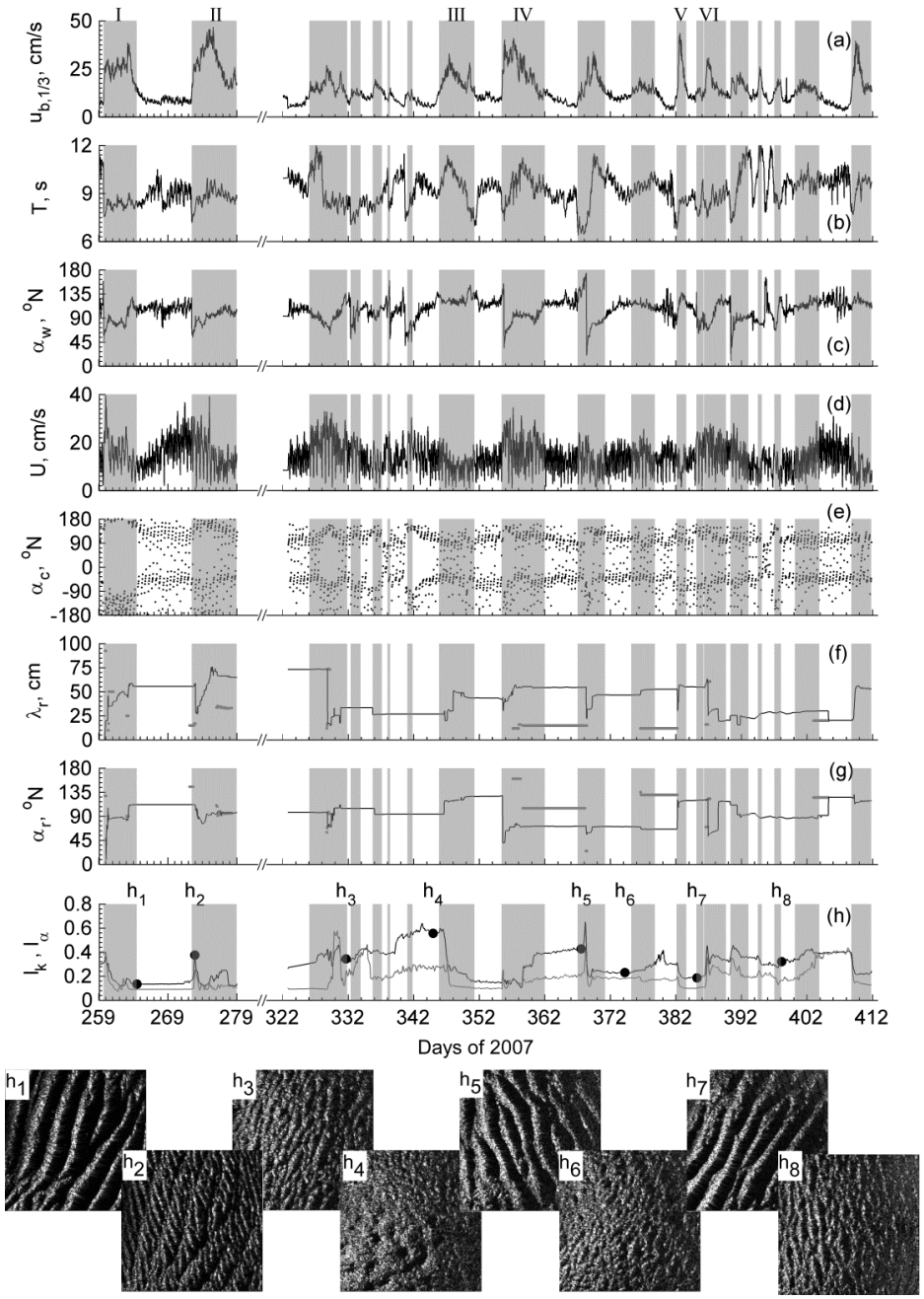

Figure 3.5. Time series of hydrodynamic and bed morphology parameters as extracted from the data collected on the Georgia shelf (GA). Hydrodynamic data: (a) significant wave orbital velocity; (b) wave period; (c) direction of wave propagation; (d) mean flow speed and (e) mean flow direction. Bedform morphology data: (f) first (solid line) and second (dots) order ripple wavelength; (g) first (solid line) and second (dots) order ripple orientation; (h) irregularity of wavenumber (I_k, black line) and orientation (I_α, gray line). Acoustic imagery of the seabed for four times with different irregularity values (denoted as h_1 to h_8 in (h)) are shown on the bottom of the figure. Shaded areas indicate periods where the combined wave and current shear stress (not shown here) exceeded the critical shear stress for sediment movement.

between large wave events, they are tidally modulated and never last more than 2 hours (see Figures 3.6 and 3.7, gray line). Nevertheless, mean currents do have an impact on increasing the total shear stress experienced by the seabed for times of the wave cycle, as this is shown through the estimates of the maximum combined wave-current shear stress (Figures 3.6 and 3.7, black line). Most of the sediment mobilization events correspond to periods when a change in prevailing wave direction occurs causing a changes in both ripple wavelength (Figure 3.5f) and orientation (Figure 3.5g). Furthermore, the ripple irregularity parameters (Figure 3.5h) indicate a significant change in seabed regularity patterns within each period of sediment mobilization. For periods when the I_k and/or I_α values are large the seabed is comprised mostly of irregularly spaced ripples (see acoustic images h_2, h_3, h_4, h_6 and h_8 in Figure 3.5) while small values of irregularity correspond to more linear, regularly spaced ripples (see images h_1, h_5 and h_7, in Figure 3.5). When compared to the LB data set, the GA data represent conditions characterized by stronger mean flows, longer period waves (due to the larger water depth, short waves do not reach the bed) and coarser sediment size.

Six periods (GA events I to VI) of sediment mobilization have been selected to be described in more detail. A summary description of each event is listed in Table 3.1 while the detailed time-series for events I - II and III - VI are shown in Figures 3.6 and 3.8, respectively. Prior to the start of the first event (before day 259), there was a period of a few months with relatively calm wave conditions, where biological benthic activity and other diffusive processes (see section 3.4.3) had led to a flat seabed (see image 1 in Figure 3.6). The sonar image suggests the existence of meter scale features, which are believed to reflect differences in acoustic intensity due to differences in grain size

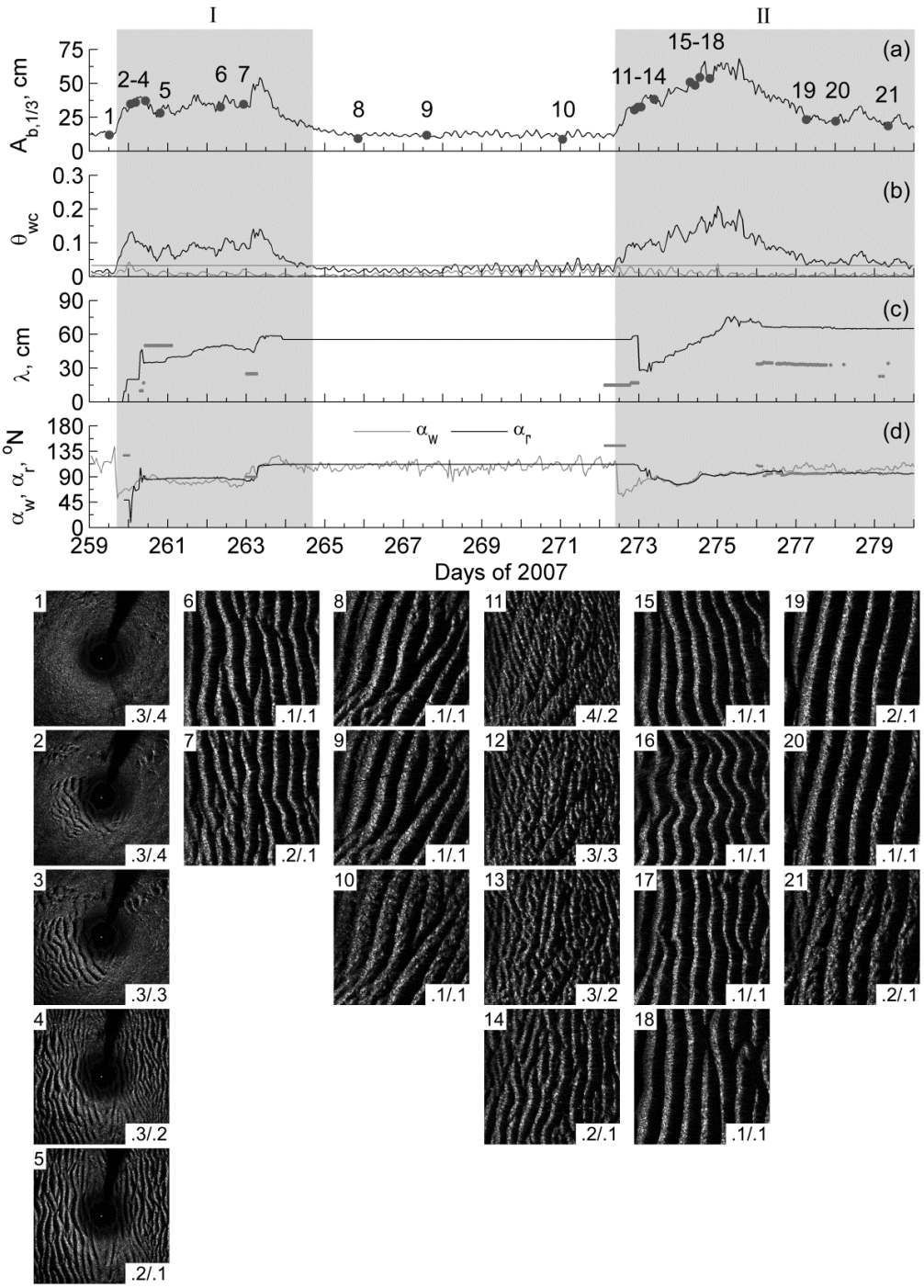

Figure 3.6. Details of the Georgia events I and II identified in Figure 3.5. (a) Wave orbital excursion amplitude; (b) maximum combined wave-current Shields parameter; (c) first (solid line) and second (dots) order ripple wavelength; (d) orientation of first (grey solid line) and second (grey dots) order ripples and waves (black solid line). Selected imagery of the seabed from each event identified by a number (1-21) is shown with the I_k/I_α values for each image shown on the bottom right corner. The images shown correspond to individual fan beam images with dimensions 4 x 4m for images 1-5 and 2 x 2m for the remaining images.

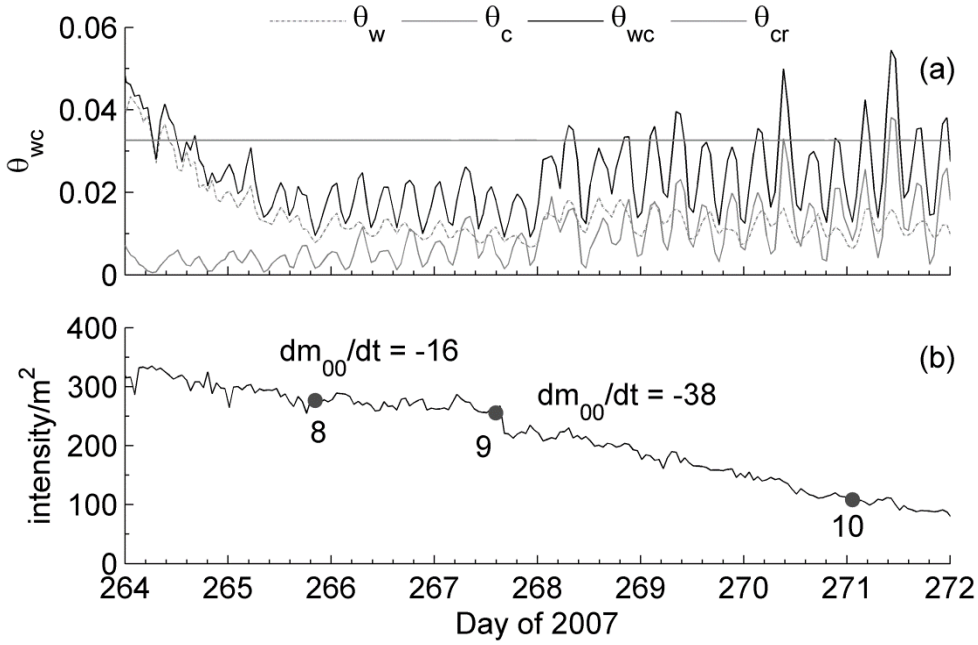

Figure 3.7. Time series from GA demonstrating ripple decay for a period of 7 days (year days 265-272) when ripple wavelength and orientation remain constant (a) wave-current Shields parameter (black line) and current Shields parameter (gray line); (b) Total spectral energy (m_{00}) from the 2-D FFT analysis of the acoustic imagery using arbitrary units for image color intensity. The marks shown on (b) indicate the times for images 8 to 10 shown in Figure 3.6.The remaining four events (III to VI) from GA are shown in Figure 3.8.

between the troughs and crest sediments of pre-existing eroded ripples. The first ripples appear on day 260, some 7 hours after θ_{wc} exceeded θ_{cr}; they are aligned with the wave direction and their formation starts from the area around the installation structure used to support the sonar. This lag between ripple formation time and when θ_{wc} first exceeded θ_{cr} is due to the time required for ripples to form from a relatively flat bed. The lag is much larger than that found in cases where the bed simply changes from one ripple scale to another (see section 3.3.1 and subsequent events). The field of ripples begins to form on the southwest side (Figure 3.6, image 2) and gradually extends to a larger area over the next several hours. The first ripples to form have a small wavelength that increases with

time. Similar ripple fields begin to form at various areas of the seabed (image 3, Figure 3.6) and after 17 hours (image 4, Figure 3.6) the bed resembles an assemblage of patches of various interconnected ripples. The ripples continue to evolve by aligning themselves with the wave direction, while the smaller wavelengths increase in size, leading to a bed, which is composed of linear ripples with a few bifurcations and wavy crests (see image 6, Figure 3.6). Between days 261.5 and 263 there is a period of relatively constant $A_{b,1/3}$ (30-35 cm) and θ_{wc} with only a slight modulation in their values. These modulations cause the crest to become slightly wavy and increase the number of bifurcations (image 7, Figure 3.6). However, there is no significant change in ripple dimensions indicating the geometry is in a nearly equilibrium state due to the nearly constant $A_{b,1/3}$ for several hours.

Following event I and before the start of event II, there is a quiescent period (day 264 to 272) where no changes in ripple wavelength or orientation is observed. The Shields parameter values due to either waves (θ_w) or currents (θ_c) alone does not indicate any sediment mobility; however, θ_{wc} does indicate periods of tidally modulated sediment mobility after day 268. Although no direct ripple height measurements are available, a broadening in the reflections on the fan beam images 8-10 (Figure 3.6) is inferred as a decrease in ripple height. Since no changes in wavelength and/or orientation are observed, this inferred ripple height decrease is interpreted as erosion off the initially sharp crestline. This process is reflected in the reduction of total spectral energy (m_{00}) estimated from the 2-D FFT analysis of the image (Figure 3.7). Between days 265 and 268, there is no mobilization due to waves or currents; however, a decay in m_{00} in Figure 3.7 and image 9 (Figure 3.6) is still present. The rate of decrease more than doubles after

day 268 (from -16 intensity/m^2/day to -38 intensity/m^2/day) indicating that the periodic mobilization of sediment accelerates the rate of ripple height decrease.

Event II started on day 272 and lasted for 8 days with the most energetic conditions attained on day 275.6. Initially, waves and relict ripples are 57° to each other; then new shorter (~17 cm) second order ripples start developing on top of the wide crest of the relict ripples, that are aligned with the prevailing wave direction (see image 11, Figure 3.6). These new ripples have a strong linear trend but are highly discontinuous. As the wave direction continuously changes, the new small ripples continue to adjust by joining with adjacent ones (see images 12 and 13) leading to the more linear, bifurcating seabed shown in image 14 (Figure 3.6). Sometime between days 274 and 275, the wave direction changes slowly while the Shields parameter and $A_{b,1/3}$ continue to increase over time. During this time, ripple wavelength approaches what appears to be an equilibrium state with linear ripples (see image 15, Figure 3.6). Slight changes in wave direction (~5°) cause the wave crests to become sinuous with an along crest periodicity of about 80 cm (image 16, Figure 3.6). As the wave direction rotates back to its original value (~90°), the ripples again become linear (image 17, Figure 3.6) and the linearity continues to increase while the wave direction stabilizes (image, Figure 3.7). During the decaying stage of the event, the ripples remain stable until day 277 when the wave stress is still above threshold conditions, but significantly reduced compared to the peak of the event. During this period, the ripples are well developed with large wavelength and presumably large ripple heights (image 19, Figure 3.6). Small oscillations are observed in wave direction that lead to the development of small bifurcating ripples along the crest of the

large ripples (Figure 3.6, image 20 and 21) resulting in a braided pattern (Figure 3.6, image 21).

Event III (days 346 to 350, Figure 3.8) demonstrates the process of ripple development from a highly disorganized bed. The seabed imagery shows the presence of some structure resembling very old remnants of ripples and pits (see section 3.4.3) with length scales of the order of 30 cm (image 1, Figure 3.8). These disorganized structures rapidly develop into bifurcating ripples (image 2, Figure 3.8) in response to increasing wave forcing. During a period of relatively steady $A_{b,1/3}$ (~ 45-50 cm) the ripples increase in wavelength and become more linear (see images 3 and 4, Figure 3.8). During the times of reducing wave energy, the ripples align with the waves and linearity increases (image 5).

In contrast to event III, during event IV (on day 355) wave energy exhibits a sudden increase in magnitude and change in wave direction by almost 90°. This change leads to the appearance of cross ripples on the pre-existing ripple field (see image 6, Figure 3.8) that continue to grow over the next several hours, while the relict ripples diminish (images 7 and 8, Figure 3.8). After 10 hrs, no traces of the relict ripples are present (image 9, Figure 3.8). These better-developed, sharp-crested ripples adjust to the changing wave direction by bifurcating with adjacent ripples (image 10, Figure 3.8) at which point they increase in linearity and the number of defects decreases (image 11, Figure 3.8). A local decline in wave energy occurs between days 357 and 361 accompanied by a slight variability in wave direction. These changes reduce the sharpness of the imaged ripple crests (Figure 3.8, image 12) indicating some erosion on the crest top. A continued rotation of the wave direction halts the development of these

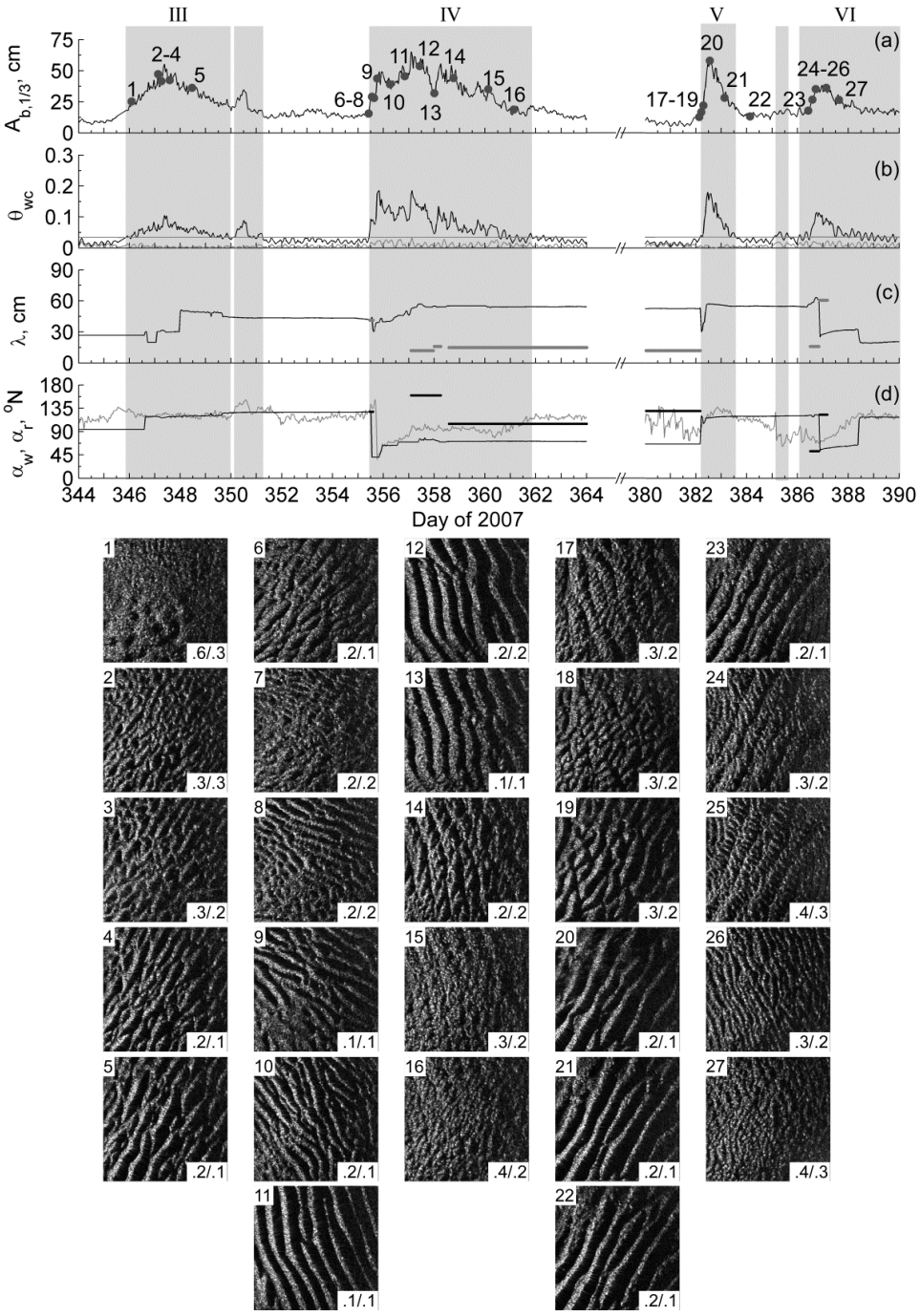

Figure 3.8. Details of the Georgia events III to VI identified in Figure 3.5. (a) Wave orbital excursion amplitude; (b) maximum combined wave-current Shields parameter; (c) first (solid line) and second (dots) order ripple wavelength; (d) orientation of first (grey solid line) and second (grey dots) order ripples and waves (black solid line). Selected imagery of the seabed from each event identified by a number (1-26) is shown with the I_k/I_α values for each image shown on the bottom right corner. The images shown correspond to individual fan beam images with dimensions 2m x 2m.

ripples (see image 14, Figure 3.8) and results in a random bed with few well defined ripples (images 15 and 16, Figure 3.8).

A clear example of cross-ripple creation is shown on day 382 (event V) when a rapid 0.5 day increase in wave energy results in $A_{b,1/3}$ and θ_{wc} values of 58 cm and of 0.18, respectively. As θ_{wc} increases, the wave direction forms a 28° angle to the ripple crest and small wavelength cross-ripples develop. As the new ripples grow in wavelength and height, the relict ripples diminish (see images 18 and 19, Figure 3.8). By the time of peak $A_{b,1/3}$ (image 20, Figure 3.8), bifurcating linear ripples with a wavelength of 56 cm cover the seabed. During the following 0.5-day period of $A_{b,1/3}$ reduction, the ripple wavelength remains constant and the ripples become more linear and well defined (images 21 and 22, Figure 3.8).

Similar to event V, event VI shows the formation of new ripples superimposed on the existing (~58 cm) ones creating cross-ripples (image 24, Figure 3.8). In this case, although the height of the relict ripples decreases, the continuously changing wave direction makes the new ripples connect with adjacent crests (image 25, Figure 3.8) forming shorter (30 cm) bifurcating, linearly trending ripples. As the wave direction continues to rotate, these ripples reorient but never reorganize due to the weakened wave strength (Figure 3.8, image 27).

3.4.3. Biological Influences

In addition to physical alteration of the seabed in response to hydrodynamic forcing as presented in the previous examples, Hay (2008) noted that biological activity could also alter ripple morphology through the mechanical action of bottom dwellers that create burrows and pits. This is also evident in the imagery from GA with an example of

it shown in Figure 3.9. On day 339, fish began creating a number of pits in close proximity to each other and over the course of 4 hours altered an approximately 3.5 m by 3.5 m area of the seabed. Indication of fish and rays (Figures 3.9a and b) are also visible as oblong shadows in the fan beam images (days 332.5 and 335.9) as well as by video and photos taken of the deployed tripod by divers (not shown in here). The roughness created by these processes is shown in Figure 3.9c and d.

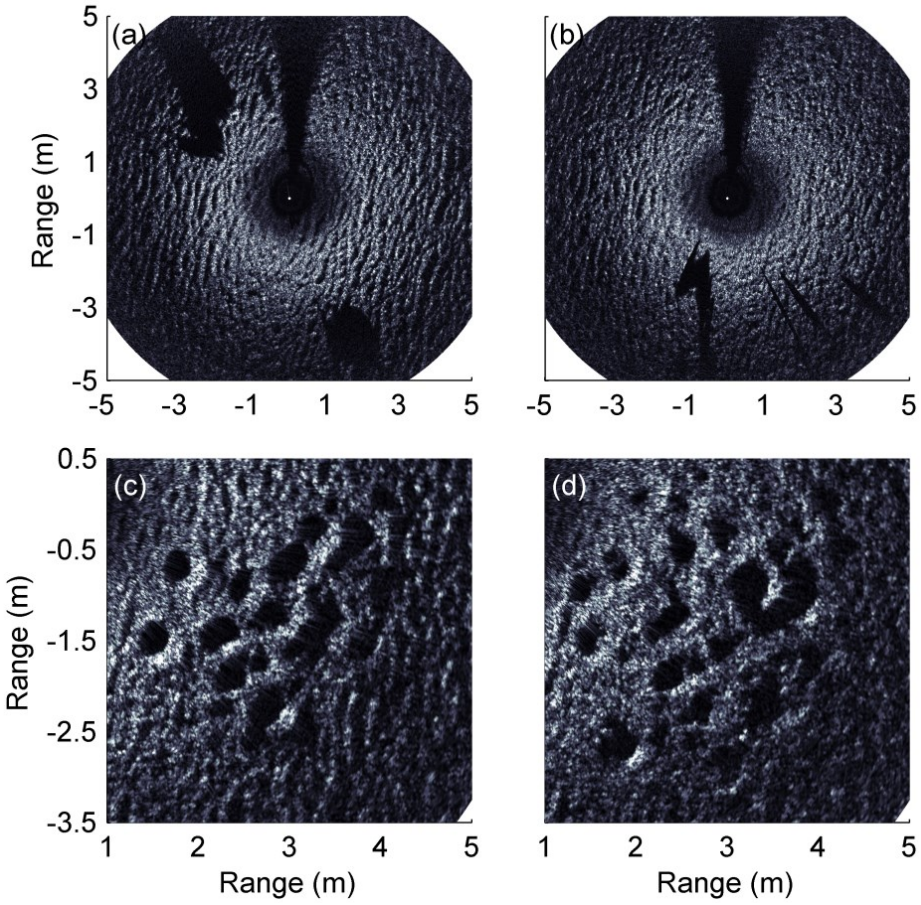

Figure 3.9. Acoustic images of the seabed from GA showing the presence and influence of organisms on the seabed. (a) Image (day 332.46) showing the presence of possibly several rays; (b) image (year day 335.9) showing the shadows (long black streaks) from fish. Images showing the development of pits on the seabed corresponding to days 339.2 (bottom left) and 339.3 (bottom right) for (c) and (d).

3.5. Discussion

3.5.1. Ripple Evolution

The observations on the temporal evolution of wave-induced ripple fields indicate that this is a dynamic process dependent upon the initial conditions of the bed, the strength and duration of the wave-induced flow but also the stability of the forcing (wave) direction. During these transitions, the bed passes through various degrees of irregularity until final equilibrium geometry is obtained, assuming sufficient time has lapsed.

3.5.1.1. Effect of wave event intensity

A synthesis of the observations from these field experiments reveals some general patterns in ripple evolution. From the LB data sets (finer sands) it was noted that during the increasing phase of a wave event (here denoted as $dA_{b,1/3}/dt>0$) ripple wavelength decreases while during the declining phase ($dA_{b,1/3}/dt<0$) ripple wavelength increases (see LB events I, II and V). This trend is in agreement with that described in chapter 1 for equilibrium ripples under irregular waves. However, for the GA data (larger ripples in coarser sandy bed), ripple wavelength often remains unchanged for $dA_{b,1/3}/dt<0$ (see GA event V). These trends agree with those from other long-term field [e.g., *Traykovski*, 2007; *Maier and Hay*, 2009] and laboratory experiments [*Davis et al.*, 2004; *Jarno-Druaux et al.*, 2004; *Testik et al.*, 2004] that have confirmed the existence of a lag time between the onset of sediment motion and the time ripples attain equilibrium. During periods when θ_{wc} just exceeds θ_{cr} (see GA event II, images 19-21), ripple evolution is much slower than during periods when $q_{wc} >> \theta_{cr}$ (see GA event II, images 15-18). Furthermore, large wavelength ripples show less modification than small scale ripples

(LB *vs.* GA events); therefore, ripple adjustment time appears to be depended on initial ripple size, sediment grain size and flow strength and duration. Given that the GA site is in the same geographical region as LB, storm duration is similar in general. However due to higher water depth, the wave energy reaching the bed (assuming the same storm intensity) is lower in GA (see maximum Shield values in Figures 3.6b and 8b) when compared with LB (see Figure 3.4b). The difference in threshold Shield parameter values (0.053 and 0.034 for LB and GA, respectively) combined with differences in wave energy between the two sites, leads to excess Shields parameter (θ_{wc}-θ_{cr}) values that are roughly equal for the two locations, for most cases. This explains the larger ripple adjustment time scales required in the GA ripples since the amount of sediment displacement is proportional to the size of the ripples.

For cases where the intensity of the forcing varies, two types of ripple evolution are revealed. When the equilibrium ripple wavelength demanded by the prevailing wave forcing is smaller than that of the existing ripples (e.g., LB event I, images 1-3; LB event II images 6-8), ripple wavelength adjustment occurs mainly by splitting the existing ripples into two or more with frequent bifurcations. If the hydrodynamics call for an equilibrium ripple wavelength larger than that of the existing ripple (e.g., LB event I, image. 3-5; LB event II images 8-9; and GA event IV, images 8-11), then two or more adjacent ripples combine until the wavelength is in equilibrium with the flow. This process is very similar to that described in the laboratory experiments of *Testik et al.* [2004].

3.5.1.2. Effect of changes in wave direction

In terms of wave direction, a small (~10-15°) change can lead to ripple orientation re-alignment with the flow. Under such conditions, the initial ripples become discontinuous with the disjointed ends rotating first to align with the wave direction. Subsequently, these ends start connecting with adjacent ripples (e.g., GA event II, images 3-5; GA event IV, images 8-11). This process of segmenting and bifurcating continues until the ripples align fully with the new wave direction. For linear ripples with large wavelengths (e.g., GA event II, images 15-18), before segmentation and bifurcation begins, the crests become sinuous. When wave direction and ripple orientation differ by more than 45°, secondary ripples form, which align with the wave direction and are superimposed on the initial ripple field generating a cross-ripple pattern (see LB events IV and V). Over time, the relict ripples degrade as the sediment is re-distributed to form the new ripple field. This process is more common in beds with smaller ripples (i.e., LB), covered with degraded relict ripples or cases where abrupt changes in wave directions occur. When well-defined larger ripples are present (i.e., GA) smaller cross-ripples, superimpose on top of the larger ones (see GA events II, V and VI and image 14). If the wave direction remains constant, these new ripples join with adjacent bedforms and begin to form a braided pattern on the crest of the relict ripples that eventually might evolve to a linear ripple field, aligned with the wave direction.

The effect of changing wave direction described earlier (i.e., decreased ripple height as the sediment is reworked to a new configuration) is something not captured by existing time-dependent ripples models. *Traykovski's* [2007] model assumes immediate response of ripples to wave direction, while the *Soulsby and Whitehouse* [2005]

formulations, for wave-dominated flows, allow for ripple wavelength, height, and orientation to evolve independently of each other. In order to demonstrate this, the *Soulsby and Whitehouse* [2005] model is used to predict the ripples for GA event VI and the results are compared with the measurements in Figure 3.10. Although no direct ripple height measurements exist for either experiment, the seabed imagery indicates a decrease in ripple height as the ripple orientation adjusts (see images 23-27 in Figure 3.8). The time-dependent model predicts (see Figure 3.10d) a slight increase in ripple height followed by a small reduction to heights even smaller than the initial ripple height. In addition, the model indicates a gradual realignment of the ripples until they are fully re-aligned (after 7 hours) with the waves. The observations, on the other hand, never show a total re-alignment of the ripple crests with the waves but cross-ripples develop on day 380.5. The model, being monochromatic cannot predict irregularities on the ripple patterns and instead predicts ripple wavelengths that have a value approximately equal to the average of the two ripples that constitute the cross rippled bed (first and second order, see Fig. 3.10c).

3.5.1.3. Effect of bed initial conditions

When the initial conditions are those of a flat bed (see GA event I) ripples start forming near a perturbation (i.e., obstructions like a stone, shells or larger sediment grains or a depression like a fish burrow, see GA Event I). The ripple field then evolves by extending away from the obstruction. This process of extension occurs by creating very short ripples that grow over time until reaching equilibrium conditions. Although, due to aliasing caused by the slow sample rate (1 image per hr) it is not possible to determine the exact bed evolution, the images suggest that no new ripples form in the

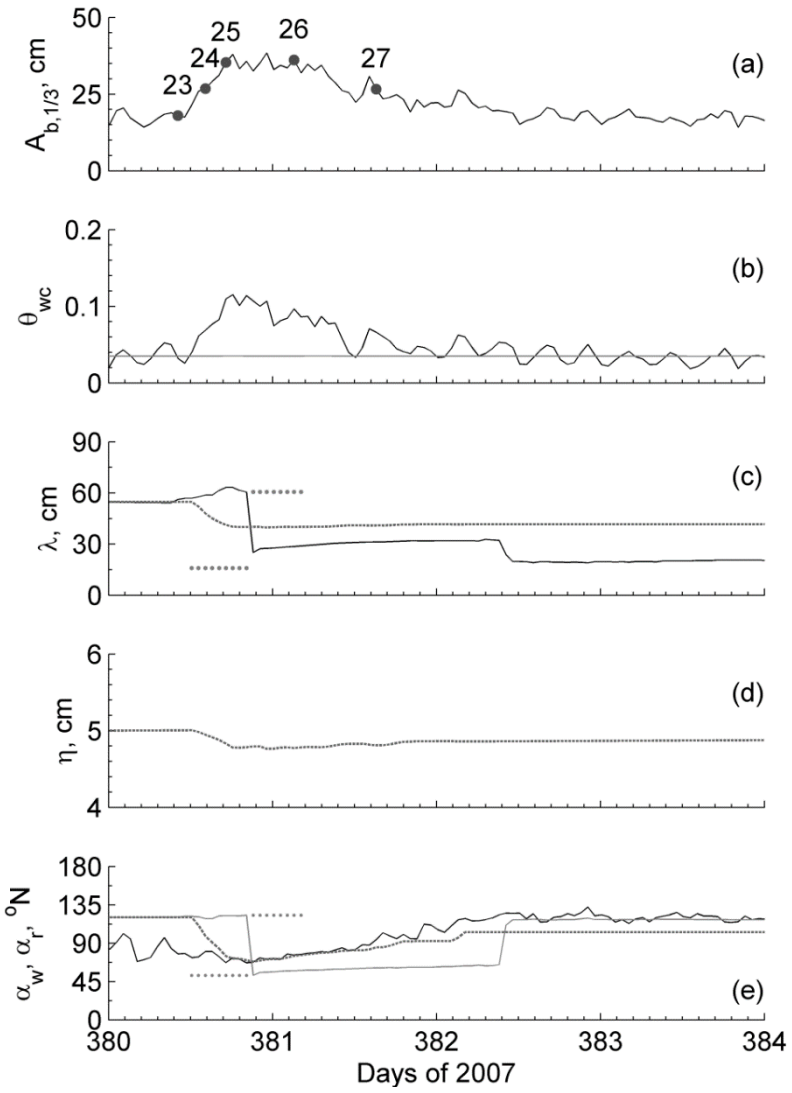

Figure 3.10. Comparison of the *Soulsby and Whitehouse* [2005] model with the data from GA, event VI (see Figures 3.5 and 3.8). (a) Wave orbital excursion amplitude (black line) where the dots correspond to images 23-27 in Figure 3.8; (b) maximum combined wave-current Shields parameter (black line) and critical Shields parameter for sediment motion (horizontal gray line); (c) measured first (solid line) and second (dots) order ripple wavelength and model prediction; (d) ripple height predicted by the model; (e) measured orientation of first (grey solid line) and second (grey dots) order ripples and waves (black solid line). The *Soulsby and Whitehouse* [2005] time-dependent model prediction of ripple orientation is shown as a dashed line.

periphery of the ripple field until the existing ripple attains its equilibrium dimensions. If the seabed is highly irregular with no clearly defined wavelength (see GA event III), the seabed quickly organizes into bifurcating ripples.

During periods of no sediment mobilizations, ripple wavelength and orientation remain unchanged but ripple height can decrease (see Figure 3.7) because of biological interaction [*Hay,* 2008] or other diffusing processes such as occasional sediment mobilization during the passage of the largest waves in a wave group. The latter process is not fully captured when using statistical description of wave energy such as significant or *rms* wave height. Sediment mobilization for short periods (few hours) under weak shear stresses ($\theta_{wc} \approx \theta_{cr}$) does not appear to significantly alter ripple wavelength and orientation but can produce a decrease in ripple height (see LB event III; GA event VI and period between events I and II) at a faster rate (see Figure 3.7).

3.5.2. Ripple Irregularity

3.5.2.1. Classification of Irregularity

The data have demonstrated that the seabed is often composed of various ripple shapes and irregularity that as explained in the introduction can have an impact on hydraulic roughness, nearbed flow structure, sediment resuspension, and transport. The two irregularity parameters I_k and I_α introduced in section 3.3.2.2 (equation (3.17)) are used in Figure 3.11 where a scatter diagram of the two parameters is presented. The LB data (Figure 3.11a) scatter over a region trending on a slope greater than that of a 1:1 line. In the area below the 1:1 line, the ripples exhibit small irregularities due to either variability in wavelength and/or direction but overall they can be classified as regular ripples. Irregularity is more prominent in the data plotted in the region above the 1:1 line,

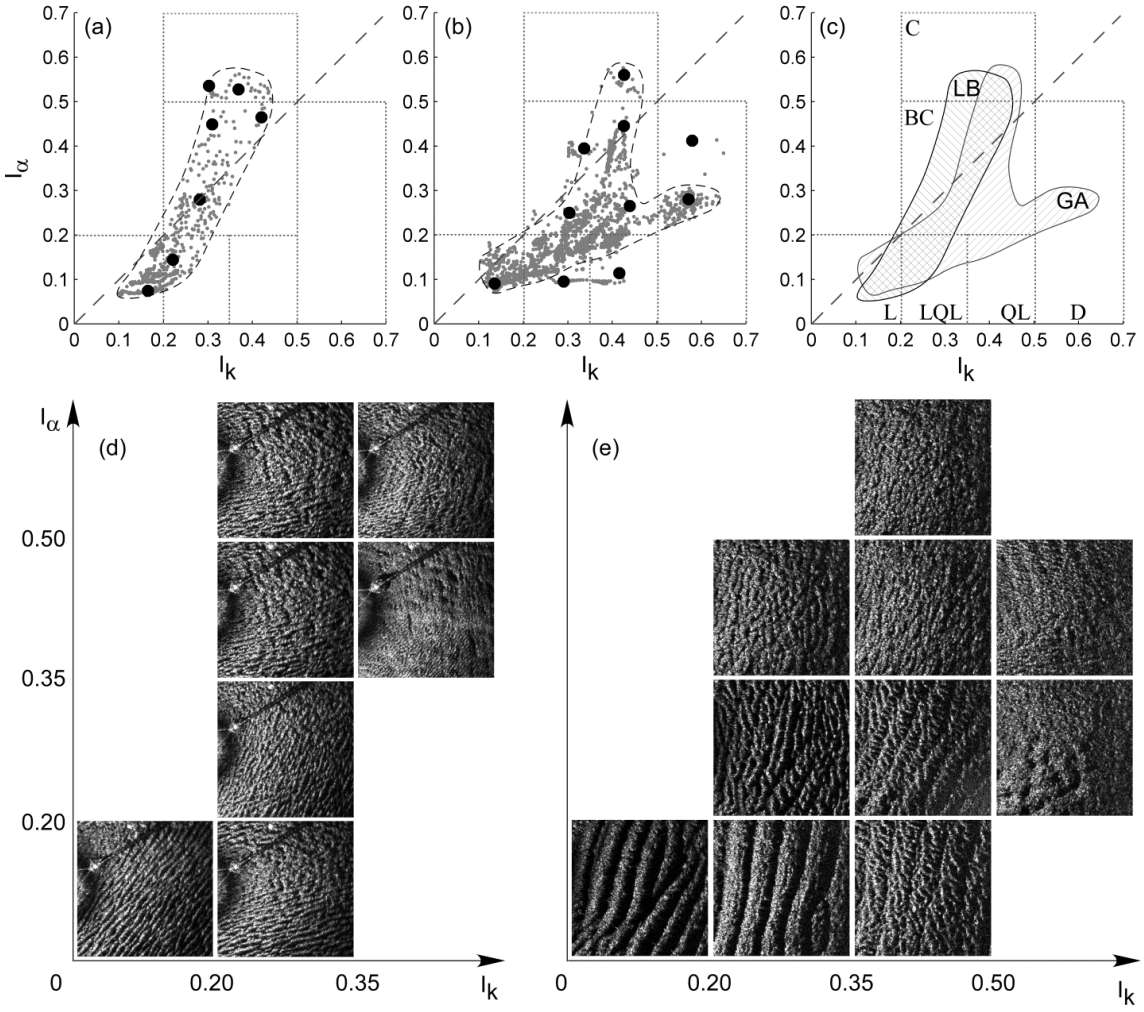

Figure 3.11. Ripple classification scheme based on wavenumber (I_k) and orientation irregularity (I_α) parameters. Scatter plots of I_α *vs.* I_k for (a) Long Bay (LB) experiment; (b) Georgia (GA) experiment; (c) comparison of LB and GA data. The black dots in (a) and (b) indicate the I_k and I_α values for the images shown in (d) and (e) which are ordered the same way as the dots. Key for ripple classification: L, Linear; LQL, Linear Quasi-Linear; QL, Quasi-Linear; D, Disorganized bed; BC, Bifurcating and Cross-ripples; and C, Cross-ripples.

mainly due to variability in ripple direction rather than to variability in wavelength scales. This agrees with the wave forcing in the area, which is mainly due to the passage of fronts (low pressure, cold, and warm fronts) that are usually associated with changes in wave direction [i.e., *Warner et al.*, 2012]. The linear trend reveals the close association of

ripple rotation with adjustments in wavelength and emphasizes the fact that these two processes depend on each other. The scatter plot for the GA data (Figure 3.11b) shows a pattern where for lower I_k values (< 0.30) wavelength variability is more dominant over angular variability. After that, two clear trends are shown: (i) for I_k values between 0.30 and 0.45, I_α varies from 0.20 to 0.60 and (ii) for I_k values between 0.35 to 0.70, I_α varies between 0.20 and 0.30. These two trends correspond to conditions of: (i) changing wave direction and small changes in ripple wavelength related to ripple realignment (similar to that described for the LB data shown in Figure 3.11a) and (ii) changing ripple wavelengths due to lack of sufficient ripple adjustment time. Regions with small values of both I_k and I_α indicate linear ripples with few bifurcations, while points plotted on regions with larger values suggest a bed with irregular ripples. Regions on the scatter plot where large I_α values are dominant represent conditions where cross ripples are prevalent. Overall, the ripples in GA exhibit greater variety of irregularities than those in LB. The superimposition of small-scale ripples, with smaller height, over a field of larger ripples (e.g., GA) leads to smaller irregularity than over a field of smaller ripples (e.g., LB). Thus most orientation driven irregularities do not occur until I_k is greater than 0.35. Based on Figure 3.11, 6 regions were defined corresponding to: (1) linear (L) 2-D ripples ($I_k < 0.20$ and $I_\alpha < 0.20$); (2) linear-quasi-linear ripples (LQL) with a low level of irregularity characterized by small variations in wavelength ($0.20 < I_k < 0.35$ and $I_\alpha < 0.20$); (3) quasi-linear (QL) ripples with high irregularity ($0.35 < I_k < 0.50$ and $I_\alpha < 0.20$) mainly due to the presence of multiple wavelength scales; (4) disorganized (D) ripples ($I_k > 0.50$) with no dominant ripple wavelength or orientation; (5) irregular ripples consisting of a combination of bifurcating and cross ripples (BC, $0.20 < I_k < 0.50$ and $0.20 < I_\alpha < 0.50$);

and (6) irregular ripples dominated by cross ripples (C) of equal size with large angles (> 45°) from each other ($I_\alpha > 0.50$). Based on this classification scheme, regular ripples are considered those with $I_k < 0.5$ and $I_\alpha > 0.2$ (i.e., L and LQL) while all other regions (QL, D, BC and C) are considered to represent irregular ripples.

3.5.2.2. Predicting Irregularity

The identification of regular and irregular ripples has been the subject of several studies, which have attempted to relate the formation of these irregular ripples to several non-dimensional hydrodynamic parameters. *Carstens et al.* [1969] attempted to relate irregularity to the ratio of the orbital excursion to the median grain diameter, suggesting that regular ripples occur when this ratio is below some threshold ($A_{b,1/3}/D_{50} < 775$). Later on, *Sato* [1987] observed a similar trend but added the Shields parameter as a prerequisite. He suggested that 3-D ripples form when:

$$A_{b,1/3} / D_{50} > 775 \quad and \quad \theta_{wc,1/3} > 0.76 \cdot \left(A_{b,1/3} / D_{50} \right)^{-0.25} \qquad 3.18$$

On the other hand, *Lofquist* [1978], using laboratory data from experiments conducted with a variety of grain sizes, concluded that ripple shape can be represented as a function of mobility number ($\psi = u_{b,1/3}^2 / \left[\left(s-1 \right) g D_{50} \right]$), suggesting that regular ripples are formed when $\psi < 21.3$.

A different criterion was developed by *Vongvisessomjai* [1984] who used laboratory data to show that ripples scale as a function of a non-dimensional parameter comprised of a sediment Froude number and an acceleration parameter; he suggested that irregular ripples form when:

$$A_{b,1/3} U_{b,1/3} / \sqrt{\left(s-1 \right) g D_{50}^3} > 5500 \qquad 3.19$$

More recently, *Pedocchi and García* [2009a] used an extensive database of published ripple shapes and geometries to determine a dependence of ripple shape on wave ($Re_w = u_{b,1/3} \cdot D_{50} / \upsilon$) and particle ($Re_p = \sqrt{(s-1) g D_{50}^3} / \upsilon$) Reynolds numbers concluding that ripples are primarily regular when

$$Re_p > 0.06 \cdot Re_w^{0.5} \qquad Re_p \geq 13 \tag{3.20}$$

$$Re_p < 4 \times 10^{-5} \cdot Re_w^{1.1} \qquad Re_p < 9 \tag{3.21}$$

with no distinction defined for $9 \leq Re_p < 13$.

The LB and GA data sets are used to evaluate the above criteria. The measured ripple wavelengths normalized by the corresponding wave semi-orbital excursion (λ/A_b) are plotted against the above parameters used to define ripple irregularity. Defining ripple shape as a function of mobility number (Figure 3.12a) fails to distinguish clearly between regular ($I_k < 0.35$ and $I_\alpha < 0.20$, types L and LQL) and irregular ripples (types QL, BC, C and D). Similarly, *Lofquist's* [1978] criterion for regularity ($\psi < 21.3$) does not appear to hold as regular ripples are still present at ψ values of 35 and irregular ripples are prevalent for values ranging from 1 to 70. This criterion characterizes regular/irregular ripples for 66% of the data shown. *Pedocchi and García's* [2009a] criteria (equations (3.20) and (3.21), shown as dashed and solid lines in Figure 3.12b) does not capture divisions between regular and irregular ripples as a function of Re_w and Re_p and correctly characterize ripple shape only 61% of the time. There is a slight decrease in the number of regular ripples for $Re_w > 1.5 \times 10^5$ and $Re_p \geq 13$ however, regular ripples are prevalent at both larger and smaller values. Similarly, *Vongvisessomjai's* [1984] criterion (Figure 3.12c) results in 36% correct predictions. The vertical line at $A_b/D_{50} = 775$ (Figure 3.12d), represents the cutoff between regular ripples (gray) and irregular ripples (black) proposed

by *Carstens et al.* [1969]. This is not the case in here as both types of ripples occur for values ranging from 300 to 3,000. The θ_{wc} criterion of *Sato* [1987] (equation (3.18), shown as gray circles for regular ripples, see Figure 3.12d) improves the overall correct classification from 39% for *Carstens et al.* [1969] to 65%, although ripples of both types scatter over the full range of observations.

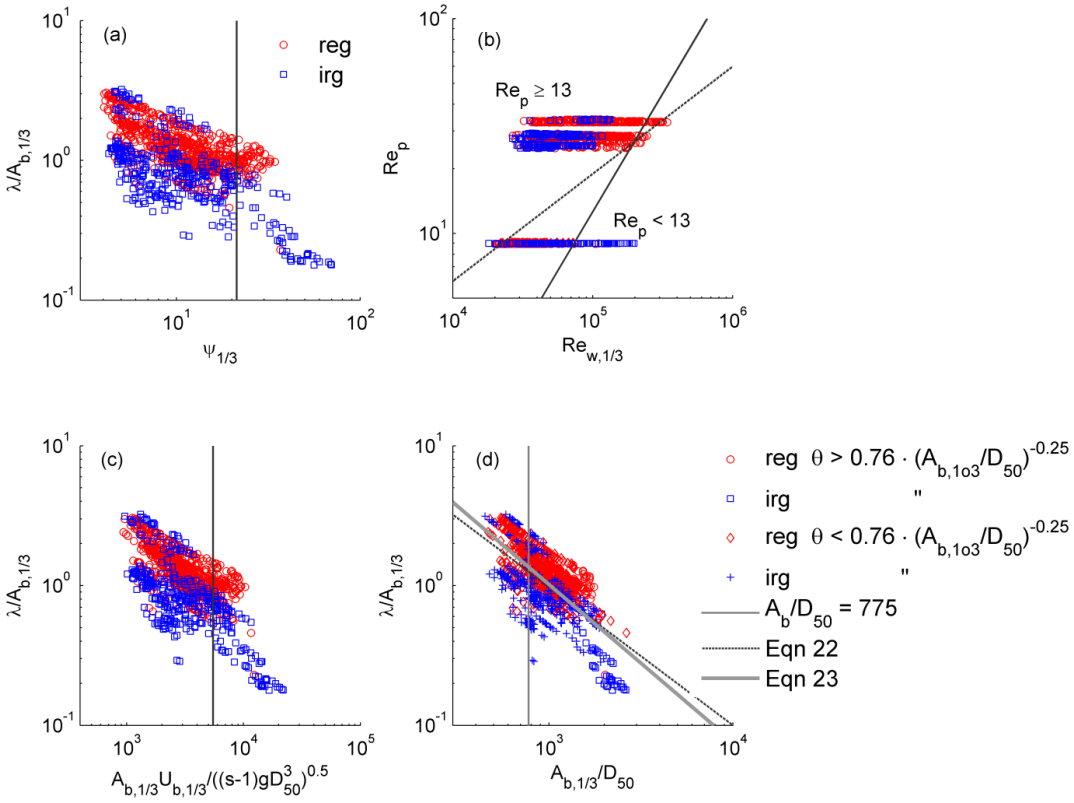

Figure 3.12. Scatter plots of regular (red) and irregular (blue) ripples for the LB and GA data sets. (a) $\lambda/A_{b,1/3}$ *vs.* mobility number ($\psi_{1/3}$) where the vertical line is the predictor of *Lofquist* [1978]; (b) Re_p vs. $Re_{w,1/3}$ where the two lines represent the predictors of *Pedocchi and García* [2009a] for $Re_p < 9$ (solid line) and $Re_p \geq 13$ (dashed line); (c) $\lambda/A_{b,1/3}$ *vs.* the product of the sediment Froude number and acceleration parameter where the solid line is the predictor of *Vongvisessomjai* [1984]; (d) $\lambda/A_{b,1/3}$ *vs.* $A_{b,1/3}/D_{50}$ with for the predictors of *Carstens et al.* [1969] and *Sato* [1987] (vertical dark gray line), equation (3.22) (dashed line) and equation (3.23) (light gray line).

While there is no clear division between regular and irregular ripples as a function of hydrodynamic forcing and sediment properties alone, a dependence on non-dimensional ripple wavelength (λ/A_b) emerges. Least-square fit analysis to irregular and regular ripple data is used to define the division between the two classes as the line lying in between the two fitted lines:

$$\lambda / A_{b,1/3} = 908 \cdot \left(A_{b,1/3} / D_{50} \right)^{-1} \qquad 3.22$$

For a given value of $A_{b,1/3}/D_{50}$, if the value of the ratio $\lambda/A_{b,1/3}$ falls below the line defined by equation (3.22), then irregular ripples are assumed. It is worth noting that equation (3.22) nearly coinsides with the equilibrium ripple wavelength equation (2.41). The difference in the coefficients is attributed to the variety and type of data used for deriving the two equations. The data chosen here include every seabed where sediment is mobilized ($\theta > \theta_{wc}$) for these two field sites whereas only equilibrium ripples from numerous field and laboratory sourses are used for chapter 1. Given the resemblence between the two equations and for practical purposes the equilibrium equation was adopted so that the irregularity occurs when

$$\lambda / A_{b,1/3} > 2.4 \times 10^{3} \cdot \left(A_{b,1/3} / D_{50} \right)^{-1.13} \qquad 3.23$$

This criterion improves the predictability of irregularity from an average of 53% for the previously presented criteria to 76% .The dependence on λ/A_b agrees with the concept of ripple irregularity is a function of seabed time history (i.e., how far is the present bed geometry from that of equilibrium). Ripples which scatter on either side of equation (3.23) are out of equilibrium and some of them will adjust to a new wavelength if conditions allow sediment mobility. During ripple transition, irregularity expressed as wavelength variability, bifurcations and other defects is present. If ripples attain a

wavelength roughly equal to equilibrium under steady forcing then they become more linear. Ripples at the equilibrium line have I_k and I_α values ranging from 0.10 to 0.35 with decreasing values above the line and increasing below the line.

3.6. Conclusions

Field observations of hydrodynamic and seabed imagery from two sites with different sediment sizes have provided insightful information on the temporal evolution of wave-induced ripples and how such evolution relates to ripple irregularity. The analysis shows that a linear rippled bed develops only if the wave direction remains constant and after sufficient time has passed to allow for sediment reorganization. For weak flows, the bed is slowly modified, while under higher intensity flows, the modification is more rapid due to increased sediment transport rates. This is something well captured by existing time dependent ripple evolution models as those of *Traykovski* [2007] and *Soulsby and Whitehouse* [2005].

However, changes in wave direction appear to delay the transition of the seabed to equilibrium conditions. During these times most of the sediment in motion is consumed to ripple re-alignment with the changing wave direction. This change in direction is usually associated with a decrease of ripple height and the formation of cross-ripples. If the orientation is continually changing, the bed becomes highly irregular preventing the ripples from becoming well organized. This process is not well captured by the existing time-dependent ripple evolution models which assume that ripple height and wavelength evolution is independent of wave direction [*Traykovski*, 2007] or that changes in wave direction affect the rotational characteristics of the ripples but not their dimensions [*Soulsby and Whitehouse*, 2005] as there is no feedback in the model formulations.

Improved future models should account for this. These results are concerned with wave-dominated environments. Similar ripple irregularities can also occur under conditions when wave- and current- induced shear stresses are of equally similar magnitude but vary in direction [e.g*., Lacy et al.*, 2007].

Finally, the 2-D spectrum of the seabed acoustic images can be used to quantify irregularity of the seabed. In general, ripples are regular/linear for values of I_k less than 0.2 and I_α less than 0.2 and irregular for larger values. For I_k values greater than 0.5 the bed becomes highly disorganized. The cutoff between regular and irregular ripples is not simply a function of hydrodynamics alone and therefore such predictors fail to predict the seabed state. Instead, the irregularity is dependent on the time-history of the seabed and on how far is the bed state from equilibrium conditions. A more robust prediction of irregularity can only be achieved using time-dependent models able to capture the feedback between changes in orientation and wavelength development.

CHAPTER 4

PREDICTING RIPPLE TEMPORAL AND SPATIAL EVOLUTION

4.1. Introduction

Ripples are sinuous sedimentary features on the seabed formed by the interaction of waves and/or currents with bed sediments. Their presence on the seabed contributes to enhancing bottom roughness leading to increased wave dissipation especially on wide continental shelves [e.g., *Ardhuin et al.*, 2003] and nearbed turbulence [*Grant and Madsen*, 1986]. Furthermore, the relative angle between ripple crest and mean current appears to modulate the total roughness experienced by the mean flow [e.g., *Powell et al.* 2000; *Barrantes and Madsen*, 2000; *Madsen et al.*, 2010], while close to the seabed the mean flow tends to align itself to the ripple crests [*Madsen et al.*, 2010], thus having significant implications on net sediment transport direction.

Given the importance of ripples in a variety of benthic marine processes, accurate prediction of their geometry is a prerequisite for a number of models that require knowledge of bed physical roughness. Improved accuracy in simulating boundary layer flow and turbulence structure require the use of ripple evolution models able to account for the occurrence and irregularity of ripples as well as the evolution of the ripple's wavelength, height, and orientation under changing intensity and directions of wave forcing.

To date a number of theoretical [e.g., *Blondeaux*, 1990; *Andersen*, 2001], laboratory [e.g., *Sleath*, 1984; *Nielsen*, 1992; and references therein], and field [e.g., *Boyd et al.*, 1988; *Amos et al.*, 1988; *Voulgaris and Morin*, 2008; *Traykovski et al.*, 1999] studies have been carried out to understand bedform development in sandy environments. These studies have characterized wave-induced ripples as: equilibrium, when their geometry is in equilibrium with the prevailing near bed wave conditions; transitional, when the ripples are out of equilibrium and continuously change their characteristics in order to achieve equilibrium; and relict ripples, describing ripples formed at different conditions and currently are under conditions below those for sediment initiation and their geometry remains "frozen."

Equilibrium geometry has been studied in several laboratory [*Yalin and Russell*, 1962; *Mogridge and Kamphuis*, 1972; *Faraci and Foti*, 2002] and field studies [*Inman*, 1957; *Miller and Komar*, 1980; *Grasmeijer and Kleinhans*, 2004] leading to the development of a number of equilibrium ripple models [e.g., *Nielsen*, 1981; *Grant and Madsen*, 1982; *Wiberg and Harris*, 1994; *Styles and Glenn*, 2002]. In chapter 1, existing equilibrium ripple data from published sources was re-analyzed to yield an equilibrium ripple predictor, which shows that for irregular/random waves, ripple wavelength best scales with the wave semi-orbital excursion normalized by the sediment grain diameter. They also showed that ripple steepness is nearly constant with a slight dependence on wavelength such that shorter wavelength ripples will be steeper than ripples with longer wavelengths. In terms of direction, equilibrium ripples align with the wave forcing (i.e., ripple crests perpendicular to wave direction) [e.g., *Maier and Hay*, 2009; also see chapter 3].

During their relict phase, ripples tend to decrease in ripple height due to biological activity or other diffusive properties [e.g., *Hay*, 2008; and chapter 3]. It has also been observed [*Traykovski et al.*, 1999; and chapter 3] that relict ripples do not always assume an equilibrium geometry corresponding to the time just prior to the cessation of sediment motion; their geometry may correspond to sometime prior to that point when higher energy flows were present. Since relict ripples can remain on the seabed for days to months until their geometry is altered [*Hay*, 2008; and chapter 3], their influence remains important in time dependent processes.

During the transient ripple phase, ripples actively adjust trying to achieve their desired equilibrium wavelength and height defined by the prevailing wave conditions in accordance with the equilibrium ripple predictor [e.g., *Davis et al.*, 2004]. For declining wave conditions, during the decreasing energy phase of a storm, *Traykovski et al.* [1999] and noted little variation in ripple geometry (also observed in chapter 3). For changes in wave direction *Traykovski et al.* [1999] and *Maier and Hay* [2009] observed that ripples rapidly align with the wave direction within 1 hour; though a longer lag time was observed for the ripples of LB and GA (chapter 3).

In order to capture the transient development of ripple geometry a number of time-dependent models have been developed [*Davis et al.*, 2004; *Jarno-Druaux et al.*, 2004; *Soulsby and Whitehouse*, 2005; *Testik et al.*, 2005; *Traykovski*, 2007] that can predict ripple evolution under varying wave conditions. *Davis et al.* [2004] presented a model that temporal ripple variability is expressed through a spectral energy parameter, which is not only an indication of ripple dimension but also an analogue for the irregularity of the seabed. *Testik et al.* [2005] described changes in ripple wavelength and

height under conditions where equilibrium ripple geometry is either greater than or less than the relict ripples present and presented individual equations to describe each transition for ripple wavelength and height separately. Later on, *Traykovski* [2007] presented a time dependent model, which represents a rippled seabed as a ripple amplitude spectrum over a range of wavenumbers. Although not explicitly stated, all of the above models assume that wave ripples respond instantly to changes in wave direction without these changes affecting the development of their height and/or wavelength. *Soulsby and Whitehouse* [2005] were the first to address the issue of changing wave direction for wave and current induced ripples. Their model has been shown to perform well in current dominated flows [*Soulsby et al.*, 2012], although its performance for wave-induced ripples under field conditions has not been thoroughly evaluated. While this model allows for continuous evolution of ripple geometry, it only allows for evolution of a single ripple and cannot distinguish between a regular, irregular, or cross ripples. Furthermore, a comparison of ripples in chapter 3 showed that changes in ripple orientation delay the development of equilibrium ripples, especially ripple height; something that has also been noted in *Hanes et al.* [2001] and *Hay* [2011] who also observed a decrease in ripple height associated with cross ripple development. This indicates an important feedback between height and orientation.

In this contribution, a new model is presented that describes the temporal evolution of a rippled seabed for wave-dominated conditions that explicitly accounts for changes in wave directionality and how this affects ripple height and wavelength development but also the development of irregular ripples as those observed in the field. In section 4.2, the theoretical development of the new transient ripple model is presented.

Its sensitivity and performance under a variety of wave forcing conditions from synthetic and field data are presented in section 4.3. The performance and applicability of the model is discussed in section 4.4 with the conclusions presented in section 4.5.

4.2. 2-D Transient Ripple Model Description

All existing field and laboratory ripple observations to date suggest that their evolution is a dynamic process that depends on the strength and duration of the flow as well as the variability of its direction. During periods of changing hydrodynamic conditions, the seabed passes through various degrees of irregularity until final equilibrium geometry is obtained. In order to capture the feedback between ripple geometry and irregularity on wave direction, as described in chapter 3, a spectral model [e.g., *Traykovski*, 2007] is best suited for such application after it is expanded into 2 dimensions, as described below.

Following *Davis et al.* [2004] and assuming regular uniform ripples (1-D), the rate of ripple adjustment decreases as its geometry approaches equilibrium (*eq*) so that:

$$\frac{dX}{dt} = \frac{X_{eq} - X_i}{T_k} \qquad 4.1$$

where X represents the ripple scale (wavelength or height) and dX/dt is the rate of change of X; T_k is the time required to attain the equilibrium scale (X_{eq}) from its initial condition X_i. This concept is also the basis of the *Traykovski* [2007] 1-D ripple evolution model. In the approach, ripple wavelength is expressed in terms of wavenumber vector ($\boldsymbol{k} = 2\pi/\lambda$) which can be decomposed into its two horizontal components such that (k_x, k_y) = ($k \cdot cos(\alpha)$, $k \cdot sin(\alpha)$) where α is the ripple orientation which is defined as the direction of a line perpendicular to the ripple crest.

Traykovski [2007] combined equation (4.1) with sediment transport principles based on seabed scour literature (see *Whitehouse* [1998]) and employed sediment continuity principles along a cross-section of the rippled bed. Under changing hydrodynamic forcing, the triangular cross-section geometry adjusts towards equilibrium. This adjustment is more rapid when the difference between the two geometries is greatest and slows down as the instantaneous geometry approaches that of equilibrium. Replacing the 1-D wavenumber scalar with a 2-D vector, the *Traykovski* [2007] model can be written as:

$$\frac{dS_{\eta\eta}(k_x,k_y,t)}{dt} = \frac{1}{(1-\phi)\cdot\eta_s(k_x,k_y)} \cdot \frac{dQ(t)}{dx} \cdot \left[S_{\eta\eta,eq}(k_x,k_y,t) - S_{\eta\eta}(k_x,k_y,t)\right] \qquad 4.2$$

where $S_{\eta\eta}(k_x,k_y,t)$ is the 2-D ripple spectrum at time t and $Q(t)$ is the volumetric sediment transport rate driven by the hydrodynamic conditions at that time; ϕ represents sediment porosity and dx is the spatial scale of flux convergence; $S_{\eta\eta,eq}(k_x, k_y,t)$ is the equilibrium ripple spectrum corresponding to the instantaneous hydrodynamic forcing. Finally, $\eta_s(k_x, k_y)$ is a scaling parameter applied to the equilibrium ripple spectrum and used to force the model. As described in *Traykovski* [2007] this parameter is constant in time and does not vary in response to forcing conditions.

The equilibrium spectrum is created from the equilibrium ripple geometry (η_{eq}, λ_{eq}) using a Gaussian distribution as:

$$S_{\eta\eta,eq}(k_x,k_y) = \sqrt{\frac{0.25\cdot\eta_{eq}}{2\pi\cdot\sigma_x\cdot\sigma_y}\cdot\exp\left(\frac{-(k_x-k_{x,eq})^2}{2\cdot\sigma_x^2} + \frac{-(k_y-k_{y,eq})^2}{2\cdot\sigma_y^2}\right)} \qquad 4.3$$

where σ_x and σ_y are the spectral widths of the distribution in the corresponding directions. The equilibrium ripple wavelength is assumed to align with the forcing direction so that corresponding components of the equilibrium wavelength are $k_{x,eq} = k_{eq}\cdot cos(\alpha_w)$ and $k_{y,eq} =$

$k_{,eq} \cdot sin(\alpha_w)$, with k_{eq} representing the equilibrium value derived from an appropriate equilibrium ripple predictor (e.g., chapter 2). The spectral energy amplitude is controlled by the equilibrium ripple height (η_{eq}) defined by the hydrodynamic forcing. For instances where sediment is mobilized and the wave-induced shear stress is greater than the skin friction due to the mean flow, the ripples will scale with the wave forcing. Likewise, when the shear stress due to mean flow is greater than that due to waves, ripples will scale with the currents such that:

$$\left(\eta_{r,eq}, \lambda_{r,eq}, \alpha_{r,eq}\right) = \begin{cases} \left(\eta_{eq,w}, \lambda_{eq,w}, \alpha_{r,eq,w}\right) & \theta_w \geq \theta_c \\ \left(\eta_{eq,c}, \lambda_{eq,c}, \alpha_{r,eq,c}\right) & \theta_w < \theta_c \end{cases} \quad 4.4$$

where the subscripts *w* and *c* represent wave and currents, respectively, and θ_w is the wave Shields parameter [*Shields*, 1936] defined as:

$$\theta_w = 0.5 f_w u_{b,1/3}^2 / [(s-1) g D_{50}] \quad 4.5$$

where *s* is the non-dimensional sediment density parameter, D_{50} is the median sediment grain diameter, *g* is the acceleration due to gravity, and f_w is the wave friction coefficient defined by *Jonsson* [1966] as:

$$f_w = \begin{cases} \exp\left[5.213 \cdot \left(2.5 \cdot D_{50}/A_{b,1/3}\right)^{0.194} - 5.977\right] & , \ A_{b,1/3}/(2.5 \cdot D_{50}) > 1.57 \\ 0.3 & , \ A_{b,1/3}/(2.5 \cdot D_{50}) \leq 1.57 \end{cases} \quad 4.6$$

with $A_{b,1/3} = u_{b,1/3} \cdot T/2\pi$, where *T* is the wave period.

The skin friction current Shields parameter is then defined as:

$$\theta_c = \mathrm{C}_{Dz} \cdot {U_z}^2 / [(s-1) \cdot g \cdot D_{50}] \quad 4.7$$

where C_{Dz} is the drag coefficient that was estimated for the elevation (*z*) of the mean flow (U_z) measurement using the law of the wall with a roughness defined by the particle size (skin friction) only, as this is the sediment mobilizing force exerted on the seabed:

$$C_{Dz} = [0.40/\ln[z/(D_{50}/12)]\,]^2 \quad 4.8$$

The total volumetric sediment transport rate (Q) in equation (4.2) defines the time required for the seabed to achieve an equilibrium ripple geometry. *Traykovski* [2007] and *Hay* [2011] have shown good agreement between observed and estimated ripple adjustment times when using the *Meyer-Peter and Müller* [1948] volumetric bed load transport formulation

$$Q = \gamma \cdot (\theta_{wc} - \theta_{cr})^{1.5} \cdot \sqrt{(s-1) \cdot g \cdot D_{50}^3}\ , for\ \ \theta_{wc} > \theta_{cr} \qquad 4.9$$

where the coefficient γ is an empirical constant, θ_{cr} is the critical Shields parameter, and θ_{wc} is the maximum wave-current skin friction Shields parameter defined using the parameterization of *Soulsby* [1995] as:

$$\theta_{wc} = \sqrt{[\theta_m + \theta_w \cdot |\cos(\alpha_{wc})|]^2 + [\theta_w \cdot |\sin(\alpha_{wc})|]^2} \qquad 4.10$$

where θ_m is the mean wave and current Shields parameter estimated as:

$$\theta_m = \theta_c \cdot \left(1 + 1.2 \cdot \left(\frac{\theta_w}{\theta_c + \theta_w}\right)^{3.2}\right) \qquad 4.11$$

Following *Traykovski* [2007] the volumetric sediment transport divergence over a ripple (dQ/dx) can be derived assuming zero transport at the ripple trough and maximum transport at the crest over a distance of half the ripple wavelength. Adjustment time $T_k(k_x, k_y)$ for each ripple wavenumber is then defined using equation (4.9) assuming that the cross-sectional shape of a rippled bedforms a triangle where its area represents sediment volume per crest line unit length ($=(1/2)\cdot\eta_{eq}(k_x,k_y)\cdot\lambda_{eq}(k_x,k_y)$). After accounting for sediment porosity (ϕ) this area can be converted to sediment volume and written in terms of wavenumber so that:

$$T_k(k_x, k_y) = \left[(1-\phi) \cdot \left(\eta_s(k_x, k_y)/\lambda_s(k_x, k_y)\right) \cdot \left(2 \cdot \pi/|\sqrt{k_x^2 + k_y^2}|\right)^2\right]/(2 \cdot Q) \qquad 4.12$$

Equation (4.12) shown above states that the time required to build a ripple from a flat bed is defined by the ratio of the cross-sectional area to the volumetric sediment transport rate. Based on these arguments, it is evident that larger ripples will require longer time to develop if a constant sediment transport rate is assumed. The ratio $\eta_s(k_x,k_y)/\lambda_s(k_x,k_y)$ of the scaling parameters is defined by the equilibrium model used and does not change with time.

When the Shields parameter is less than the critical value required for sediment motion, the seabed does not respond to changes in forcing direction or magnitude. In this case, ripple wavelength and orientation remain constant and the ripples present reflect previous hydrodynamic conditions before $\theta_{wc}<\theta_{cr}$ (relict ripples). However, bioturbation and other diffusive processes still take place leading to a natural decay of ripple height while no changes are expected to occur in either ripple length or orientation [*Hay et al.*, 2008]. *Voulgaris and Morin* [2007] used regression analysis through the spectral intensity energy of seabed acoustic imagery spectra and found an exponential decrease in ripple height with a time decay constant (T_D) of 550 hours (22.9 days). Thus when $\theta_{wc} < \theta_{cr}$, ripple height will decay while ripple wavelength and orientation remain constant so that:

$$S_{\eta\eta}(k_x, k_y, t + \Delta t) = S_{\eta\eta}(k_x, k_y, t)\cdot\exp\left(-\Delta t/T_D\right) \qquad 4.13$$

where Δt represents the time step. When a ripple is subjected to new wave forcing, it will rapidly change its form and start aligning to the new wave direction and will continue adjusting its geometry through sediment movement until it reaches a ripple geometry that is in equilibrium with the hydrodynamics. The amount of change to occur (equation (4.1)) can be formulated combining equations (4.2) and (4.12) in terms of the ripple spectrum as follows:

$$\frac{dS_{\eta\eta}(k_x,k_y,t)}{dt} = \frac{S_{\eta\eta,eq}(k_x,k_y,t) - S_{\eta\eta}(k_x,k_y,t)}{T_k(k_x,k_y,t)} \quad 4.14$$

where *dt* is the integration time step.

Ripple height, wavelength, and orientation can be estimated from the 2-D spectra $S_{\eta\eta}(k_x,k_y)$ predicted from equations (4.13) and (4.14) for each time step (t) using the spectral moment:

$$m_{pq} = \int\int k_y^q \cdot k_x^p \cdot S_{\eta\eta}^2(k_x,k_y) \cdot dk_x \cdot dk_y \quad 4.15$$

where p and q denote the spectral moment order in the x (eastward) and y (northward) directions, respectively. Average wavelength and orientation is then calculated by determining coordinates of the spectrum's center of gravity which is given by

$$(\overline{k_x},\ \overline{k_y}) = (m_{10}/m_{00}\,, m_{01}/m_{00}) \quad 4.16$$

such that mean ripple wavenumber is $\bar{k} = \sqrt{\overline{k_x}^2 + \overline{k_y}^2}$. Similarly, mean orientation of the ripple (defined as the orientation of a line perpendicular to ripple crest) is

$$\alpha_r = \tan^{-1}(\overline{k_y}/\overline{k_x}) \quad 4.17$$

Ripple height is calculated from the zero order moment as

$$\eta = 4 \cdot m_{00} \quad 4.18$$

where the multiplier of 4 arises from ripple amplitude being multiplied by 0.25 in equation (4.3), similar to the calculation of significant wave height.

When multiple peaks are present in the spectrum, each individual peak is identified using the watershed functions [*Meyer,* 1994] as implemented in the Matlab© image processing toolbox. Equations (4.15) to (4.18) are then applied for each peak region identified to estimate the multiple ripple geometries (i.e., height, wavelength, and orientation) present; subsequently each individual ripple field is ranked in terms of ripple

height with the largest being the main ripple and the second in significance called the 2nd order ripple. Although higher order ripples might be identified, they usually are not considered in this analysis.

The ripple spectrum also yields information about the variability in ripple wavelength and orientation. This variability is calculated using the same methods as in chapter 3 for acoustic images of the seabed. The method utilizes the central spectral moments m'_{02} and m'_{20} of the spectrum which are defined as the moments centered on the mean wavenumbers and is applied after the wavenumber components are converted to a polar coordinate system (k, α). From which the directional and wavenumber spectral widths can be deducted using:

$$(\sigma_k,\ \sigma_\alpha) = \left(\sqrt{m'_{k,2}/m_{k,0}}\,, \sqrt{m'_{\alpha,2}/m_{\alpha,0}}\right) \qquad 4.19$$

For the same variability in wavelength, the value of σ_k will vary depending on the absolute value of the ripple wavelength. Therefore, the σ_k value is normalized by the value of the mean wavenumber present. The wavenumber irregularity (I_k) and orientation irregularity (I_α) parameters are then defined as:

$$[I_k,\ I_\alpha] = \left[\sigma_k/\bar{k}\,, \sigma_\alpha/(\pi/2)\right] \qquad 4.20$$

The above model can be used to solve for a time-dependent ripple geometry given wave semi-excursion (or wave height), wave period, wave direction, sediment grain diameter, sediment density, kinematic viscosity, current speed, current direction, and elevation of current measurement.

4.3. Results

4.3.1. Simulated Forcing

In order to demonstrate the behavior of the 2-D model presented above, simulations are presented assuming an ideal synthetic wave forcing that varies over a period of 36 hours (Figure 4.1). The model results are compared to estimates from the *Traykovski* [2007] (1-D) and the *Soulsby and Whitehouse* [2005] (SW) models. For consistency purposes, in all simulations the equilibrium predictor presented in chapter 2 for combined regular and irregular waves is used.

The two cases (case 1 and 2) represent wave forcing with a constant nearbed orbital velocity (25 cm/s) but variable direction. The wave periods assumed are 6 and 9 s for case 1 and 2, respectively. The initial ripple dimensions correspond to the equilibrium ripple geometry predicted by the equilibrium formulation in chapter 2 for combined regular and irregular waves using the hydrodynamics of the first time step, and an orientation defined by the direction of the wave at this time. During each simulation the wave direction changes 4 times; the rate of wave direction change is increased uniformly so that the first transition occurs over a period of 4 hours while the last transition occurs within a period of 1 hour (see Figure 4.1), corresponding to rotation rates of 0.375, 0.5, 0.75 and 1.5 °/min, respectively. A constant spectral width value of 1.5 rad/m is assumed for both σ_x and σ_y values. The *Meyer-Peter and Müller* [1948] formula for bed load transport rate is used for all cases with a γ of 8.

Case 1 (Figure 4.1a-d) demonstrates the model's response to a wave regime (6 s period and 25 m/s orbital velocity) with a direction varying from 0° to 90°N and then

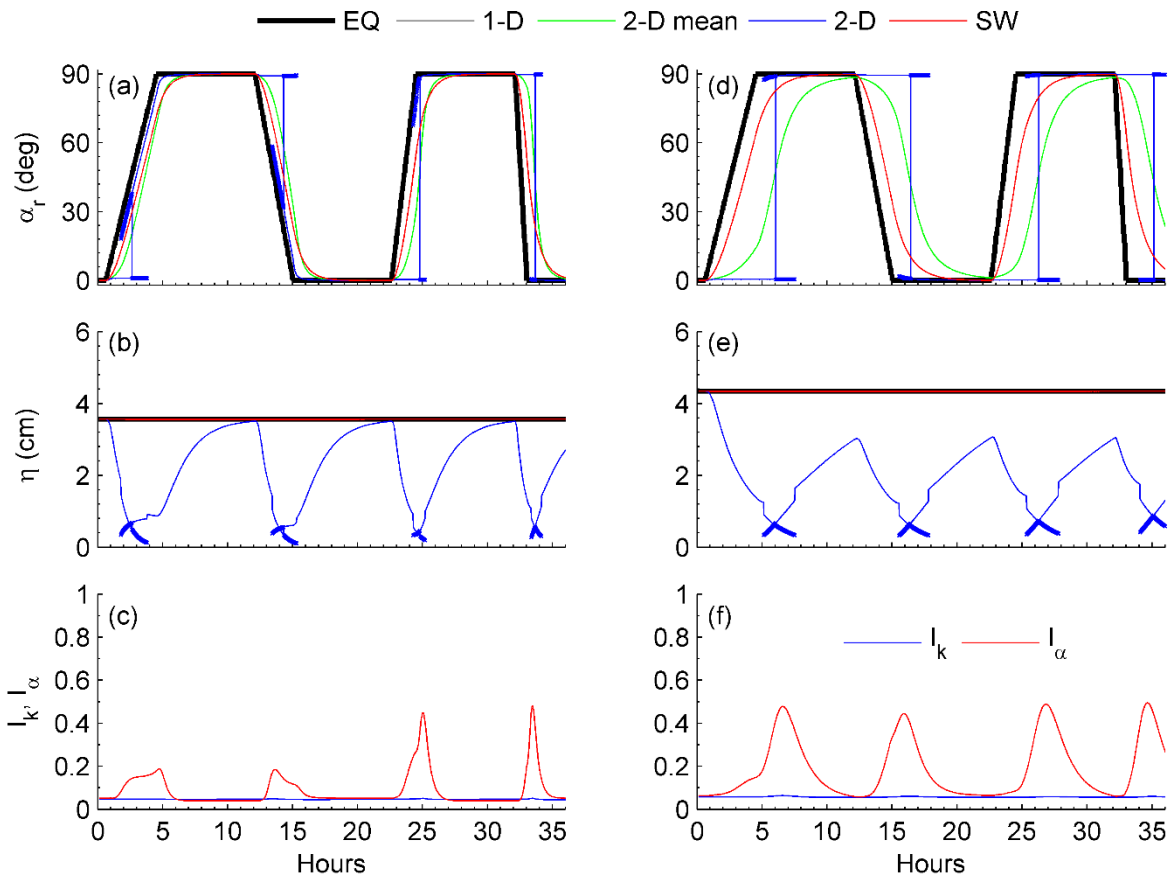

Figure 4.1. Time series of predicted ripple characteristics from the *Soulsby and Whitehouse* [2005] (SW), the *Traykovski* [2007] (1-D), and the new 2-D model. Synthetic wave forcing is used with a changing wave direction under constant wave intensity representing high energy waves (case 1: a-c, $u_{b,1/3}$ = 25cm/s, T=6 s, λ=27.8) and weak energy waves (case 2: d-f, $u_{b,1/3}$ = 25cm/s, T=9 s, λ=34.2 cm). (a, d) Ripple orientation; (b, e) ripple height; (c, f) ripple wavenumber and orientation irregularity.

returning back to 0°N (see Figure 4.1a). This leads to an excess Shields (θ - θ_{cr}) value of 0.05. As both wave period and orbital velocity remain constant, the corresponding equilibrium wavelength (27.8 cm) and height (3.6 cm) remain unchanged throughout the whole simulation period. Thus, any changes observed are attributed to the response of the seabed to a changing wave direction. Given the forcing, the 1-D, 2-D, and SW models predict no change in ripple wavelength leading to a constant I_k value (see Figure 4.1c), while the 1-D and SW models also predict no change in ripple height (see Figure 4.1b) as

these models do not relate ripple height to changes in ripple orientation. In terms of mean ripple orientation, the SW and the 2-D models yield similar results but the SW model suggests a more rapid adjustment at the onset of a changing wave direction. During periods of changing wave direction, the 2-D model predicts the development of cross ripples. The development of cross-ripples results in a decrease in ripple height as during this time the available sediment is distributed between the two ripple fields that constitute the cross-ripples. The re-orientation of the ripples occurs in stages. At the onset of the transition, the ripple height decreases as the waves change direction. Then, once the forcing direction remains constant, the ripples start increasing again in height. During the rotation in the forcing direction, the ripple's orientation irregularity (I_α) increases indicating a more irregular seabed forming for faster rotational rates. The length of time required for the seabed to become regular also decreases with increasing rotation rates under constant forcing assumed in this example.

Case 2, corresponds to weaker wave forcing, due to the longer wave period (9 s). In this case (Figure 4.1d-f), both ripple orientation and height lag further behind equilibrium than what was shown for case 1. The forcing results in a constant wavelength of 34.2 cm and a θ - θ_{cr} value of 0.04. Second order ripples do not appear until the forcing direction is at a 90° angle to the relict ripples. However, during the transition, the orientation irregularity (I_α) gradually increases, attaining values of nearly 0.5 while the wavenumber irregularity remains unchanged. For ripple orientation, the SW model predicts a relatively fast rotation in response to changing wave directions that lags the wave direction change by approximately 2 hours. The 2-D model; however, shows that the rotation is happening through a process where the initial ripples diminish in height

and a new ripple field grows along the new wave direction. In terms of ripple height (Figure 4.1e), the 2-D model does not attain equilibrium but attains a maximum height just prior to a next change in forcing direction. Similar to case 1, the peak ripple height does not increase until the second order ripple becomes primary sometime after the forcing direction becomes constant. Overall, these results show that according to the 2-D model results the change in wave direction is occurring through a process of destruction of the initial ripple field and growth of a ripple field along the new direction. This process corresponds with the development of a cross-rippled bed when both the initial and the final ripples are present.

4.3.2. Field Data

4.3.2.1. Hydrodynamics

Data from two field experiments conducted in the South Atlantic Bight offshore South Carolina and Georgia (USA) are used to evaluate the performance of the 2-D model under natural variable wave and current forcing and changing wave directions. The experimental setup, hydrodynamic conditions, and ripple evolution during these experiments are described in detail in *Voulgaris and Morin* [2008], *Warner et al.* [2012], and in chapter 3.

The first data set represents data from a fine-grained sandy bed (D_{50} of 177 μm) located off the northern part of South Carolina (USA) off Long Bay (hereafter referred to as LB). The data collection was a part of the U.S. Geological Survey's South Carolina Coastal Erosion Study, which took place from October 2003 to April 2004 [*Sullivan et al.*, 2006; *Schwab et al.*, 2009; *Warner et al.*, 2012]. Data from two Sontek ADV sensors and an Imagenex 881 rotating sonar deployed in 9.5 m deep water were collected during

a 1.5-month period (30 January 2004 to 15 March 2004) and are used in this study. LB is a wave-dominated environment with a 7 s mean period and mean and maximum bottom wave orbital velocities of 17 and 44 cm/s, respectively. Currents were primarily wind driven while the tidal currents are too weak to mobilize bed sediment with an average speed of 3.8 cm/s.

The second data set, corresponds to a site with medium to coarse sand (D_{50} = 388 μm) bed located on the continental shelf off the coast of Georgia (hereafter referred to as GA). Hydrodynamic (ADVs) and bedform imagery (rotating sonar) data collected during two periods (16 September 2007 to 7 October 2007 and 18 November 2007 to 15 February 2008) are used in this study. The greater water depth (27.5 m) of this site leads to attenuation of the short waves, resulting in a longer bottom wave period (9 s) than that observed in LB. Furthermore, due to the weaker wave forcing, mean current induced shear stresses occasionally surpasses that of waves.

4.3.2.2. Model Setup

As described earlier (equation (4.3)) the 2-D model requires a seabed spectral width parameter, which represents the width of the expected equilibrium spectrum. Theoretically, this value should be small and correspond to linear ripples, but may depend on the site's characteristic hydrodynamic and sediment properties. In order to determine the minimum σ_x and σ_y for LB and GA, these parameters were calculated from the spectra of the seabed sonar images following the same methods described in chapter 3 and equation (4.19), replacing $S^2_{\eta\eta}(k_x, k_y)$ with the 2-D FFT spectral energy of the acoustic imagery. Figure 4.2 shows the sonar imagery and corresponding 2-D spectrum representing the smallest σ_x and σ_y, and hence most linear ripples observed for each site.

Taking the average of all minima (Figure 4.3) for each site leads to an average of 3.76 and 2.12 rads/m for LB and GA, respectively. These values represent the inherent irregularity of the seabed due to irregular wave forcing characteristics.

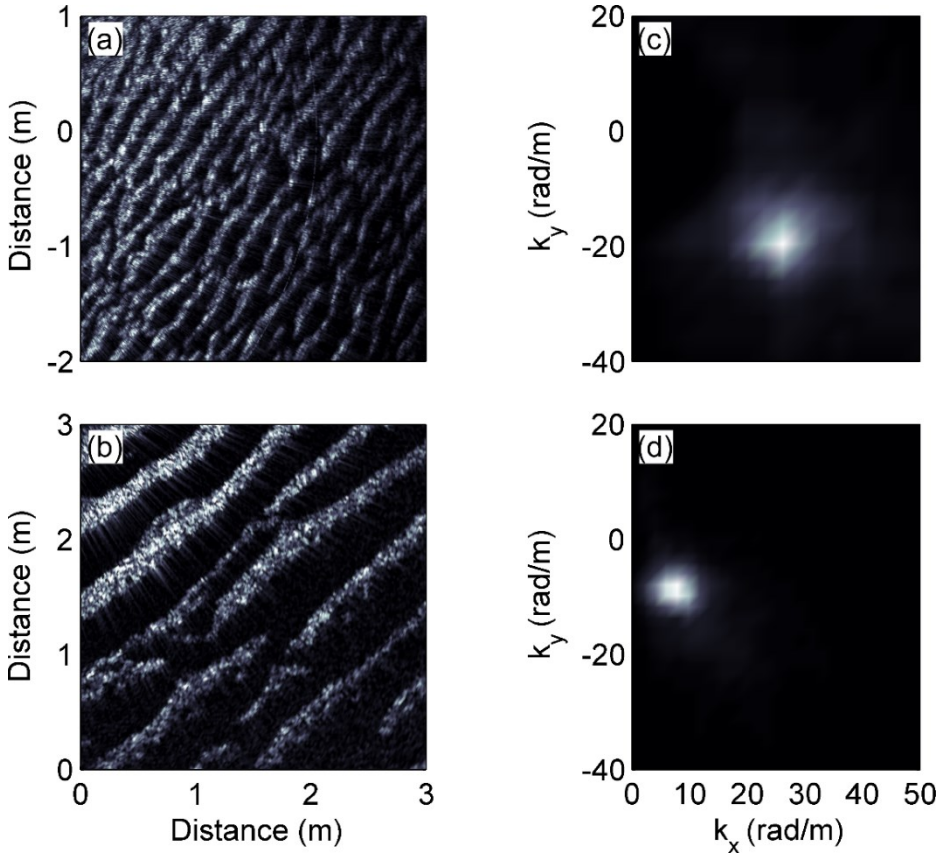

Figure 4.2. Seabed imagery (a and b) and corresponding 2-D FFT spectra (c and d) representing instances of the smallest σ_x and σ_y present at Long Bay (a and c) and Georgia (b and d).

Another important parameter for any time dependent model is the choice of equilibrium predictor, which acts as the target geometry for the seabed under given wave forcing. The equilibrium predictors from chapter 2 are plotted against the LB and GA equilibrium ripple wavelengths, corresponding to periods when sufficient time has elapsed for ripples to obtain equilibrium ($0 < d\theta_{wc}/dt < 0.1 \cdot \theta_{wc}(t)/T_k(t)$) [see *Traykovski*,

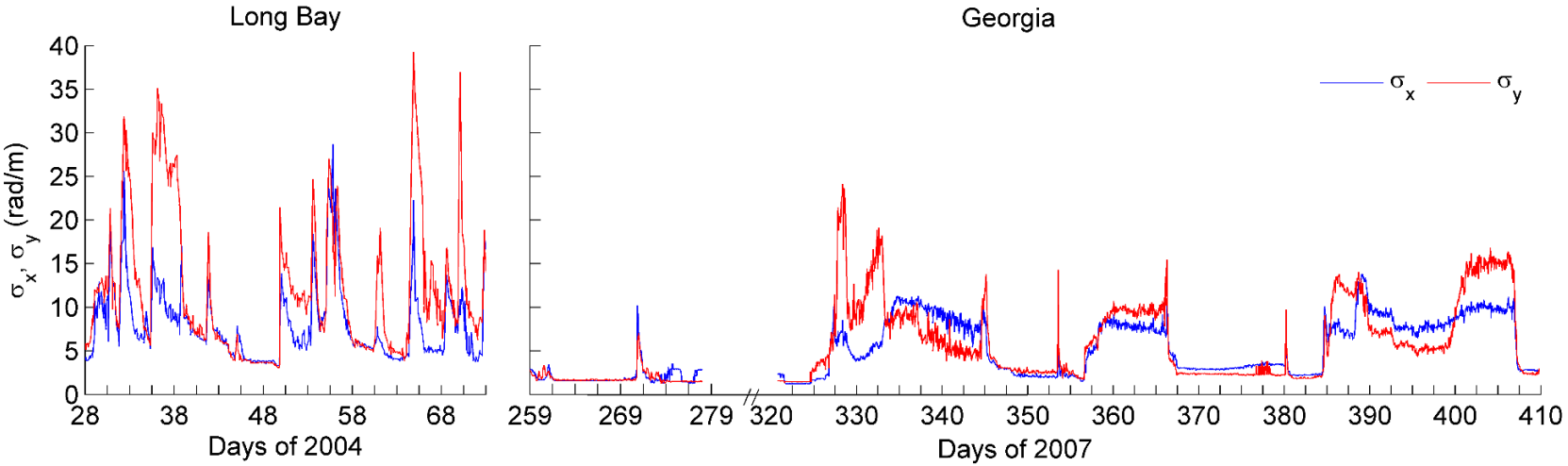

Figure 4.3. Time series of σ_x (blue line) and σ_y (red line) for the Long Bay (days of 2004) and Georgia (days of 2007) deployments.

2007; and chapter 2] and normalized by the wave semi-orbital excursion are plotted against the ratio $A_{b,1/3}/D_{50}$ in Figure 4.4. The equilibrium ripple wavelength data exhibit a

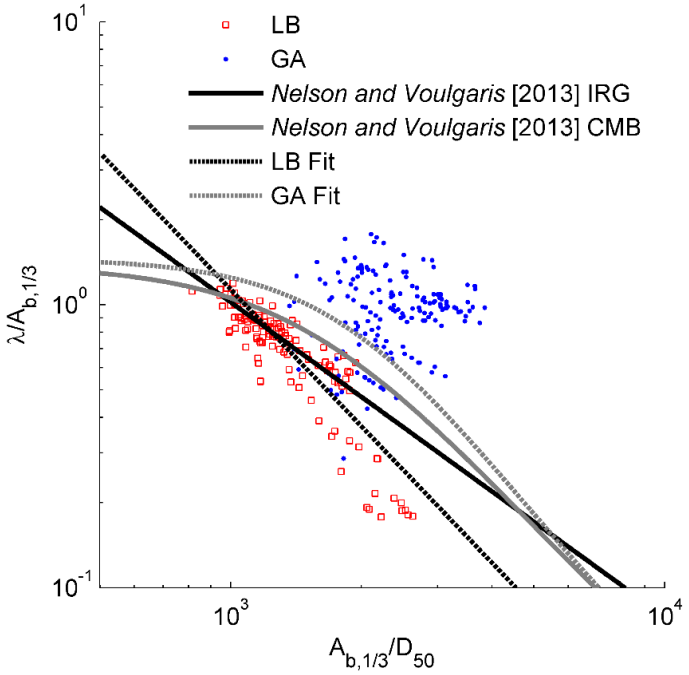

Figure 4.4. Scatter plot of $\lambda/A_{b,1/3}$ *vs.* $A_{b,1/3}/D_{50}$ for expected equilibrium ripples during Long Bay (red squares) and Georgia (blue dots) deployments corresponding to times when sufficient time has elapsed for ripples to obtain equilibrium ($0 < d\theta_{wc}/dt < 0.1 \cdot \theta_{wc}(t)/T_k(t)$) (see text for details). Also plotted are the equilibrium ripple predictors for irregular (line) and irregular/regular (dashed line) wave condition from *Nelson et al.* [2013] and the adjusted fits for Long Bay (dash-dot line) and Georgia (dotted line).

large scatter around the chapter 1 equations; LB data plot at smaller $A_{b,1/3}/D_{50}$ and $\lambda/A_{b,1/3}$ values but they appear to define a linear (in a log-log scale) relationship. The GA data seem to scatter over a larger region. From Figure 4.4 the equilibrium predictors from chapter 2 are shown [i.e.: *Nelson et al.* 2013] although they represent well the existing

data available in the literature, miss some of the characteristics present in each one of the study sites. Since the focus of this study is the performance of the 2-D model framework, in order to minimize discrepancies due to the equilibrium predictor, the chapter 2 formulas are modified to present the best possible fit for each site as in *Traykovski* [2007]. The new site specific equilibrium predictors still scale with $A_{b,1/3}/D_{50}$ and $\lambda/A_{b,1/3}$, however, LB strongly correlates with the form of the equation used for irregular waves while GA correlates better with that for combined regular and irregular waves. This is not surprising as the shallow water depths at Long Bay allow ripples to be exposed to a greater variety of wave frequencies, while the deeper waters of GA acts as a filter; attenuating higher frequencies such that the seabed experiences a more regular wave forcing. The fitted ripple wavelength equation for Long Bay is:

$$\lambda/A_{b,1/3} = 74{,}000 \cdot \left(A_{b,1/3}/D_{50}\right)^{-1.605} \quad 4.21$$

while that for Georgia is:

$$\frac{\lambda}{A_{b,1/3}} = 1.05 \cdot \left(0.72 + 2.01 \times 10^{-3} \cdot \frac{A_{b,1/3}}{D_{50}} \cdot \left\{1 - \exp\left[-\left(1.57 \times 10^{-4} \cdot \frac{A_{b,1/3}}{D_{50}}\right)^{1.5}\right]\right\}\right)^{-1} \quad 4.22$$

Since ripple height was not measured, the equilibrium height developed in chapter 2 of $\eta = 0.12 \cdot \lambda^{0.944}$ is used for both sites.

While there were no instances of current ripples present at LB or GA, there were occasions when $\theta_c > \theta_w$ and sediment was in motion and as such for these instances the equilibrium dimension for current ripples suggested by *Soulsby and Whitehouse* [2005] is used.

In chapters 2 and 3 a strong agreement was observed between the onset of sediment motion and θ_{wc} when $u_{b,1/3}$ was used to calculate the Shields parameter. While

the SW model was designed to use $u_{b,1/10}$, this exhibited poor agreement with the current data sets. Therefore all models were run using 1/3 wave statistics. Furthermore, in order to be consistent all models were run using the equilibrium geometry defined by equations (4.21) and (4.22) for LB and GA, respectively. In addition, the ripple decay for relict conditions ($\theta_{wc} < \theta_{cr}$) from equation (4.13) is used for both the 2-D and SW models.

4.3.2.3. Long Bay

The Long Bay time series (Figure 4.5) represents a high-energy wave dominated environment. All models were run with and without currents included and there was no difference observed. However, a better agreement for the 2-D model was observed when a γ of 10 was used for calculating bed load transport in equation (4.9).

For most events, the wavelength and orientation predictions of the SW, 1-D, and 2-D models closely agree. Slight differences between the models occur during relict conditions, while the strongest agreement happens during the highest energy waves, when ripples are expected to be at or close to equilibrium. Both models predict similar ripple orientation that closely follows that of the waves. The SW model does predict a more rapid transition than the 2-D model. Specifically, during the event on day 51 the SW model predicts a change in ripple orientation 16 hours before there is one observed, while the 2-D model predicts a transition 2.6 hours early. While there were no measurements of ripple height, the predictions of the SW, 1-D, and 2-D models are shown in Figure 4.5e. The 2-D model consistently yields the smallest ripple heights; deviating from the 1-D predictions only during periods when there is a change in wave direction. During energetic conditions, there is close agreement between all models particularly during days 33 and 57-59 when there is little variation in ripple orientation,

while for the rest of the time the SW model provides consistently higher ripple heights with a steepness closer to equilibrium.

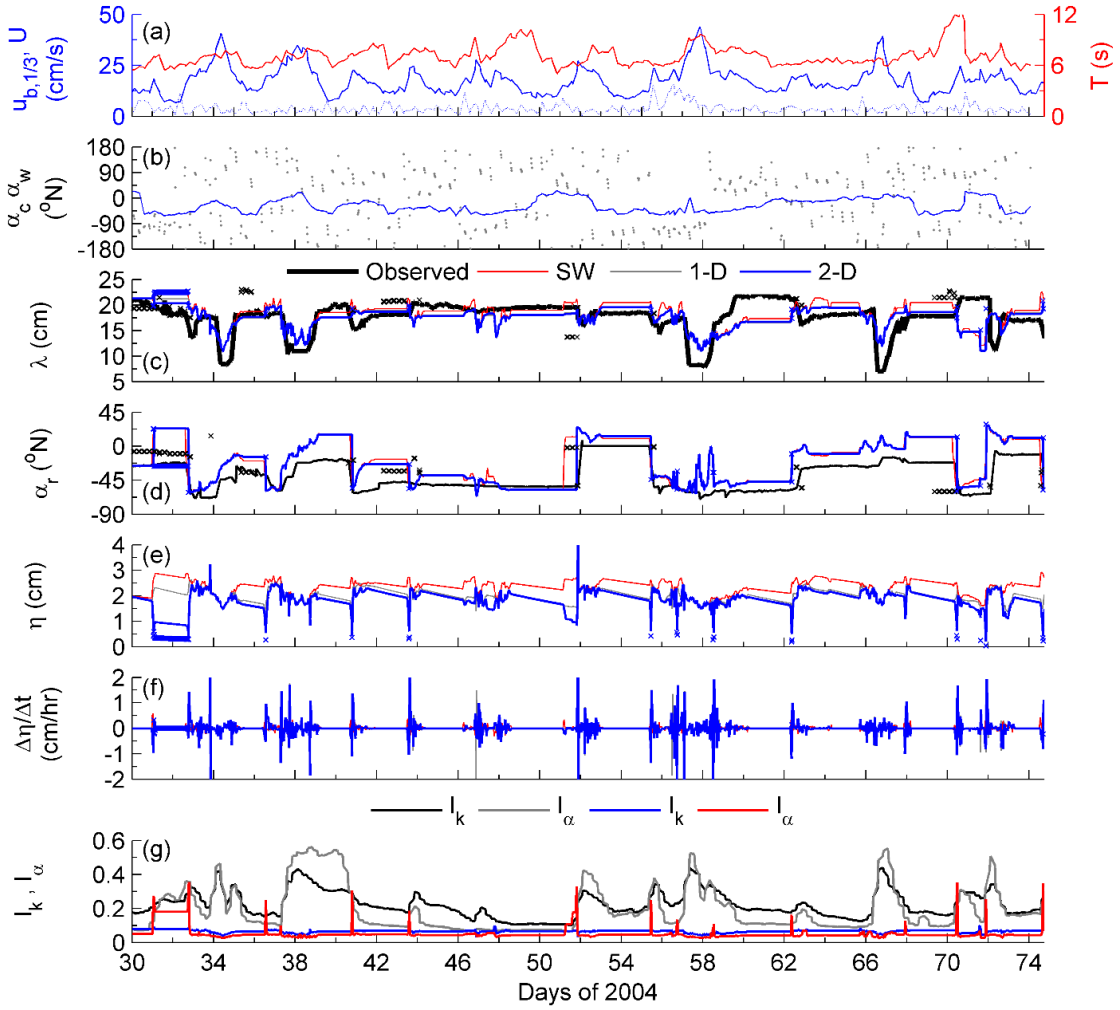

Figure 4.5. Long Bay time series of hydrodynamics: (a) significant wave orbital velocity (blue line), current speed (blue dotted line), and wave period (red line); (b) wave direction (blue line) and current direction (blue dots); and measured bedform geometry (black line) plotted with model predictions of *Soulsby and Whitehouse* [2005] (red line); *Traykovski* [2007] (gray line), and the 2-D model (blue line), with 2nd order ripples are represented as (×) for ripple (c) wavelength, (d) orientation, (e) height, and (f) change rate of change in ripple height (cm/hr). Shown in (g) are the measured wavenumber (black) and orientation (gray) irregularity plotted with the 2-D model predicted wavenumber (blue) and orientation (red) irregularity.

The estimates of 2nd order ripples by the 2-D model are primarily the result of changes in ripple orientation and are associated with a sharp decrease in ripple height (e.g. days 36.5, 43.6 and 55.5). The appearance of 2nd order ripples is often short in duration and occurs following those observed. Their occurrence is associated with large I_α values. The 2-D model accurately captures the onset of increased orientation irregularity for many events but does not predict the increased irregularity during the event but instead returns to smaller values more representative of linear ripples. The wavenumber irregularity remains small throughout and does not capture the observed trend.

4.3.2.4. Experiment GA

The Georgia data set (Figure 4.6) represents a lower energy wave dominated environment with stronger mean flows than LB. This along with the larger grain size leads to the formation of ripples with longer wavelength. The 2-D model was run for various values of γ and the best results were observed for a value of 4. Using a larger value leads to more rapid transitions than observed. Furthermore, due to the stronger mean flows, the use of θ_{wc} as opposed to θ_w for the calculation of sediment initiation and bed load transport results in better agreement.

The SW, 1-D, and 2-D models yield similar estimates of wavelength during the most energetic wave conditions. However, during relic conditions, the 1-D and 2-D models capture the observed relict ripple wavelength, while the SW model continues to adjust rapidly towards equilibrium wavelengths, which are generally much shorter than the observed wavelength during these periods.

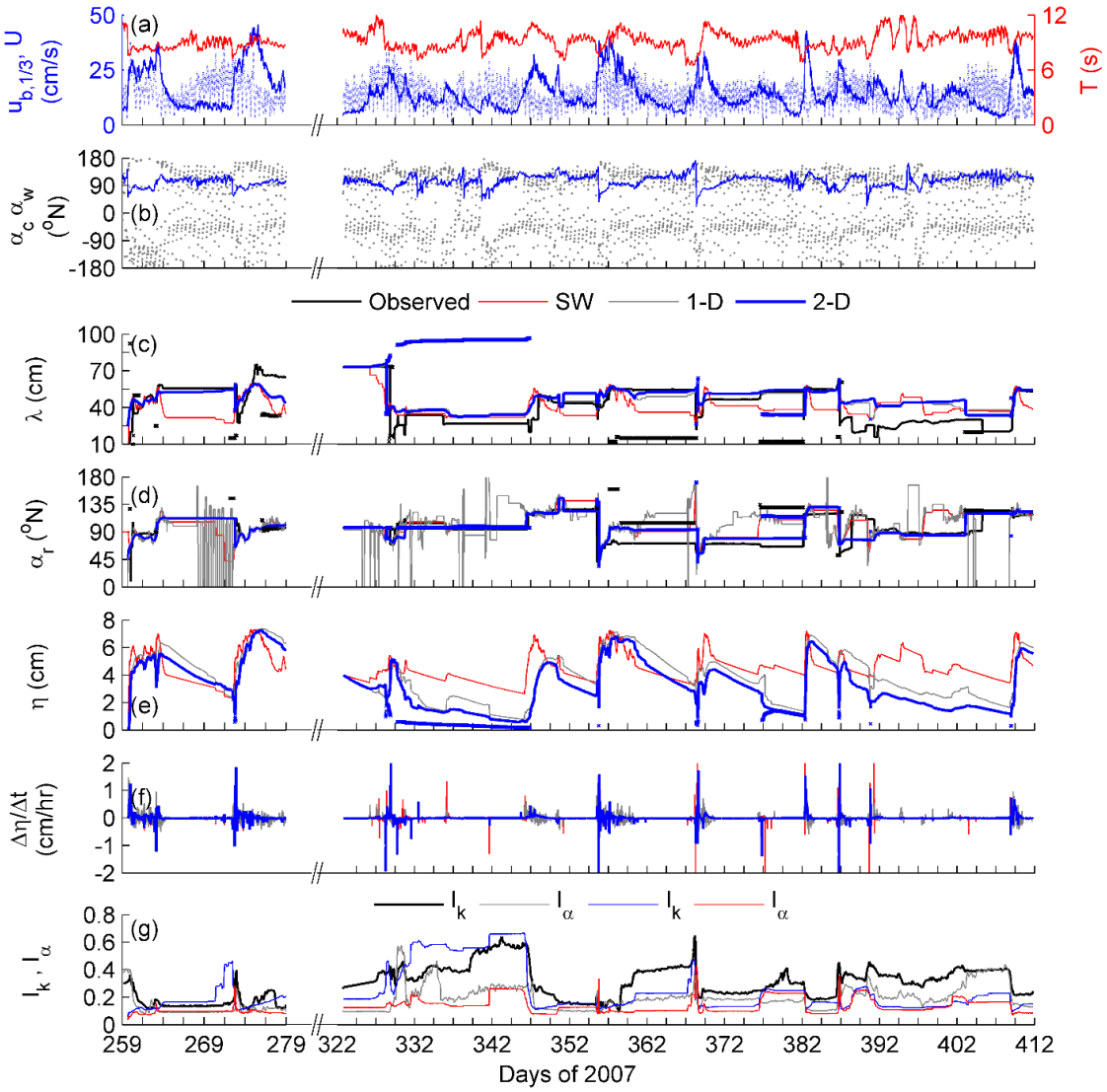

Figure 4.6. Georgia time series of hydrodynamics: (a) significant wave orbital velocity (blue line), current speed (blue dotted line), and wave period (red line); (b) wave direction (blue line) and current direction (blue dots); and measured bedform geometry (black line) plotted with model predictions of *Soulsby and Whitehouse* [2005] (red line); *Traykovski* [2007] (gray line), and the 2-D model (blue line), with 2nd order ripples are represented as (×) for ripple (c) wavelength, (d) orientation, (e) height, and (f) change rate of change in ripple height (cm/hr). Shown in (g) are the measured wavenumber (black) and orientation (gray) irregularity plotted with the 2-D model predicted wavenumber (blue) and orientation (red) irregularity.

A strong agreement in ripple orientation is observed between the SW and 2-D models; however, the SW model predicts changes in ripple orientation earlier than that

shown by the data. The 2-D model is more accurate in capturing the timing of the change in ripple orientation. The 1-D model exhibits less agreement than either the SW or 2-D model as it assumes that the ripples always align with the flow when $\theta_{wc} \geq \theta_{cr}$. The rapid reorientations predicted by the 1-D model (i.e., days 265-270 in Figure 4.6d) correspond to periods where currents are more dominant than waves ($\theta_c > \theta_w$). As such, the ripples will align with the currents during these instances.

The 2-D model predicts smaller ripple heights compared to the SW model except for periods after a peak in wave energy. The SW predicts a more rapid transition to smaller ripples during the waning energy than the 2-D model. Since the SW predictor responds more rapidly to short periods of sediment mobilization, it never attains the same small height during long relict conditions as the LB model.

The 2-D model seems to be more accurate in predicting the irregularity (Figure 4.6f) for the GA data set than it did for LB. Although the magnitude and timings vary, the overall trend of increases and decreases is similar. 2nd order ripples are also more prevalent in the observed and predicted time series. The 1-D model often predicts a longer duration of 2nd order ripples than the 2-D model, which is a result of the spectral peak of the 2-D model becoming elongated (increased irregularity) as opposed to two peaks forming which tends to agree more with the observations.

4.4. Discussion

4.4.1. Active/Relict Conditions

For strong flows, when sediment is mobilized, all models tend to yield the same peak ripple geometries as the ripples rapidly attain their equilibrium geometry. For weaker waves, the SW model deviates from the 1-D and 2-D models, as it predicts ripple

dimensions that adjust towards equilibrium at a faster rate than the other models. As shown here, under field conditions during an energetic event the rate of adjustment is smaller after the peak of the event. This behavior is similar to what is seen in the predictions of the 2-D model suggesting that this latter model is more accurate in representing bed evolution under changing wave conditions.

For the higher energy wave environment of LB, both the 2-D and SW models yield nearly identical results for ripple wavelength and orientation. The model performance *vs*. observations is shown in Figure 4.7 as a scatter plot of predicted vs. observed values. Both models yield nearly identical scatter for both active ($\theta_{wc} \geq \theta_{cr}$) and relict ($\theta_{wc} < \theta_{cr}$) ripples. Ripple wavelength scatters around the 1:1 line for wavelengths greater than 15 cm, while for smaller wavelengths the models over predict the wavelength by a few cm. In terms of ripple orientation, both models seem to predict slightly higher orientation angles than the measurements. The model performance is quantified using the root mean square deviation (*RMSD*) and normalized (*NRMSD*) value defined as:

$$RMSD = \sqrt{\sum \left(X_p - X_o\right)^2 / N} \qquad 4.23$$

where X is either wavelength, orientation, or height; the subscripts p and o indicate predicted and observed while N is the number of measurements. The *RMSD* values are normalized by the range of observations to find *NRMSD*. The *RMSD* values for active, relict, and all conditions are listed in Table 4.1.

As can be seen from the values shown in Table 4.1, the 2-D model yields the least errors for LB but the differences are small so effectively both the SW and 2-D models seem to perform equally well. For the case of relict ripples, an error of 2.04 and 2.27 cm

(13.2 and 14.7 %) for the 2-D and SW model respectively is found while the 2-D model yields an orientation error of 22.7° for all conditions just 1° smaller error than was found for the SW model.

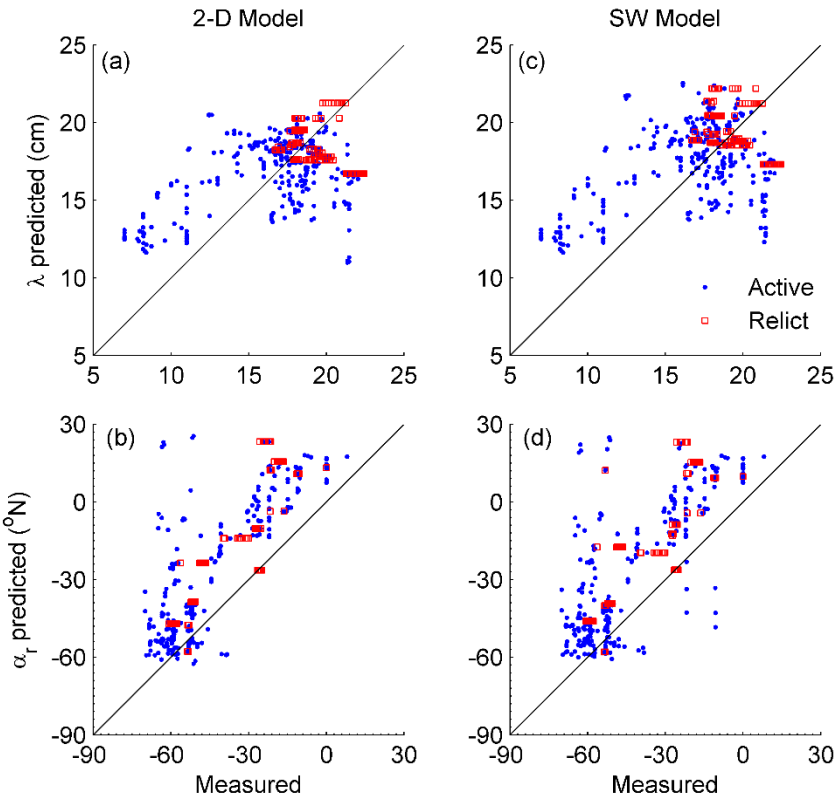

Figure 4.7. Scatter plot of predicted *vs.* measured wavelength (a and c) and orientation (b and d) from Long Bay for active ($\theta_{wc} \geq \theta_{cr}$, blue dots) and relict ($\theta_{wc} < \theta_{cr}$, red squares) ripples. The results of the 2-D model are shown in plots (a) and (b) and the results of the *Soulsby and Whitehouse* [2005] model are shown in (c) and (d). The black line indicates unity.

Although there is little difference between the model predictions for the highly energetic LB data set, the 2-D model performs better for the weaker energy GA environment. The model results plotted against the observed geometries is shown in

Table 4.1. Root mean square deviations and normalized deviations in ( ) of the model predictions compared to observed ripple wavelength and orientation.

		Wavelength, cm (%)			Orientation (deg)		
		Active[a]	Relict[b]	All	Active[a]	Relict[b]	All
LB	Eq[c]	3.69 (23.9)	3.96 (25.7)	3.80 (24.6)	25.77	24.79	25.37
	SW	3.57 (23.1)	2.27 (14.7)	3.10 (20.1)	24.15	23.57	23.91
	2-D	3.50 (22.7)	2.04 (13.2)	2.98 (19.3)	22.73	22.77	22.75
GA	Eq	18.18 (24.0)	24.40 (33.2)	21.81 (28.8)	36.22	62.22	52.05
	SW	14.72 (19.4)	14.29 (18.8)	14.48 (19.1)	20.75	19.76	20.21
	2-D	11.76 (15.5)	8.92 (11.8)	10.31 (13.6)	15.36	12.49	13.86

[a]Active conditions defined as ($\theta_{wc} \geq \theta_{cr}$)
[b]Relict conditions defined as ($\theta_{wc} < \theta_{cr}$);
[c]Assuming ripples are in equilibrium

Figure 4.8. The 2-D model reduces the overall scatter and yields a wavelength error of 10.3 and 14.5 cm (13.6 and 19.1%) for the 2-D and SW models. The SW model yields a nearly consistent error of 14.5 cm (19%) for both relict and active conditions, while the 2-D model yields a smaller error of 8.92 cm (11.8%) for the relict ripples. The 2-D model also performs equally well for ripple orientation with an error of 13.9° and 20.2° for the 2-D and SW models, respectively.

4.4.2. Ripple Height

One of the largest deviations between the different models is the prediction of ripple height. The 2-D model yields the smallest predictions especially during changes in ripple orientation. The one exception to this is during weakening wave energy conditions following a storm event. If the equilibrium height is smaller than that during a storm, then the 2-D model yields larger values than the SW model.

The smaller ripple height predicted by the 2-D model has important implications for ripple steepness. Figure 4.9 shows the model results for Long Bay (Figure 4.9a) and Georgia (Figure 4.9b). These time-series show that the SW model consistently predicts

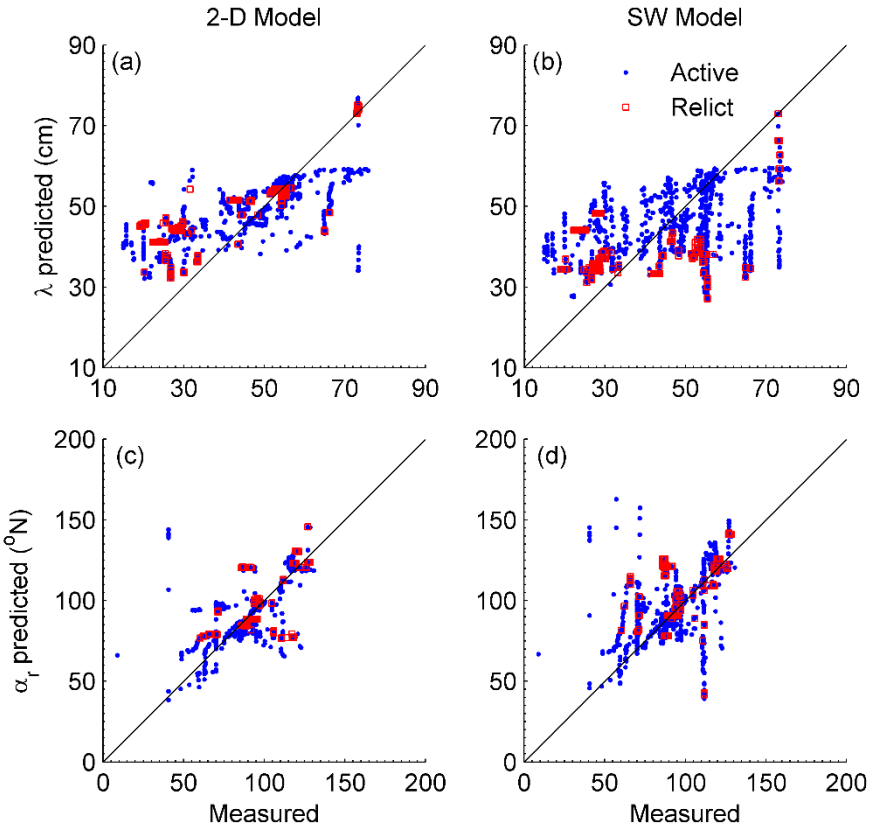

Figure 4.8. Scatter plot of predicted *vs.* measured wavelength (a and c) and orientation (b and d) from Georgia for active ($\theta_{wc} \geq \theta_{cr}$, blue dots) and relict ($\theta_{wc} < \theta_{cr}$, red squares) ripples. The results of the 2-D model are shown in plots (a) and (b) and the results of the *Soulsby and Whitehouse* [2005] model are shown in (c) and (d). The black line indicates unity.

greater steepness that is closer to equilibrium, while a greater deviation is observed with the 2-D model. Although ripple height was not directly measured, the ADVs and Acoustic Backscatter Systems deployed on each tripod provide single point measurements of the distance to the bed; the lateral displacement of those sensors allows for multiple measurements of bed elevation so that the variability of those values can be assumed to represent variability due to presence of ripples. For Long Bay, 5 measurements of bed elevation are obtained (3 from the 3 ABS transceivers and 2 from

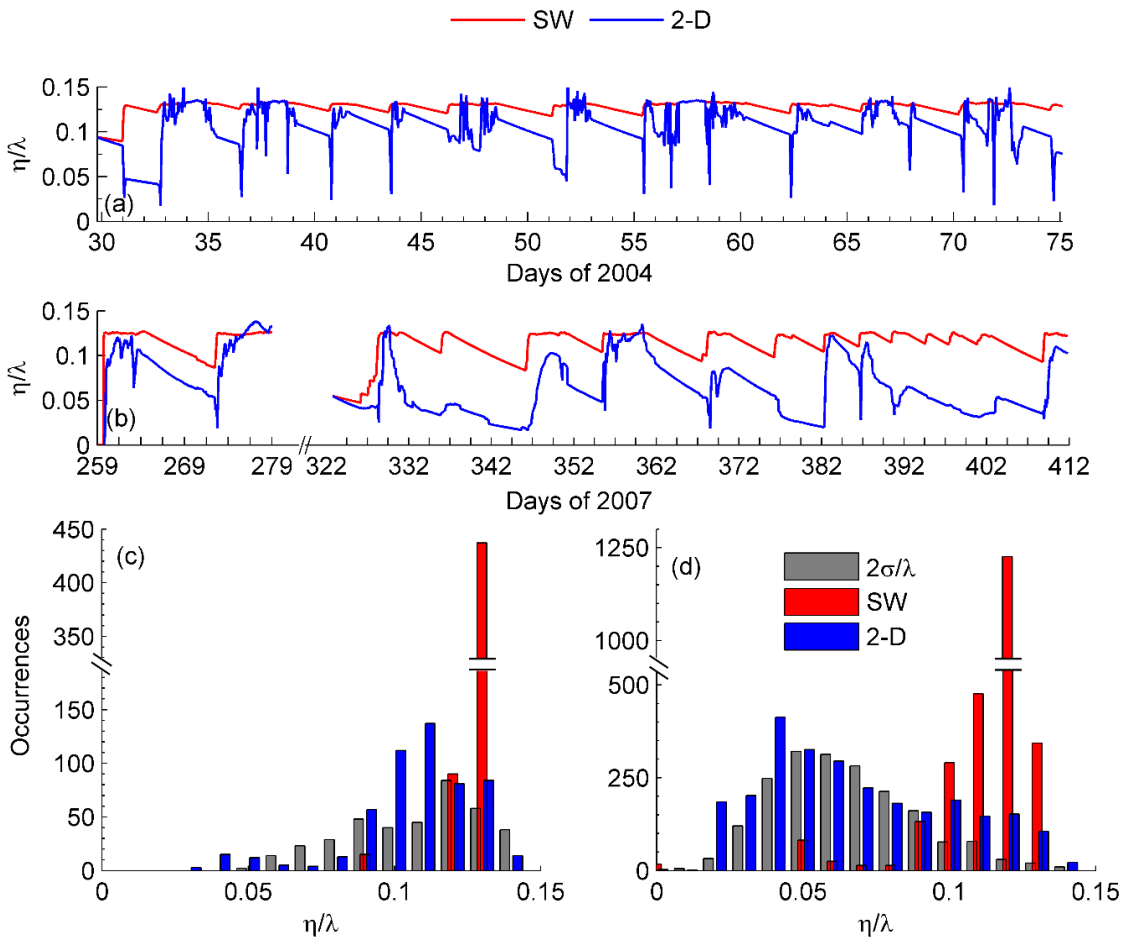

Figure 4.9. Ripple steepness predictions from the 2-D (blue) and *Soulsby and Whitehouse* [2005] model (red lines, SW) for (a) Long Bay and (b) Georgia. The expected ripple height assuming equilibrium with the ripple wavelength is shown in dashed lines. Histograms showing the distribution of ripple steepness from the two models as well as the calculated ripple steepness (gray) from the variance of the seabed elevations below the ADV and ABS sensors for (c) Long Bay and (d) Georgia (see text for details).

the ADVs). Considering the small ripple wavelength, an estimate of the ripple height can be calculated as $\eta_\sigma=2\sigma_b$, where σ_b is the standard deviation of the distance to the bed (normalized to the ABS elevation). While this approach does not prove accurate for an instantaneous ripple height due to the possibility of measurements not including the trough and crest and the vertical spatial resolution of the instruments, when normalized

by the measured wavelength, it does provide an indication of the distribution of ripple steepness observed. Figure 4.9c, shows that the 2-D model predicts a distribution of ripple steepness similar to that calculated using the aforementioned method. For Georgia, the ADVs were installed too high to provide range data so only measurements from the ABS were used. Since the ABS transceivers were configured in a circular pattern, they only provided measurements over a 6 cm diameter section of the seabed. Thus, the slope of the ripple over these 6 cm (η_σ/6 cm) is equivalent to (η_σ/λ/2) so the steepness (η/λ) can be estimated as (η_σ/12 cm). The resulting distribution is shown in Figure 4.9d and more closely resembles that from the 2-D model than the SW model.

4.4.3. 2nd Order Ripples and Irregularity

While the 2-D model is capable of predicting 2nd order ripples, the predictions do not often correspond to the timing or duration of the observations. Some of this can be attributed to 2nd order ripples being manually identified due to the poor performance of the 2-D FFT in identifying 2nd order peaks over background noise. Furthermore, the spectral peaks often become broad as opposed to two individual peaks, thereby increasing the ripple irregularity but not forming 2nd order ripples. The I_k and I_α parameters are more representative for the detection of multiple ripple systems.

The predictions of I_k and I_α agree better with that of the GA data set than the LB data set. One possibility for the poor agreement with LB is that the shallower water depths allow for more wave frequencies and directions to be influencing the bed, a process not captured in the model by using the $u_{b,1/3}$ and a single wave direction. The deeper water depths at GA would attenuate many of these high frequency oscillations and directions such that a single velocity and direction would better describe the bed and

might explain the improved predictions for the GA data set. This is also evident in the equilibrium ripples being better described by the combined regular/irregular wave equations for GA; while for LB the irregular wave equation results in better predictions.

4.4.4. Rate of Change

While the 2-D model predicts the expected ripple wavelength and orientation, LB and GA required different values of γ. Various bed load transport formulas were tested including *Wiberg and Smith* [1989], *Nielsen* [1992, equation (2.3.12)], and *Ribberink* [1998]. It was found here that a γ of 10 and 4 applied to equation (4.9) worked best for LB and GA, respectively. In an attempt to quantify these two parameters, various method were tested including adjusting the bed load fraction using a fitted equation to the *Laursen* [1958] ratio of suspended sediment to total sediment transport (q_s/q_t) to reduce the bed load at times of high shear stress when suspended sediment would dominate. However, this failed to improve the data fit when applied to these equations. The critical Shields parameter was also adjusted to take into account the slope of the ripple [see *Kobayashi and Madsen*, 1985, equation (4.24)]; however, this also had no improvement to the GA data set and led to a poorer agreement for the LB data set. *Maier and Hay* [2009] observed a similar issue with ripples at Duck, North Carolina, which required a longer adjustment time than predicted. They attributed this to sediment bypassing with some grains skipping over ripples as suspended sediment; however, *Hay* [2011] found this did not occur for small-scale linear transition ripples (i.e.: linear-quasi-linear and bifurcating ripples). While it does not appear that bypassing is occurring for LB, in fact the adjustment is faster than the *Meyer-Peter and Müller* [1948] equation predicts by a factor of 1.25, the rate is slower at GA by a factor of 0.5. Therefore, the longer ripples

may contribute to a form of sediment bypassing or trapping. Further investigation as to the reasons for the differences is necessary to improve ripple geometry and sediment transport predictions.

4.5. Summary and Conclusions

Field and synthetic data were used to evaluate a new 2-D time dependent ripple model for the prediction of the temporal evolution of ripple geometry and irregularity. Predictors such as *Traykovski* [2007] predict the temporal evolution of wavelength and height but do not predict the temporal evolution of orientation. The *Soulsby and Whitehouse* [2005] model predicts ripple orientation but does not take into account the dynamic feedback between orientation, wavelength, and height; instead the model predicts their evolution as independent quantities. A detailed study of these ripples in chapter 3 showed that changes in orientation affect the time required for ripple height to obtain an equilibrium geometry, something not captured by these two models. This study presents the development of a 2-D spectral model that captures the dependence of ripple geometry on changes in orientation.

The 2-D model was compared against the models of *Traykovski* [2007] and *Soulsby and Whitehouse* [2005] for both synthetic and field data. Analysis against the synthetic data showed the 2-D model predicts the decreased ripple height associated with ripple realignment due to a changing forcing direction. Furthermore, the model predicts the formation of 2^{nd} order (cross) ripples, and an increase in the seabed irregularity, features not predicted by the *Soulsby and Whitehouse* [2005] model. The SW predictions of orientation closely follow that of the mean predictions from the 2-D model, though it predicts more rapid transitions. This model further indicates that ripple wavelength and

orientation are the first parameters to adjust to a new forcing and height; and only increases once these dimensions are nearly stable.

Comparison to the field data showed that under strong wave forcing conditions observed at Long Bay, all models yield similar results for ripple wavelength and orientation; however, the 2-D model consistently yielded the smallest height except during the strongest wave forcing when the ripples obtained an equilibrium value resulting in smaller steepness. This smaller steepness more closely resembles the distribution of field observations and has important implications for calculations of form drag and sediment resuspension. Under the weaker wave environment of the Georgia data set, the 2-D model yields improved predictions or wavelength and orientation, especially for relict ripples as the SW model adjusts more rapidly towards equilibrium conditions.

The new model appears to better simulate ripple conditions at times when wave direction changes by predicting the development of cross ripples. At these times, it also predicts a decrease in ripple height more than half that of the expected equilibrium ripple. Therefore, this model might be more suitable for inclusion in numerical models for ripple prediction and subsequent form drag estimation for generation of bottom turbulence. The capability of this model to predict ripple direction allows the use of form drag formulations that account for relative angle between ripple crest and mean current direction as suggested by *Powel et al.* [2000] and *Madsen et al.* [2010].

CHAPTER 5

TURBULENCE AND BOTTOM ROUGHNESS IN THE PRESENCE ON BEDFORMS

5.1. Introduction

As discussed in the previous chapters, ripples are dynamic sedimentary bedforms found on the seafloor, which can form at a variety of length scales, orientations, and shapes depending on the strength, variability, and duration of the waves and mean flow. Although the size of the sedimentary grains define the elementary roughness element in the bottom boundary layer (skin friction), ripples on the seabed also contribute to one of the most prevalent bottom boundary layer roughness element (form drag) in the nearshore region. Bottom boundary layer roughness plays an important role in defining nearbed turbulence intensity, thereby affecting the ability of the flow to keep sediment in suspension, affecting its vertical distribution, and contributing to the creation of different depositional patterns [e.g., *Gutierrez et al.*, 2005]. The enhanced roughness also alters the vertical structure of the mean current in the benthic boundary layer [e.g., *Grant and Madsen*, 1986].

The form roughness has been found by many investigators to be proportional to ripple geometry [*Grant and Madsen*, 1982; *Nielsen*, 1992; *Kim*, 2004 and references therein]. Assuming that ripple steepness (η/λ) is constant, *Wikramanayake and Madsen* [1994] suggested a form drag estimation that relates to ripple height alone. In addition to ripple height and wavelength, *Powel et al.* [2000] and more recently *Madsen et al.* [2010] observed that total bed roughness is dependent on the angle between the ripple crest and

the current direction, such that maximum roughness is experienced when the current is perpendicular to the ripple crest. While the size and orientation of the ripple is important, the spatial configuration (irregularity) may also play a factor in determining bottom form drag. *Bhaganagar and Hsu* [2009] used direct numerical simulations to show how turbulence statistics and the resultant flow structures depend on whether the ripples are regular or irregular. However, little attention has been given to the differences in seabed roughness for various ripple types.

In the present contribution, seabed roughness due to a variety of ripple geometries, orientations, and geometric configurations for two field sites using in situ measurements of bottom shear stress was examined. The study is organized so that the methods of calculating shear stress are discussed in section 5.2, the hydrodynamics and shear stress calculations are presented in section 5.3. The dependence of the form roughness on the various ripple geometries is analyzed in section 5.4 while a discussion of the findings and conclusions are presented in section 5.5.

5.2. Bed Shear Stress Estimation Methods

Shear stress within the boundary layer can be measured from one or more velocity measurements using a variety of methods [e.g., *Sherwood et al*., 2006]. For this study, the data available are from two ADV sensors so the Eddy Correlation (EC) and Inertial Dissipation (ID) methods are the most appropriate and are evaluated. These two methods provide estimates of turbulence production (EC method) and dissipation (ID method) and under ideal cases (no turbulence advection or local turbulence sinks or sources other than the seabed), these estimates are equal.

5.2.1. Eddy Correlation

The eddy correlation stress estimates relate turbulence production to horizontal and vertical fluctuations in velocity (u', v', w'). The eastward, u, northward, v, and upward, w, velocities are composed of a mean, oscillatory (wave), and turbulent component (ignoring noise). The horizontal components for this study are rotated to such a way that U is the downstream current velocity. The EC shear velocity (u_{*EC}) can then be calculated as

$$u_{*,EC} = \sqrt{-\langle U'w' \rangle} \qquad 5.1$$

where the brackets denote time averaged quantities. The advantage of this method is that it requires only one measurement of velocity; however, when waves are present the slightest inclination of the sensor off the vertical provides significant bias in the estimates [e.g., *Grant and Madsen*, 1986]. These biases are due to contamination of the vertical velocity by the wave signal Coastal Dynamics ‘97due to sensor misalignment. One method to remove the wave bias is to use the velocity time series of two point measurements and take the difference between the horizontal and vertical velocities. The two sensors must be spaced such that the spacing is much smaller than the surface wavelength of the waves but larger than the correlation scale of the turbulence with the latter scaling with the elevation above the seabed. Such spacing allows the wave signal recorded by the two sensors to be correlated while the turbulence signal becomes uncorrelated [*Trowbridge*, 1998; *Voulgaris et al.*, 1997). This method provides a nearly wave-free average estimate of Reynolds stress between the two sensors. This method is presented in detail in *Trowbridge* [1998] and the Reynolds stress is calculated as:

$$\langle u'w' \rangle = 0.5 \cdot \mathrm{cov}(\Delta U, \Delta w) \qquad 5.2$$

where $\Delta U = U_1 - U_2,\ \Delta w = w_1 - w_2$ the subscripts 1 and 2 correspond to the two horizontally separated sensors and cov is the covariance.

A further refinement to this method, still based on two point measurements, is that of *Shaw and Trowbridge* [2001]. They found that equation (5.2) could fail under high wave energy conditions. In order to improve this instead of simple differencing, they developed a technique where a least squares fitting is used to estimate the coherent component of the velocity at one sensor with the velocity records at the second sensor and then remove this part from the signal. The filter represents the relationship between the wave-induced fluctuations at the two locations and can be applied to either the horizontal component (U) or the vertical component (w) such that:

$$\langle u'w' \rangle = \mathrm{cov}(\Delta \mathrm{U}_i, w_i) \qquad 5.3$$

$$\langle u'w' \rangle = \mathrm{cov}(U_i, \Delta w_i) \qquad 5.4$$

where $\Delta U_i = U_i - \widehat{U}_{ij}$, $\Delta w_i = w_i - \widehat{w}_{ij}$, and w $\widehat{U}_{ij}$ and $\widehat{w}_{ij}$, represent the coherent component of oscillatory flow between the two spatially separated sensors i and j as estimated with the linear regression fit.

5.2.2. Inertial Dissipation

Another method for the calculation of shear stress is the inertial dissipation method (ID). This method was first developed for atmospheric boundary layer conditions by *Deacon* [1959] and allows for the estimation of shear velocity from a single point measurement of horizontal and vertical velocity. While the EC method is a measurement of turbulent production, the ID method is an estimate of turbulence dissipation (ϵ) making use of theoretical global relationship between turbulent energy production and dissipation as first introduced by *Kolmogorv* [1941]. Turbulent motions are generated as large scales

eddies that scale with the elevation above the bed which dissipate by cascading to smaller scales until all energy is dissipated as heat with a dissipation length scale of $(\nu^3/\epsilon)^{1/4}$, where ν is the kinematic viscosity of water [*Kolmogorv*, 1941]. The region of frequencies at which this energy cascade occurs is known as the inertial subrange. The energy of the turbulent motions ($E_{ww}(f)$, where f is the frequency of the turbulent motions) decreases at a constant -5/3 slope for increasing f. These frequencies can be related to the spatial eddies the Taylor's "frozen turbulence" hypothesis, which assumes that if the eddy's horizontal motion is faster than the rate of decay then at a high sampling frequency the spatial characteristics can be recorded. Using this hypothesis, the wavenumber can be rewritten as $k_u=2\pi f/U$ and the spectrum of the vertical velocity ($E_{ww}(f)$) can be rewritten as a function of k_u as $E_{ww}(k_u)= E_{ww}(f)U/(2\pi)$. Based on Kolmogorov's turbulent spectra model [*Tennekes and Lumley*, 1989] and the modification of *Trowbridge and Elgar* [2001] for the presence of waves, the turbulence of the vertical velocity is:

$$E_{ww}(k_u) = \frac{12}{55} 1.5\epsilon^{2/3} k_u^{-5/3} I\left(u_{b,1/3}/U\,, \alpha_{wc}\right) \qquad 5.5$$

where ϵ is the turbulence dissipation rate, 1.5 is the empirical Kolmogorov constant. The term $I\left(u_{b,1/3}/U\,, \alpha_{wc}\right)$ is a correction for the enhancement of energy due to turbulence advection by waves [*Trowbridge and Elgar*, 2001], defined as:

$$I\left(u_{b,1/3}/U\,, \alpha_{wc}\right) = \frac{1}{\sqrt{2\pi}} \left(\frac{u_{b,1/3}}{U}\right)^{\frac{2}{3}} \int_{-\infty}^{+\infty} \left[x^2 - 2\frac{U}{u_{b,1/3}}\cos(\alpha_{wc})x + \frac{U^2}{u_{b,1/3}^2}\right]^{\frac{1}{3}} \exp\left(-\frac{1}{2}x^2\right) dx \qquad 5.6$$

where $u_{b,1/3}$ is the significant wave orbital velocity, α_{wc} is the angle between the waves and currents, and x is a variable for integration. Since production balances dissipation and

if a logarithmic boundary layer (constant stress region) exists then ϵ, in equation (5.5), can be related to the shear velocity (u_*) as:

$$\epsilon = u_*^3/(\kappa z) \quad 5.7$$

where ϵ is calculated within the inertial subrange for $1.8/(\kappa z) < k_u < (v^3/\epsilon)^{1/4}$ [*Tennekes and Lumley*, 1989], κ is the von Kármán constant (=0.4), and z is the elevation above the bed that U was measured.

5.2.3. Drag Coefficient

The shear velocity calculated from the above methods is related to the bottom shear stress (τ_b) as

$$\tau_b = \rho u_*^2 \quad 5.8$$

In addition, shear stress can be related to the mean flow by a fluid-drag coefficient (C_D) which varies depending on the roughness elements present on the seabed, and can be written as:

$$\tau_b = \rho C_{D_z} U_z^2 \quad 5.9$$

By setting equations (5.9) and (5.10) equal to one another, C_{Dz} can be written as:

$$C_{Dz} = u_*^2/U_z^2 \quad 5.10$$

and the equation denotes it depends on the elevation the mean velocity is measured.

The above measurements of τ_b, from the EC and ID methods, result in the calculation of the mean bottom shear stress when averaged over a sufficiently long sampling period that captures the natural variability of the flow. This shear stress incorporates the effects of bottom roughness elements as well as the wave boundary layer which usually is considered as an additional roughness element [*Grant and Madsen*, 1986] leading to increased mean flow shear velocity.

5.3. Data Description

5.3.1. Hydrodynamics

Details of the hydrodynamics and ripple properties for both Long Bay and Georgia are discussed in detail in chapter 3. Given below is the important instrument deployment information relevant to estimating the shear velocity values that define bottom turbulence.

The data sources used in this study consist of two field sites located along the South Atlantic Bight offshore Georgia (GA) and Long Bay, South Carolina (LB). The Long Bay field site consisted of two bottom boundary layer tripods (A and B). Tripod A included two SonTek Acoustic Doppler Velocimeters (ADV) both installed at an elevation of ~31 cm above the bed, but spatially separated by a distance of ~ 1 m. Tripod B included an Imagenex 881 rotating sector-scanning sonar, which provided images of the seabed at a rate of 1 burst every 30 min for 1.5 hours; the sampling scheme was repeated every 5 hours. Also included on tripod B was an Aquatec Acoustic Backscatter sensor, which provided profiles of acoustic intensity with a spatial resolution of 11 mm every hour. The system consisted of 3 transceivers operating at 1, 2.5, and 5 MHz. The data presented in this section are from the period January to March 2004. During this deployment (Figure 5.1), the mean water depth was 9.5 m, with a median sediment grain size (D_{50}) of 177 μm. The site is primarily wave dominated with a mean current speed of 3.8 cm/s, incapable of mobilizing bed sediments. The deployment was characterized by numerous storm events associated with the passage of frontal systems [*Warner et al.*, 2012], during which time the ripples present on the seabed changed in geometry, aligned

with the wave direction, and adjusted towards equilibrium geometries (chapters 3 and 4). The ripples were primarily small scale with a maximum wavelength less than 30 cm.

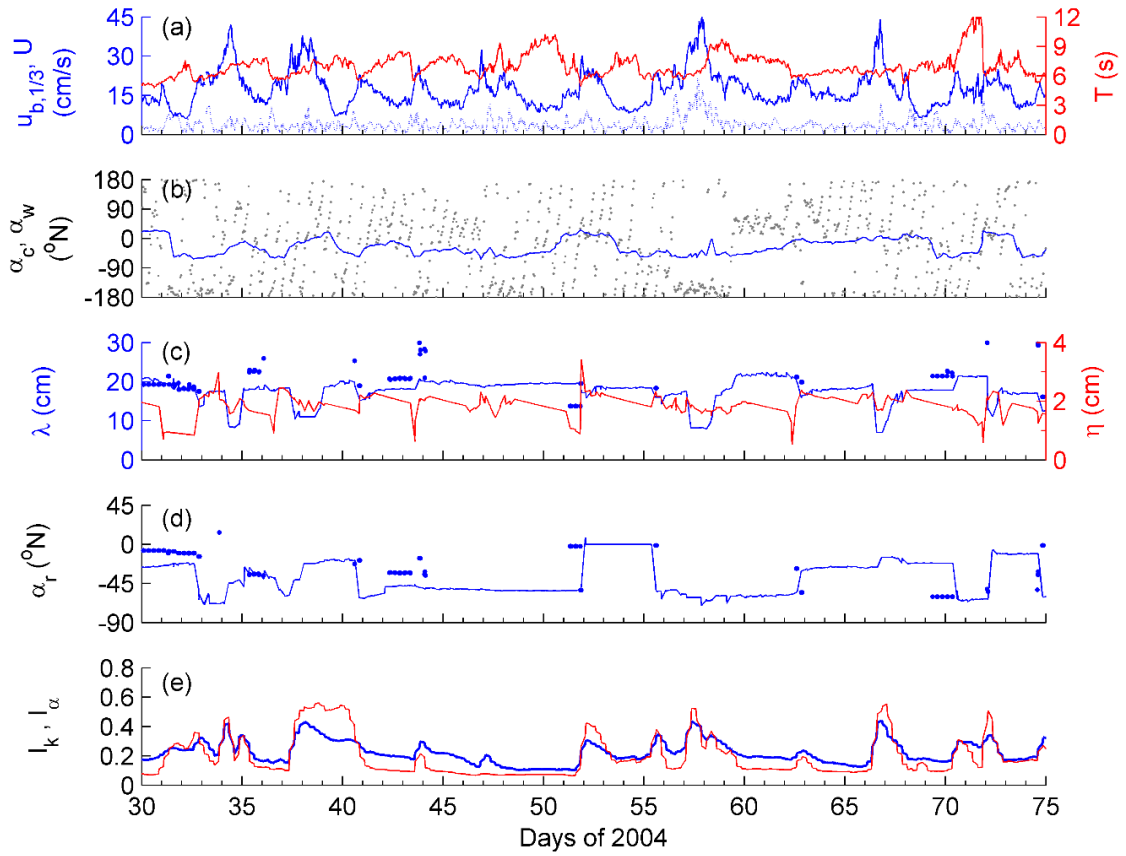

Figure 5.1. Time Series of hydrodynamics and bedform geometries for the Long Bay, SC field experiments showing: (a) significant wave orbital velocity (blue - left axis) and wave period (red - right axis); (b) downstream current direction (gray dots) and wave direction of propagation (blue line); (c) ripple wavelength (blue - left axis) and height (red - right axis) where the dots indicate second order geometries; (d) ripple orientation (red); and (e) ripple wavenumber (blue) and orientation (red) irregularity.

The second data set (GA) (Figure 5.2) consisted of the deployment of a single tripod during 2007 and 2008 that was turned over every few months. These tripods were equipped with two Sontek ADV sensors installed at nominal heights of 52 and 67 cm above the bed for data collected between 16 September and 7 October 2007 (hereafter

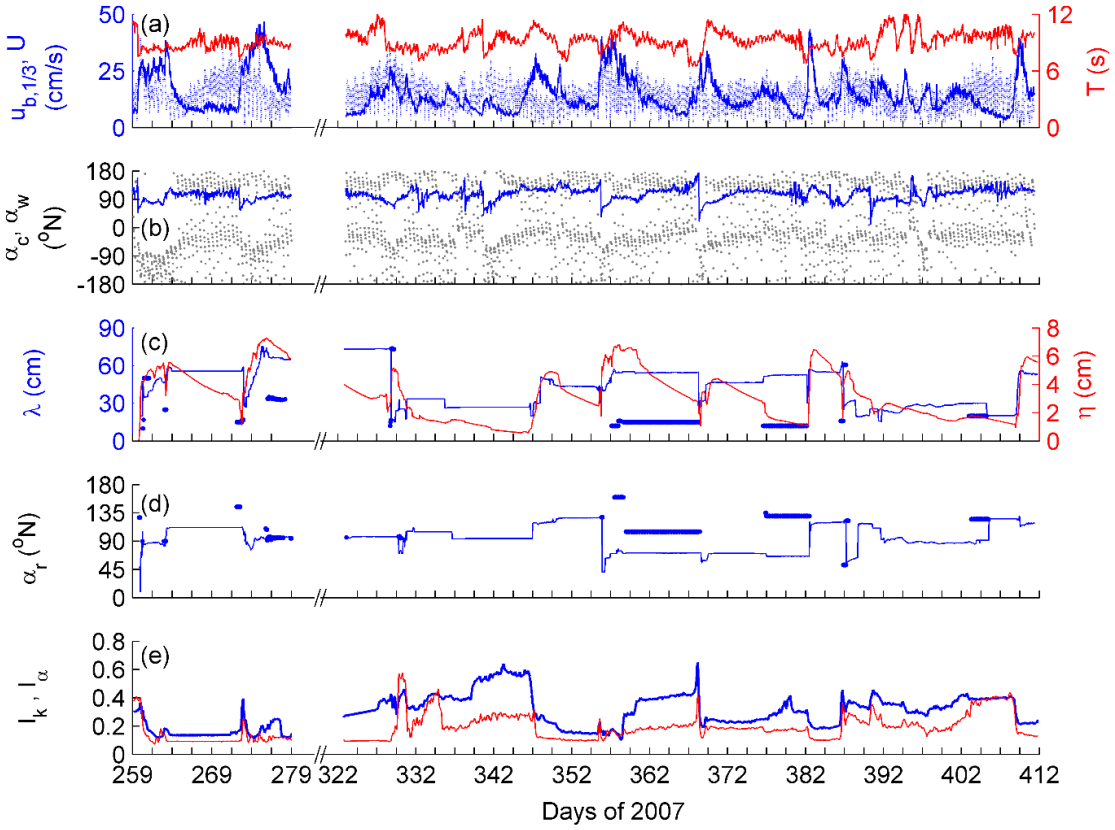

Figure 5.2. Time Series of hydrodynamics and bedform geometries for the Georgia field experiments showing: (a) significant wave orbital velocity (blue - left axis) and wave period (red - right axis); (b) downstream current direction (gray dots) and wave direction of propagation (blue line); (c) ripple wavelength (blue - left axis) and height (red - right axis) where the dots indicate second order geometries; (d) ripple orientation (red); and (e) ripple wavenumber (blue) and orientation (red) irregularity.

referred to as GA1) and at 45 and 31 cm for data collected between 22 November 2007 and 15 February 2008 (hereafter referred to as GA2). Also included on this tripod was an ABS system with 4 downward looking transceivers operating at 1, 2.5, 4 and 5 MHz. Installed separately but near each tripod was a rotating sector scanning sonar system attached to a jetted pipe which provided imagery of the seabed at 1 image ever hour [*Voulgaris and Morin*, 2008]. The instrumentation was deployed in 27.5 m water depths with a median sediment grain size of 388 μm. These sites were wave dominated with a

mean significant wave orbital velocity ($u_{b,1/3}$) of 14.7 cm/s and period of 9.2 s; however, currents were stronger than LB with a mean speed of 14.3 cm/s. Bedforms at GA changed geometry and orientation with changing wave forcing and direction and were larger than LB with a maximum wavelength of 76 and mean of 43 cm.

Ripple height was not directly measured by the instrumentation included in the GA and LB deployments; therefore, the ripple height was predicted by the 2-D time dependent model described in chapter 4. This data agrees favorably with measurements of the distance to the seabed, measured by the ADVs and Acoustic Backscatter Systems deployed on each tripod. For the Georgia deployments, the ADVs failed to recognize the seabed consistently while the 4 ABS transceivers provided measurements of the seabed. For Long Bay, the 3 ABS transceivers and both ADV yielded measurements. Considering the small ripple wavelength for LB, an estimate of the ripple height can be calculated as $\eta_\sigma=2\sigma_b$, where σ_b is the standard deviation of the distance to the bed (normalized to the ABS elevation). As η_σ is heavily dependent on whether the measurements encompass both the crest and trough of the ripple and the vertical special resolution of the measurements, the instantaneous values are not a realistic measurement of ripple height. However, the measurements do give an indication of the distribution of ripple heights expected which closely agree with the 2-D model predictions (see chapter 4). For Georgia, the ABS transceivers were configured in a circular pattern, such that they only provided measurements over a 6 cm diameter section of the seabed. Thus, the slope of the ripple over these 6 cm (η_σ/6 cm) is equivalent to ($\eta_\sigma/\lambda/2$) so the steepness (η/λ) can be estimated as (η_σ/12 cm). This is only valid if all measurements occurred over the sloping stoss or lee side of the ripple. If the measurements were over the trough or crest then the

height and steepness will be smaller than predicted. The resulting distributions are shown in Figure 5.3c and 5.3d and agree with the ripple height and steepness predicted by the 2-D model. Therefore, all ripple height used will be that predicted by the 2-D model.

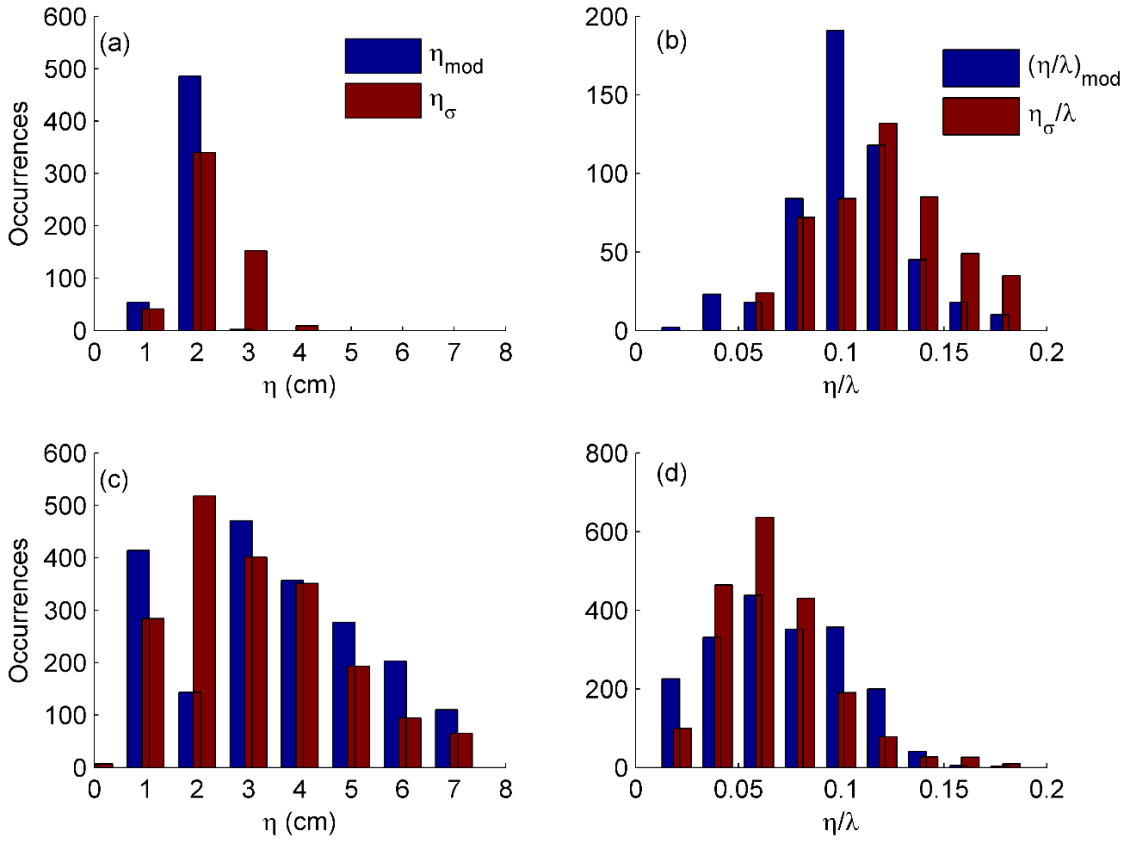

Figure 5.3. Histograms showing the distribution of ripple height (η, a and c) and (b and d) steepness (η/λ) for predictions of the 2-D time dependent model of chapter 4 and estimates from the various measurements of distance to the bed for ADV and ABS systems for Long Bay (a and b) and Georgia (c and d).

The calculation of turbulence can be affected when the ADV are in the wake of the tripod legs. This occurs when the ADV and tripod leg are aligned in the same direction as the current and causes an increased velocity for that sensor. This increases the velocity of that ADV and for the lower ADV results in a larger velocity than the top

ADV. This is counter to the increasing velocity with elevation above the bed present in the constant stress layer. In Figure 5.4, the ratio of the top/bottom ADV mean current speed is plotted as a function of current direction. For GA1, there is tripod leg interference for currents flowing to the south (-180°N). There is also some indication of influence around -40° and 40°N, though to a lesser extent. Any top/bottom ratio <0.9 is considered to be leg interference and the measurement is excluded from the data set. This results in the removal of 10% of the data for GA1. For GA2 tripod leg influences are present around -50°, 75°, and 150°N and applying the same criterion as above removes

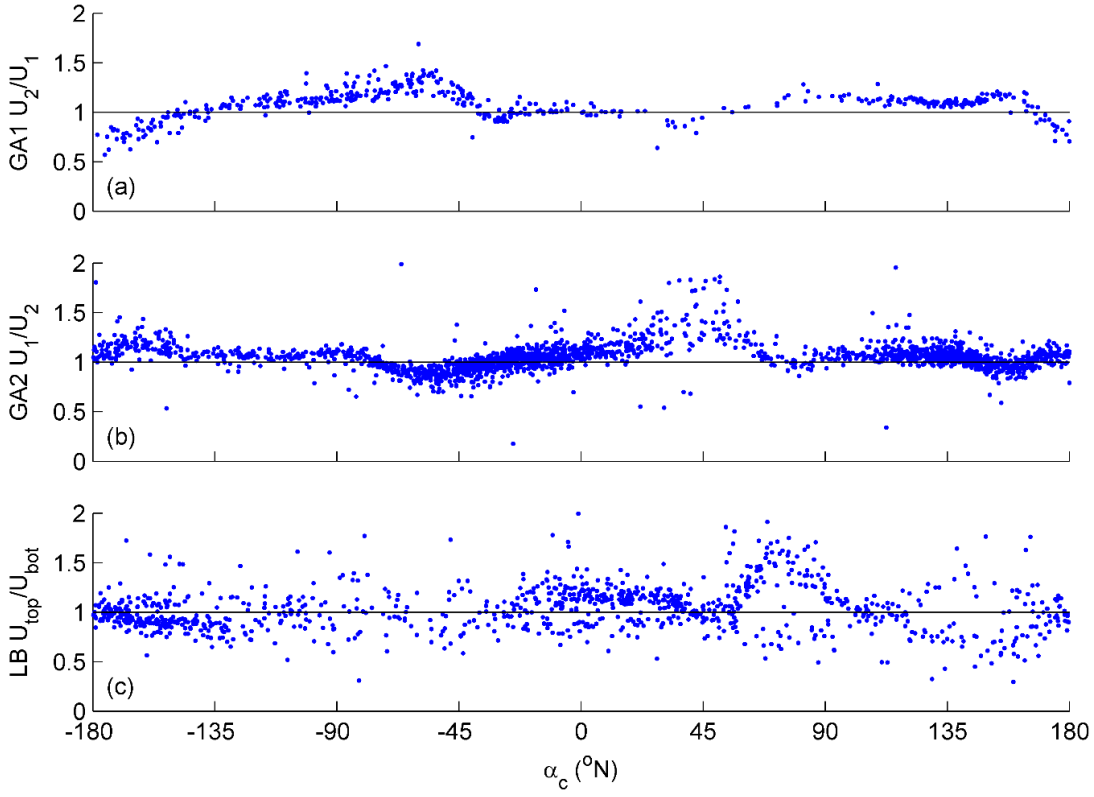

Figure 5.4. Scatter plot of the ratio of the current speed measured at the upper ADV to the speed at the lower ADV plotted as a function of current direction for: (a) GA1; (b) GA2; (c) LB. The solid black line represents (U_{top}/U_{bot}=1).

8.6% of the data. For LB, the instruments sampled at approximately the same elevation. Distance to the bed was recorded and the velocity measurements were arranged such that U_{top} corresponds to the uppermost ADV for a specific burst. Even so, it is likely the measurements have a degree of error so the ratio should vary around 1. Based on this, there is no clear trend as observed for GA1 and GA2, instead periods where the mean flows can be higher on one or the other sensor for the same mean direction are observed. This suggests that most of the data points are contaminated or the signal-to-noise ratio is very weak (given the low mean velocities observed in this site) so that no significant shear stress estimates can be obtained. At this stage, all data were retained for analysis and re-evaluation at a later stage.

5.3.2. Shear Stress

The two data sets described above were subsequently used to calculate the shear velocity using the EC method and the ID method. Using the EC methods lead to 5 separate estimates of shear velocity using equations (5.2)-(5.4) for each ADV1 and ADV2; and the ID method leads to two estimates utilizing the two ADV sensors.

5.3.2.1. EC Shear Velocities

The shear velocity (u_{*EC}) was calculated using the two EC methods (differencing and filtering) and for all possible sensor combinations and the results are shown in Figure 5.5. The shear velocity follows a tidal variability for the Georgia and Long Bay deployments. Periods of higher u_{*EC} correspond to storm events associated with wind induced flows that coincide with large $u_{b,1/3}$ values (Figures 5.1 and 5.2). For Long Bay, the larger u_{*EC} between days 55-60 is associated with strong currents due to wind induced flows. Compared to LB, the u_{*EC} estimates for GA were much larger with maximums of

~3 cm/s while the u_{*EC} for LB attained a maximum of 1.5 cm/s. The main difference between the two field sites is that GA experienced stronger tidal flows by a factor of ~10 compared to LB, while LB was subjected to more energetic waves due to its shallower location.

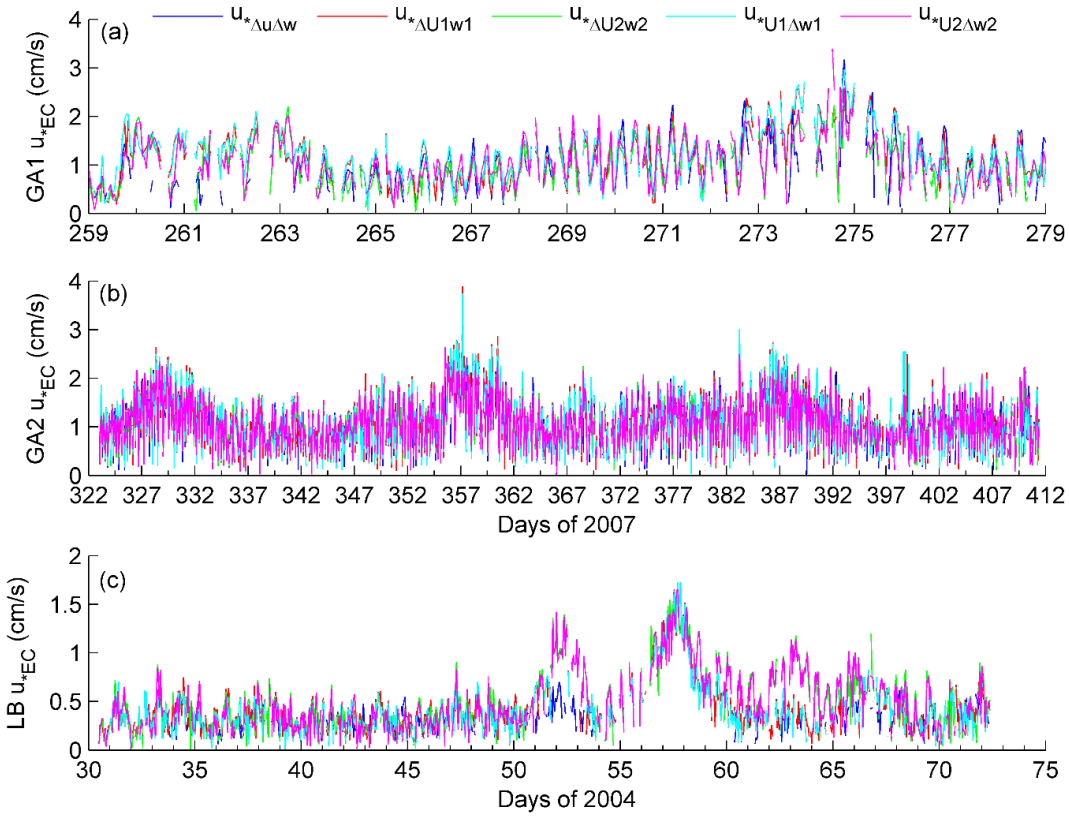

Figure 5.5. Time series plots of shear velocity (u_*) attained from the EC methods described in equations (5.2)-(5.4) for (a) GA1; (b) GA2; (c) LB.

For comparison purposes, the various u_{*EC} values shown as a time series in Figure 5.5 are plotted against each other in Figures 5.6 and 5.7. For the majority of time, the various estimates agree with each other. The greatest differences occur during strong wave conditions (see Figure 5.5). Among the various methods, the differencing methods of *Trowbridge* [1998] failed most often as it produced positive Reynolds fluxes ($<u'w'>$

> 0) , see missing data in Figure 5.5) and when valid fluxes were estimated this method yielded smaller values than the other methods (equations (5.3)-(5.4)), suggesting some bias possible due to failure of the technique to fully remove wave contamination.

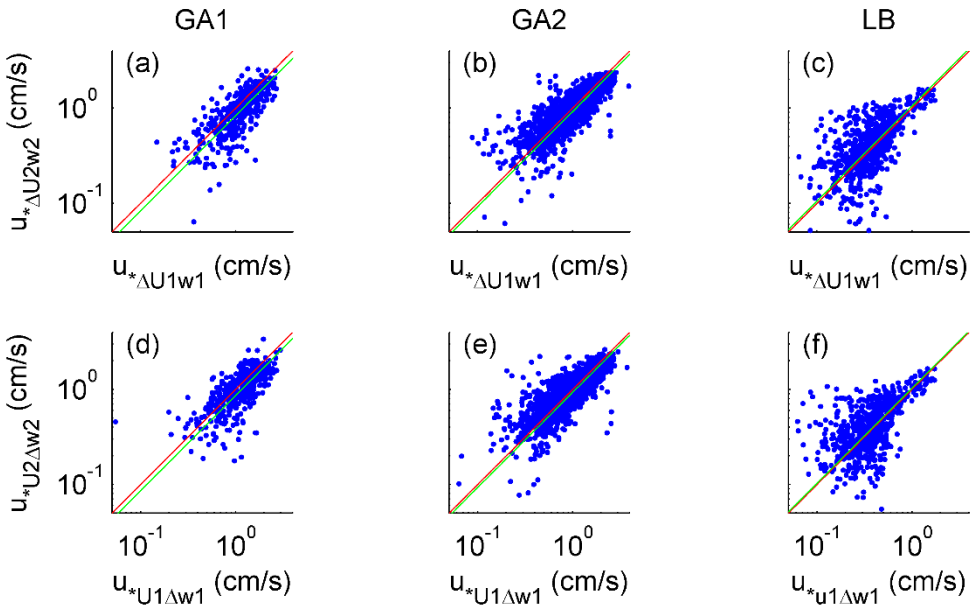

Figure 5.6. Scatter plot of u_* for GA1 (a,d), GA2 (b,e) and LB (c,f) calculated by equation (5.3) (top row) and equation (5.4) (bottom row) for the velocity measurements of ADV1 (x-axis) and ADV2 (y-axis). The solid red line indicates unity and the green line is a best fit through zero.

The least square filtering technique for the removal of the coherent signal between the two sensors (i.e., waves) can be applied either on the horizontal (equation (5.3)) or the vertical (equation (5.4)) velocity component for each sensor allowing for a total of 4 (not independent though since the same signal is used in all of them) estimates of shear velocity. The agreement between the filtered estimates using the two different sensors is shown in the form of scatter diagram in Figure 5.6 for GA1, GA2, and LB. Overall the

estimates from the different combinations (equations (5.3) and (5.4)) seem to agree and do not show any statistically significant differences. When the calculations of u_{*EC} from

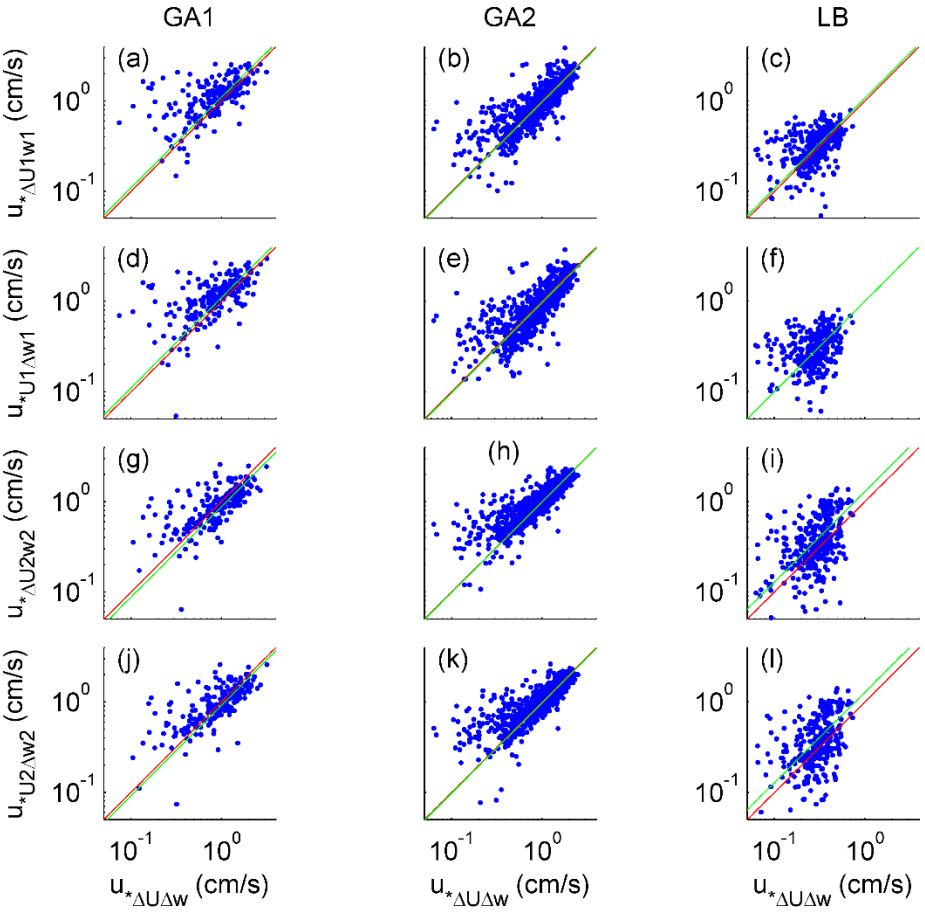

Figure 5.7. Scatter plot of u_* for GA1 (a, d, g and j), GA2 (b, e, h, and k) and LB (c, f, i, l) with the u_* calculated by equation (5.3) and equation (5.4) (y-axis) plotted aginst the u_* from equation (5.2) (x-axis) for the velocity measurements of ADV1 (top 2 rows) and ADV2 (bottom two rows). The solid red line indicates unity and the green line is a best fit through zero.

equations (5.3) and (5.4) are compared to that of the differencing method (equation (5.2), Figure 5.7), a slight deviation from the 1:1 line is observed. For the Georgia cases, $u_{*\Delta U\Delta w}$ is larger than the wave filtered u_* (equations (5.3)-(5.4)) for small values (~<0.5-1.0

cm/s) and smaller for larger shear velocities for ADV2. For ADV1, the $u_{*\Delta U \Delta w}$ usually results in smaller values for GA1 while the trend becomes less evident for GA2. For LB measurements from ADV1, the two methods tend to agree, while for ADV2, the wave-filtered results yield larger values for larger u_{*EC}

Despite the small differences, the standard deviation among the methods only results in an average of 0.17, 0.12, and 0.07 cm/s for GA1, GA2, and LB, respectively. These values are significantly less than the mean u_{*EC} of 1.09, 1.06, and 0.4 cm/s for GA1, GA2, and LB, respectively. In order to determine the error associated with the various methods, the error of the covariance was taken as:

$$\varepsilon_{EC} = \frac{1}{N_{df}}\left(\frac{C_{uu}C_{ww}}{C_{uw}}\right) \quad 5.11$$

where C_{uu} and C_{ww} are the variances of the downstream and vertical velocity, respectively and C_{uw} is the covariance between the two velocity components. The values used for u and w are the corresponding values (filtered or not) used for the estimation of the Reynolds flux depending on the method used (i.e., equations (5.2), (5.3), or (5.4)). The number of degrees of freedom (N_{df}) is calculated as:

$$N_{df} = \frac{|U|n}{zf} \quad 5.12$$

where n is the number of samples per burst and f is the sampling frequency. This is a measure of the number of unique eddies that are expected to pass by the sensor given the mean downstream speed. For GA1 this leads to a median N_{df} of 164 (burst values ranging from 16 to 459) while for GA2 the median N_{df} is 242 (range from 16 to 626); for LB, the weaker current speed results in a median N_{df} of 69 with a range of 2 to 450 eddies per burst.

Histograms of the number of occurrences for the error values ($\varepsilon_{EC,}$) calculated by each method and site are shown in Figure 5.8 with the error values in percentage. For GA1 and GA2 a larger percentage of the data has ε_{EC} values less than 75% while the errors are much greater for LB, likely a result of weak currents resulting in a smaller signal-to-noise ratio or tripod induced wake not readily apparent in Figure 5.4. In order to reduce the uncertainty in the shear velocity calculations and since the prediction of each method was in close agreement with each other, only data from each method with an error $\varepsilon_{EC} \leq 50\%$ are used and the resulting predictions from each method are subsequently averaged together. This hybrid u_{*EC} reduces the time series to 69%, 83%, and 28% of the original measurement points.

5.3.2.2. ID Shear Velocities

While the EC method estimates u_{*EC} from turbulence production, the ID method estimates u_{*ID} from dissipation of turbulence. The vertical velocity spectra (E_{ww}) normalized by the total energy is plotted as a function of frequency, f, for each burst in Figure 5.9. A noise level was present for many of the GA spectra during low energy conditions while a noise level was prevalent for nearly all LB spectra. The noise floor was not constant and varied in energy and frequency between bursts and sensors. The noise floor for each spectra was identified manually and the energy subsequently removed from the spectra ($E_{ww}(f)$-noise) prior to the calculation of u_{*ID}. Characteristic of the turbulence dissipation in the inertial subrange is the -5/3 slope in the spectra. The subrange was identified for wavenumbers $k_u > 2\pi 1.8/(\kappa z)$ with an upper limit arbitrarily defined as 10 times this value. The theoretical upper limit of $k_u < 0.55(\nu^3/\epsilon)^{1/4}$ [*Tennekes and Lumley*, 1989] was larger than the wavenumber at which the noise floor

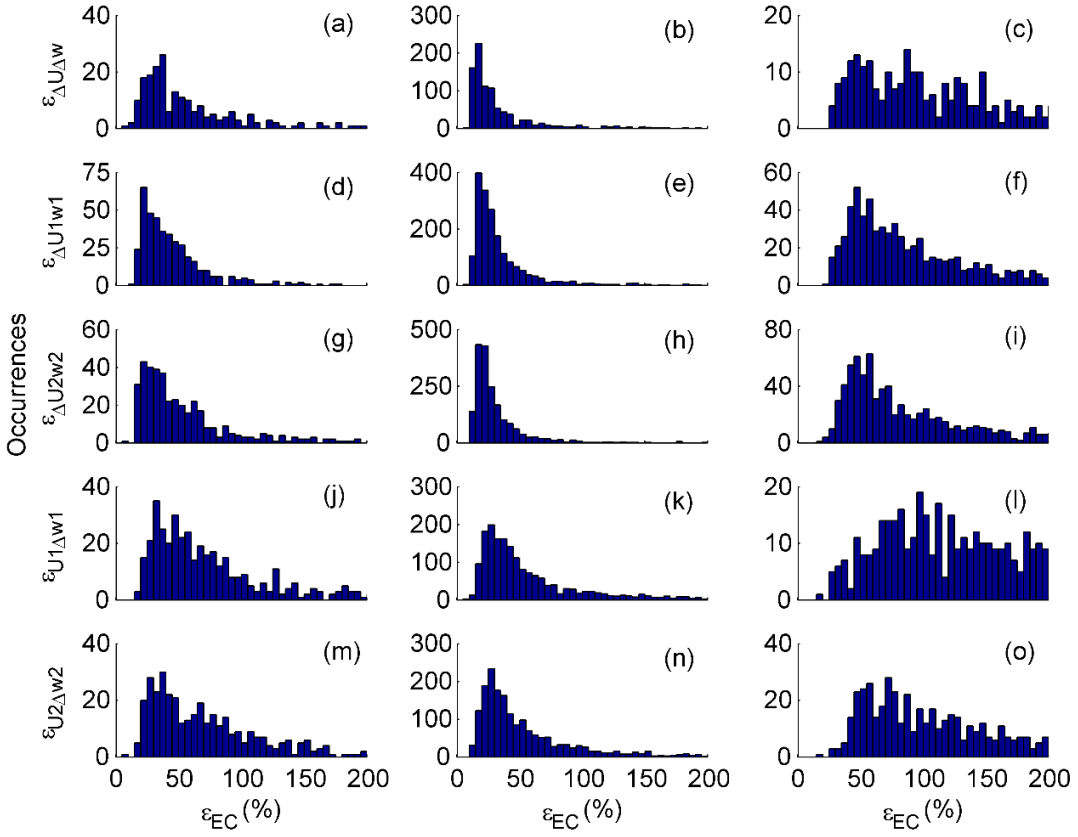

Figure 5.8. Histograms of the standard error of covariance for each EC method for GA1 (first column), GA2 (second column), and LB (third column). The top row (a-c) is the error for $<\Delta U \Delta w>$, the second row (d-f) is for $\Delta u_1 w_1$ ADV1, the third row (g-i) is for $\Delta u_2 w_2$ ADV2, the fourth row (j-l) is for $u_1 \Delta w_{f1}$ ADV1, and the fifth row (m-o) is for $u_2 \Delta w_2$.

occurred. The slope of $E_{ww}(f)$ corresponding to the subrange for each spectra is plotted against time in Figure 5.10. The slope varies around the theoretical value (black line) for all sites but more variation is observed for LB. The difference between the calculated and theoretical slope (ε_{slp}=[*slope*-(-5/3)]/(-5/3)) results in average differences of 3.9 and -0.16% for GA1 ADV1 and ADV2, respectively. Larger values were found for GA2 of 5.9 and 14.3%. For LB, the average error was consistent for each sensor at 5.4 and 5.1%. Deviations in slope greater than ~1/3 correspond to either poorly defined subranges due to either low energy conditions where the noise floor contaminated high frequencies, high

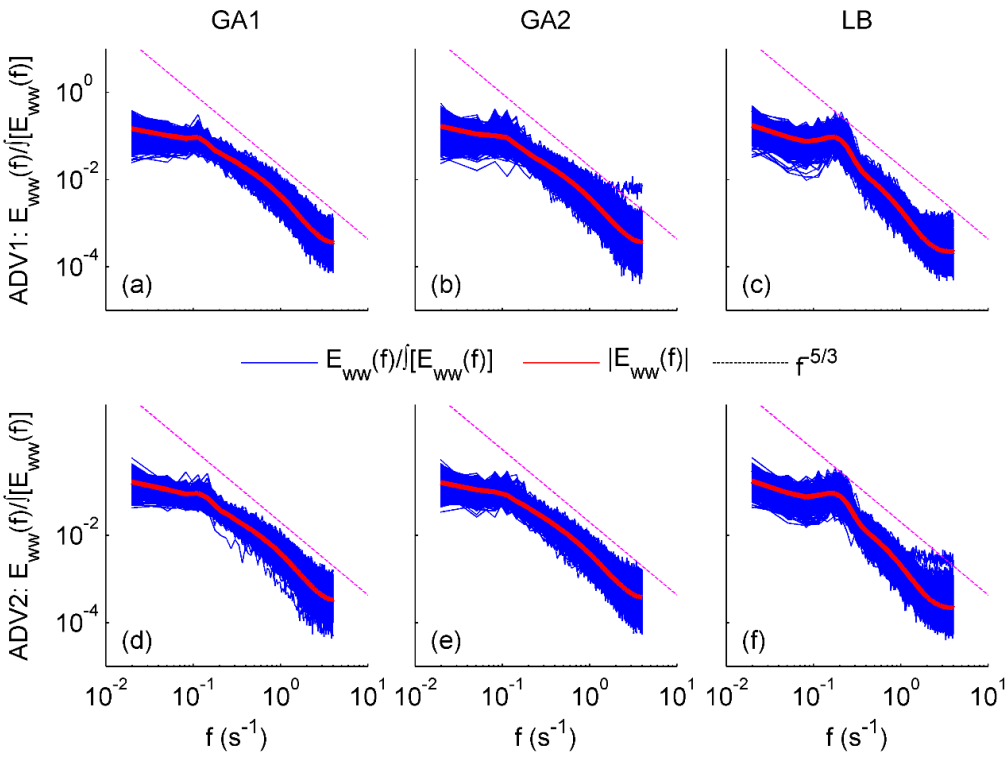

Figure 5.9. Plots of normalized by the total energy turbulence spectra (E_{ww}) as a function of frequency (f) for GA1 (a, d), GA2 (b, e), and LB (c, f) calculated for ADV1 (a-c) and ADV2 (d-f). The blue lines are the individual spectra while the red line is the average of all sepectra. The theoretical -5/3 slope is shown as the dashed magenta line.

wave energy conditions where low frequencies are contaminated, or tripod interference. As these values are erroneous, estimates with a slope greater than -4/3 and less than -6/3 were removed from the data set.

The calculated u_{*ID} for ADV1 and ADV2 are plotted against each other in Figure 5.11 although some significant scatter is present. For GA1 (Figure 5.11a), the scatter is larger and a linear regression fit through zero revealed a slope of s=0.79 with a correlation r= 0.39 between the two ADV sensors. For GA2 (Figure 5.11b), the scatter is reduced (r=0.68), however ADV1 yields smaller u_{*ID1} values similarly to Figure 5.11a as

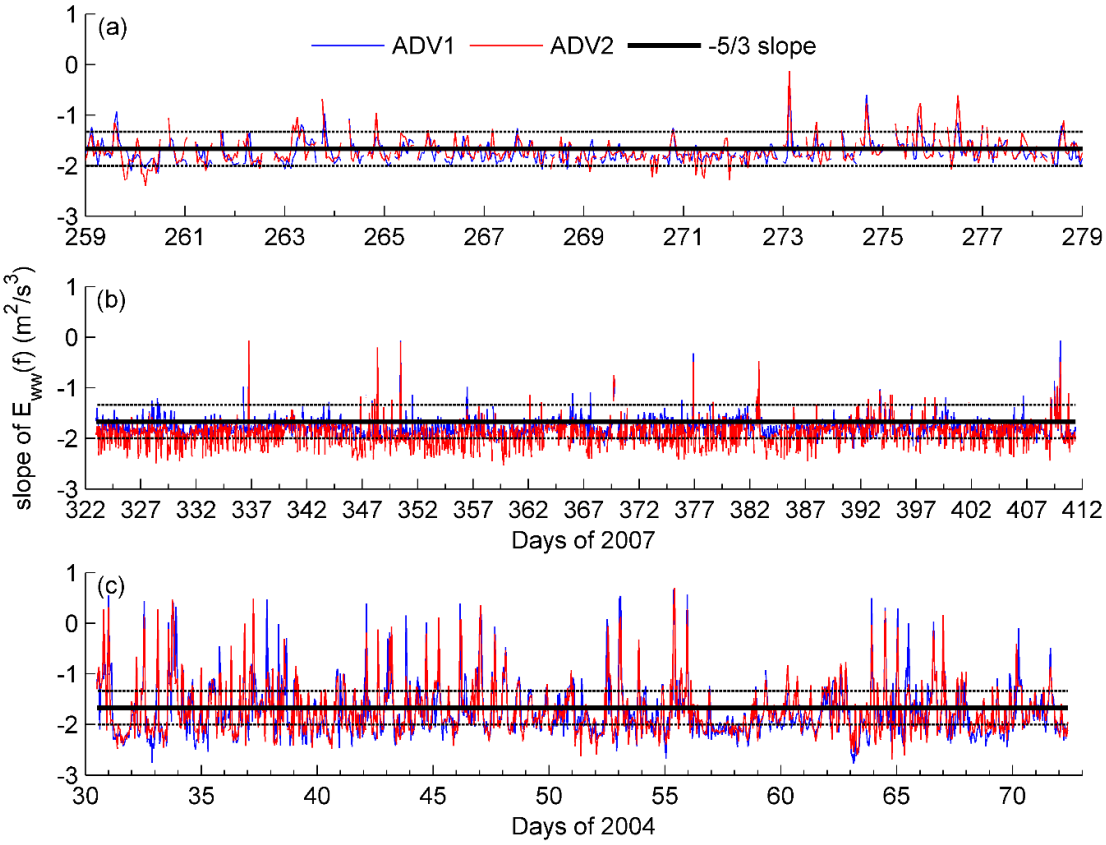

Figure 5.10. Time series of the inertial subrange slope identified from the wavenumber spectra ($E_{ww}(k_u)$) of the vertical velocity component defind as the range $20\pi 1.8/(\kappa z) > k_u > 2\pi 1.8/(\kappa z)$ for (a) GA1, (b) GA2, and (c) LB. The blue and red lines are the calculated slope from spectra derived from sensors ADV1 and ADV2, respectively, the solid black line indicates the theoretical -5/3 slope while the dashed black lines indicate slopes of (-5±1)/3.

the best-fit line has a similar slope of s=0.73). For LB, the data exhibit less scatter between the two ADV and the best-fit line through zero has a slope of 1.05 with a correlation r= 0.79. It should also be noted that the u_{*ID} for LB are much smaller than GA. Though at these smaller values u_{*ID} yields similar agreement and scatter for GA1 and GA2.

The calculated u_{*ID} for each site are plotted as a function of time in Figure 5.12. The large scatter between the two ADV for GA1 (Figure 5.11a) is evident (Figure 5.12a)

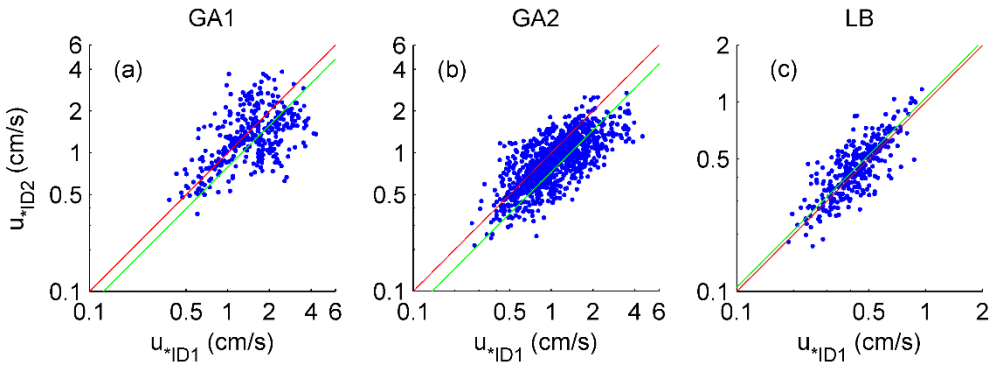

Figure 5.11. Scatter plots of the calculated shear velocity (u_*) using the inertial dissipation method for: (a) GA1, (b) GA2, and (c) LB. The calculated u_* for ADV1 is on the *x*-axis while that of ADV2 is on the y-axis. The solid red line indicates unity and the green line is a best fit through zero.

in the two u_{*ID} being nearly out of phase between days 259.5-265 and 272-278, something not present with u_{*EC}. The u_{*ID} for GA2 (Figure 5.12b) are more often in phase; however ADV1 yields significantly larger values. For LB (Figure 5.12c) there is improved agreement between the two ADV. One possibility for the larger disagreement between ADV1 and ADV2, despite the velocity differences is the uncertainty in the instantaneous value of *z* for each ADV. However even if one sensor is above the crest and another above the trough of an 8 cm high ripple, the difference would only be ~0.2 cm/s for the average GA conditions; not enough to explain the large deviations observed. Based on the large scatter and disagreement between the u_{*ID} for GA it appears that these estimates are less reliable than u_{*EC}.

5.3.2.3. EC vs. ID

A comparison between the EC and ID methods is shown in Figure 5.13. For GA1 (Figure 5.13a and d), the u_{*ID} result in increasingly larger values of u_{*ID} for increasing u_{*EC} (ADV1: s=1.3, r= 0.64; ADV2: s=1.1, r= 0.69). The same is also present for GA2

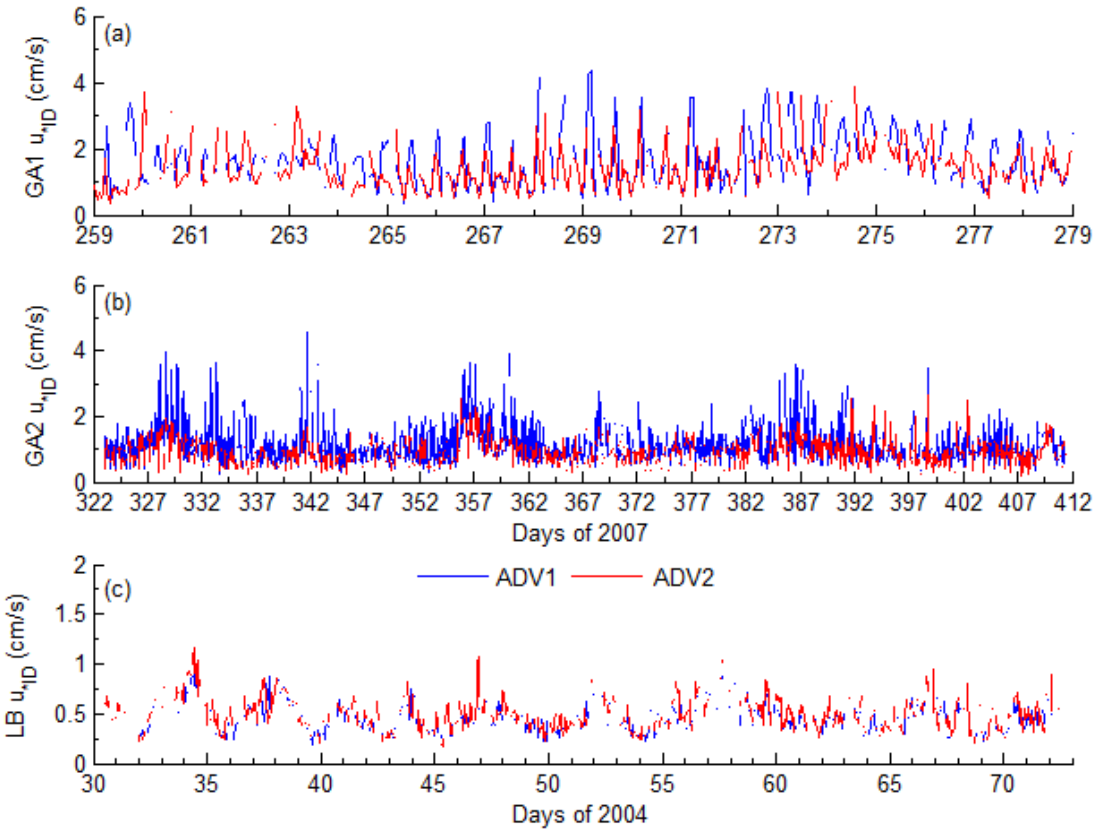

Figure 5.12. Time series of u_{*ID} calculations for: (a) GA1, (b) GA2, and (c) LB where the blue and red lines are the cacluations using ADV1 and ADV2, respectively.

ADV1 (Figure 5.13b, s=1.0, r= 0.70); however $u_{*ID}<u_{*EC}$ for increasing u_* for ADV2 (Figure 5.13e, s=0.80, r= 0.84). LB shows good agreement for small values (u_{*EC} < 0.6) while u_{*ID} results in smaller values for increasing u_{*EC} (Figures 5.13c and f, ADV1: s=0.72, r= 0.76, ADV2: s=0.82, r= 0.76). Deviations, for the GA estimate, begin to diverge around 3 cm/s and are removed from the data set.

Sherwood et al. [2006] found that when stratification is present in the boundary layer, the ID estimates are biased. They calculated the Monin-Obukov stability parameter (ζ) as:

$$\frac{u_{*ID}^3}{u_{*EC}^3} = 1 + (\beta - 1)\zeta \qquad 5.13$$

where β is a constant (4.7±0.5, [*Businger et al.*, 1971]) and a ζ>1 indicates stratified flows. For the reduced data set using the average of u_{*ID1} and u_{*ID2}, the stratification was

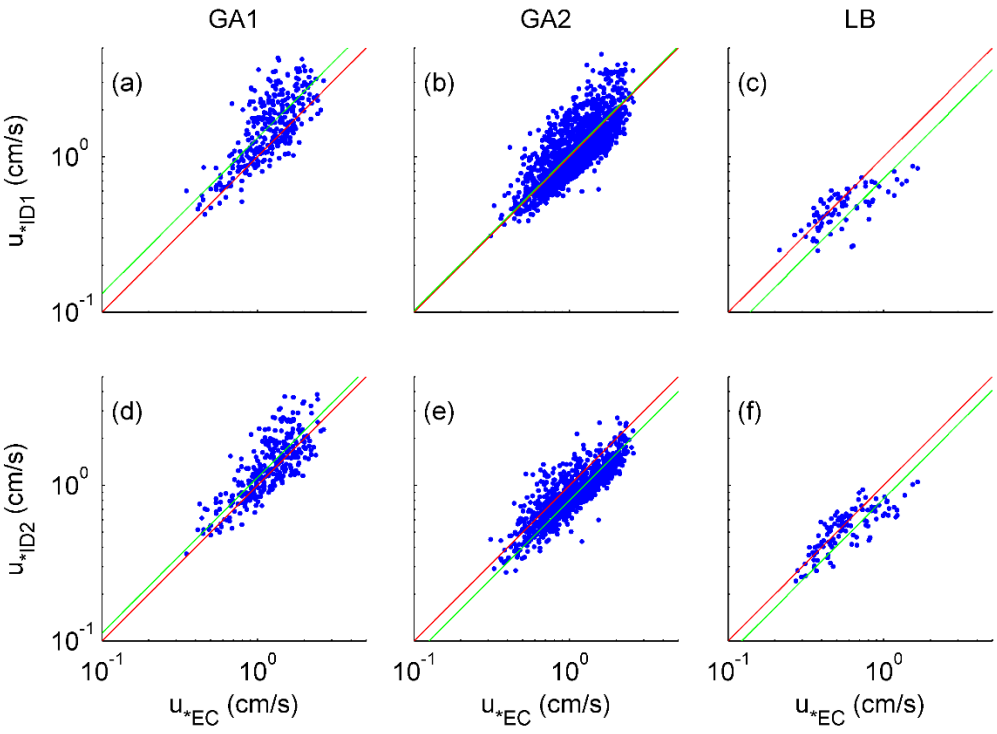

Figure 5.13. Scatter plots of the comparission of u_* calcuated using the ID method (y-axis) vs. the u_* attained trough the EC method (x-axis) for (a,d) GA1, (b,e) GA2, and (c,f) LB where a-c are the cacluations using ADV1 and d-f are from ADV2. The solid red line indicates unity and the green line is a best fit through zero.

weak (Figure 5.14), for most instances. The small median values of 0.14, -0.07, and -0.06 for GA1, GA2, and LB, respectively, indicate that stratification did not play a significant role for these samples.

In theory, production rate should equal dissipation rate, such that:

$$-< u'w' > \frac{dU}{dz} = \epsilon \qquad 5.14$$

or using the above averaged values:

$$u_{*EC}^2 \frac{dU}{dz} = \frac{u_{*ID}^3}{\kappa z} \qquad 5.15$$

where *dU*/*dz* is the difference between the two sensor velocities and elevations. These values are plotted as scatter diagrams in Figure 5.14 (d through e). These show a large degree of scatter but an overall trend of agreement with s=1.6 for GA1 and s=0.8 for GA2. One source of error could be that *z* for each sensor is estimated from the distance to the bed recorded by the ABS system and the difference between the deployed elevation

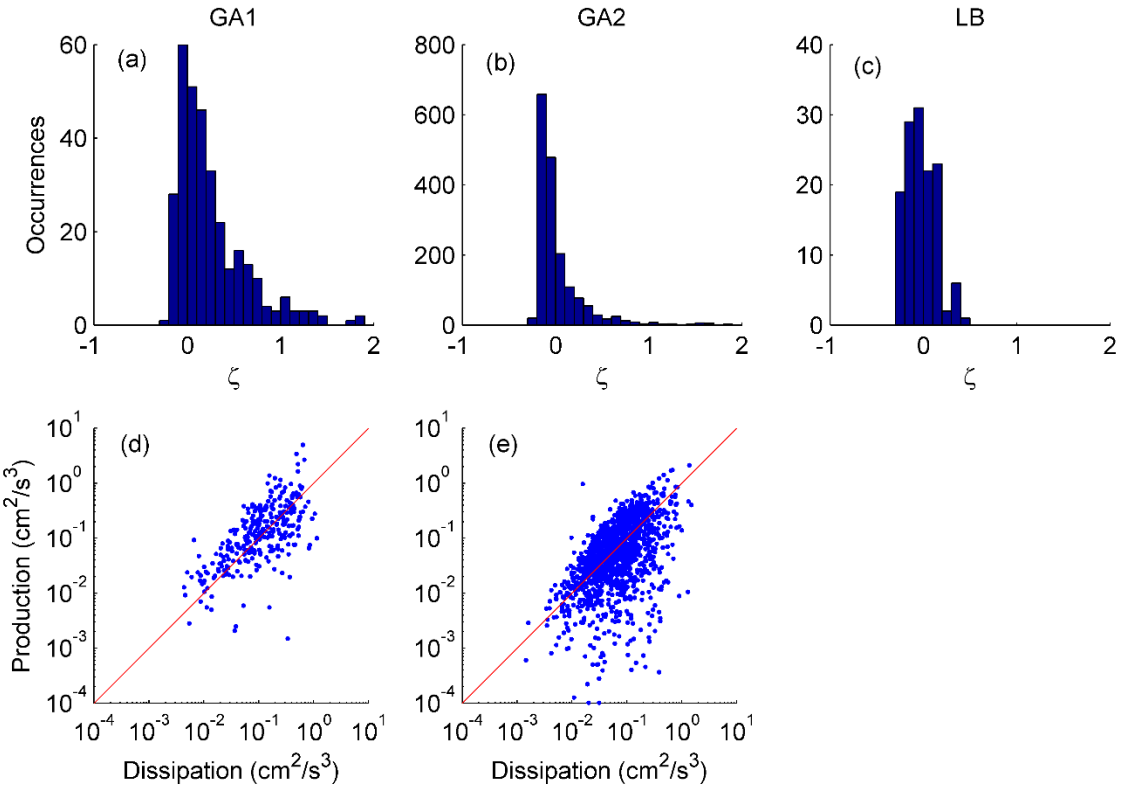

Figure 5.14. Histograms of the stability parameter (ζ top row) and scatter plots for production *vs.* difference with the 1:1 red line shown (bottom row) indicates unity for (a, d) GA1, (b, e) GA2, and (c) LB.

of the ABS and ADV. For LB, dUdz cannot be resolved due to both sensors sampling at nearly the same elevation. Comparisons of u_{*EC} and u_{*ID} do not indicate this degree of difference in the data. While *Sherwood et al.* [2006] found that $u_{*ID} > u_{*EC}$, this is not the case for the site average data sets of GA2 and LB as shown in in Table 5.1. The values are similar and differ only slightly with u_{*EC} greater for GA1 while u_{*EC} is larger for GA2 and LB. Since the u_* estimates yield similar results despite the variations present in production and dissipation, u_{*EC} and u_{*ID} are averaged together.

Table 5.1. Site averaged shear velocities.

Site	$\lvert u_{*EC} \rvert$ (cm/s)	$\lvert u_{*ID} \rvert$ (cm/s)
GA1	1.26	1.48
GA2	1.16	1.10
LB	0.67	0.53

Using equation (5.11), the drag coefficient can be estimated from u_* and the mean velocity U. Since C_{Dz} varies with elevation above the bed, it is common practice to define C_{Dz} at an elevation of 100 cm above the bed. At this elevation, C_{Dz} values of 0.006 are common for a rippled bed, while values around 0.002 are more common over flat sandy beds (without waves present) [*Soulsby*, 1997]. The mean velocity at 100 cm was calculated assuming a law of the wall profile:

$$U(z) = \frac{u_*}{\kappa} \ln\left(\frac{z}{z_o}\right) \qquad 5.16$$

where z_o is the apparent bed roughness and can be calculated by rearranging equation (5.16) as:

$$z_o = z \exp\left[-\frac{U\kappa}{u_*}\right] \qquad 5.17$$

z_o was calculated using the mean current speed U_m and u_*. This value is then used in equation (5.16) with z=100 cm to calculate $U(z$=100 cm) (U_{100}). A scatter plot of the averaged u_*^2 values versus the U_{100}^2 is shown in Figure 5.15. For GA1 and GA2 the u_* estimates are well constrained by C_D=0.002 and 0.02 (best fits of $C_{D,100}$=0.004). Even though LB has the smallest velocities, it has a larger $C_{D,100}$ of 0.005. These values tend to agree with the values expected for a rippled seabed.

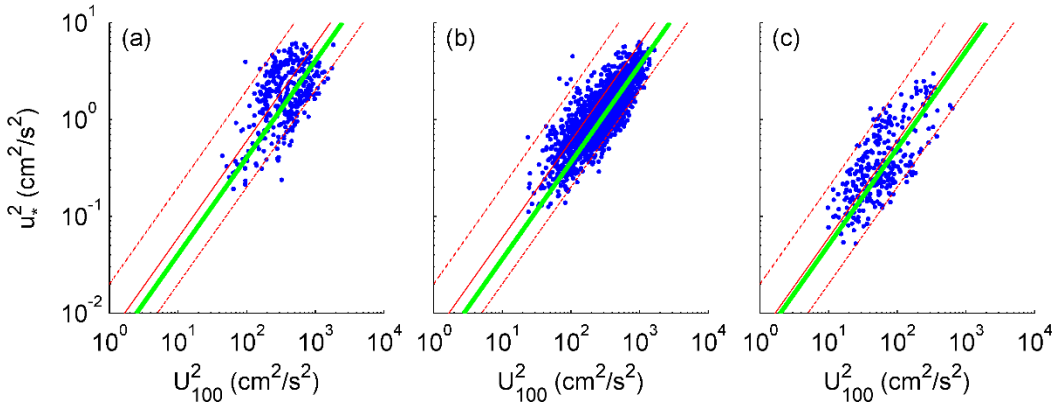

Figure 5.15. Scatter plots of the average u_*^2 vs. mean U_m^2 for: (a) GA1, (b) GA2, (c) LB. The red lines represent C_D values of 0.002, 0.006, and 0.020, while the green line is a best-fit through zero (see text for details).

5.4. Analysis

5.4.1. Effect of Ripples

As seen in Figure 5.15, the drag coefficient exhibits significant variations, which can be attributed to roughness elements in the boundary layer. These roughness elements consist of the bedforms, the grain roughness if the sediment is not in motion, or movable bed roughness if the grains are in motion. Furthermore, the wave boundary layer can

impose an additional roughness experienced by the current. As both sites are wave dominated, the wave boundary layer imposes a significant roughness on the seabed, which might help explain the large C_{D100} in Figure 5.15. Since direct measurements within the wave boundary layer were not performed, in an attempt to isolate the wave boundary layer effect the available u_* values were categorized into bins with similar mean current and wave forcing. The bin limits were defined using the 33rd and 66th percentiles of each velocity (U and $u_{b,1/3}$) separately for GA (Figure 5.16a and 5.16b) and LB (Figure 5.16c and d), respectively. The limits identified are for $u_{b,1/3}$ 9.8 and 14.9 cm/s and U of 13.2 and 18.2 cm/s for GA while for LB the corresponding limits are 13.3, 19.6 and 5.3 and 7.9 for $u_{b,1/3}$ and U, respectively. This yields 1,826 measurements for GA and 85 measurements for LB from which further analysis of the effect of bedforms will be performed. Due to the limited number of samples for LB when subsampled for U and $u_{b,1/3}$, only analyses on all the bulk data is performed. Therefore, majority of the analysis will focus on the GA data set.

In the subsequent sections the characteristics of the ripple geometry on bed roughness (defined as the C_d value) will be evaluated using the following ripple parameters: (1) ripple type; (2) ripple height; (3) wavelength; (4) ripple steepness (η/λ); (5) ripple asymmetry η^2/λ; and (5) orientation relative to the mean current.

5.4.2. Ripple Type

The variation in C_{D100} as a function of ripple type is explored in Figures 5.17 and 5.18. In approximate order of increasing irregularity, ripples have been identified as: (L) linear ripples; (LQL) linear-quasi-linear; (QL) quasi-linear; (BC) bifurcating- and cross-ripples; (C) cross-ripples; and (D) disorganized bed. As a function of ripple type, C_{D100}

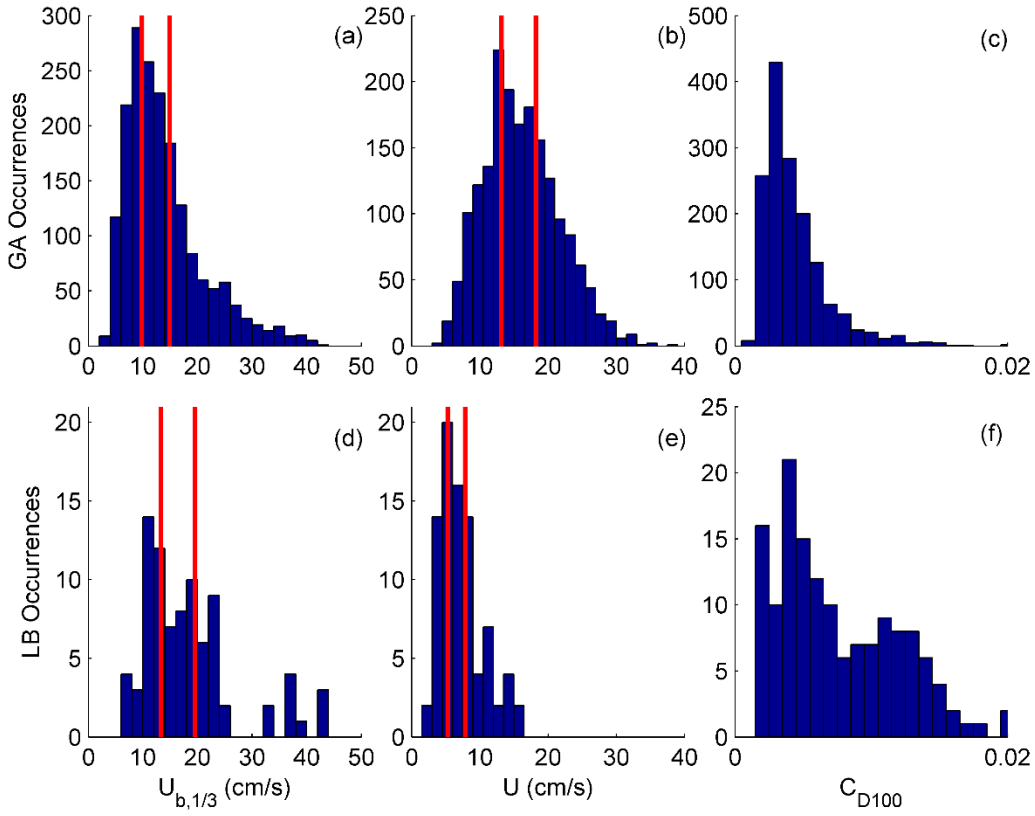

Figure 5.16. Histograms of $u_{b,1/3}$ (left column), U (middle column), and C_{D100} (right column) for GA (top row) and LB (bottom row) for instances where $\varepsilon \leq 50\%$. The vertical red lines indicate the 33 (left) and 66 (right) percentile.

exhibits significant variation for each shape, defined by the error bars equal to 1 standard deviation, for both GA (Figure 5.17a) and Long Bay (Figure 5.17g). Overall, the mean value indicates a decreasing C_{D100} for increasing irregularity for GA. The C_{D100} values for LB exhibit a significant amount of scatter and due to the limited data, does not yield a complete trend. While these represent all wave and current conditions, in Figure 5.18 the data have been segmented in groups of similar mean current speed and wave forcing using the 33 and 66 percentile divisions shown in Figure (5.16) for GA. For large U, there is a small decrease in C_{D100} with increasingly irregular ripple types based on the

mean values, though the scatter is larger than this deviation. This trend becomes less apparent for smaller U and larger $u_{b,1/3}$ where the C_{D100} remains nearly constant.

5.4.3. Ripple Height

While the shape might not yield any definitive relation to the drag coefficient, the height and wavelength might be more representative of the roughness experienced. The drag coefficient is plotted against, η for all $u_{b,1/3}$ and U combination for GA in Figure 5.17b and LB in Figure 5.17h. There is an increasing trend in the mean C_{D100} value for GA and LB with increasing η, though large scatter exists. When grouping the data by $u_{b,1/3}$ and U (Figure 5.19) and plotting for each ripple type, the trend becomes less dominant but still apparent for U<18.2 cm/s. At larger $u_{b,1/3}$ values, the trend becomes less significant with no trend observed for weak U and strong $u_{b,1/3}$. The various ripple types, plotted as different colored lines do not exhibit any clearly deviating trends.

5.4.4. Wavelength

The drag coefficient is plotted as a function of the ripple wavelength in Figure 5.17c and 5.17i for GA and LB, respectively. As with the other cases, a large degree of scatter exists but a generally increasing C_{D100} is seen for increasing λ in the GA data set. This is also present when the data is grouped by $u_{b,1/3}$, U, and ripple type in Figure 5.20 with a larger increase in C_{D100} present for larger current velocities and weaker waves. As ripple height varies for a specific wavelength, it is likely that a better roughness is defined by either η or η/λ.

5.4.5. Steepness

For ripple steepness (η/λ), the variation of C_{D100} is plotted in Figure 5.17d and 5.17j for GA and LB, respectively. Though a high degree of scatter exists, there is an

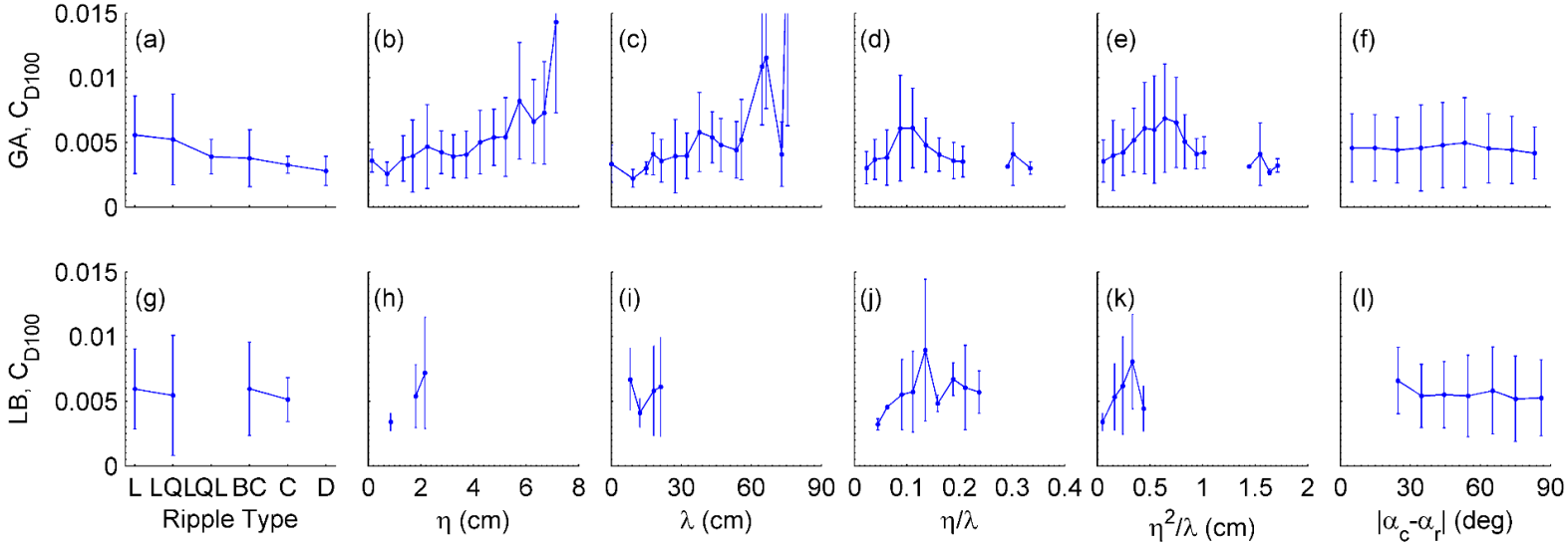

Figure 5.17. Scatter plots of bin averaged (C_{D100}) for GA (top row) and LB (bottom row) plotted as a function of (a, g) ripple type (KEY: L – Linear Ripples; LQL – Linear-Quasi-Linear Ripples; QL – Quasi Linear Ripples; BC – Bifurcating-Cross-Ripples; C – cross-ripples; D – Disorganized Bed); (b, h) ripple height; (c, i) ripple wavelength; (d, j) ripple steepness (η/λ); (e, k) η^2/λ; (f, j) orientation between ripple crests and current direction (perpendicular at 90°). The error bars represent 1 standard deviation

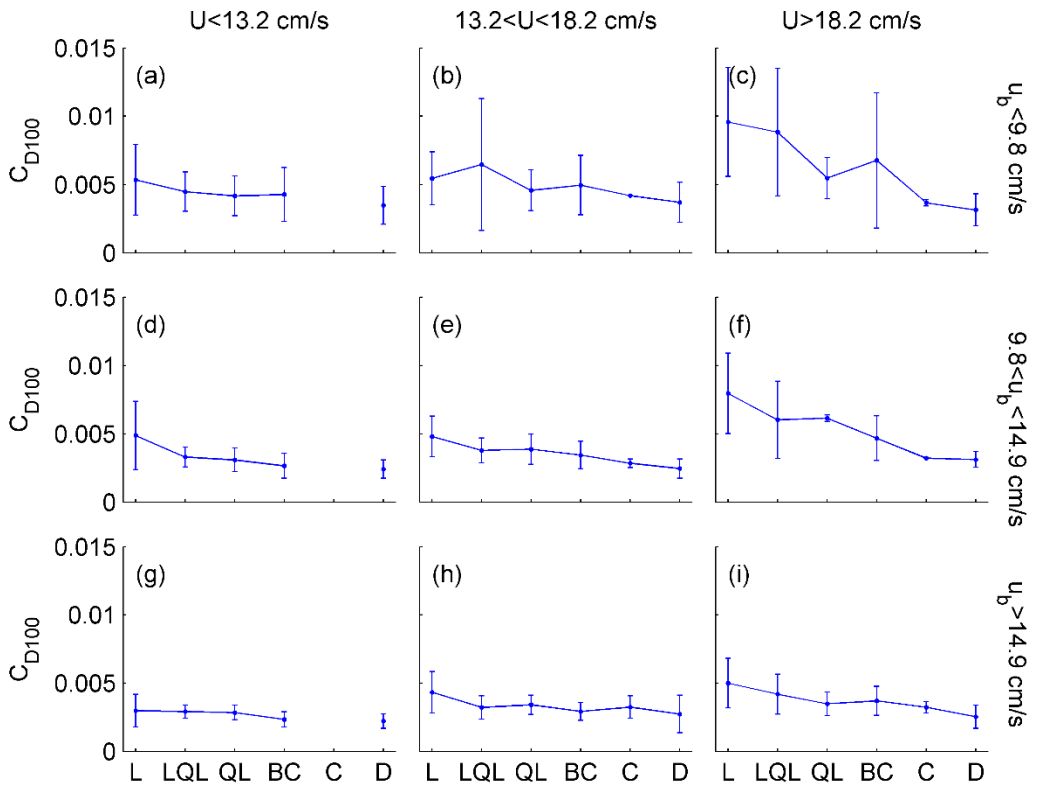

Figure 5.18. Scatter plots of bin averaged C_{D100} for GA plotted as a function of ripple type (KEY: L – Linear Ripples; LQL – Linear-Quasi-Linear Ripples; QL – Quasi Linear Ripples; BC – Bifurcating-Cross-Ripples; C – cross-ripples; D – Disorganized Bed) for various hydrodynamic conditions of $u_{b,1/3}$ (increasing from top row to bottom row) and U (increasing from left column to right column). The error bars indicate 1 standard deviation.

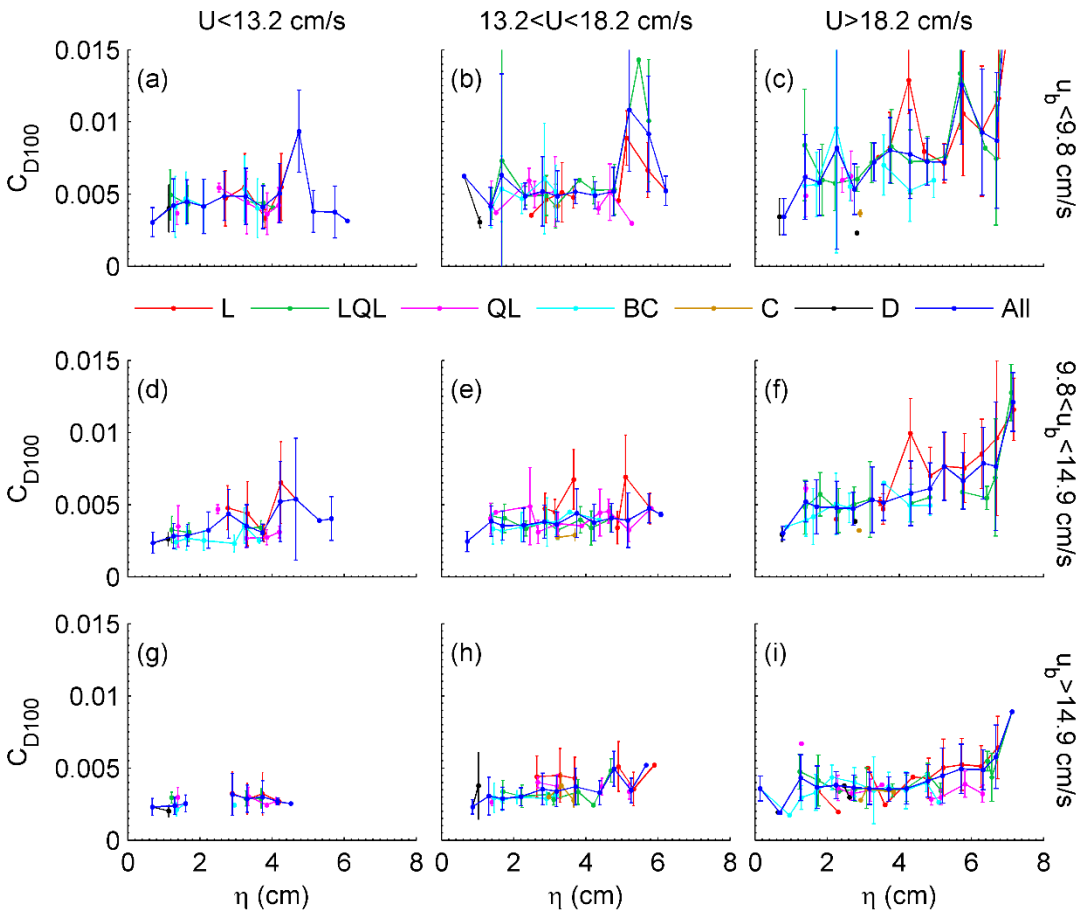

Figure 5.19. Scatter plots of bin averaged C_{D100} for GA plotted as a function of ripple height (η) for various ripple types (KEY: L – Linear Ripples; LQL – Linear-Quasi-Linear Ripples; QL – Quasi Linear Ripples; BC – Bifurcating-Cross-Ripples; C – cross-ripples; D – Disorganized Bed). The data in the individual plots correspond to various hydrodynamic conditions of $u_{b,1/3}$ (increasing from top row to bottom row) and U (increasing from left column to right column). The error bars indicate 1 standard deviation.

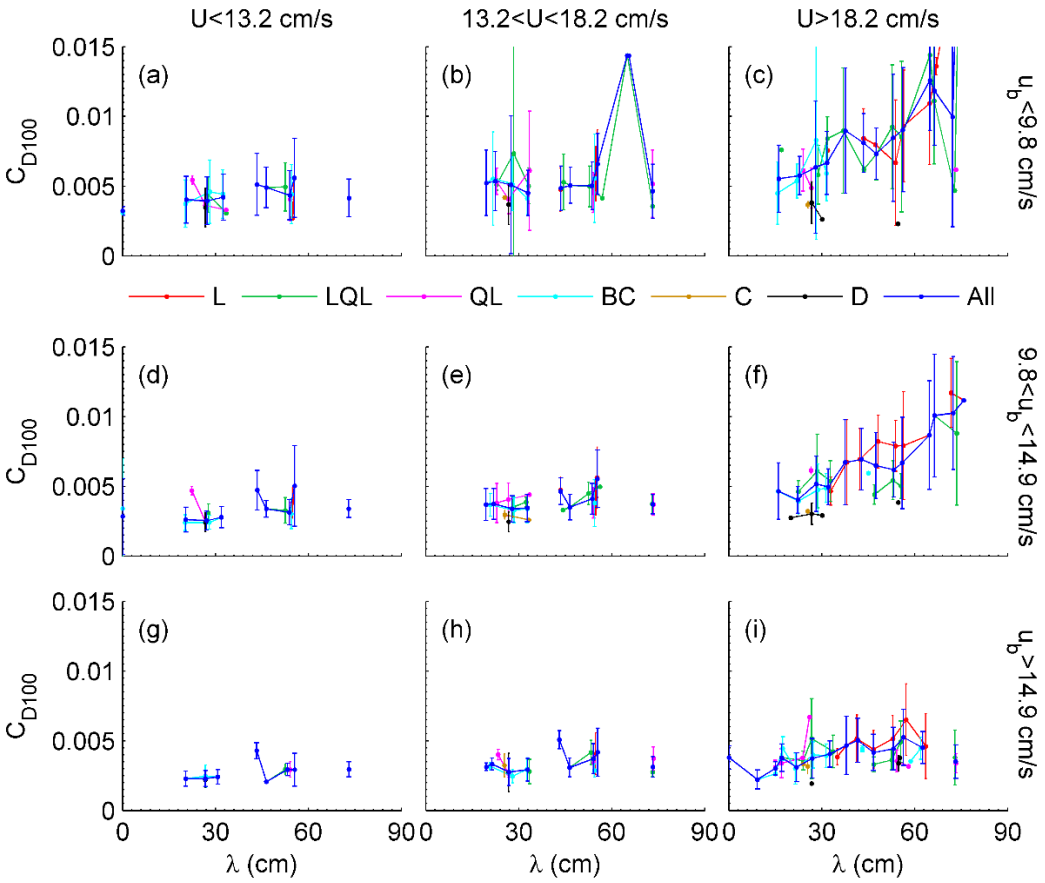

Figure 5.20. Scatter plots of bin averaged C_{D100} for GA plotted as a function of ripple wavelength (λ) for various ripple types (KEY: L – Linear Ripples; LQL – Linear-Quasi-Linear Ripples; QL – Quasi Linear Ripples; BC – Bifurcating-Cross-Ripples; C – cross-ripples; D – Disorganized Bed). The data in the individual plots correspond to various hydrodynamic conditions of $u_{b,1/3}$ (increasing from top row to bottom row) and U (increasing from left column to right column). The error bars indicate 1 standard deviation.

increase in mean roughness up to η/λ =0.1, followed by a decrease. Vortexes are assumed to form on the lee side of ripples beginning at a η/λ of 0.1, though the subsequent decrease cannot be explained. The trend is still apparent but does not become any better defined for various ripple types, $u_{b,1/3}$, or U in Figure 5.21.

5.4.6. Asymmetry

A similar pattern is observed for η^2/λ in Figure 5.17e and 5.17k for GA and LB, respectively, and the binned data in Figure 5.22. There is a large degree of scatter present with the data, despite an increasing mean value of $\eta^2/\lambda<0.7$. As with the other ripple geometry parameters, there is no unique trend observed between the different ripple types.

5.4.7. Ripple Orientation

In addition to ripple size and shape, the orientation of the ripple crest in relation to the mean current direction has been found to influence the roughness experienced by the flow [*Drake*, 1992; *Powel et al.*, 2000; *Madsen et al.*, 2010]. These studies found that the roughness was greatest when the ripple crest and current were perpendicular to one another. In the present convention, this is $|\alpha_c-\alpha_r|=90°$. However, as with the above cases, there is significant scatter observed for GA (Figure 5.17f) with no differentiation observed for various ripple types (Figure 5.23).

5.5. Summary and Conclusions

Field data from two experiments were used to evaluate the dependence of bedforms on the roughness experienced by the mean current. This was accomplished by calculating the shear velocity through the eddy correlation and inertial dissipation methods. These two methods, which in theory should agree, yielded varying results as a whole. For the EC method, many of the bursts had a poor covariance between the horizontal and vertical velocity while the spectra were often contaminated at low wavenumbers (k_u) for the LB and GA2-ADV2 data sets leading to erroneous u_*. When

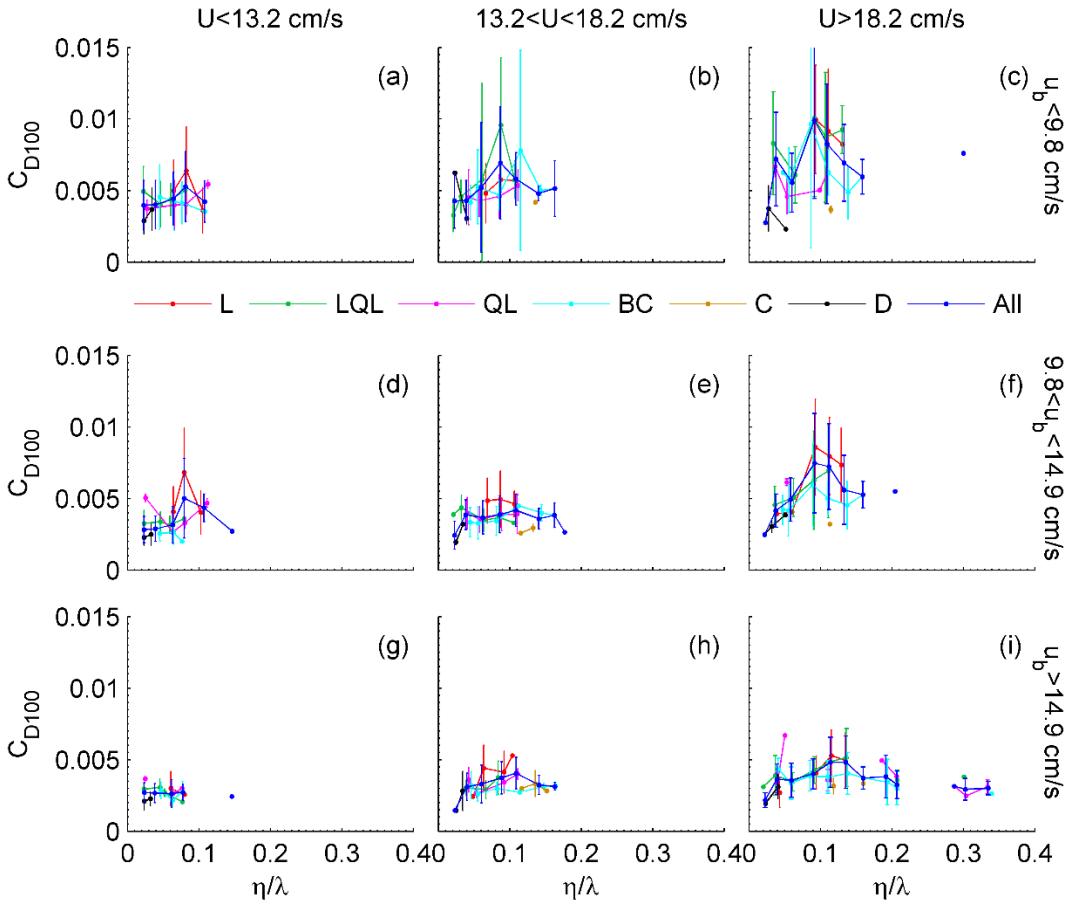

Figure 5.21. Scatter plots of bin averaged C_{D100} for GA plotted as a function of ripple steepness (η/λ) for various ripple types (KEY: L – Linear Ripples; LQL – Linear-Quasi-Linear Ripples; QL – Quasi Linear Ripples; BC – Bifurcating-Cross-Ripples; C – cross-ripples; D – Disorganized Bed). The data in the individual plots correspond to various hydrodynamic conditions of $u_{b,1/3}$ (increasing from top row to bottom row) and U (increasing from left column to right column). The error bars indicate 1 standard deviation.

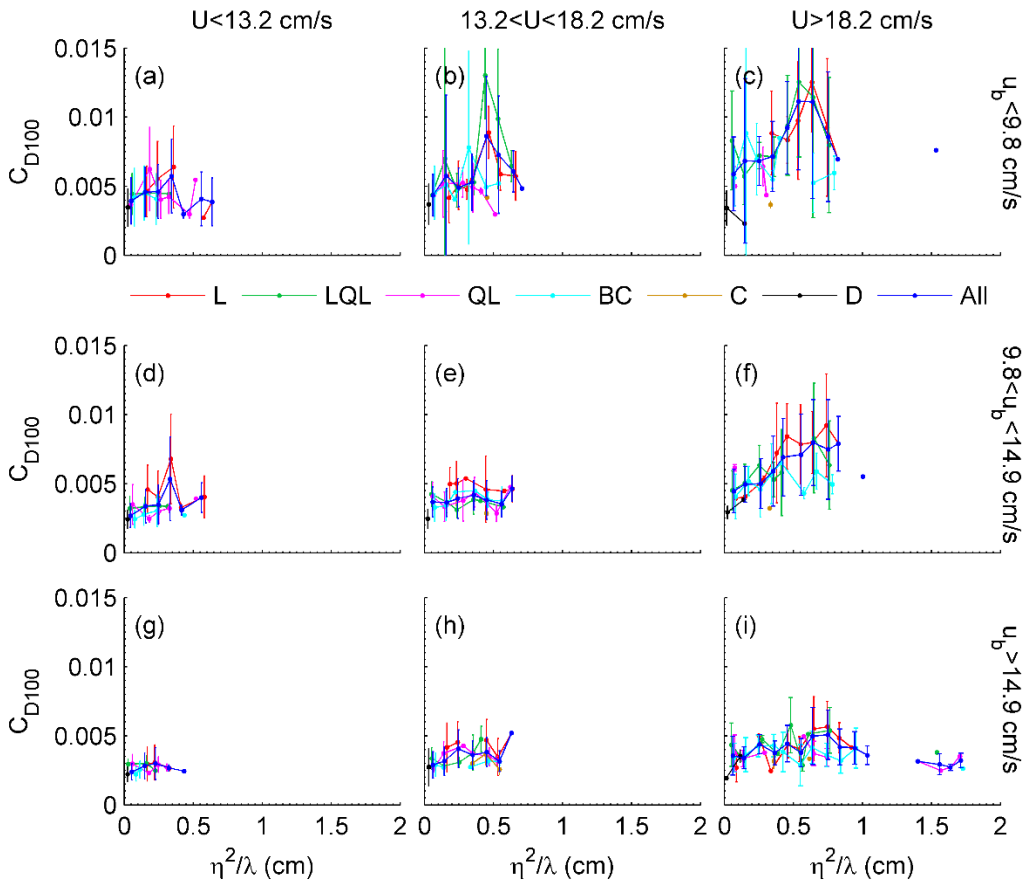

Figure 5.22. Scatter plots of bin averaged C_{D100} for GA plotted as a function of (η^2/λ) for various ripple types (KEY: L – Linear Ripples; LQL – Linear-Quasi-Linear Ripples; QL – Quasi Linear Ripples; BC – Bifurcating-Cross-Ripples; C – cross-ripples; D – Disorganized Bed). The data in the individual plots correspond to various hydrodynamic conditions of $u_{b,1/3}$ (increasing from top row to bottom row) and U (increasing from left column to right column). The error bars indicate 1 standard deviation.

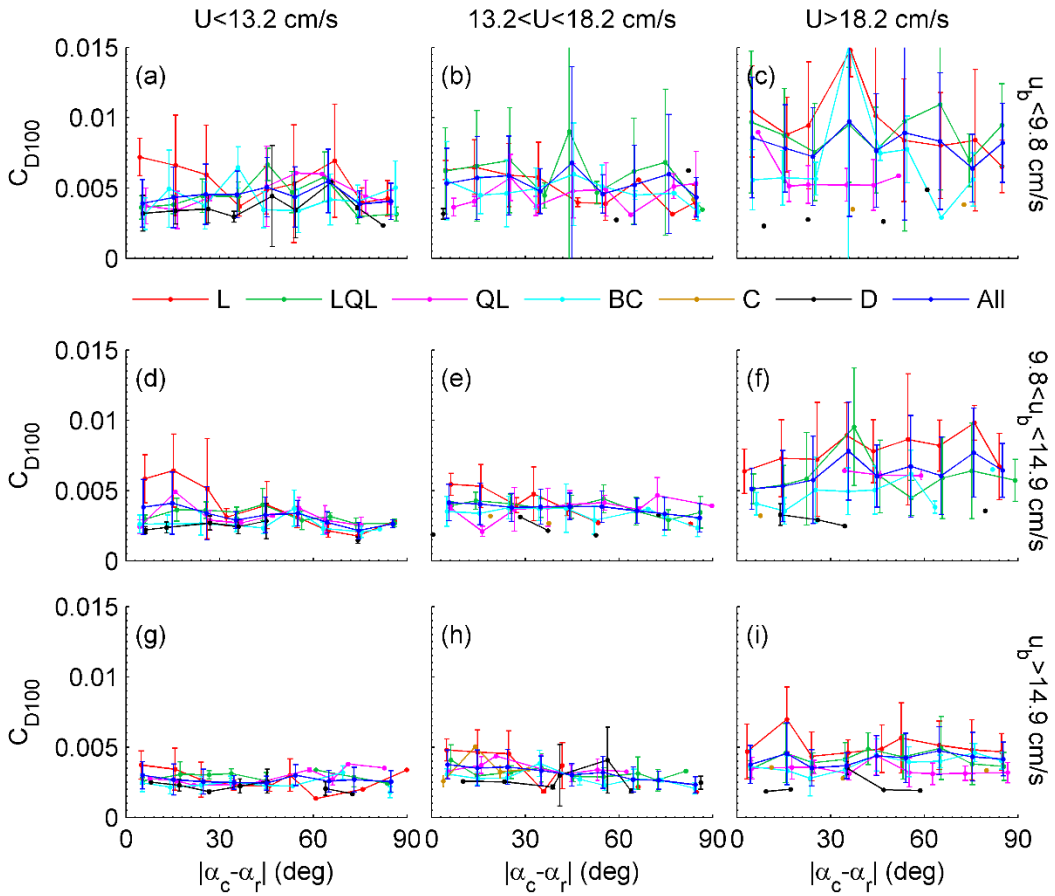

Figure 5.23. Scatter plots of bin averaged C_{D100} for GA plotted as a function of the difference between the ripple orientation (α_r) and the current direction (α_c) ($|\alpha_c - \alpha_r|$) for various ripple types (KEY: L – Linear Ripples; LQL – Linear-Quasi-Linear Ripples; QL – Quasi Linear Ripples; BC – Bifurcating-Cross-Ripples; C – cross-ripples; D – Disorganized Bed). The data in the individual plots correspond to various hydrodynamic conditions of $u_{b,1/3}$ (increasing from top row to bottom row) and U (increasing from left column to right column). The error bars indicate 1 standard deviation.

these data were removed, the remaining data indicated an average balance between production and dissipation for GA while slightly greater production was observed for LB.

The fluid drag coefficient (C_D) was calculated from the shear velocities and compared to ripple type, ripple geometry, and ripple orientation. While binned average values indicated some dependence on ripple height, ripple wavelength, steepness, and

asymmetry, the degree of scatter was larger than any trend present; therefore, no definitive conclusions can be derived. Of the parameters tested, C_D varied least with the ripple's shape and orientation relative to the current direction. It is possible that the ripples present at these two sites were either too small in height and/or wavelength to significantly affect the current at various angles. In addition, majority of the ripple present exhibited some degree of irregularity in the orientation, even for the most linear ripples observed. Therefore, any deviation in orientation may have an impact no matter how great the angle is. However, the most likely explanation is the weak current speeds present for both sites. The overall scatter and lack of a clearly defined trend for the various ripple shapes and orientations is the dominance of the waves for both sites, despite methods used to remove the overall wave signal [*Trowbridge*, 1998; *Shaw and Trowbridge*, 2001; and *Trowbridge and Elgar,* 2001]. Binning the data by wave and current conditions still leads to significant scatter with the most scatter present at high current speeds ($U > 18.2$ cm/s) and low wave orbital velocities ($u_{b,1/3} < 9.8$ cm/s). The mean trend however, indicates that the dependence on the bottom roughness is less significant when the current strength is weak and/or the wave strength is large.

Based on the data available for this study, ripple height is the dominant roughness element its influence decreasing under increasing wave strength or decreasing current speed. However, the high degree of scatter in the data precludes any definitive assumption.

CHAPTER 6

THE INFLUENCE OF THE RIPPLE GEOMETRY AND SHAPE ON SUSPENDED SEDIMENT CONCENTRATION

6.1. Introduction

The presence of ripples on the seabed can affect sediment resuspension processes including the vertical distribution of sediment concentration. This occurs through the enhancement of near bed turbulence and the associated vertical diffusivity but also by the development of vortices that can contribute to the ejection of sediment to the water column. Sediment becomes suspended when the particle lifting forces (i.e., vertical component of turbulent eddies) reach or exceed the downward directed forces (i.e., gravity). For conditions when suspension is possible, a concentration gradient forms where the greatest concentration exists at the seabed and decreases with increasing elevation above the bed. The concentration profile is typically defined by a reference concentration (C_r) near the bed that defines the amount of sediment available for distribution throughout the water column and a vertical distribution (gradient) of the sediment lifted off the bed.

Two of the most commonly used suspension profiles are the diffusive (Rouse) [see *Soulsby*, 1997] and the convective (exponential) profile [*Nielsen*, 1992]. The Rouse profile describes sediment distribution through the water column as a diffusive process, which is more prevalent in the absence of ripples; the convective profile accounts for increased sediment distribution in the vertical due to ripple-induced vortex ejection. In

the presence of waves and currents the profile can change shape between the wave and current boundary layers which requires the use of a multi-layer model [e.g., *Glenn and Grant*, 1987; *Styles and Glenn*, 2000].

Recently, *Bolanos et al.* [2012] used an Acoustic Backscatter System (ABS) to measure sediment concentration distribution in the benthic boundary layer (from within 1 cm of the bed) and to evaluate the *Lee et al.* [2004] and *Nielsen* [1992] reference concentration formulations. The *Lee et al.* [2004] formulation uses a shear stress based on skin friction only while that of *Nielsen* [1992] uses a skin friction shear stress that takes into account the flow enhancement near the crest of vortex ripples [*Du Toit and Sleath*, 1981]. *Bolanos et al.* [2012] found that the *Lee et al.* [2004] model agreed better with their observed data for overall error despite the fact that bedforms are not used explicitly in modifying the bed shear stress. However, this model is empirical and the product of numerically fitting 2 parameters; thus indirectly the fitting process takes into account the influence of the particular bedforms present. *Dolphin and Vincent* [2009] observed no correlation between reference concentration and bedform geometry when broadly categorizing ripple type as tidal ripples, short wave ripples, 2D long wave ripples, 3D long wave ripples, and upper-phase plane bed. Yet these broad categories with the exception of 2D long wave ripples, exhibit varying degrees or wavelength and irregularity, which could contribute to the lack of correlation.

In this chapter, suspended sediment profiles are examined to determine if there is a dependence of ripple characteristics on the nearbed reference concentration and the shape of the profile. This chapter is organized such that the methodology used to convert backscatter into suspended sediment is first presented in section 6.2. In section 6.3, the

data and extraction methods for this study are shown. The suspended sediment concentration profiles derived by this analysis are examined against the prevailing hydrodynamic conditions and bedform configurations to determine the role of ripple characteristics on sediment resuspension in section 6.4. Finally, a discussion and the conclusions are presented in section 6.5.

6.2. Extraction of ABS Data Theory

The ABS is an active sonar system, which uses a transceiver (i.e., a combined transmitter and receiver) to emit and receive a pulse of sound that propagates through the water column. Any particle, in the path of the transmitted sound wave, backscatters some of that energy with part of it directed back to the receiver while the rest continues to propagate in the direction of sound emission. The backscatter can be caused by sediment particles, air bubbles, biota, turbulence fluctuations, and/or layers of different mean density (thermal or saline). Of these, particles are the most dominant scattering mechanism in many marine environments. The distance each backscatterer is located away from the transducer, is measured in the time domain, which is subsequently converted into distance assuming known speed of sound in the water column. The intensity of the recorded signal is reduced as a function of the distance from the sensor (geometric spreading), attenuation due to the water and sediments, and depends on the total concentration of suspended particles that can enhance the backscattered signal for their particular range but can also reduce the amount of sediment available to be backscattered from particles in suspension at larger ranges. In terms of rms voltage received by the transceiver, the received signal can be expresses through the equation [*Thorne and Hardcastle*, 1997; *Thorne and Hanes*, 2002]:

$$V_{rms} = \frac{k_s k_t}{\Psi r} C^{1/2}\, e^{-2r(\alpha_w + \alpha_s)} \qquad 6.1$$

where V_{rms} is the root-mean-square returned echo intensity recorded as a voltage, k_s is a parameter related to the sediment backscattering properties, α_w is the sound attenuation due to water absorption, α_s is the attenuation due to sound propagation through a suspension of sediment, r is the distance from the transceiver face, k_t is a system constant, Ψ is the transceiver near-field correction, and C is the concentration of sediment in suspension. These terms are further described in the following sections.

6.2.1. Geometric Spreading and Nearfield Effects

As the sound wave propagates away from the source, the total intensity is spread over a larger surface area so that the intensity (i.e., energy per surface area) becomes increasingly smaller due to the spherical spreading of the wave front. Since the energy in the sound pulse must remain the same, the signal amplitude decreases as it propagates further from the source as a function of the square of the radius (r^2). After integrations explained in *Thorne et al.* [1991] and *Thorne and Hanes* [2002] in terms of rms Voltage, this simplifies to r shown in the denominator of equation (6.1).

In the near-field, the spreading loss is different from the far-field, due to imperfections of the transceiver that leads to a stretched signal close to the transceiver that does not follow the normal geometric spreading. The correction for spreading loss in the near-field was described by *Downing et al*. [1995] as:

$$\Psi = [1 + 1.35r_z + (2.5r_z)^{3.2}]/[1.35r_z + (2.5r_z)^{3.2}] \qquad 6.2$$

where $r_z = r/r_{crit}$ were $r_{crit} = \pi a_t^2/(c/f_t)$ is the range defining the near-field range of the transducer.

6.2.2. Form Function – Signal Backscattering Characteristics

The amount of backscatter returned to the transducers also relates to the degree to which the sediment reflects the signal. The variation in scattering is associated with the detailed particle shape. The scattering characteristics of a body are described by the form function (f) that depends on the particle radius (a) and wavenumber of the insonifying sound. The form function can be found for a single radius of an ideal scatter, like a sphere, as [*Thorne and Buckingham*, 2004]:

$$f = \left| \frac{2}{i(k_c a_i)} \sum_{n=0}^{n=\infty} (-1)^n (2n+1) b_n \right| \quad 6.3$$

where b_n is a function of spherical Bessel and Hankel functions of the first kind and their derivatives, n is the function order (increased iteratively until a threshold is met), k_c is the wavenumber of sound in water ($=2\pi f_t/c$), f_t is the transceiver frequency, and c is the speed of sound in water. When various sphere sizes are present in a population, the form function can be calculated for each grain size fraction (i) and after weighing for the percentage of each fraction (P) a mean form function is defined as:

$$\langle f \rangle = \sqrt{\left(\sum_{i=1}^{i=N} a_i \cdot P_i \right) \frac{\sum_{i=1}^{i=N} (a_i)^2 (f \cdot \gamma)^2 P_i}{\sum_{i=1}^{i=N} (a_i)^3 P_i}} \quad 6.4$$

where N is the number of size fractions, and angle brackets (< >) represent averaging over the whole range of particle sizes present in the acoustic field. For cases of irregular particles such as those of sand particles present in the marine environment, an enhanced scattering has been observed [*Thorne and Buckingham*, 2004]. This enhancement is accounted for using the coefficient γ (γ =1 for glass spheres), which are defined as [*Thorne and Buckingham*, 2004]:

$$\gamma = \frac{\beta (k_c a_i)^3 + 0.5 (k_c a_i) + 3.5}{(k_c a_i)^3 + 3.5} \quad 6.5$$

where β is a constant (=1.7) and k_c is the wavenumber of sound in water.

The sediment backscattering property denoted by the term k_s in equation (6.1) is defined as:

$$k_s = \langle f \rangle / \sqrt{\rho_s \langle a_s \rangle} \qquad 6.6$$

where ρ_s is the sediment density.

6.2.3. Sound Attenuation due to Sediment

Attenuation is independent of geometrical spreading and can be caused by the medium of propagation (thermal attenuation, viscous absorption), and scattering caused by sediments. The attenuation due to the sediments is small in typical concentration found in the marine environment but during storm events and/or higher current velocities, grain size and concentrations within the boundary layer can be high. Therefore, under these conditions accurate attenuation values due to sediment are required.

In a similar manner to the calculation to the form function, the total scattering cross section (χ), which describes the scattering attenuation characteristics of the scatters, is defined [*Thorne and Buckingham*, 2004] as:

$$\chi = \left| \frac{-2}{(k_c a_i)^2} \sum_{n=0}^{n=\infty} (2n+1) \mathrm{RE}(b_n) \right| \qquad 6.7$$

where *RE* denotes the real part of the complex expression and a mean χ is defined as:

$$\langle \chi \rangle = \sqrt{\left(\sum_{i=1}^{i=N} a_i \cdot P_i \right) \frac{\sum_{i=1}^{i=N} (a_i)^2 (\chi \cdot \gamma) P_i}{\sum_{i=1}^{i=N} (a_i)^3 P_i}} \qquad 6.8$$

The sediment attenuation is then given by:

$$\alpha_s = \frac{1}{r} \int_0^r \xi C \, dr \qquad 6.9$$

where ξ is the normalized total scattering cross section defined as:

$$\xi = \frac{3\chi}{4\rho_s\langle a_s\rangle} \qquad 6.10$$

Since the calculation of α_s in equation (6.9) requires knowledge of C, the solution can only be achieved solving iteratively equation (6.1). Furthermore, the particle size near the boundary layer can vary drastically from coarse material near the bed to fine grains further up the water column; necessitating the need for particle size measurements.

6.2.4. Sound Attenuation Due to Water

While sediment attenuation is important during high-energy conditions and close to the seabed, attenuation due to water is the most significant and occurs by the conversion of sound energy into heat due to shear viscosity and bulk viscosity. Absorption caused by shear viscosity is due to friction between adjacent layers of a liquid whereas; absorption caused by bulk viscosity is due to a lag-time required for water molecules to flow on a molecular level.

Since seawater contains a mixture of various chemical components, the absorption is greater than pure water. This excess absorption is the result of dissolved magnesium sulfate and boric acid molecules in seawater [*Leonard et al*, 1949; *Wilson and Leonard*; 1954 and *Bies*, 1955]. The time required for molecular reordering in response to changing pressure is called the relaxation time (t_r) and is inversely proportional to c^2 and when the relaxation frequency, $F=(2\pi t_r)^{-1}$, and transceiver frequency (f_t) are similar, the attenuation is greatest.

The total sound absorption coefficient due to water (α_w) is the sum of the attenuation due to these dissolved components and pure water. This can be estimated by [*Medwin and Clay*, 1998] as:

$$\alpha_w = \frac{A_1 P_1 F_1 f_t^2}{f_t^2 + F_1^2} + \frac{A_2 P_2 F_2 f_t^2}{f_t^2 + F_2^2} + A_3 P_3 f_t^2 \qquad 6.11$$

where α_w is the sound absorption due to water coefficient, A is the attenuation rate per frequency, P is a constant dependent on water depth, F is the relaxation frequency $(=2\pi t_r)^{-1}$, f_t is the transceiver frequency, and the subscripts 1, 2, and 3 indicate boric acid, magnesium sulfate, and pure water, respectively. This equation indicates that the attenuation is greatest at higher frequencies. For boric acid, the coefficients in equation (6.11) can be found as:

$$A_1 = (8.68/c)10^{(0.78\text{pH}-5)} \quad 6.12$$

$$F_1 = 2.8(S/35)^{0.5}10^{[4-1245/(273+T)]} \quad 6.13$$

and P_1=1, pH is the pH of seawater, S is the salinity in psu, and T is the temperature in °C. For magnesium sulfate the coefficients are:

$$A_2 = 21.44(S/c)(1 + 0.025T) \quad 6.14$$

$$P_2 = 1 - 1.34\text{x}10^{-4}d + 6.2\text{x}10^{-9}d^2 \quad 6.15$$

$$F_2 = \frac{8.17\cdot 10^{[8-1990/(273+T)]}}{1+0.0018(S-35)} \quad 6.16$$

where d is water depth. For the pure water component the coefficients are:

$$A_3 = \begin{cases} 4.934\text{x}10^{-4} - 2.59\text{x}10^{-5}T + 9.11\text{x}10^{-7}T^2 - 1.50\text{x}10^{-8}T^3, & T \leq 20℃ \\ 3.964\text{x}10^{-4} - 1.146\text{x}10^{-5}T + 1.45\text{x}10^{-7}T^2 - 6.5\text{x}10^{-10}T^3, & T > 20℃ \end{cases} \quad 6.17$$

Equation (6.11) gives α_w in dB/km. For consistency with the equations described above (based on that from *Thorne and Hanes* [2004]) for an Aquatec ABS, the units need to be converted to Nepers per meter through the following equation:

$$\alpha_w = \alpha_w/\log_{10}[\exp(20)]/1000 \quad 6.18$$

6.2.5. System Constant

Each ABS system has unique properties as well as various settings, which can alter the recorded voltage. These include the receiver sensitivity (R), which can include

any fixed or time varying gain, the reference pressure (P_o), the voltage transfer function (T_v), and the transmit pulse length ($c\tau_p$), where c is the speed of sound in water and t_p is the pulse duration. The interaction and influence of these parameters can be aggregated into a single parameter so that:

$$k_t = RT_v P_0 r_0 \left\{\frac{3\tau_p c}{16}\right\}^{1/2} \frac{0.96}{k_c a_t} \quad 6.19$$

Since many of these parameters are set by the manufacturer, they are unique to the instrument used and not easily obtained without access in the hardware and the use of specialized equipment. By rearranging equation (6.1), k_t can be estimated for a signal collected in a known suspension of particles and other environmental conditions as follows:

$$k_t = \frac{V_{rms}\Psi r}{k_s C^{1/2}} e^{2r(\alpha_w+\alpha_s)} \quad 6.20$$

This is usually performed in the laboratory, under controlled conditions of sediment concentration, size, shape, and density, water salinity, and temperature, assuming a uniform sediment mixture.

6.2.6. Calculation of Suspended Sediment Concentration

Once the system constant is identified, suspended sediment concentration estimates can be obtained by rearranging the terms in equation (6.1) as:

$$C(r) = \left(\frac{V_{rms}\Psi r}{k_s k_t}\right)^2 \exp[4r(\alpha_s + \alpha_w)] \quad 6.21$$

Replacing α_s with equation (6.9), equation (6.21) is written as:

$$C(r) = \left(\frac{V_{rms}\Psi r}{k_s k_t}\right)^2 \exp\left[4r\left(\frac{1}{r}\int_0^r \xi C(r)\, dr + \alpha_w\right)\right] \quad 6.22$$

Estimation of sediment concentration as a function of range requires an iterative solution of equation (6.22) as a function of range.

6.3. Data Description

6.3.1. Data Collection

The data sources used in this study consist of two sets collected at field sites located along the South Atlantic Bight offshore Georgia (hereafter referred to as GA) and Long Bay, South Carolina (hereafter referred to as LB) (USA). The Long Bay field site data were collected using two bottom boundary layer tripods (A and B). Tripod A was equipped with two SonTek Acoustic Doppler Velocimeters (ADV), both installed at an elevation of ~31 cm above the bed and an Aquatec Acoustic Backscatter sensor. The latter provided vertical profiles of acoustic intensity with a range resolution of 11 mm at a rate of a burst every hour. The ABS system consisted of 3, 10 mm diameter transceivers operating at 1, 2.5, and 5 MHz. Tripod B was equipped with an Imagenex 881 rotating sector-scanning sonar, which provided images of the seabed at a rate of 1 burst every 30 min for 1.5 hours; the sampling scheme was repeated every 5 hours. The seabed was composed of fine (D_{50}=177 mm) quartz sand (Figure 6.1) with a standard deviation of 71 μm (0.38 in ψ units).

The second data set (GA) was the result of the deployment of a tripod at a location offshore Georgia during 2007 and 2008. The tripods used were equipped with two Sontek ADV sensors installed at 52 and 67 cm above the bed during the 16 September to 7 October 2007 deployment and at 45 and 31 cm for the period 22 November 2007 to 15 February 2008. In addition, this tripod was equipped with an ABS system with 4 downward looking transceivers operating at 1, 2.5, 4, and 5 MHz. In the vicinity of the tripod was a rotating sector scanning sonar system attached to a jetted pipe which provided imagery of the seabed at 1 image ever hour [*Voulgaris and Morin*, 2008].

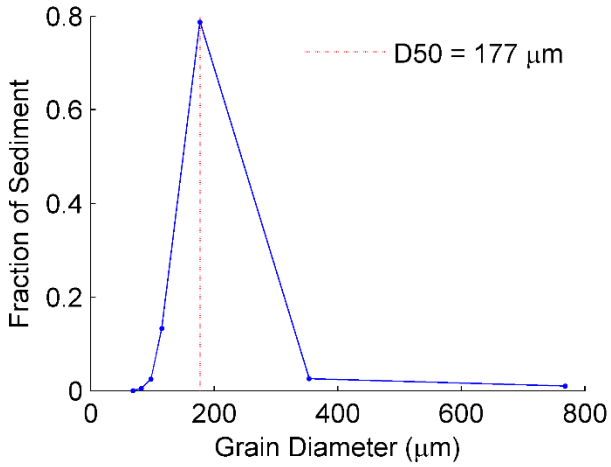

Figure 6.1. Grain Size Distribution for Long Bay, South Carolina (LB).

6.3.2. Calculation of Concentration Methodology

Suspended sediment concentration and grain size profiles were extracted from the recorded ABS signal using the methods described in section 6.2.1. In the following sections, the calibration of the instrumentation and calculation of suspended sediment and grain size profiles is described.

6.3.2.1. System Constant

The system constant was calculated for both the LB and GA ABS systems as they were unique and had different configurations. For the LB ABS, the signal included a time variable gain (TVG). At that time, the TVG was set in the hardware so that it could not be altered nor easily measured and therefore could not be accounted for directly. In this case, the TVG and system constant were aggregated into one variable and the system constant was assumed to be a function for each frequency/transceiver. For the GA ABS, no variable gain was used and as such, a single scalar for each frequency was estimated using a calibration process.

In order to estimate the system constant (calibration), acoustic intensity profiles were collected in a calibration chamber that contained a known volume of water and known sediment grain size and concentration. The calibration chamber consisted of a large cylinder open on the top with a funnel shaped bottom connected to a pneumatic diaphragm pump. Water and sediment were continuously recirculated to the top of the tank using the pump; creating a closed re-circulation system. Several design modifications were made to the calibration chamber until the system was able to maintain a uniform distribution of sediment resuspension throughout the whole length of the tank. Initially, for the LB system, a trawling motor was installed at the bottom to prevent sediment from settling on the funnel and thus creating a vertical variation in sediment concentration in the tank water column. In addition, a propeller composed of two paddles with holes was run at low speeds (approximately 1-2 Hz) at the top of the chamber where the sediment was re-introduced to the tank. This helped distribute the sediment, which settled uniformly through the chamber. Design modification, after the LB calibration, included the removal of the trawling motor, as it was determined it was affecting the acoustic signal due to enhanced turbulence. Furthermore, it was noted that a steady state between sediment entering the funnel is attained after running the pump for an hour or more. In addition, jets at the top of the chamber were modified such that sediment was re-introduced to the chamber vertically and at multiple (8) locations, which increased uniformity and eliminated the need for the mixer. Between the jets and the funnel, particles settled with a uniform concentration and this range was used for calibration. During each run, the temperature of the water was recorded and sediment concentration was sampled. The sample was subsequently filtered, dried, and weighed to yield an

accurate concentration within the chamber, which was always less than that added due to the sediment accumulation at the bottom of the tank. Another difference between the two calibrations is that for LB, in situ sediment was used while for GA glass spheres were used which eliminated uncertainty in sediment scattering (γ=1 in equations (6.3) and (6.7)) in the deriving the system constant.

The calibration of the LB ABS system was performed for 4 concentrations (22, 46, 77 and 117 mg/L) with each run lasting 10 min with a sampling rate of 64 Hz with every 64 samples averaged and recorded by the ABS. The samples for each concentration were subsequently averaged over the 10 min and k_t was solved using equation (6.20). All transceivers were calibrated at the same time so that each signal was recorded using the same concentrations. The recorded voltages and system constants for each concentration are shown in Figure 6.2. One characteristic unique to the 1 MHz is a high return between 66 and 80 cm. This was consistent for all concentrations and present in clear water experiments. The cause was not determined, but it is assumed to be the result of acoustic reverberation in the chamber at that frequency, as this signal was not recorded by the other transceivers. The system constant exhibited variations at longer ranges between the different concentrations, but tend to be on the same order. The averaged k_t values are shown for each transceiver in Figure 6.3. Since some variation in the k_t is likely the result of occasional variations in concentration with range and an average cannot be taken due to the instrument gain, a linear fit was applied to the data for ranges >10-23 cm (solid lines in Figure 6.3). At closer ranges, the slope drastically changed, perhaps the result of a different time varying grain setting for closer and longer ranges. At these ranges, the calculated k_t was used as opposed to the fitted value.

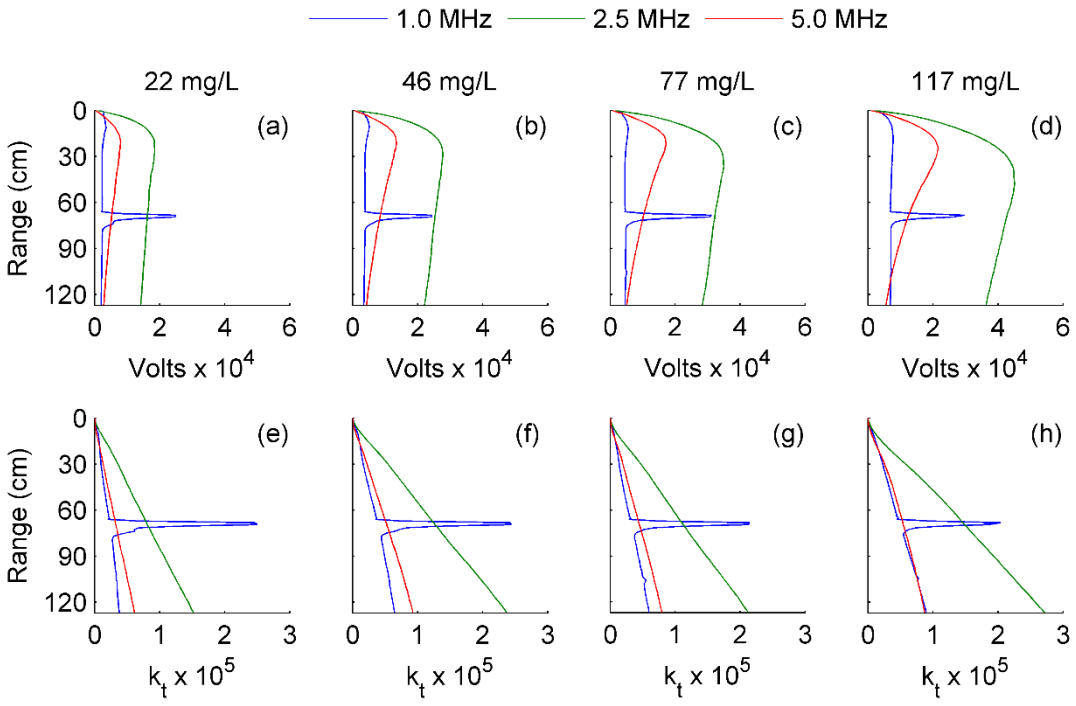

Figure 6.2. Recorded Voltage (top row) and calculated system constant (k_t) for (a and e) C=22 mg/L; (b and f) C=46 mg/L; (c and g) C=77 mg/L; and (d and h) C=177 mg/L for the 1 MHz (blue), 2.5 MHz (green) and 5 MHz (red) transceivers.

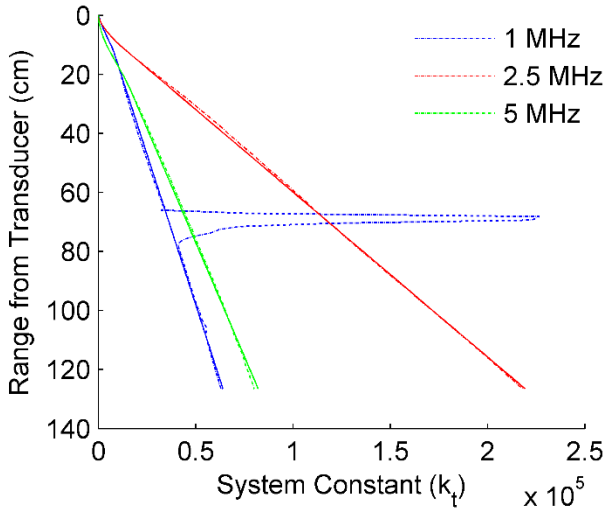

Figure 6.3. Average k_t for LB for each transceiver.

This k_t value was subsequently used to solve for C and determine an expected error, ($\varepsilon = \left[\left(C_p - C_o\right)^2\right]^{1/2}/C_o$), where C_p is the predicted concentration (equation (6.21)) and C_o is the concentration during the calibration. This results in an error of 26% when the concentration from each transceiver is averaged.

A similar calibration was performed for the ABS used in the Georgia data collection. However, since no gain was applied, the system constant was not range dependent allowing for the calculation of a single k_t (i.e., constant with range) for each frequency. The calibration was run for 20 min sampling at 4 Hz with every 16 samples average by the ABS. Three concentrations (100, 200, and 300 mg/L) and 3 glass sphere grain sizes (165, 231, and 275 μm) were used in the calibration. The system had a blanking distance of 20 cm and a bin size of 10 mm. The two samples for each concentration were averaged over the 20 min burst and subsequently averaged together. From this k_t was calculated for each grain size and concentration. The voltages for each transceiver for all concentrations and grain sizes are shown in Figure 6.4 while k_t is shown in Figure 6.5. Unlike LB, the voltages are several orders of magnitude smaller due to no gain being applied. Some variation in k_t (Figure 6.5) is observed at long ranges from the transceiver so the k_t was calculated between 40-80 cm where there the strongest agreement for various concentrations and grain sizes was observed. This resulted in k_t values of 0.0145, 0.0054, 0.0074, and 0.0039 for the 1, 2.5, 4, and 5 MHz transceivers, respectively. This calibration results in an overall error of 14% for all ranges but only 3.5% for ranges of 125 cm from the transceivers (the maximum distance to the seabed for the GA deployment).

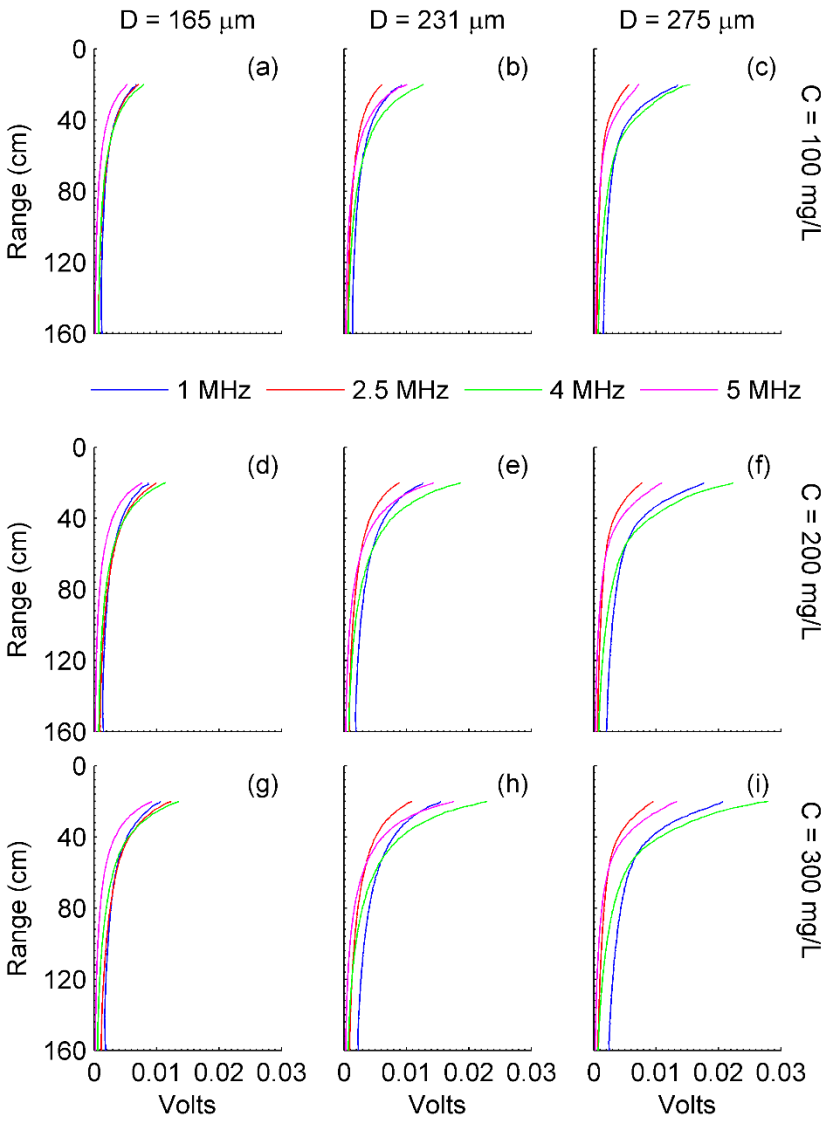

Figure 6.4. Recorded Voltage for GA ABS transceiver calibration for C=100 mg/L (top row); C=200mg/L; (2nd row) and C=300 mg/L (bottom row), for grain sizes of 165 μm (left column), 231 μm (middle column) and 275 μm (right column).

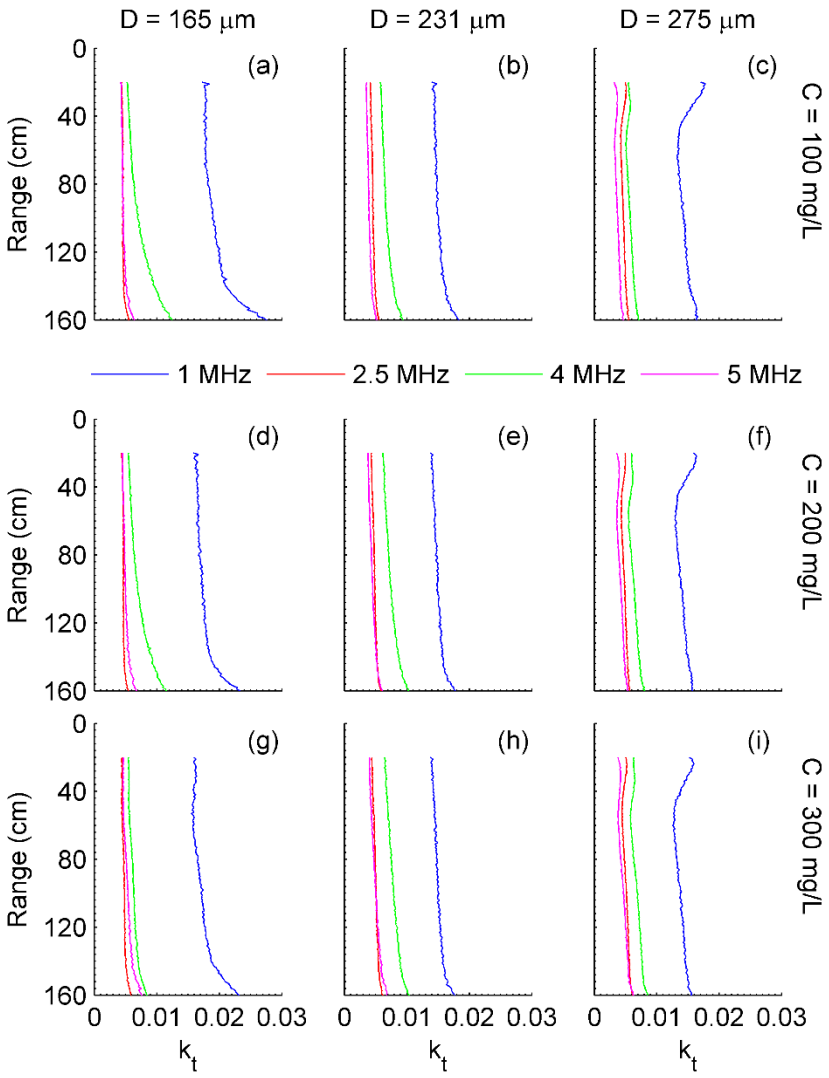

Figure 6.5. Calculated k_t for GA ABS transceiver calibration for C=100 mg/L (top row); C=200mg/L; (2nd row) and C=300 mg/L (bottom row), for grain sizes of 165 μm (left column), 231 μm (middle column) and 275 μm (right column).

6.3.2.2. Concentration and Grain Size Profile

The ABS for LB and GA had multiple transceivers operating and each can yield a recorded voltage and hence a concentration profile after inverting the signal. Since all transceivers sample the same area, the concentration values derived from each sensor should be identical. The inversion technique requires a priori knowledge of sediment size

as this defines the value of the sediment attenuation constant and the values of the form function used for the inversion (see equations (6.4) and (6.9)). In the approach followed here, the iteration was performed for each frequency assuming a normal distribution of sediment with a range of mean particle sizes. This iteration was performed at each elevation (starting with the one closer to the transducer) for a range of mean particle size (defined by the range of sizes found on the seabed on each site). Some problems with this approach are outlined in *Thorne and Hanes* [2002]. However, this approach yields good results and usually converged in 4-5 iterations with an accuracy of 1×10^{-6} kg/m^3. This iterative process requires an initial value of concentration for the first bin (bin closer to the transducer face). The standard deviation between the concentration measurements for each frequency was then taken (for each bin and grain size) and the value that provided the smallest standard deviation in sediment concentration was adopted as the final solution. The corresponding mean size was selected as that present, in the water column, at the particular bin level. This procedure was then repeated for the next bin.

The choice of grain sizes to sample over was limited for each site to prevent erroneous values, such as largest grain sizes at higher elevations or grain sizes larger than observed. A limit was applied to each bin such that the largest sizes were at the bed and logarithmically decayed to a minimum at the bin closest to the transceiver. For LB, the grain size limits chosen correspond to 75 and 177 μm, with a standard deviation of 0.38ψ, while for GA, the limits were 75 and 388 μm. A range of grain sizes were tested between these limits and a $\langle f \rangle$ was calculated for each grain size with a standard deviation of 0.38ψ. Temperature and salinity values recorded by a CT located near the tripods were

used for the LB calculation. For GA, the ABS measured temperature while a constant salinity of 35 was assumed.

Once the acoustic profiles were inverted to sediment concentration profiles they were converted from range to elevation above the seabed. The seabed range was estimated from the acoustic data by detecting the location of the strongest backscatter return. Since the instruments had a resolution of 11 and 10 mm for LB and GA, respectively, the bed determination was made using a 2nd order polynomial fit to the 5 bins on either side of the bin with the maximum acoustic intensity and the location of the maximum of the parabola was assumed to represent the location of the seabed.

6.3.2.3. Near Bed Bin Contamination

Due to signal filtering techniques employed by the ABS systems the bottom bins closest the bed are contaminated by the bed reflection and do not yield reliable results. This is usually indicated by a kink or oscillations in the signal, often indicating an increasing concentration over the first few cm above the bed. This varied for each system at 7.0 cm for GA and 9.9 cm for LB. These data were subsequently removed from further analysis.

6.3.3. Data sets

6.3.3.1. Georgia

The Georgia data set is characterized by numerous periods of sediment motion with durations of 1 day or longer. During these events, ripples changed in geometry with wavelength ranging from a few cm up to near 1 m and formed numerous three-dimensional shapes (see chapter 3 for further details). The driving mechanism for the ripple evolution were changes in wave forcing and direction, however, the additional

stress of the currents led to ripple modification when waves alone were not sufficient to mobilize bed sediment. While this data set is several months in duration, the suspended sediment concentration was low and often below the digital detection limit of the ABS, resulting in limited data. The one consistent event captured, occurred between days 273 and 277 of year 2007 (Figure 6.6). During this event, ripples were primarily linear to linear-quasi-linear in shape based on the wavelength (I_k) and orientation irregularity (I_a) values (Figure 6.6e). The ripple wavelength (measured) and height (based on the 2-D model results, chapter 4) each increased from days 273.25 to 275.25 after which they remained constant. The ripple steepness was consistently greater than 0.1, which is the steepness required for eddies to form on the lee side of ripples [*Sleath*, 1984]. Waves were aligned with the peak ripple orientation throughout this event, however, the tidally driven currents varied from parallel to perpendicular. Based on the vertical concentration profile (Figure 6.6f), the orientation between the mean flow and ripples has no influence on the gradient. Since waves were always perpendicular to the ripples, it cannot be determined if this would influence the concentration profile. The calculated mean suspended grain size (D_m) is shown in Figure 4g and indicates that grain sizes up to 200 μm can be suspended up to 25 cm in the water column, however; the larger grain sizes do not always correlate with large concentrations and might be an artifact of the inversion method when agreement between the transceivers was poor.

6.3.3.2. Long Bay

The Long Bay data set (Figure 6.7) was characterized by several large storm events, which coincide with the passage of frontal systems [*Warner et al*., 2012]. Compared to GA, LB has more energetic wave events with weak current speeds. The

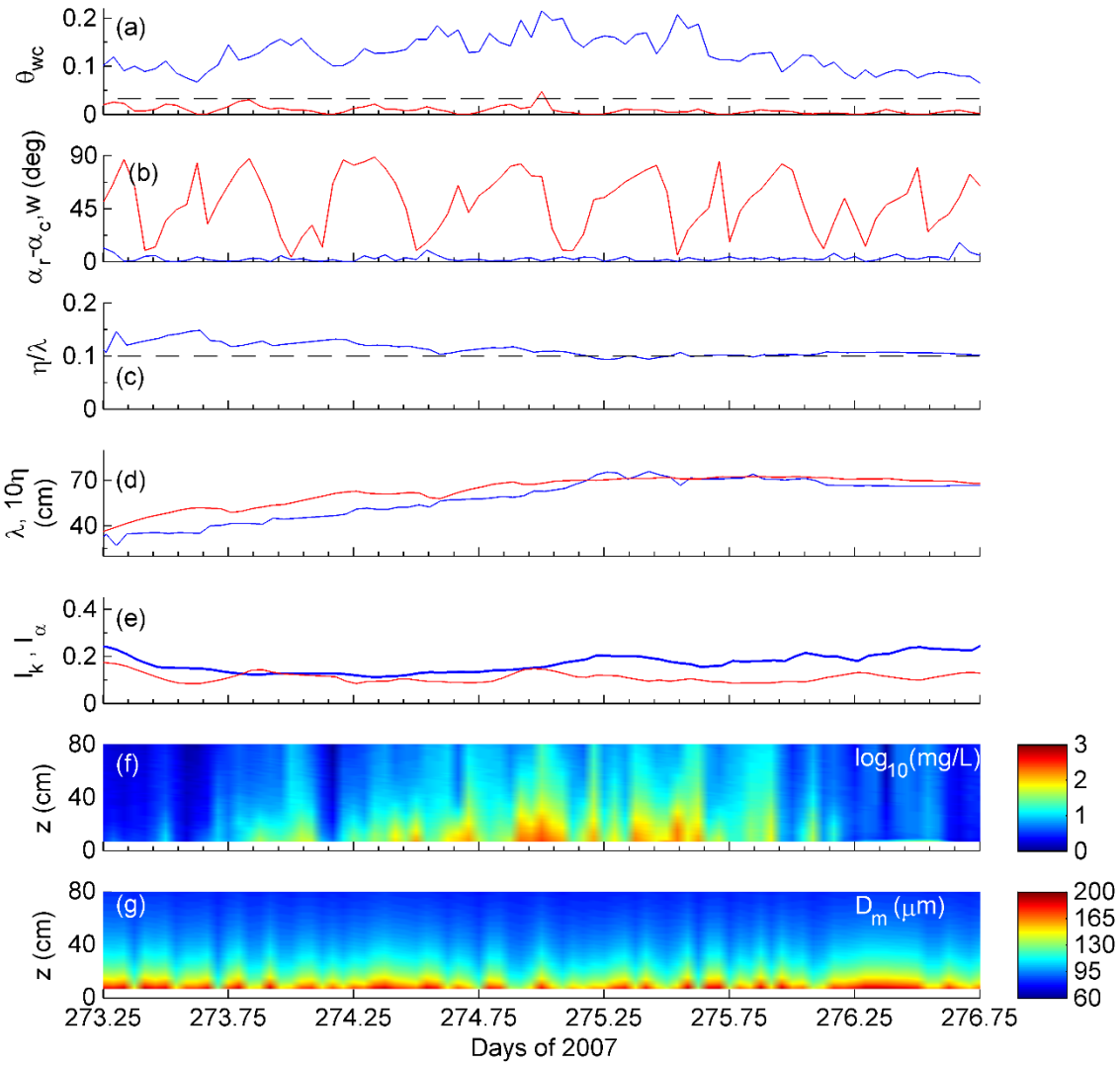

Figure 6.6. Time Series showing: (a) maximum wave-current skin friction Shields Parameter (blue), current skin friction Shields parameter (red), and the critical Shields Parameter for sediment motion (black dashed line); (b) difference between the ripple orientation and the direction of propagation for wave (blue) and currents (red) in degrees; (c) ripple steepness (η/λ) where vortex formation is likely to occur for η/λ =0.1 (dashed line); (d) ripple wavelength (blue) and 10 × ripple height (red); (e) ripple wavelength (blue) and orientation (red) irregularity; (f) suspended sediment concentration profile where the color bar has units of $\log_{10}$(mg/L); and (g) suspended grain size profile in μm for the GA site.

ripples were also smaller with a maximum wavelength less than 25 cm and heights less than 3 cm. While the ripple steepness and irregularity were variable during this

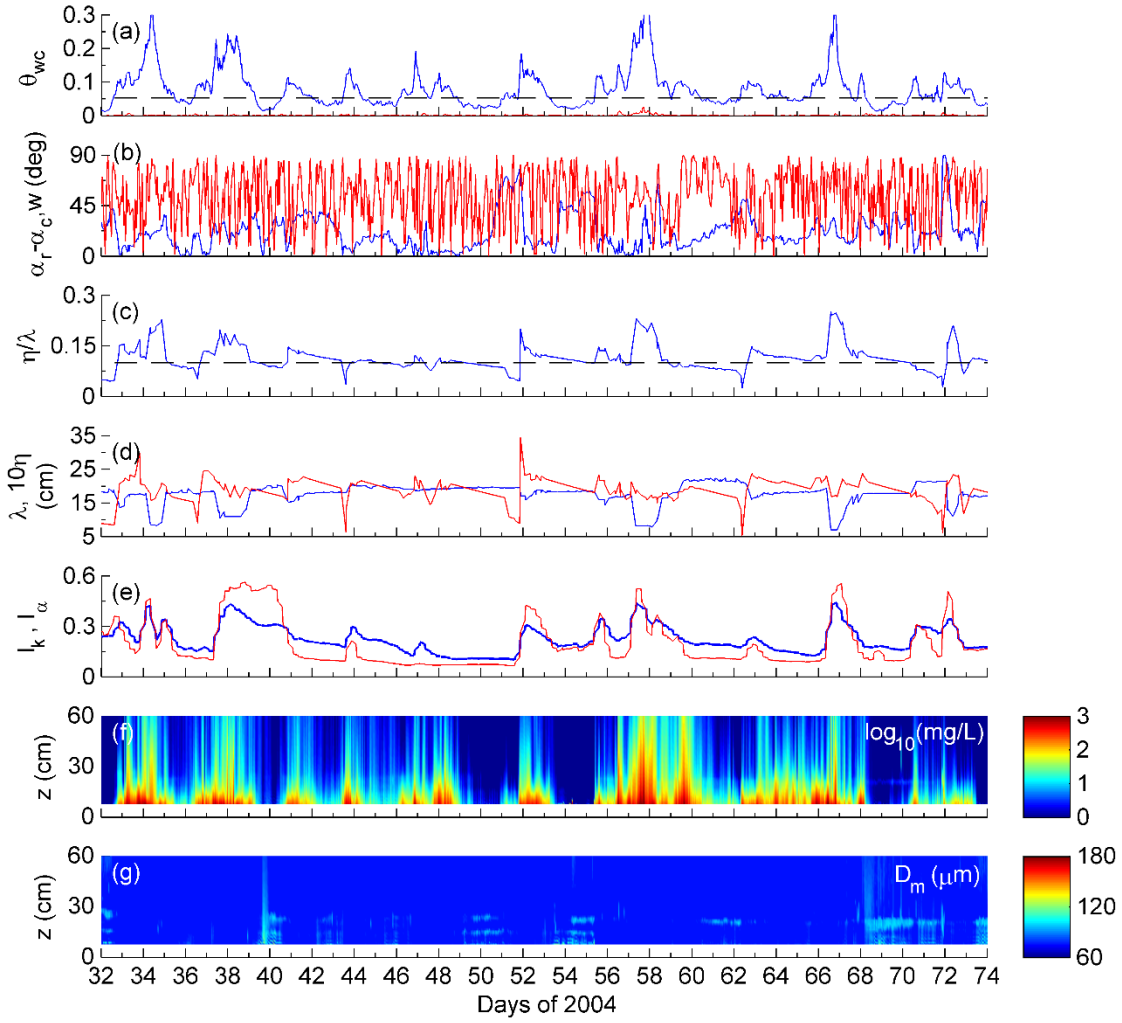

Figure 6.7. Time Series showing: (a) maximum wave-current skin friction Shields Parameter (blue), current skin friction Shields parameter (red), and the critical Shields Parameter for sediment motion (black dashed line); (b) difference between the ripple orientation and the direction of propagation for wave (blue) and currents (red) in degrees; (c) ripple steepness (η/λ) where vortex formation is likely to occur for η/λ =0.1 (dashed line); (d) ripple wavelength (blue) and 10 × ripple height (red); (e) ripple wavelength (blue) and orientation (red) irregularity; (f) suspended sediment concentration profile where the color bar has units of $\log_{10}$(mg/L); and (g) suspended grain size profile in μm for the LB site.

deployment, changes in geometry occurred synchronously with forcing, as did the sediment suspension profile. Periods of greatest sediment suspension occur with large θ_{wc}, large ripple irregularity, and the greatest concentration 50 cm above the bed occurs

when ripples were steepest (same time a high θ_{wc}). While grain size was calculated, there is little variation present, indicating possibly only fine sediment in the water column.

The noise present in the concentration and grain size profile around 25 cm appears to be the same as that from the calibration, though at a different range. This appears to be an artifact of the instrument but it is less prevalent when concentration is large. This signal was also present on the other frequencies so eliminating the 1 MHz transceiver has little affect.

6.4. Analysis

Calculation of sediment resuspension profiles is dependent on the amount of sediment available for resuspension (reference concentration) and the method through which sediment is dispersed through the water column. The LB and GA data sets will be used to evaluate these parameters in the following sections.

6.4.1. Reference/Near Bed Concentration

The reference concentration is the suspended sediment concentration at some elevation close to the seabed that is available to be dispersed through the water column. The amount of sediment available is typically a function of forcing strength and grain size.

Smith and McLean [1977a] defined a reference concentration (C_r) to be proportional to the excess shear stress, which indicates the degree to which the hydrodynamics can mobilize and suspend sediment:

$$C_r = \frac{C_b \cdot \gamma_o \cdot T_s}{(1+\gamma_o \cdot T_s)} \qquad 6.22$$

where C_b is the bed volumetric concentration (usually 0.65), γ_o is an empirical constant (=1.95×10-3 for a single size class at an elevation of 10 cm above the bed, or a general

value of 2.4x10-3 from *Smith and McLean* [1977b]) and T_s is the excess shear stress defined as $T_s = (\tau_b{}' - \tau_{cr})/\tau_{cr}$,where the accent indicate skin friction shear stress. This formulation has since been tested against laboratory and field data by numerous researches and many have proposed improvements to the formulation coefficients [e.g., *Vincent and Green*, 1990; and *Grant and Glenn*, 1983].

Van Rijn [1984] found the reference concentration based on T_s to be best described by:

$$C_r = 0.015\rho_w \frac{D_{50}}{z_r} \frac{T_s^{1.5}}{D_*^{0.3}} \qquad 6.23$$

where $D_* = D_{50} \cdot [(s-1) \cdot g \cdot \upsilon^{-2}]^{1/3}$ is a non-dimensional particle diameter and z_r is taken at $\eta/2$.

Nielsen [1992] proposed an alternative reference concentration equation, which is based on the enhanced Shields parameter (θ_r), which takes into account the flow enhancement near the ripple crest as defined by *DuToit and Sleath* [1981]. This equation relates the reference concentration directly to the shear stress and does not consider critical shear stress for sediment motion and is defined as:

$$C_r = \delta\rho_w\theta_r^3 \qquad 6.24$$

where δ is an empirical constant at a reference height corresponding to the ripple height found to be 0.005 and:

$$\theta_r = \frac{\theta_w}{(1-\pi\eta/\lambda)^2} \qquad 6.25$$

where θ_w is the wave Shields parameter defined as $\theta_w = u_{*w}^2/\big((s-1)gD_{50}\big)$, and u_{*w} is the skin-friction shear velocity. *Green and Black* [1999] evaluated this formula for field conditions and found it works well but the concentration can also be described by using the skin friction alone with δ=0.1. The shear stress in equation (6.24) was also found to

agree well when the skin friction for waves was used. *Dolphin and Vincent* [2009] found best agreement between reference concentration and θ_r as $C_r = 0.00156\rho_w\theta_r^{1.84}$

Another empirical predictor for reference concentration is that of *Lee et al.* [2004]:

$$C_r = \rho_w A\left(\theta_{sf}\frac{u_{*sf}}{w_s}\right)^B \qquad 6.26$$

where A and B are empirical constants defined as 2.58±1.7 and 1.45±0.04 and the reference concentration was measured at 1 cm above the bed.

These methods were tested by extrapolating the ABS suspension profile for LB and GA to the seabed by fitting an exponential (log(z)-C) line. Values were calculated at z=0, z=η/2, and z=1 cm above the bed, for comparison with the above predictors and the results are shown in Figure 6.8. The bed reference concentration at z_r=0 cm is shown in Figure 6.8a as a function of wave skin friction Shields parameter ($\theta_{w,sf}$) for each ripple type along with the prediction of *Green and Black* [1999] (gray line) and a best fit through the data (red). The predictions of *Green and Black* [1999] tend to agree with the observations and there is a correlation with $\theta_{w,sf}$. When reference concentration is plotted against θ_{wr} (Figure 6.8b), a greater degree of scatter is present, resulting in a best fit line which deviates significantly from that predicted by *Nielsen* [1992]. The C_r at a height of 1 cm above the bed is plotted as a function of $\theta_{w,sf}\,u_{*\mathrm{w}sf}/w_s$ in Figure 6.8c where w_s was calculated using the method of *Gibbs et al*. [1971] with a grain size of D_{50} (=177

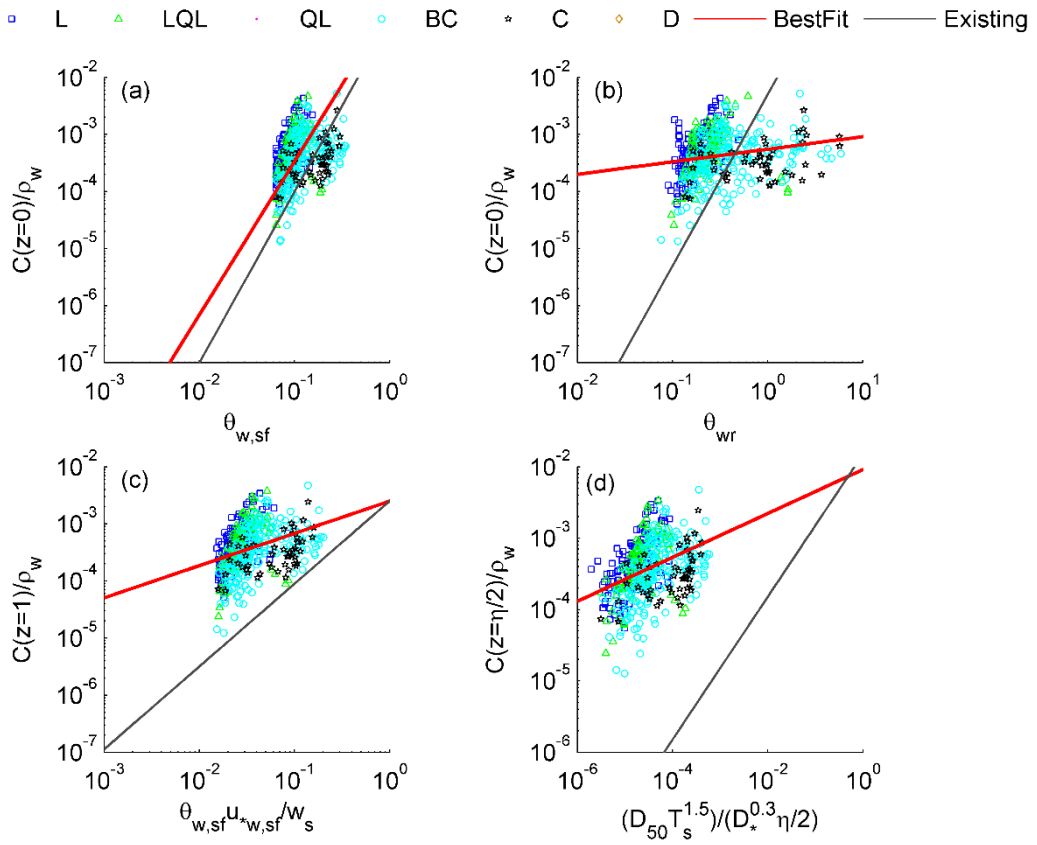

Figure 6.8. Reference concentration from LB with best fit lines (red) as a function of: (a) θ_{wsf} at z=0 where the black line is that prediction of *Green and Black* [1999]; (b) θ_{wr} at z=0 with the black line the predictor of *Nielsen* [1993]; (c) $\theta_{wsf}u_{*wsf}/w_s$ at z=1 cm with the black line the predictor of *Lee et al.* [2004]; (d) $(D_{50}T_s^{1.5})/(D_*^{0.3}h/2)$ with the black line the predictor of *Van Rijn* [1984]. The blue symbols correspond to ripple shape shown in the legend where: (L) Linear, (LQL) Linear-Quasi-Linear; (QL) Quasi-Linear; (BC) Bifurcating-Cross; and (D) Disorganized.

μm). The predictions of *Lee et a*l. [2004] under predict the current data set, as do those of *Van Rijn* [1984] in Figure 6.8d.

Also shown on Figure 6.8 are the reference concentrations for the various ripple shapes. There is no clear separation between the various ripple types indicating a lack of dependence on ripple shape. This is expected as the skin friction component acts on each sediment grain and is responsible for mobilizing the bed sediment.

Reference concentrations were also calculated for the GA data set and are shown along with the LB concentration in Figure 6.9. The scatter of the data indicates that a best fit is observed for $\theta_{w,sf}$ and the predictions best agree with that of *Green and Black* [1999].

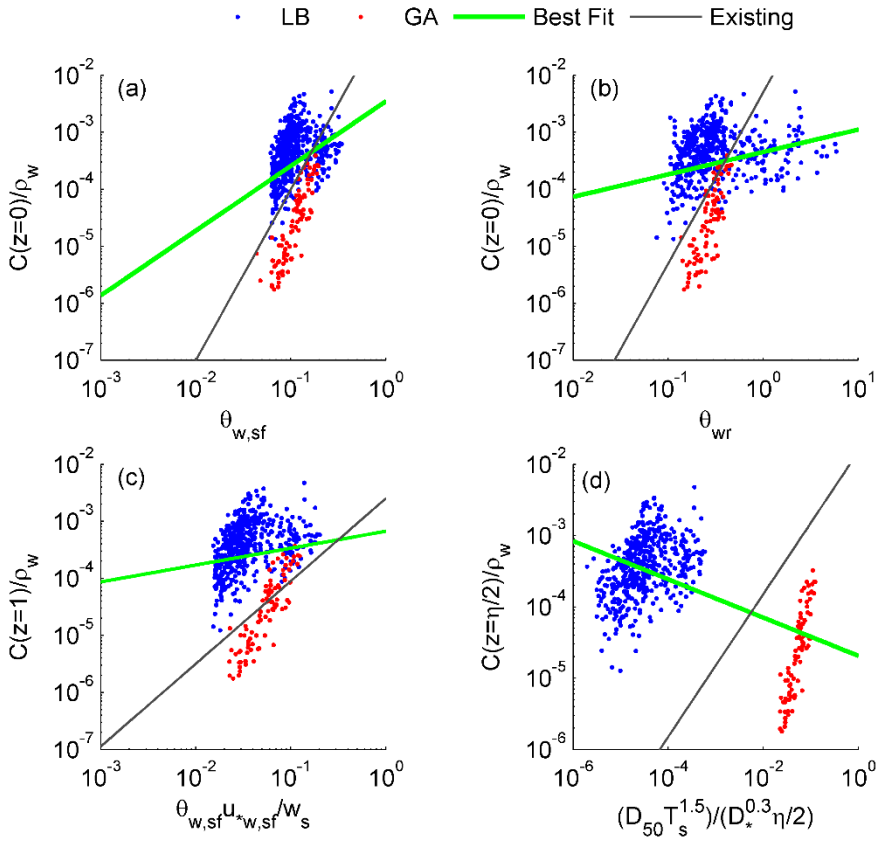

Figure 6.9. Reference concentrations from LB (blue) and GA (red) with best fit lines (green) as a function of: (a) θ_{wsf} at z=0 where the black line is that prediction of *Green and Black* [1999]; (b) θ_{wr} at z=0 with the black line the predictor of *Nielsen* [1993]; (c) $\theta_{wsf}u_{*wsf}/w_s$ at z=1 cm with the black line the predictor of *Lee et al.* [2004]; (d) $(D_{50}T_s^{1.5})/(D_*^{0.3}h/2)$ with the black line the predictor of *Van Rijn* [1984].

6.4.2. Suspension Shape

Sediment is suspended into the water column by two main physical methods. One method is by diffusion and another is convection caused by vortex ejection from ripples during flow reversals. The diffusive profile is often found to agree with the *Rouse* [1937] distribution, which is a power law fit defined as:

$$C(z)/C_r = (z/z_r)^{-P} \quad 6.27$$

where z is elevation, z_r is the elevation of the reference concentration and P is the Rouse parameter defined as:

$$\mathrm{P} = \mathrm{w_s}/(\kappa \cdot \mathrm{u_*}) \quad 6.28$$

where w_s is the sediment fall velocity, κ is the von Karman constant equal to 0.4, and u_* is the shear velocity. For large P, the suspended sediment profile is steeper with sediment remaining near the bed while for small values the sediment is uniformly distributed [*Van Rijn*, 1993]. *Glenn and Grant* [1987] and later *Styles and Glenn* [2000] showed that this profile is composed of multiple layers with the concentration profile different above and below the wave boundary layer (~1 cm for the wave present). Above the wave boundary layer, the profile is a result of the wave-current shear stress due to the form drag.

In a rippled environment, the bedforms enhance the turbulence near the bed and lead to the formation of eddies when the ripple steepness approaches 0.1. This convective method can alter the suspension profile near the bed. *Nielsen* [1992] presented formulations that describe this suspension profile by a vertical scale of decay:

$$C(z)/C_r = \exp(-z/L_s) \quad 6.29$$

where L_s is a mixing length defined as:

$$L_s = \begin{cases} \frac{0.75\cdot\left(A_{b,1/3}\omega\eta\right)}{w_s} & , \ \frac{A_{b,1/3}\omega}{w_s} < 18 \\ 1.4\eta & , \ \frac{A_{b,1/3}\omega}{w_s} \geq 18 \end{cases} \quad 6.30$$

Normalized suspension and grain size profiles for the GA event are shown in Figure 6.10 for linear (blue) and linear-quasi-linear (red) ripples. When taken over the entire storm event (Figure 6.10a), there is a large variation with some distinctions between the mean profiles of the two ripple types. In Figure 6.10c only conditions where $2.2<\theta_{wcsf}/\theta_{cr}<4$ are shown. These profiles show a similar distinction between the two ripple types. Both show strong agreement in the first 25 cm of the profile and then diverge with linear ripples obtaining smaller values of C/C_r at greater elevations. However, the variations are small compared to the standard deviation. At $\theta_{wcsf}/\theta_{cr}>4$, both mean profile are nearly identical and indicate a convective component of the suspension up to around 30 cm. On a z-log(C) plot, the convective fit from equation (6.29) appears as a straight line. Above this value, the profile agrees closer with the diffusive profile in equation (6.27). The trend is less apparent for lower wave speeds, indicating a dependence on forcing strength. As both ripples are quite similar, it is difficult to say if any variation exists.

All the grain size profiles exhibit similar slopes. The only difference is the nearbed grain size, which varies from 130 to 200 μm. One reason for the similar slopes is probably a forcing by the inversion process to decrease the size with increasing elevation above the bed. This was enacted since the routine tended to find best agreement at large grain sizes when no sediment was suspended. Therefore, these profiles do not give clear indications of the importance of wave energy nor ripple type.

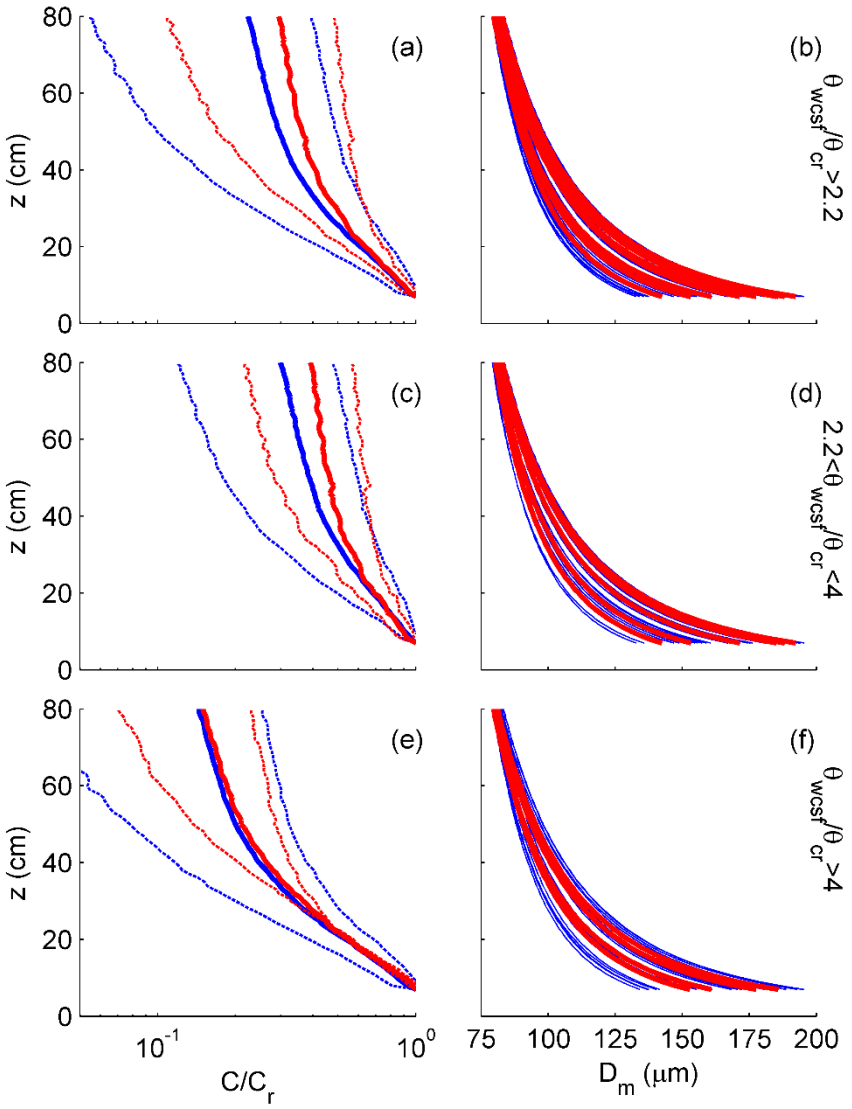

Figure 6.10. Mean normalized concentration (±1 standard deviation dashed lines) left column) and grain size (right column) profiles for GA. The top row represents all forcing conditions while the middle row is for $\theta_{wcsf}/\theta_{cr}$ >4 while the bottom row is for weaker $\theta_{wcsf}/\theta_{cr}$ but greater than 2.2. The red lines correspond to linear-quasi-linear ripples while the blue lines correspond to linear ripples.

The longer LB data set included a variety of wave forcing conditions and various ripple types. The normalized suspension profiles for each ripple type and comparisons of each are show in Figure 6.11. As ripples of various irregularity are present, a distinction

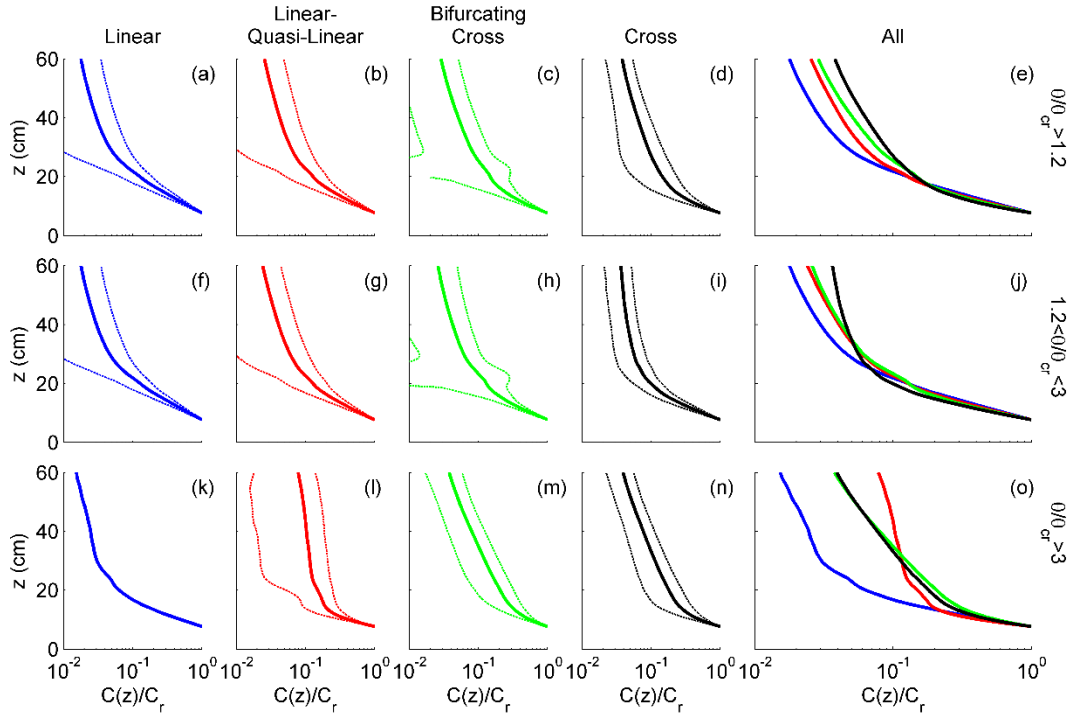

Figure 6.11. Mean suspension profiles (solid line) for linear (blue), linear-quasi-linear (red), bifurcating and cross (green), and cross (black) ripples for the Long Bay field deployment. The mean (±1 standard deviation dashed lines) is calculated over all forcing conditions where sediment is in suspension, in the middle row the mean is calculated for conditions where sediment is in suspension but $\theta/\theta_{cr}<3$, while the bottom row is all conditions when $\theta/\theta_{cr}>3$.

between the vertical extents of sediment convection becomes apparent. For all wave forcing conditions (Figure 6.12) it is seen that for linear ripples (Figure 6.12a), the convective profile fits the mean profile up to an elevation of 20.9 cm, after which the profile begins to conform with a diffusive fit. The extent is less (16.5 cm) for linear-quasi-linear ripples while it is only 13.2 cm for bifurcating and cross ripples and 11 cm for cross-ripples. The profiles in Figure 6.11 maintain a similar shape for all forcing conditions. The one exception is linear-quasi-linear ripples for high wave energies (Figure 6.11 l and o), though only 3 profiles are present, leading to a high degree of uncertainty.

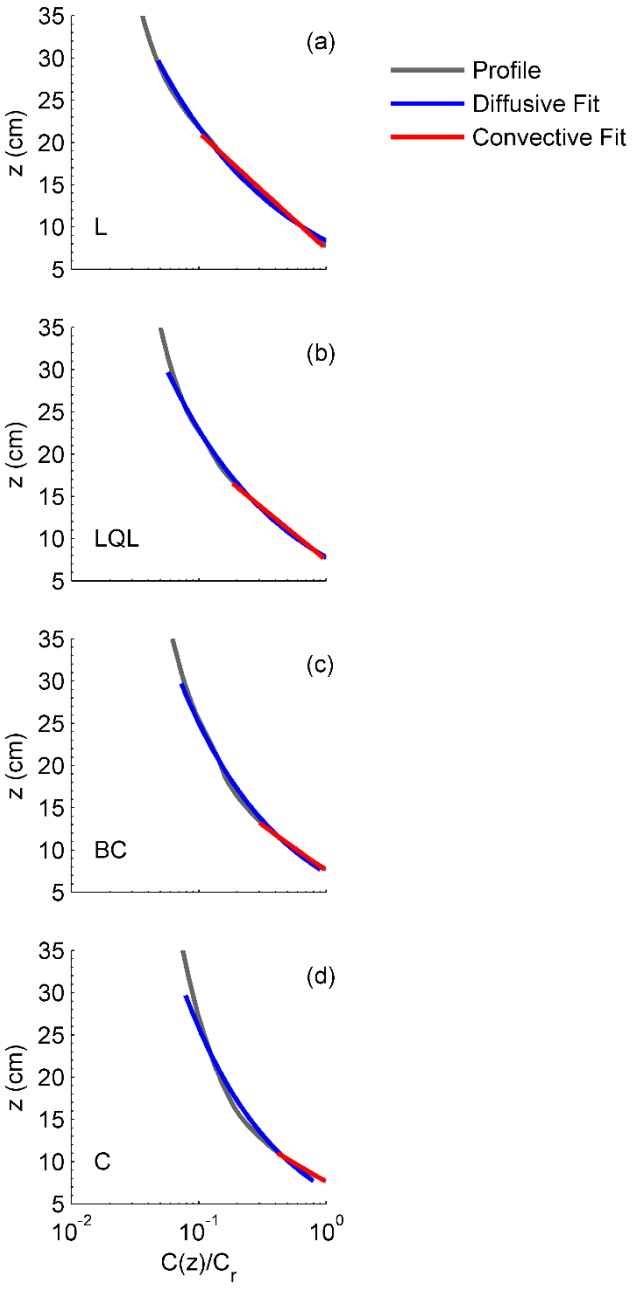

Figure 6.12. Mean suspended sediment profiles (black line) for (a) linear ripples (L), (b) linear-quasi-linear (LQL) ripples, (c) bifurcating and cross ripples (BC), and (d) cross ripples (C) for LB showing the differences between the convective (red) and diffusive fits.

Based on the above observations, the suspended sediment concentration profile can be represented as:

$$C(z) = \begin{cases} C_r \exp(-z/L_s) & z < z_{cv} \\ C(z = z_{cv})(z/z_r)^{-P} & z > z_{cv} \end{cases} \quad 6.31$$

where z_{cv} is the vertical extent of convection and dependent on the ripple shape. The values for P and L_s are not evaluated in this study. P requires measurement of the shear velocity and no measurements are available for the GA event, and too few are available for LB to draw significant conclusions (see chapter 5).

Since linear ripples exhibit the least variation in orientation (I_α), a dependence of z_{cv} upon the angle between waves and ripples will be apparent. However, since linear ripples are only stable when aligned with the wave forcing direction, there are very few measurements for large angles. The available profiles for linear ripples are plotted in Figure 6.13 for the angle between the ripple orientation and wave forcing direction (α_{wr}). A comparison of all the angles shows that for $\alpha_{wr}<35°$ and $\alpha_{wr}>60°$, the profiles are similar up to 25 cm, after which the profile for $\alpha_{wr}>60°$ diverges to smaller C/Cr ratios. However, based on the shape of the profile, $\alpha_{wr}>60°$ tends to resemble a diffusive profile compared to smaller angles. The one outlier is for angles between 35° and 60°. As with $\alpha_{wr}>60°$, there were very few measurements for this angle (N=7) while there were 54 and 57 measurements for $\alpha_{wr}<10°$ and $10<\alpha_{wr}<35°$, respectively. As such, it is difficult to determine if a unique process is occurring at this angle or if it is just noise. Furthermore, at larger angles, linear ripples become unstable and may have been in a transitional state during the ABS burst but still linear at the time of the sonar scan.

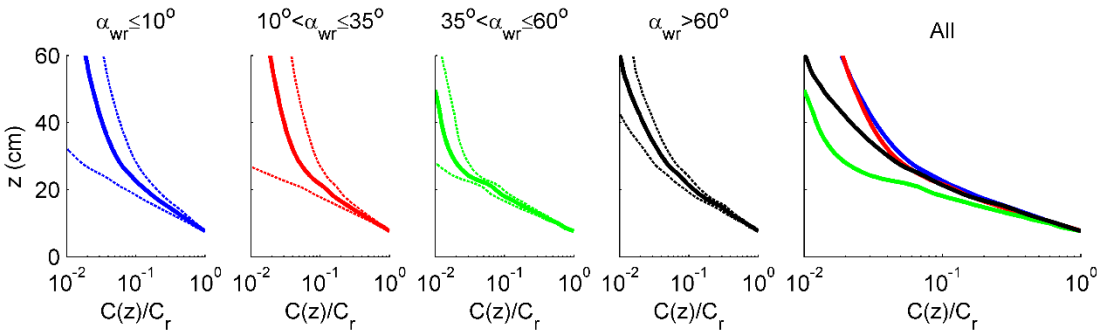

Figure 6.13. Mean suspension profiles for linear ripples (solid line) for the angle between waves and ripples with (α_{wr})<10° (blue), 10°< α_{wr}<35° (red), 35°<α_{wr}<=60° (green), and α_{wr}>60° (black) for the Long Bay field deployment. The mean (±1 standard deviation dashed lines) is calculated over all forcing conditions where sediment is in suspension.

6.5. Summary and Conclusion

Field data from two experiments were used to evaluate the influence of bedforms on the vertical suspension of sediment. This was accomplished by converting backscatter measured by an ABS to concentration. The resulting profiles were used to determine a nearbed reference concentration and subsequently compared to the predictors of *Nielsen* [1993], *Green and Black* [1999], *Lee et al.* [2004] and *Van Rijn* [1984]. The data shows that the reference concentration best correlates to the wave skin friction Shields parameter. The correction for ripples proposed by *Nielsen* [1992] increased the scatter while *Lee et al.* [2004] and *Van Rijn* [1984] did not yield consistent results between the Long Bay and Georgia data sets. No diverging trend was observed for the various ripple types present at either LB or the two mostly linear ripples present at GA. This is not surprising since sediment initiation is primarily dependent on skin friction (grain roughness) while form drag plays a larger role in maintaining suspension of sediment.

The concentration and grain size profiles from GA did not show significant variation with ripple type though a slight decrease in the vertical extent of convection was

present. As both ripples were nearly the same shape, the overall similarity was expected. However, the Long Bay profiles indicated that convection dominated suspension near the bed, while for greater elevations diffusive suspension becomes more dominant. The elevation of this transition appears to depend on the ripple type present with convection dominant to greater elevations when linear ripples are present and decreases for increasingly irregular ripples. It should be noted that while the overall mean trends indicate this dependence, significant variation was present for each ripple type. Laboratory experiments where ripple orientation and shape can be controlled would be beneficial to determine the overall importance of these findings.

CHAPTER 7

CONCLUSIONS

The key questions addressed in this dissertation are:

(1) What are the temporal and spatial evolutionary characteristics of a seabed in response to a changing wave forcing and orientation?

(2) Does the ripple shape (irregularity) influence seabed roughness or sediment resuspension profiles?

7.1. Ripple Evolution

In chapters 2 to 4, the temporal and spatial evolution of ripple geometry and irregularity were evaluated for a variety of wave forcing conditions. In chapter 2, a large database of equilibrium ripple geometries was compiled from literature and enhanced with ripples from the two field sites disused in this dissertation (Long Bay, SC (LB) and Georgia (GA)). These ripples were compared to a diverse set of hydrodynamic and sediment parameters and it was found that as an entire set, ripples scaled best with the ratio of the wave semi-orbital excursion to the median grain diameter ($A_{b,1/3}/D_{50}$) and ripples formed by monochromatic waves scaled differently than those of random waves. Monochromatic waves, which for this data set were solely laboratory experiments, scaled more strongly with the semi-orbital excursion while random waves, a mixture of laboratory and field ripples, scaled more with sediment diameter. When treated as a whole, the trends of ripples formed by both irregular and regular waves can be predicted by equation (2.44).

While the wavelength scaled differently for two wave types, there was less deviation observed for ripple steepness, which was nearly constant with a slight decrease for increasing wavelength.

In chapter 3, it was shown that ripple evolution is a dynamic process where magnitude, direction, and duration of wave forcing controls ripple geometry and irregularity. Under high-energy events, ripples adjust rapidly toward a new equilibrium geometry and quickly become linear. However, under weaker conditions, the ripples become more irregular as bifurcations and terminations begin to appear. Under constantly changing forcing magnitude and/or direction, the rippled bed becomes highly disorganized until the flow becomes stable.

The intensity of the wavenumber (I_k) and orientation (I_α) irregularity present on the seabed was quantified by taking a 2-D FFT of the sonar imagery, calculating the spectral width of the wavenumber and orientation (polar coordinates), and normalizing by the mean wavenumber and π. It was observed that for specific ranges of irregularity, similar ripple plan-form shapes occurred. For small values, the seabed was composed of linear 2-D ripples while for larger values more irregularity was present. Based on these values, ripples were classified as linear (L), linear quasi-linear (LQL), quasi-linear (QL), cross-ripples (C), bifurcating cross-ripples (BC) and disorganized beds (D).

Another observation was an apparent decrease in ripple height when the ripple orientation changed. While, in situ measurements of ripple height were not recorded during these deployments, there is an apparent flattening of the ripple crests (from the sonar images) during reorientation, which signifies a decrease in height.

In order to predict the spatial and temporal evolution of the ripples, the 1-D time depended ripple model from *Traykovski* [2007] was expanded into two dimensions, which allowed the seabed evolution to be represented as a 2-D spectrum. Choosing a spectral model allows for the calculation of multiple ripple trains as well as the calculation of I_k and I_α. This model was run for both LB and GA. Better agreement was found between the observed ripple dimensions and that of the 2-D model compared to that of *Soulsby and Whitehouse* [2005], *Traykovski* [2007], and assuming equilibrium geometry. Furthermore, this model captured the decrease in ripple height when ripples reoriented to a new forcing direction.

7.2. Roughness and Suspended Sediment Concentration

In chapters 5 and 6, ripple geometry, irregularity, and orientation were evaluated to determine their influence on the seabed roughness experienced by the mean flow and the influence of ripple shape on the sediment suspension profile. In chapter 5, a large degree of scatter was present for bin averaged C_D, however, comparing mean values indicated that C_D increases with increasing ripple height while decreasing with increasing ripple irregularity. No deviation was observed between the ripple orientation and current direction, though this is attributed to the weak current strengths.

For sediment resuspension (chapter 6), reference concentration were found not to be dependent on the ripple shape but on the skin friction Shields parameter. However, the suspension profiles indicate that convection is capable of suspending sediment to greater elevations when linear ripples are present than when more irregular ripples are present.

7.3. Future Directions

7.3.1. Ripple Height

One of the significant findings from the 2-D model and visual interpretation of seabed imagery is an apparent decrease in ripple height when the ripple adjusts orientation. This is something not predicted by the SW method but had been noted for field ripples by *Hay* [2011]. While these results appear to agree with the sonar imagery and bed elevations measured by the instrumentation, the actual behavior of this model against data where ripple height is known would be an invaluable calibration tool. The uncertainty in ripple height might explain some of the large scatter seen in the analysis in section 5.4 and the poor trend observed for ripple asymmetry, a value typically associated with form roughness.

7.3.2. 2nd order ripples and wave spectrum

While the 2-D model in chapter 4 improves the prediction of ripple wavelength and orientation, there are two factors, which need further development. The model developed uses a statistical representation of the wave forcing ($u_{b,1/3}$, T, α_w). These accurately characterize the peak ripple spacing and orientation, but often the model fails to predict the occurrence of 2nd order ripples and yield irregularities much smaller than the observed seabed. It is likely the spatial variability is influenced by the wave spectrum and the various directions and forcing that occur over a wave group. It would be worth expanding this model to accept a wave spectrum as an input to determine if the various forcings improve predictions of irregularity.

7.3.3. Bed load Transport and Ripple Adjustment Time

One observation while running the 2-D model (chapter 4) is the adjustment time scale (T_k, equation (4.12)) required a scaling factor to be applied in order to improve the agreement with the LB and GA. This scaling factor is assumed a result of uncertainty in the bed load transport rate as several prediction methods exists. Many of these were tested as well as various other adjustments but none yield improvements to both LB and GA. Determining the differences was outside the scope of this study but it is possible that the shape of the ripple and/or angle between the ripple crest and wave direction might alter the sediment transport rate or adjustment time scale. An ideal experimental setup would be in a laboratory where the shape of the ripple and wave forcing can be controlled while continuous high-resolution observations can be made.

7.3.4. Convective Sediment Resuspension

Analysis from chapter 6 indicates an importance upon the vertical extent of convective sediment resuspension and ripple shape. However, the dependence upon ripple orientation for linear ripples was inconclusive since nearly all occurrences are for small angles when the ripple crest and the wave direction are nearly perpendicular. It is unusual for linear ripples to occur when the waves are at a large angle, as irregularities would begin to develop. However, for large ripples where the adjustment time is longer, this is likely to occur. As such, experiments where the wave direction can be varied under constant forcing and the concentration profiles measured would be helpful in determining if any dependence exists.

REFERENCES

Amos, C. L., Bowden, A. J., Huntley, D. A., and F. M. Lewis (1988), Ripple generation under the combined influences of waves and currents on the Canadian continental shelf, *Cont. Shelf Res*., *8*, 1129-1153.

Andersen, K. H. (2001), A particle model of rolling grain ripples under waves, *Phys Fluids.*, *13*, 58-64.

Ardhuin, F., Drake, T. G., and T. H. C. Herbers (2002), Observations of wave-generated vortex ripples on the North Carolina continental shelf, *J. Geophys. Res.*, *107*(C10), 3143, doi:10.1029/2001JC000986.

Ardhuin, F., O'Reilly, W. C., Herbers, T. H. C, and P. F. Jessen (2003), Swell Transformation across the Continental Shelf. Part I: Attenuation and Directional Broadening, *J. Phys. Oceanogr.*, *33*, 1921–1939.

Bagnold, R. A. (1946), Motion of Waves in Shallow Water. Interaction between Waves and Sand Bottoms. Proceedings of the Royal Society of London, *Series A, Mathematical and Physical Sciences*, *187*, pp. 1-18.

Baldwin, W. E., Morton, R. A., Denny, J. F., Shawn, W. C., Gayes, P. T., and N. W. Driscoll (2004), Maps showing the stratigraphic framework of South Carolina's Long Bay from Little River to Winyah Bay, USGS Open-File Report: 2004-1013, http://pubs.er.usgs.gov/publication/ofr20041013.

Barnhardt, W. A. (ed.) (2009), Coastal change along the shore of northeastern South Carolina—the South Carolina Coastal Erosion Study: U.S. Geological Survey Circular 1339, 77.

Barrantes, A. I., and O. S. Madsen (2000), Near-bottom flow and flow resistance for currents obliquely incident to two-dimensional roughness elements, *J. Geophys. Res.*, *105*(C11), 26,253-26,264.

Bhaganagar, K., and T. J. Hsu (2009), Direct numerical simulations of flow over two-dimensional and three-dimensional ripples and implication to sediment transport: Steady flow. *Coastal Eng.*, *56*(3), 320-331.

Bies, D. A. J. (1955), Attenuation in magnesium sulfate solutions, *Chem. Phys.*, *23*, 428.

Blondeaux, P. (1990), Sand ripples under sea waves. Part 1. Ripple formation, *J. Fluid Mech*, *218*(1), 17.

Bolanos, R., Thorne, P. D., and J. Wolf (2012), Comparison of measurements and models of bed stress, bedforms and suspended sediments under combined currents and waves, *Coastal Engineering*, *62*, 19-30.

Bosman, J. J. (1981), Bed Behaviour and Sand Concentration Under Oscillatory Water Motion, *Rep. on Model Investigation M 1695 Part 1*, Delft Hydraulics Lab., Delft, The Netherlands.

Boyd, R., Forbes, D. L., and D. E. Heffler (1988), Time-sequence observations of wave-formed sand ripples on an ocean shoreface, *Sedimentology*, *35*, 449-464, doi:10.1111/j.1365-3091.1988.tb00997.x.

Brown, J. (2006), Sea-bed response to non-breaking waves. B.S. thesis, Ohio State University, United States.

Businger, J. A., Wyngaard, J. C., Izumi, Y., and E. F. Bradley (1971), Flux profile relationships in the atmospheric surface layer, *J. Atmos. Sci.*, *28*, 190-201.

Carstens, M. R., Neilson, F. M., and H. D. Altinbilek (1969), Bed forms generated in the laboratory under an oscillatory flow: Analytical and experimental study. *Tech. Memo. 28*, 105 pp., U.S. Army Corps of Engineers, Coastal Engineering Research Center, Vicksburg, MS, United States.

Collins, M. B. and G. Voulgaris (1993), Empirical Field and Laboratory Evaluation of a Real-Time Acoustic Sea Bed Surveying System, *Proc. Inst. Acoustics*, *15*(2), 343-351.

Chotiros, N. P., Smith, E., and J. N. Piper (2002), Refraction and scattering into a sandy ocean sediment in the 30-40-kHz band. *IEEE J. Ocean. Eng.*, *27*(3), 362-375.

Clifton, H. E. (1976), Wave-formed sedimentary structures: A conceptual model, in Beach and Nearshore Sedimentation, Edited by R. A. Davis Jr. and R. L. Ethington, *Spec. Publ. SEPM Soc. Sediment. Geol.*, *24*, 126-148.

Clifton, H. E., and J. R. Dingler (1984), Wave-formed structures and paleoenvironmental reconstruction, *Mar. Geol.*, *60*, 165-198, doi:10.1016/0025-3227(84)90149-X.Dietrich, W.E. (1982), Settling velocity of natural particles, *Water Resour. Res.*, *18*, 1615-1626, doi:10.1029/WR018i006p01615.

Davis, J. P., Walker, D. J., Townsend, M., and I. R. Young (2004), Wave-formed sediment ripples: Transient analysis of ripple spectral development, *J. Geophys. Res.*, *109*, C07020, doi:10.1029/2004JC002307.

Deacon, E. L. (1959), The measurement of turbulent transfer in the lower atmosphere, *Adv. Geophys.*, *6*, 211-228.

Dingler, J. (1974), Wave-formed ripples in nearshore sands, Ph.D. thesis, Univ. of Calif., San Diego, United States.

Dolphin, T. and C. Vincent (2009), The influence of bed forms on reference concentration and suspension under waves and currents, *Cont. Shelf. Res.*, *29*, 424-432.

Doucette, J. S. (2000), The distribution of nearshore bedforms and effects on sand suspension on low-energy, micro-tidal beaches in Southwestern Australia, *Mar. Geol.*, *165*(1), 41-61, doi:10.1016/S0025-3227(00)00002-5.

Doucette, J. S. (2002), Geometry and grain-size sorting of ripples on low-energy sandy beaches: field observations and model predictions. *Sedimentology*, *49*(3), 483-503, doi:10.1046/j.1365-3091.2002.00456.x.

Doucette, J. S., and T. O'Donoghue (2006), Response of sand ripples to change in oscillatory flow, *Sedimentology*, *53*(3), 581-596, doi:10.1111/j.1365-3091.2006.00774.x.

Downing, A., Thorne, P. D., and C. E. Vincent (1995), Backscattering from a suspension in the near field of a piston transducer, *The Journal of the Acoustical Society of America*, 97, 1614.

Drake, D. E., Cacchione, D. A., and W. D. Grant (1992), Shear Stress and Bed Roughness Estimates for Combined Wave and Current Flows Over a Rippled Bed, *J. Geophys. Res.*, *97*(C2), 2319-2326.

Dumas, S., Arnott, R. W. C., and J. B. Southard (2005), Experiments on oscillatory-flow and combined-flow bed forms: implications for interpreting parts of the shallow-marine sedimentary record, *J. Sediment. Res.*, *75*(3), 501-513, doi:10.2110/jsr.2005.039.

Du Toit, C. G., and J. F. Sleath (1981), Velocity measurements close to rippled beds in oscillatory flow, *J. Fluid Mech.*, *112*, 71-96, doi:10.1017/S002211208100030X.

Faraci, C., and E. Foti (2001), Evolution of small scale regular patterns generated by waves propagating over a sandy bottom, *Phys. of Fluids*, *13*, 1624, doi:10.1063/1.1367871.

Faraci, C., and E. Foti (2002), Geometry, migration and evolution of small-scale bedforms generated by regular and irregular waves, *Coastal Eng.*, *47*(1), 35-52, doi:10.1016/S0378-3839(02)00097-2.

Gibbs, R. J., Matthews, M. D., and D. A. Link (1971), The relationship between sphere size and settling velocity, *J. Sediment. Res.*, *41*(1), 7-18, doi:10.1306/74D721D0-2B21-11D7-8648000102C1865D.

Glenn, S. M., and W. D. Grant (1987), A Suspended Sediment Stratification Correction for Combined Wave and Current Flows, *J. Geophys, Res*. *92*(C8), 8244-8264.

Grant, W. D., and O. S. Madsen (1982), Movable bed roughness in unsteady oscillatory flow, *J. Geophys. Res.*, *87*(C1), 469-481, doi:10.1029/JC087iC01p00469.

Grant, W. D., and O. S. Madsen (1986), The continental-shelf bottom boundary layer. *Annu. Rev. Fluid Mech.*, *18*(1), 265-305, doi:10.1146/annurev.fl.18.010186.001405.

Grasmeijer, B. T., and M. G. Kleinhans (2004), Observed and predicted bed forms and their effect on suspended sand concentrations. *Coastal Eng.*, *51*(5), 351-371, doi:10.1016/j.coastaleng.2004.05.001.

Grasmeijer, B. T., and L. C. van Rijn (1999), Transport of fine sands by currents and waves. III: Breaking waves over barred profile with ripples, *J. Waterw. Port Coast. Ocean Eng.*, *125*(2), 71-79, doi:10.1061/(ASCE)0733-950X(1999)125:2(71).

Gutierrez, B. T., Voulgaris, G., and E. R. Thieler (2005), Exploring the persistence of sorted bedfroms on the inner-shelf of Wrightsville Beach, North Carolina, *Cont. Shelf Res.*, *25*, 65-90.

Gutierrez, B. T., Voulgaris, G., Work, P. A. (2006), Cross-shore variation of wind-driven flows on the inner shelf in Long Bay, South Carolina, United States, *J. Geophys. Res.*, *111*, C03015, doi:10.1029/2005JC003121.

Hanes, D. M., Alymov, V., Chang, Y. S., and C. Jette (2001), Wave-formed sand ripples at Duck, North Carolina, *J. Geophys. Res.*, *106*(C10), 22575-22592, doi:10.1029/2000JC000337.

Hay, A. E. (2008), Near-bed turbulence and relict waveformed sand ripples: Observations from the inner shelf, *J. Geophys. Res*., *113*, C04040, doi:10.1029/2006JC004013.

Hay, A. E. (2011), Geometric bed roughness and the bed state storm cycle, *J. Geomphys. Res. Oceans*, *116*, C04017, doi:10.1029/2010JC006687.

Hay, A. E., and D. J. Wilson (1994), Rotary sidescan images of nearshore bedform evolution during a storm, *Mar. Geol.*, *119*(1), 57-65, doi:10.1016/0025-3227(94)90140-6.

Hayakawa, N., Tsujimoto, G., and H. Hashimoto (1983), Velocity distribution and suspended sediment concentration over large-scale ripples, *Coast. Eng. Jpn.*, *26*, 91-100.

Herbers, T. H. C., Elgar, S., Guza, R. T. (1999), Directional spreading of waves in the nearshore, *J. Geophys. Res.*, *104*(C4), 7683-7693.

Horikawa, K., and A. Watanabe (1967), A study on sand movement due to wave action, *Coast. Eng. Jpn.*, *10*, 39-57.

Huettel, M., Ziebis, W., Forster, S., and G. W. Luther III (1998), Advective transport affecting metal and nutrient distributions and interfacial fluxes in permeable sediments, *Geochim. Cosmochim. Acta*, *62*(4), 613-631, doi:10.1016/S0016-7037(97)00371-2.

Hume, T. M., Green, M. O., and J. W. Oldman (1999), What happens at the seabed off a headland during a tropical cyclone, In *Coastal Sediments (1999)*, edited by N. C. Kraus and W. G. McDougal, Reston, VA., United States, ASCE, pp. 1836-1851.

Huntley, D. A., Coco, G., Bryan, K. R., Murray, A. B. (2008), Influence of "defects" on sorted bedform geometry, *Geophysical Research Letters*, *35*(L02601), doi:10.1029/2007GL030512.

Inman, D. L. (1957), *Wave-generated ripples in nearshore sands* (No. TM-100), Scripps Institution of Oceanography, La Jolla, CA, United States.

Jackson, D. R., Williams, K. L., Thorsos, E. I., and S. G. Kargl, S. G. (2002), High-frequency subcritical acoustic penetration into a sandy sediment, *IEEE J. Ocean. Eng.*, *27*(3), 346-361, doi:10.1109/JOE.2002.1040923.

Jarno-Druaux, A., Brossard, J., and F. Marin (2004), Dynamical evolution of ripples in a wave channel. *European J. of Mechanics B/Fluids*., *23*, 695-708.

Jonsson, I. G. (1966). Wave Boundary Layers and Friction Factors. *Proc. Coastal Eng.*, *1*(10), Tokyo, Japan, doi:10.9753/icce.v10.

Kennedy, J. F., and M. Falcon (1965), *Wave-generated sediment ripples*, Hydrodynamics Laboratory, Department of Civil Engineering, Massachusetts Institute of Technology.

Khelifa, A., and Y. Ouellet (2000), Prediction of sand ripple geometry under waves and currents, *J. Waterw. Port Coast. Ocean Eng.*, *126*(1), 14-22, doi:10.1061/(ASCE)0733-950X(2000)126:1(14).

Kim, H. (2004), Effective Form Roughness of Ripples for Waves, *J. Coastal Res.*, *20*(3), 731-738, doi:10.2112/1551-5036(2004)20[731:EFRORF]2.0.CO;2.

Kobayashi, N., and O. S., Madsen (1985), Turbulent flows over a wavy bed, *Journal of Geophysical Research: Oceans (1978–2012)*, *90*(C4), 7323-7331.

Kolmogorov, A. N. (1941), The Local Structure of Turbulence in Incompressible Viscous Fluid for Very Large Reynolds Numbers, *Dokl. Akad. Nauk SSSR*, *30*, 301-305. Rpt. In *Proceedings: Mathematical and Physical Sciences* (1991), Turbulence and Stochastic Process: Kolmogorov's Ideas 50 Years On, *434*(1890), 9-13.

Komar, P. D. (1974), Oscillatory ripple marks and the evaluation of ancient wave conditions and environments, *J. Sediment. Res.*, *44*(1), 169-180.

Lacy, J. R., D. M. Rubin, H. Ikeda, K. Mokudai, and D. M. Hanes (2007), Bed forms created by simulated waves and currents in a large flume, *J. Geophys. Res.*, 112, C10018.

Laursen, E. M., (1958), The Total Sediment Load of Streams, Journal of the Hydraulics Division: Proceedings of the American Society of Civil Engineers, 84(HY 1 paper 1530), 1-36.

Lee, G. H., Dade, W. B., Friedrichs, C. T., and C. E. Vincent (2004), Examination of reference concentration under waves and currents on the inner shelf, *J. of Geophys. Res.: Oceans (1978–2012)*, *109*(C2).

Leonard, R. W., Combs, P. C., and L. R. Skidmore (1949), Attenuation of sound in sea water, *J. Acoust. Soc. Am*., *21*, 63.

Li, M. Z., C. L. Amos (1998), Predicting ripple geometry and bed roughness under combined waves and currents in a continental shelf environment, *Cont. Shelf Res.*, *18*(9), 941-970, doi:10.1016/S0278-4343(98)00034-X.

Lofquist, K. E. (1978). *Sand ripple growth in an oscillatory-flow water tunnel* (No. CERC-TP-78-5). Coastal Engineering Research Center, Fort Belvoir, VA, United States.

Madsen, O., Negara, A., Lim, K., and H. Cheong (2010), Near-Bottom Flow Characteristics of Currents at Arbitrary Angle to 2D Ripples, *Proc. Coastal Eng., 1*(32), 12 pp., doi:10.9753/icce.v32.currents.36.

Maier, I., and A. E. Hay (2009), Occurrence and orientation of anorbital ripples in near-shore sands, *J. Geophys. Res. Oceans*, *114*(F04022), doi:10.1029/2008JF001126.

Malarkey, J., and A. G. Davies (2003), A non-iterative procedure for the Wiberg and Harris (1994) oscillatory sand ripple predictor, *J. Coast. Res.*, *19*(3), 738-739.

Medwin, H. and C. S. Clay (1998), *Fundamentals of Acoustical Oceanography*, Academic Press, San Diego, CA, 712 pp.

Meyer, F. (1994), Topographic distance and watershed lines, *Signal processing*, *38*(1), 113-125.

Meyer-Peter, E., and R. Müller (1948), Formulas for bed-load transport. In *Proceedings of the 2nd Meeting of the International Association for Hydraulic Structures Research,* Delft: International Association of Hydraulic Research, pp. 39-64.

Miller, M. C., and P. D. Komar (1980), A field investigation of the relationship between oscillation ripple spacing and the near-bottom water orbital motions, *J. Sediment. Res.*, *50*(1), 183-191.

Mogridge, G. R. (1972), Wave Generated Bed Forms, Ph.D. Thesis, Department of Civil Engineering, Queen's University at Kingston, Vancouver, Canada, 1123-1142.

Mogridge, G. R., Davies, M. H., and D. H. Willis (1994), Geometry prediction for wave-generated bedforms, *Coastal Eng.*, *22*(3), 255-286, doi:10.1016/0378-3839(94)90039-6.

Mogridge, G. R., and J. W. Kamphuis, J. W. (1972). Experiments on bed form generation by wave action. *Proc. Coastal Eng.*, *1*(13), doi:doi:10.9753/icce.v13.

Murray, A. B., E. R. Thieler (2004), A new hypothesis and exploratory model for the formation of large-scale inner-shelf sediment sorting and "rippled scour depressions", *Cont. Shelf Res.*, *24*, 295-315.

Nelson, T. R., Voulgaris, G., and P. Traykovski (2013), Predicting wave-induced ripple equilibrium geometry, *J. Geophys. Res. Oceans*, 118, 3202–3220, doi:10.1002/jgrc.20241.

Nielsen, P. (1979), Some basic concepts of wave sediment transport, *Series Paper No. 20*, Technical University of Denmark, Institute of Hydrodynamics and Hydraulic Engineering, Lyngby, Denmark.

Nielsen, P. (1981), Dynamics and geometry of wave-generated ripples, *J. Geophys. Res.*, *86*(C7), 6467-6472, doi:10.1029/JC086iC07p06467.

Nielsen, P. (1984), Field measurements of time-averaged suspended sediment concentrations under waves, *Coastal Eng.*, *8*(1), 51-72, doi:10.1016/0378-3839(84)90022-X.

Nielsen, P. (1992), Coastal Bottom Boundary Layers and Sediment Transport, World Sci,. Singapore.

Nieuwjaar, M., and T. Van der Kaay (1987), Sediment Concentration and Transport in case of irregular Non-Breaking Waves with a Current, Delft Tech. Univ., Civ. Eng. Dep., Delft, The Netherlands.

O'Donoghue, T., and G. S. Clubb (2001), Sand ripples generated by regular oscillatory flow, *Coastal Eng.*, *44*(2), 101-115, doi:10.1016/S0378-3839(01)00025-4.

O'Donoghue, T., Doucette, J. S., Van der Werf, J. J., and J. S. Ribberink (2006), The dimensions of sand ripples in full-scale oscillatory flows, *Coastal Eng.*, *53*(12), 997-1012, doi:10.1016/j.coastaleng.2006.06.008.

Pedocchi, F., and M. H. García (2009a), Ripple morphology under oscillatory flow: 1. Prediction, *J. Geophys. Res.*, *114*, C12014, doi:10.1029/2009JC005354.

Pedocchi, F., and M. H. García (2009b), Ripple morphology under oscillatory flow: 2. Experiments, *J. Geophys. Res.*, 114, C12015, doi:10.1029/2009JC005356.

Powell, H., Voulgaris, G., Collins, M. B., and A. C. Bastos (2000), Wave-current interaction over bedforms: observations and model predictions, *Marine Sandwave Dynamics*, March 23-24 2000, Lille 1 University, Lille, France, edited by Trentesaux, A. and Garlan, T., pp. 153-160.

Powell, H., Voulgaris, G., Collins, M. B., Bastos, A. C., and R. L. Soulsby, (2000), Sediment transport rates over bedforms: observations and model predictions. *Marine Sandwave Dynamics*, March 23-24 2000, Lille 1 University, Lille, France, edited by Trentesaux, A. and Garlan, T., pp. 161-168.

Precht, E., and M. Huettel (2003), Advective pore-water exchange driven by surface gravity waves and its ecological implications, *Limnol. Oceanogr., 48*(4), 1674-1684.

Precht, E., and M. Huettel (2004), Rapid wave-driven advective pore water exchange in a permeable coastal sediment, *J. Sea Res.*, *51*, 93-107, doi:10.1016/j.seares.2003.07.003.

Ribberink, J. S. (1998), Bed-load transport for steady flows and unsteady oscillatory flows, *Coastal Engineering*, *34*(1), 59-82.

Ribberink, J. S., and A. A. Al-Salem (1994), Sediment transport in oscillatory boundary layers in cases of rippled beds and sheet flow, *J. Geophys. Res.*, *99*(C6), 12707-12727, doi:10.1029/94JC00380.

Ribberink, J., L. C. van Rijn (1987), Influence of Wave-asymmetry and Wave-irregularity on Time and Bed Averaged Sediment Concentrations, *Report H186-00-1*, Delft Hydraulics, Delft, The Netherlands.

Rocha, C. (2008), Sandy sediments as active biogeochemical reactors: compound cycling in the fast lane, *Aquatic Mictobial Ecology*, *53*, 119-127, doi:10.3354/ame01221.

Rouse, H. (1937), Modern conceptions of the mechanics of fluid turbulence, *Transactions of ASCE*, *102*(1937), 463-505.

Sakakiyama, T., Shimizu, T., Kajima, R., Saito, S., and K. Maruyama (1986), Sand ripples generated by prototype waves in a large wave flume, *Coast. Eng. Jpn.*, *28*, 147-160.

Sato, S. (1987), Oscillatory boundary layer flow and sand movement over ripples. Ph.D. thesis, Univ. Of Tokyo, Tokyo.

Schwab, W. C., Gayes, P. T., Morton, R. A., Driscoll, N. W., Baldwin, W. E., Barnhardt, W. A., Denny, J. F., Harris, M. S., Katuna, M. P., Putney, T. R., Voulgaris, G., Warner, J. C., and E. E. Wright (2009), Coastal Change Along the Shore of Northeastern South Carolina-The South Carolina Coastal Erosion Study, Edited by W. A. Barnhardt, USGS Circular 1339, 77 pp.

Shaw, W. J., and J. H. Trowbridge (2001), The direct estimate of near-bottom turbulent fluxes in the presence of energetic wave motions. J. Atmos. Oceanic Technol., 18(9), 1540-1557, doi: 10.1175/1520-0426(2001)018<1540:TDEONB>2.0.CO;2.

Sleath, J. F. (1984), Sea bed mechanics John Wiley and Sons Inc. New York, NY, USA, 335 pp.

Smith, J. D. and S. R. McLean (1977). Spatially averaged flow over a wavy surface, *J. Geophys Res.*, *82*(12), 1735-1746.

Smith, J. D., and S. R. McLean (1977), Boundary layer adjustments to bottom topography and suspended sediment, *Bottom Turbulence: 8th Liege Colloquium on Ocean Hydrodynamics*, 123-152.

Sherwood, C. R., Lacy, J. R., and G. Voulgaris (2006), Shear Velocity estimates on the inner shelf off Grays Harbor, Washington, USA, *Cont. Shelf Res.*, *26*, 1995-2018.

Shields, A. (1936), Application of similarity principles and turbulence research to bed-load movement, *Communications of the Prussian Laboratory of Hydraulics*, *26*, Prussian Laboratory of Hydraulics, Berlin, Germany.

Sleath, J. F. A., (1984), *Sea Bed Mechanics*, Wiley.

Sleath, J. F. A., and S. Wallbridge (2002), Pickup from Rippled Beds in Oscillatory Flow, *J. Waterw. Port Coast. Ocean Eng.*, *128*, 228-237, doi: 10.1061/(ASCE)0733-950X(2002)128:6(228).

Smith, D., and J. F. A. Sleath (2005), Transient ripples in oscillatory flows, *Cont. Shelf Res.*, *25*, 485-501, doi:10.1016/j.csr.2004.10.012.

Soulsby, R. L. (1995), Bed shear-stresses due to combined waves and currents. In: *Advances in Coastal Morphodynamics*, Eds: Stive, M. J. F., De Vriend, H. J. Fredsøe, J., Hamm, L., Soulsby, R. L., Teisson, C., and J. C. Winterwerp,4-20 - 4-23, Delft Hydraulics, Delft, NL.

Soulsby, R. L. (1997), *Dynamics of marine sands: a manual for practical applications*. Thomas Telford Publications, London, England, 249 pp.

Soulsby, R. L., and R. J. S. Whitehouse (2005), Prediction of Ripple Properties in Shelf Seas, Mark 2 Predictor for Time Evolution, *Tech. Rep.TR 154 Release 2.0*, HR Wallingford, Wallingford, U. K.

Soulsby, R. L., Whitehouse, R. J. S., and K. V. Marten (2012), Prediction of time-evolving sand ripples in shelf seas, *Cont. Shelf Res*, *38*, 47-62, doi:10.1016/j.csr.2012.02.016.

Southard, J. B., Lambie, J. M., Federico, D. C., Pile, H. T., and C. R. Weidman (1990), Experiments on bed configurations in fine sands under bidirectional purely oscillatory flow, and the origin of hummocky cross-stratification, *J. Sediment. Res.*, *60*(1), 1-17.

Steetzel, H. J. (1984), Near bottom sediment suspension under oscillatory water motion, *MSc Thesis*, Civ. Eng. Dept. Coast. Div., Techn. Univ. Delft, Delft, The Netherlands.

Styles, R., and S. M. Glenn (2002), Modeling bottom roughness in the presence of wave-generated ripples, *J. Geophys. Res.*, *107*(C8), 3110, doi:10.1029/2001JC000864.

Sullivan, C. M., Warner, J. C., Martini, M. A., Voulgaris, G., Work, P. A.; Haas, K. A., and D. Hanes (2006), South Carolina Coastal Erosion Study, Data Report for Observations, October 2003 – April 2004, *USGS Open-File Report 2005-1429*.

Tennekes, J., and J. L. Lumley (1989), *A First Course in Turbulence*, The MIT Press, 300pp.

Testik, F. Y., Voropayev, S. I., and H. J. S. Fernando (2005), Adjustment of sand ripples under changing water waves, *Physics of Fluids*, *17*, 072104-1:8.

Thorne, P. D., and M. J. Buckingham (2004), Measurements of scattering by suspensions of irregularly shaped sand particles and comparison with a single parameter modified sphere model, *The Journal of the Acoustical Society of America*, *116*, 2876.

Thorne, P. D., and D. M. Hanes (2002), A review of acoustic measurement of small-scale sediment processes, *Continental Shelf Research*, *22*(4), 603-632.

Thorne, P. D., Vincent, C. E., Hardcastle, P. J., Rehman, S., and N. Pearson (1991), Measuring suspended sediment concentrations using acoustic backscatter devices, *Marine Geology*, *98*(1), 7-16.

Thorne, P. D., J. J. Williams, and A. G. Davies (2002), Suspended sediments under waves measured in a large-scale flume facility, *J. Geophys. Res.*, 107(C8), doi:10.1029/2001JC000988.

Thorsos, E. I., and M. D. Richardson (2002), Guest editorial, *IEEE J. Ocean. Eng.*, *27*(3), 341-345, doi: 10.1109/JOE.2002.1040922.

Traykovski, P. (2007), Observations of wave orbital scale ripples and a nonequilibrium time-dependent model, *J. Geophys. Res.*, *112*(C06026), doi:10.1029/2006JC003811.

Traykovski, P., Hay, A. E., Irish, J. D., and J. F. Lynch (1999), Geometry, migration, and evolution of wave orbital ripples at LEO-15, *J. Geophys. Res.*, *104*(C1), 1505–1524, doi:10.1029/1998JC900026.

Trowbridge J., and S. Elgar (2001), Turbulence Measurements in the Surf Zone, *Am. Meteorol. Soc.*, *31*(8), 2403-2417, doi:10.1175/1520-0485(2001)031<2403:TMITSZ>2.0.CO;2.

Van Rijn, L. C. (1984), Sediment transport, Part II: Suspended load transport. *Journal of Hydraulic Engineering*, *110*(11), 1613-1641.

Van Rijn, L.C. (1987), Database Sand Concentration Profiles for Currents and Waves, *Tech. Rep. M 1695-04*, Delft Hydraulics, Delft, The Netherlands.

Van Rijn, L.C. (1993), *Principles of Sediment Transport in Rivers, Estuaries and Coastal Seas*, Aqua Publications, Amsterdam, The Netherlands.

Van Rijn, L. C., and F. J. Havinga (1995), Transport of fine sands by currents and waves. II, *J. Waterw. Port Coast. Ocean Eng.*, *121*(2), 123-133, doi:10.1061/(ASCE)0733-950X(1995)121:2(123).

Van Rijn, L. C., Nieuwjaar, M. W., van der Kaay, T., Nap, E., and A. van Kampen (1993), Transport of fine sands by currents and waves, *J. Waterw. Port Coast. Ocean Eng.*, *119*(2), 123-143, doi:10.1061/(ASCE)0733-950X(1993)119:2(123).

Vongvisessomjai, S., 1984. Oscillatory ripple geometry. J. Hydraul. Eng., 110, 247-266.

Voropayev, S. I., McEachern, G. B., Boyer, D. L., and H. J. S. Fernando (1999), Dynamics of sand ripples and burial/scouring of cobbles in oscillatory flow, *Applied Ocean Research*, *21*, 249-261.

Voulgaris, G., Collins, M. B., Davis, J., and M. Wilkin (1992), RoxAnn Sea Bed Discrimination System: In Situ and Laboratory Evaluation, *Tech. Rep. SUDO/TEC/92/4C*, Department of Oceanography, University of Southampton, U. K.

Voulgaris, G., and J. P. Morin (2008), A long-term real time sea bed morphology evolution system in the South Atlantic Bight, In *Current Measurement Technology, 2008. CMTC 2008. IEEE/OES 9th Working Conference*, IEEE., pp. 71-79, doi:10.1109/CCM.2008.4480847.

Voulgaris, G. and J. H. Trowbridge (1998), Evaluation of the Acoustic Doppler Velocimeter (ADV) for Turbulence Measurements, *J. Atmos. Oceanic Technol.*, *15*(1), 272-289, doi:10.1175/1520-0426(1998)015<0272:EOTADV>2.0.CO;2.

Voulgaris, G., Trowbridge, J. H., Shaw, W. J., and A. J. Williams III (1997), High Resolution Measurements of Turbulent Fluxes and Dissipation Rates in the Benthic Boundary Layer, *Proc. Coastal Dyanmics '97*, *ASCE*, Plymouth, UK, 177-186.

Warner, J. C., Armstrong, B., Sylvester, C. S., Voulgaris, G., Nelson, T., Schwab, W. C., and J. F. Denny (2012), Storm-induced inner-continental shelf circulation and sediment transport: Long Bay, South Carolina. *Cont. Shelf Res.*, *42*, 51-63, doi:10.1016/j.csr.2012.05.001.

Whitehouse, R. J. S., (1998), Scour at marine structures, Scour at Marine Structures: A Manual for Practical Applications. Thomas Telford Publications, London, 198 pp.

Wiberg, P. L., and C. K. Harris (1994), Ripple geometry in wave-dominated environments, *J. Geophys. Res.*, *99*(C1), 775-789, doi:10.1029/93JC02726.

Wiberg, P.L., and C. R. Sherwood (2008), Calculating wave-generated bottom orbital velocities from surface wave parameters, *Comput. Geosci.*, *34*(10), 1243-1262, doi:10.1016/j.cageo.2008.02.010.

Wiberg, P. L., and J. Dungan Smith, (1989), Model for calculating bed load transport of sediment, *Journal of hydraulic engineering*, *115*(1), 101-123.

Wikramanayake P. N., and O. S. Madsen (1994), Calculation of movable bed friction factors, *Tech. Rep. DRP-94-5*, Coastal Engineering Research Center, U.S. Army Corps of Engineers, Vicksburg, MS, United States.

Williams, J. J., Bell, P. S., Thorne, P. D., Metje, N., and L. E. Coates (2004), Measurement and prediction of wave-generated suborbital ripples, *J. Geophys. Res.*, 109(C2), C02004, doi:10.1029/2003JC001882.

Williams, J. J., Bell, P. S., Thorne, P. D., Trouw, K., Hardcastle, P. J., and J. D. Humphery (2000), Observed and predicted vertical suspended sediment concentration profiles and bedforms in oscillatory-only flow, *J. Coast. Res.*, *16*(3), 698-708.

Willis, D. H., Davies, M. H., and G. R. Mogridge (1993), Laboratory observations of bedforms under directional irregular waves, *CAN. J. CIV. ENG.*, *20*(4), 550-563, doi:10.1139/l93-072.

Wilson, O. B. and R. W. Leonard (1954), Measurement of sound absorption in aqueous slat solutions by a resonator method, *J. Acoust Soc. Am.*, *26*, 223-226.

Xu, J.P. (2005), Observations of plan-view sand ripple behavior and spectral wave climate on the inner shelf of San Pedro Bay, California, *Cont. Shelf Res.*, *25*(3), 373-396, doi:10.1016/j.csr.2004.10.004.

Yalin, S., and R. Russell (1962), Similarity in Sediment Transport Due to Waves, *Proceedings of the 8th International Conference on Coastal Engineering*, Mexico City, Mexico, doi:10.9753/icce.v8.12.

APPENDIX A – CHAPTER 2 COPYRIGHT CLEARANCE

JOHN WILEY AND SONS LICENSE
TERMS AND CONDITIONS
May 30, 2013

This is a License Agreement between Timothy R Nelson ("You") and John Wiley and Sons ("John Wiley and Sons") provided by Copyright Clearance Center ("CCC"). The license consists of your order details, the terms and conditions provided by John Wiley and Sons, and the payment terms and conditions.

All payments must be made in full to CCC. For payment instructions, please see information listed at the bottom of this form.

License Number: 3158940477023
License date: May 30, 2013
Licensed content publisher: John Wiley and Sons
Licensed content publication: Journal of Geophysical Research: Oceans
Licensed content title: Predicting wave-induced ripple equilibrium geometry
Licensed copyright line: ©2013. American Geophysical Union. All Rights Reserved.
Licensed content author: Timothy Robert Nelson, George Voulgaris, Peter Traykovski
Licensed content date: May 21, 2013
Start page: n/a
End page: n/a
Type of use: Dissertation/Thesis
Requestor type: Author of this Wiley article
Format: Print and electronic
Portion: Full article
Will you be translating?: No
Order reference number: TRN_DISSERTATION
Total: 0.00 USD